A MICROFABRICATED MICROCANTILEVER ARRAY: A PLATFORM FOR INVESTIGATION OF CELLULAR BIOMECHANICS AND MICROFORCES IN VITRO

By

Kweku A. Addae-Mensah

Dissertation

Submitted to the Faculty of the

Graduate School of Vanderbilt University

in partial fulfillment of the requirements

for the degree of

DOCTOR OF PHILOSOPHY

in

Biomedical Engineering

December, 2008

Approved:

Professor John P. Wikswo

Professor Franz Baudenbacher

Professor Michael Miga

Paul E. Moore M.D

Professor Kevin K. Parker

To the omniscient God almighty the source of all knowledge

and

To my wife Adubea, my siblings, and my parents for their love and support

ACKNOWLEDGEMENTS

I would like to thank the members of my committee for their time and for the support they offered in various ways during my graduate school career. I would like to especially thank my graduate advisor, Dr. John P. Wikswo, for the guidance and help he provided me throughout this process. It has been a truly rewarding experience working in his lab.

I would also like to thank Nicholas Kassebaum, who originally began work on portions of this project and for helping me with the initial fabrication techniques when I first joined the lab. His patience in getting me trained on the tools while on a hectic medical school schedule deserves special mention.

The support and help from Ron Reiserer cannot be overemphasized. His suggestions for alternative protocols and ideas were essential in getting some of my projects done. I really appreciate his valuable time when I needed anything done in the machine shop. I thank Phil Samson for allowing me to "pick" his brains on some occasions.

Support from other VIIBRE staff members was also invaluable. Thanks to Don Berry, Cheryl Cosby, and especially Allison Price for her patience and valuable time in editing the three published manuscripts as well as painstakingly going through this dissertation.

Some other people in other labs also deserve special mention: Dr. Lisa McCawley for introducing me to the "joys" of cell culture and helping me get my very first flask of cells going. Dr. Laura Pentassuglia for her work on isolating and culturing the cardiac myocytes and also for her precious time spent on the confocal microscope; as well as Dr. Doug Sawyer for offering financial support during part of my graduate studies. I would also like to thank Dr. Susan Opalenik for her help with culturing the "notorious" mesenchymal stem cells and her advice and encouragement over the past six months.

I would like to acknowledge VIIBRE, The Whitaker Foundation, and the NIH(R01 HLO68144) for providing financial support in various ways during my graduate studies.

Of course Maame Adubea deserves the most thanks of all. Without her support, patience and understanding through all the decisions I had to make I would not have reached my goals. She has been there through thick and thin.

Lastly I would like to thank my family members for their undying support throughout.

My brothers for letting me see the funny side of things when I was less inclined to do so. My sister for always reminding me that God was ever present in every step that I took, my mum for all the advice and for believing in me and to my dad and his two brothers for being an inspiration.

TABLE OF CONTENTS

LIST OF TABLES

Table **Page**

LIST OF FIGURES

Figure **Page**

2D	Two dimensional.
ADM	Adipogenic differentiation media.
ADP	Adenosine diphosphate.
AFM	Atomic force microscopy.
ATP	Adenosine-5'-triphosphate.
BioMEMS	The application of MEMS technologies and concepts to diverse areas in biomedical research and clinical medicine.
BoN	Bed-of-nails.
CAD	Computer aided design.
CCM	Complete culture medium.
CCP	Capacitively coupled plasma.
DI	De-ionized.
DIC	Differential interference contrast.
DRIE	Dry reactive ion beam etching.
DWP	Dispensing well plate.
e-beam	Electron beam.
EC-coupling	Excitation contraction coupling.
ECM	Extracellular matrix.
ESC	Embryonic stem cell.
FCS	Fetal calf serum.
FFT	Fast fourier transform.
FRAP	Fluorescence recovery after photobleaching.
HASM	Human airway smooth muscle.
HSC	Hematopoietic stem cell.
IC	Integrated circuit.
ICP	Inductively coupled plasma.
IPA	Isopropyl alcohol.
KCL	Potassium chloride.

LED	Light emitting diode.
MEMS	Microelectromechanical systems.
MSC	Mesenchymal stem cell.
MTC	Magnetic twisting cytometry.
NBF	Neutral buffered formalin.
nN	1×10^{-9} Newtons.
ODM	Osteogenic differentiation media.
PBS	Phosphate buffered saline.
PDMS	Polydimethylsiloxane.
pN	1×10^{-12} Newtons.
PVA	Poly (vinyl) alcohol.
RASM	Rat aortic smooth muscle.
RF	Radio frequency.
RIE	Reactive ion etching.
RMS	Root mean square.
rpm	Revolutions per minute.
SAP	Subsarcolemmal adhesion plaques.
sccm	Standard cubic centimeters per minute.
SCREAM	Single-crystal reactive etching and metallization.
SEM	Scanning electron micrograph.
SFLS	Stress fiber like stucture.
SLA	Subcellular laser ablation.
UV	Ultra violet.
VIIBRE	Vanderbilt Institute for Integrative Biosystems Research and Education.

CHAPTER I

INTRODUCTION

Kweku A Addae-Mensah

Department of Biomedical Engineering

Vanderbilt University, Nashville, TN

Over the past few decades, a number of studies have been conducted to establish connections between the structure, mechanical responses, and function of biological tissues, such as the lung, heart, blood vessels, and cardiac muscle. More recently, this trend has led to the development of tools and techniques for probing and manipulating single cells and for monitoring forces arising from cellular processes. These tools and techniques are sensitive enough to detect forces in the nanonewton (nN) to piconewton (pN) range. Most of these techniques have been developed mainly for *in vitro* studies. However Stopak *et al*[1] for example, have been able to show a connection between *in vitro* traction forces generated by cells and formation of large-scale anatomical structures.These results amongst others underscore the importance of using these tools and techniques for *in vitro* studies.

Cells engage in a variety of mechanical activities, many of which are based on mechanical cues, both inside and outside the cell. Evidence suggests that these activities are linked to myriad cellular processes such as locomotion, differentiation, and proliferation. Cells also have attributes similar to common materials, such as mechanical deformation in response to external forces. The forces experienced by and within cells in their physiological environment vary over a wide range. For example the greatest level of shear stress experienced by the vascular endoluminal surface and arterial circulatory system ranges between 1 and 7 Pa[2,3]. These values are relatively constant irrespective of the part of the arterial network considered[3]. A 1 cm length of a typical artery 10 mm in diameter would therefore experience shear forces on the order of 0.5 μN to 5 μN. On the other hand, cartilage typically experiences stresses of 20 MPa, causing the constituent cells (chondrocytes) to alter expression of glycosaminoglycans[4]. Using an estimate of an average of 14.5 cm^2 surface cross-sectional area for articular cartilage[5], this translates to forces of about 30 kN. The forces or stresses experienced *in vivo* by individual cells are determined not only by these shear stresses, which represent macroscopic averages, but also by the details of cell size, geometry, and the local mechanical environment (including intracellular and extracellular heterogeneities). That said, the strength of physiologically significant forces or stresses can easily span a dozen orders of magnitude, from the piconewton and subpiconewton forces detected by single outer and vestibular hair cells in the cochlea[6,7] to

tensile forces which exceed 10 kN in the Achilles and patellar tendons[8]. This range is far larger than that available, for example, to bioelectric signaling.

The mechanical properties of cells, as well as their dysfunction, have been implicated in many aspects of human physiology and pathophysiology. For example, the stiffness of a blood vessel wall is controlled by vascular smooth muscle contraction and deformation, an attribute that is of vital importance in understanding blood distribution, hypertension, and other cardiovascular diseases. Heart failure can result from the inability of cardiac myocytes to contract reliably[9]. When the axons on neural cells are severely stretched due to brain injury, it can lead to cell death[10]. Flow of air through the respiratory tract is likewise dependent on the mechanical properties of airway smooth muscle. Asthma is a disease characterized by excessive airway tightening caused by a spasm of airway smooth muscle cells and a subsequent inability to relax normally[11].

Objectives

The overall goal of this dissertation research was to develop a tool that could be used as a platform to investigate cell mechanobiology and also examine cell traction phenomena on a real-time basis. This goal was evaluated by examining the use of such a system in combination with cell and substrate probing tools for investigation of the relationship between cell stiffness and tensile stress as well as the reactions of cells to mechanical agitation of their underlying substrate. We also investigated how specific substrate geometries affected the way in which cardiac myocytes attach and adapt to their underlying substrates. These studies could lead to a better understanding of cardiac myocyte modulation and could also have implications in cardiac tissue engineering.

Specific Aims

1. Design and fabrication of a BioMEMS device as well as introduction of analysis tools that be can be reliably used to investigate cell mechanical properties and microforces *in vitro*

a. *Microfabricate, using soft lithography techniques, a vertical microcantilever array of polydimethylsiloxane (PDMS) Bed-of-Nails (BoN) to be used for studying cell forces*. A number of strategies to detect cell traction forces have been attempted. Original methods employ the use of continuous fabricated material such as silicone sheets, silicone sheets with embedded beads or fluorescently labeled polyacrylamide sheets. These methods suffer from the need for complex numerical deconvolution to obtain force distributions. The microfabricated microcantilever array (BoN) provides a platform for measuring forces where each force generated at each nail is independent of other forces,hence a complex deconvolution algorithm is not required.

b. *Demonstrate the use of fluorescent Quantum Dot-labeled Bed-of-Nails (BoN) for measuring cellular forces*. Manual tracking of the microcantilever tips to generate displacement and force data was burdensome when the number of images to analyze was large. An automatic tracking routine based on colloidal studies was modified for tracking the microcantilever displacements. Using just the differential interference contrast DIC images for the tracking process proved to be inadequate. The cells introduced artifacts which reduced contrast between the Gaussian-like profile that the microcantilever tips created in (DIC) mode and the cells. Microcontact printing of fluorescent organic dyes on the microcantilever tips eliminated this problem but the cells interacted with these dyes and reduced their signal. To be able to overcome this drawback, the microcantilever array was labeled with fluorescent hydrophobic quantum dots which enabled accurate tracking of the microcantilever array. The quantum dots were less prone to photobleaching than the fluorescent organic dyes and the cells did not interact with them. The fluorescent signal produced by the quantum dots provided much better contrast than bright field or DIC microscopy.

c. *Develop a technique to attach structures to the microcantilevers that will serve as an avenue to allow mechanical perturbation of the microcantilevers*. Original attempts to move individual microcantilevers with pulled glass mi-

cropipettes were successful. The main problem that was encountered with this system was that only microcantilevers on the edges of the array could be moved reliably without too much difficulty. An alternative method was introduced that allowed easier manipulation of the microcantilever arrays. Structures were attached to the arrays by direct lithography. Poly (vinyl alcohol) PVA was used as a lift-off agent to release the composite structures.

2. Demonstrate the implementation of the vertical microcantilever array in biological experimentation.

    a. *Examine the role of myocyte adaptation to underlying substrate and focal adhesion modulation in determining traction force and sarcomere remodeling in isolated rat cardiac myocytes.* Mechanical signaling and force transmission within and outside the cardiac myocyte are important players in the mechanotransduction process, and the cytoskeleton is a significant link between the force-generating sarcomere, the cell membrane, and intracellular stress-sensing components. Another mechanical factor involved in the maintenance of cardiac myocytes is attachment. Cardiac myocytes are known to form focal adhesions for attachment at the distal ends. However, they have also been shown to form cytoskeletal-sarcolemmal attachments normally at points where their Z lines form. These sites are termed costameres and have certain attributes that make them similar to focal adhesions. Also of clinical significance to cardiac research are changes in cell shape, size and contractility as a result of adaptation due to changes in the physiological and pathophysiological environment of cardiac myocytes. We examine the adaptation, attachment, and remodeling of primary adult rat cardiac myocytes to the microfabricated microcantilever arrays. We also examine force distributions for contracting myocytes on the microcantilever arrays.

    b. *Investigate the responses of mesenchymal stem cells to the microcantilever arrays with varying stiffness.* Mesenchymal stem cells are multipotent progenitor cells that are found mainly in the bone marrow of adults. They have

the capability to differentiate and form tissue that is mesenchymal in nature, such as bone, cartilage, muscle, ligament, tendon adipose and stroma. The inductive agents that cause entrance into a particular lineage of mesenchymal stem cells (MSC) leading to eventual formation of a specific tissue/cell type are normally provided by the niche to which they attach after circulation from their site of origin. These external signals include factors secreted by other cell types, cell-cell interactions, as well as cell-extracellular matrix interactions. It has been shown that the extracellular matrix elasticity has an effect on lineage specification. We examine whether microcantilever arrays designed to have different shear stiffness will potentiate differentiation of mesenchymal stem cells when the cells are incubated in culture medium known to cause an entrance into a particular lineage when cells are cultured *in vitro* in plastic well plates.

References

[1] Stopak, D., Wessells, N. K., Harris, A. K. Morphogenetic Rearrangement of Injected Collagen in Developing Chicken Limb Buds. *Proc Natl Acad Sci* **82**, 2804–2808, 1985.

[2] Ali, M., Schumacker, P. Endothelial responses to mechanical stress: Where is the mechanosensor? *Critical Care Medicine* **30**, S198–S206, 2002.

[3] Lehoux, S., Tedgui, A. Cellular mechanics and gene expression in blood vessels. *Journal of Biomechanics* **36**, 631–643, 2003.

[4] Grodzinsky, A., Levenston, M., Jin, M., Frank, E. Cartilage tissue remodeling in response to mechanical forces. *Annual Review of Biomedical Engineering* **2**, 691–+, 2000.

[5] Herberhold, C., *et al.* In situ measurement of articular cartilage deformation in intact femoropatellar joints under static loading. *Journal of Biomechanics* **32**, 1287–1295, 1999.

[6] Liao, Z., Feng, S., Popel, A., Brownell, W., Spector, A. Outer hair cell active force generation in the cochlear environment. *Journal of the Acoustical Society of America* **122**, 2215–2225, 2007.

[7] van Netten, S., Kros, C. Gating energies and forces of the mammalian hair cell transducer channel and related hair bundle mechanics. *Proceedings of the Royal Society of London Series B-Biological Sciences* **267**, 1915–1923, 2000.

[8] Maffulli, N., Wong, J. Rupture of the Achilles and patellar tendons. *Clinics in Sports Medicine* **22**, 761–776, 2003.

[9] Yin, S., Zhang, X., Zhan, C., Wu, J., Xu, J., Cheung, J. Measuring single cardiac myocyte contractile force via moving a magnetic bead. *Biophys.J.* **88**, 1489–1495, 2005.

[10] Smith, D. H., Wolf, J. A., Meaney, D. F. A New Strategy to Produce Sustained Growth of Central Nervous System Axons: Continuous Mechanical Tension. *Tissue Engineering* **7**, 131–139, 2001.

[11] Shore, S. A., Moore, P. E. Regulation of [beta]-adrenergic responses in airway smooth muscle. *Respiratory Physiology & Neurobiology* **137**, 179–195, 2003.

CHAPTER II

BACKGROUND AND SIGNIFICANCE

Kweku A Addae-Mensah,

Department of Biomedical Engineering,

Vanderbilt University, Nashville, TN

Portions of this chapter have been published in:

Kweku A. Addae-Mensah and John P. Wikswo. "Measurement techniques for cellular biomechanics in vitro." *Experimental Biology and Medicine.* 233(7):792809, July 2008.

Techniques that have been developed to study the mechanical properties of cells can be classified in many ways. One broad distinction between the techniques is whether they are "active" or "passive." Methods that apply forces or mechanically load cells in order to deform the cell in a particular manner can be referred to as active methods. Other techniques only sense the mechanical forces (traction forces) generated by cells, but do not themselves apply any forces. These are referred to as passive methods. Since these methods measure a variety of physical quantities, the units of measurement used to represent them can be different. Table 2.1 shows the relationships between the different quantities being measured and their units.

Table 2.1 A summary of various biomechanical parameters and their dimensions, SI units, and ranges of values.

Biomechanical Quantity	Basic Formula	SI or SI Derived Unit	Measured values in biological systems	References
Spring Constant	Force/Distance	Nm^{-1}	2 ± 6 mN/m, 40 pN/nm	[1]
Shear Stress	Force/Area	Pa	1 Pa - 20 MPa	[2–4]
Traction Force	Force	N	4 nN - 140 nN	[5–12]
Dynamic Viscosity	$\frac{Force}{Area} \times Time$	Pa s	$0.6 \times 10^{-4} - 4 \times 10^{-4}$ Pa s	[13]
Youngs/Shear Modulus	Force/Area	Pa	1.130 Pa - 100 kPa	[14–19]

Continued on next page

Table 2.1 (continued)

Biomechanical Quantity	Basic Formula	SI or SI Derived Unit	Measured values in biological systems	References
In-plane shear modulus (Thin incompressible membrane). Analogous to surface tension	Force/Distance	Nm^{-1}	1.7 μN/m - 13.3 μN/m	[20,21]

Active Methods

Cell deformation, whether elastic or viscoelastic, can be studied using tools that generate compressive or tensile forces, shear forces, bending forces, twisting forces, or a combination of some of these methods.

Atomic force microscopy(AFM)

This method involves the use of a sharp tip attached to a flexible cantilever. The tip is used to probe the cell and the relative deformation of the cell and tip can then be used to estimate the force applied and the stiffness of the cell. Figure 2.1 shows the setup used by Radmacher et al[22–24] to investigate the viscoelastic properties of human platelets

Weisenhorn et al[16]examine the local deformation of soft surfaces using the AFM. Included in the samples examined are metastatic smooth muscle cells from human lungs. They generate force-versus-indentation curves for different cell orientations, with the assumption that the cell is homogenous within all areas tested. They report Youngs modulus for the cells between 0.013 and 0.15 MPa. They do report some problems with this

technique, however. Deformation of the cell membrane by the tip without any applied force leads to an overestimation of the force-versus-indentation curve and subsequently an overestimation of the Youngs modulus of the cell. Scanning with too high a force on the tip also leads to cell damage. Hoh et al[25] have employed AFM to investigate the surface morphology and mechanical properties of MDCK cells grown as monolayers. They find that the plasma membrane has an average spring constant of 0.002 ± 0.0006 N/m over a deflection range of ~35 nm (2.2 nN). From stiffness curves they report a stiffness of ~0.035 N/m at 1μm depth. Mathur et al[14] use AFM to investigate the viscous and elastic properties of endothelial, cardiac and skeletal muscle cells. For endothelial cells, they report a variation in elastic modulus across the cell, ranging from ~1.4 ± 0.1 kPa near the edge to ~6.8 ± 0.4 kPa over the nucleus. They report no variation in either skeletal or cardiac muscle with an elastic modulus of 100.3 ±10.7 kPa across cardiac cells and 24.7 ± 3.5 kPa for skeletal muscle.

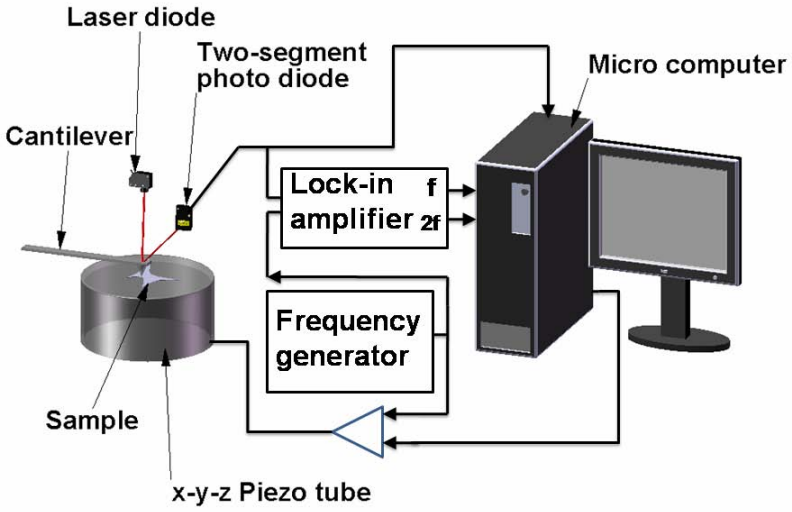

Figure 2.1 Schematics of AFM setup which incorporates optical lever detection and includes electronics for investigating viscoelastic properties of samples. (Adapted from Radmacher et al[22] with permission of the authors and the Biophysical Society.)

Though AFM has been used to successfully study the mechanical properties of the cell,

it still has a number of weaknesses. One of the weaknesses inherent to the technique is the fact that the variable shape of the tip determines the nature of the force-deformation curve. This curve is used to deduce the mechanical properties, so any bias introduced by different shapes would be propagated throughout the data analysis steps. Also, it is difficult to use commercially available AFMs with scanning electron microscopes (SEMs) to accurately visualize the structural deformation of the cell that occurs when the cell is stretched or indented by the AFM tip.

Magnetic tweezers and magnetic twisting cytometry(MTC)

These techniques have been used for many studies on the physical properties of biological tissues. Both methods require that beads are first exposed to magnetizing coils, which induce a magnetic dipole on the beads. A weaker, directional magnetic field is then applied to either move the beads linearly as shown in Figure 2.2, (magnetic tweezers/magnetic pulling cytometry, Lele et al[26]) or generate a torque to twist the beads through a specific angle (MTC). In both cases, the force or torque generated is dependent on the strength of the magnetic field applied as well as on bead properties. Ziemann et al[28] use this technique

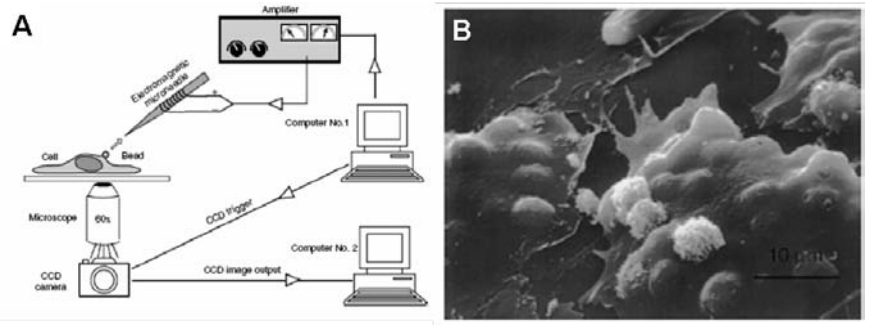

Figure 2.2 A) Schematic of magnetic tweezer set up used by Lele et al. to analyze single cell mechanics. (From Lele et al[26]). B) A scanning electron micrograph (SEM) of human umbilical vein endothelial cells (HUVECs) after Arg-Gly-Asp (RGD)-coated magnetic beads were bound for 1 h. Most of the beads were internalized, and each cell on average internalized 7-12 beads. (From Chen et al[27] Used with permission of the American Journal of Physiology-Cell Physiology.)

to measure local viscoelastic moduli of entangled actin networks. Baush et al[29] use a

modification of the Ziemann et al setup to conduct local measurements of viscoelastic parameters of adherent cell surfaces. They are able to bring the magnetic pole piece to within 10 - 100μm of the sample and are able to generate forces of ~10000 pN.

Wang et al[30] use another design to investigate cell cytoskeleton mechanics and mechanotransduction. The surface of ferromagnetic beads, normally around 0.2μm, is functionalized with specific receptor ligands that promote cell attachment without cell spreading. Cells are made to attach to these beads and then a uniform magnetic field in a specific direction is applied to the beads to magnetize them. A twisting coil mounted in tandem with the magnetizing coil is used to generate a weaker magnetic field orthogonal to the initial magnetic field. This induces a twisting moment on the beads, thereby causing portions of the cell to deform. Wangs group uses this to exert controlled shear stresses in the range from 0 to 68 Pa ($dynes/cm^2$) on cell surface receptors. They measure the angular strain as a function of the bead rotation and, for a stress of about 40 Pa, get an angular strain of about 30 °.

There are some disadvantages associated with this system as well. First, it is difficult to control the region of the cell to which the beads bind. If they preferentially attach at the periphery, or near the nucleus, measurements of the mechanical properties could be biased accordingly. Next, there is no way to ensure complete binding of the beads to the cell surface, which could result in underestimation of cell stiffness. Finally, and perhaps most importantly, the beads lose magnetization with time and must be re-magnetized at specific time intervals to maintain the torque applied. Regardless, there is inherent signal degradation over time and, subsequently, experiments lasting longer than one to two hours are not generally feasible with this technique.

Micropipette aspiration

In this method also known as elastimetry, a cell is deformed by applying gentle suction to a micropipette that is placed on the surface of the cell. The geometry of the resulting deformation together with the applied pressure is used to calculate the force applied. Mechanical properties of cells can then be inferred from this data.

Chein et al[13] use this technique to investigate the viscoelastic properties of erythrocyte membranes. They find that deformation occurs in two phases. The initial (rapid) phase exhibits a membrane viscosity in the range of 0.6×10^{-4} to 4×10^{-4} Pa. The second (slower) phase shows a high membrane viscosity with a mean value of about 2×10^{-2} Pa. Schmid-Schonbein et al[15] use micropipette aspiration to investigate the mechanical properties of human leukocytes. For rapid motion of the cell into the pipette, they find the shear modulus to be *sim*506 Pa and for slow motion *sim*130 Pa. Jones et al[17] examine the alterations of Youngs modulus of chondrocytes from normal and osteoarthritic human cartilage. They find no appreciable difference between the Youngs modulus of normal chondrocyte cells (0.65 ± 0.63 kPa) and of the osteoarthritic chondrocyte cell (0.67 ± 0.86 kPa). A more recent study was completed by Alexopoulos et al[18] on chondrocyte cells surrounded by a pericellular matrix for both normal and osteoarthritic cartilage. They find that for the normal cells, the Youngs modulus is the same for cells isolated from the surface (68.9 ± 18.9 kPa) as that from the middle and deep layers (62 ± 30.5 kPa). However, in osteoarthritic cartilage, the mean Youngs modulus significantly decreases from the surface zone (66.5 ± 23.3 kPa) to the middle and deep layers (41.3 ± 21.1 kPa). They conclude that the pericellular matrix has an important depth-dependent influence on the stress-strain environment of chondrocytes.

Chu et al[31] use a dual micropipette assay for a slightly different application. They use their system to quantify the strength of cadherin-dependent cell-cell adhesion (Figure 2.3 (B)–(D)). Doublets of S180 cells stably transfected to express E-cadherin are allowed to adhere to each other with different times of contact. They find that separation force is strongly dependent on the time allowed for contact. A mean force of 20 nN was required to separate cells with a 30 s contact time and this increased rapidly to ~ 200 nN after 1 h of contact. They also report a greater separation force (350 versus 200 nN) for preexisting doublets. However, they find that preexisting doublets of S180 cells without E-cadherin have separation forces of only 50 nN.

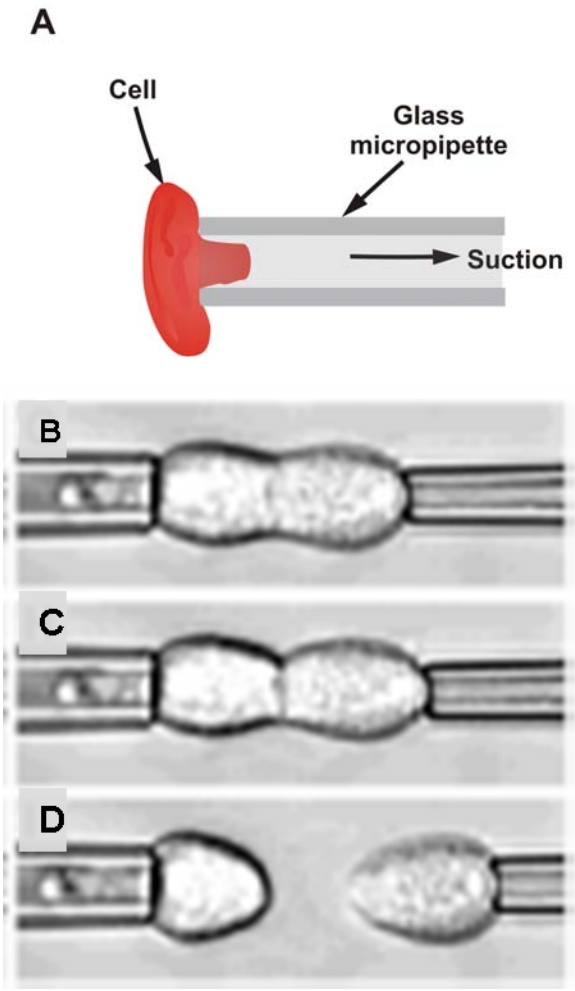

Figure 2.3 A) Schematic showing principle of micropipette aspiration of representative human red cell. B) - D) Sequence of images showing separation of cells using dual micropipette assay (Reproduced from The Journal of Cell Biology, 2004, 167:1183-1194. Copyright 2004, The Rockefeller University Press.)

Optical tweezers

This is a variation of magnetic tweezers where optical forces instead of magnetic forces are used to tug and pull, creating linear forces. A laser beam is used in tandem with a dielectric bead of high refractive index to generate these optical forces. The bead surface, which is functionalized, is bound to the cell surface as in MTC. The high intensity laser beam creates a ”trap”, an optical field that attracts the bead to its focus, thereby generating a force which deforms the cell.

Hénon et al[21] use this method to determine the shear modulus of the human erythrocyte membrane. They find that the elastic shear modulus ranges from 1.7 to 3.3 μ N/m with an average value of 2.5 ± 0.4 N/m. Dao et al[20] also use this tool to examine the mechanics

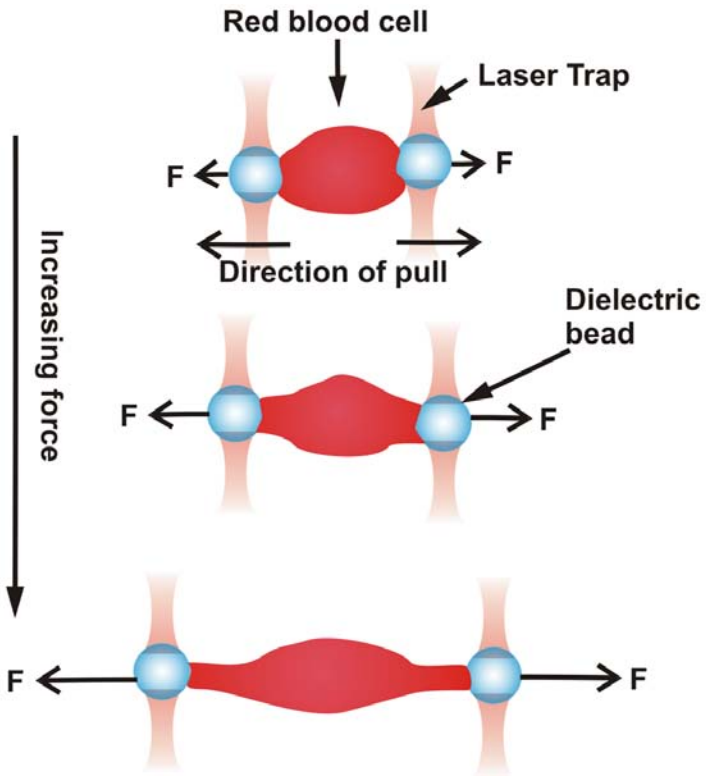

Figure 2.4 Schematic showing how optical tweezers are used to pull on representative red blood cell

of human erythrocyte deformation figure 3.1, generating forces 10 orders of magnitude greater than Hénon et al. Using a combination of simulation and experimental methods they estimate the membrane shear modulus to be 13.3 *mu*N/m. Limitations of this method include possible photo damage due to the wavelength and power of the lasers, and upper limits on the amount of force that can be generated.

Micromachined force sensors and actuators

With the exception of AFM, which can use micromachined tips, the techniques we have described above use macroscopic instruments fabricated by conventional means. The semiconductor photolithography and fabrication techniques developed for the manufacture of integrated circuits have been adapted and extended to create microelectromechanical systems (MEMS), primarily out of single-crystal silicon.[32] This approach has been extended to what is termed ”soft lithography,” wherein polymeric materials such as silicone are used to create optically transparent and flexible microfluidic devices.[33,34] Collectively,

when applied to biology, these technologies are referred to as biomicroelectromechanical systems (BioMEMS). As an example of silicon MEMS applied to biomechanics, a recently reported technique uses a novel micromachining method SCREAM (single-crystal reactive etching and metallization) to fabricate a force sensor for active probing and measurement of the deformation dynamics and stiffness of cells. Yang et al[35]present a force sensor that consists of a probe attached to a backbone structure that is free to move on its axis. The backbone structure is attached to flexible beams that are anchored at both ends to nonmovable bases. The chip on which the whole sensor is fabricated is driven by a piezo actuator on a movable stage with six degrees of freedom of movement. The actuator moves the probe in one direction and the resulting deflection of the attached sensor beams is recorded using optical methods. This deflection is used to estimate the force that the probe applies to the cell. The obvious advantage of this tool over others similar to it, such as the AFM and the micropipette, is the ease of calculation of the force applied to the cell based on the stiffness of the flexible beams and the deflection observed. Also, the device is set up such that it can be used to determine multidimensional (x and y) force responses of cells, unlike other methods that only probe forces in one direction. Though the device overcomes limitations of previous techniques, the production of SCREAM devices is a complicated, 10-step process involving deposition, lithography, and wet and dry etching techniques. In addition to being time-intensive, the tools and methods may either be not readily available or the process may be quite expensive. Serrell et al.[36] use standard surface micromachining to microfabricate a bioMEMs device for the application of strain to a cell. The principle of operation of the device is similar to a displacement- controlled uniaxial tensile machine (Figure 2.5(B)). It consists of a disk, divided in half, that serves as a platform for cell attachment. The cells attach to the disk, and because it spans the narrow gap between the two halves, the tensile properties of the mid-section of the cell can be measured. To provide actuation of the cell, one of the semicircular halves is connected to one end of a polysilicon beam, which has an annulus at the other end. A standard MEMs probe-station tip can be inserted into this annulus and used to pull one half of the platform away from the other. The polysilicon beam is supported by several folded- beam cantilever

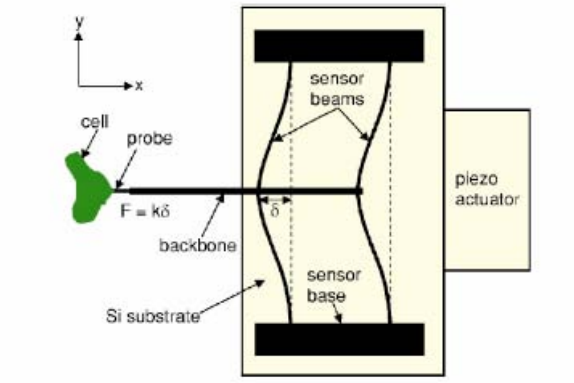

(A)

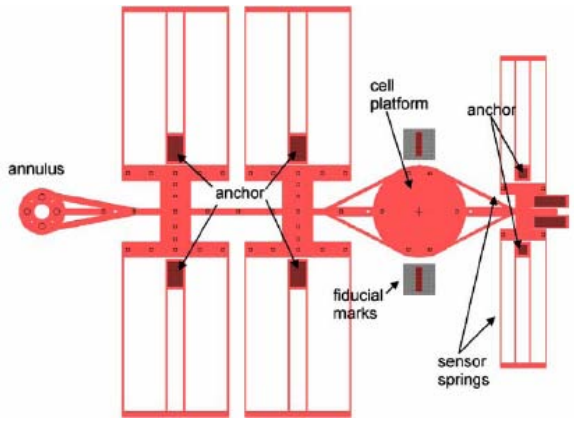

(B)

Figure 2.5 Micromachined force sensors and actuators (A) Schematic of force sensor fabricated using SCREAM technique (Image from Shengyuan et al.[35]) (B) Schematic of uniaxial BioMEMs device (Image from Serrell et al.[36])

springs. The opposite half of the platform provides the force sensing for the device using, a series/parallel combination of cantilever beams to create a spring. Movement of the two platform halves is monitored with standard optics and recorded using fast cameras. Serrell's group reports a linear force vrs time curve for a single fibroblast cell attached to the platform, and also a de-adhesion force of about 1500 nN. They attribute this high value to the surface roughness of the platform, the manner in which the shear force is being applied, and the protein used to facilitate cell adhesion.

Shear flow methods

Experiments using this method consist of two basic configurations

1. A cone-and-plate viscometer with a stationary flat plate and a rotating inverted cone

which can generate laminar or turbulent flows, or

2. A parallel-plate flow chamber in which cells can be subjected to laminar flow.

Figure 2.6(A) – 2.6(C) show schematics of the two basic configurations.

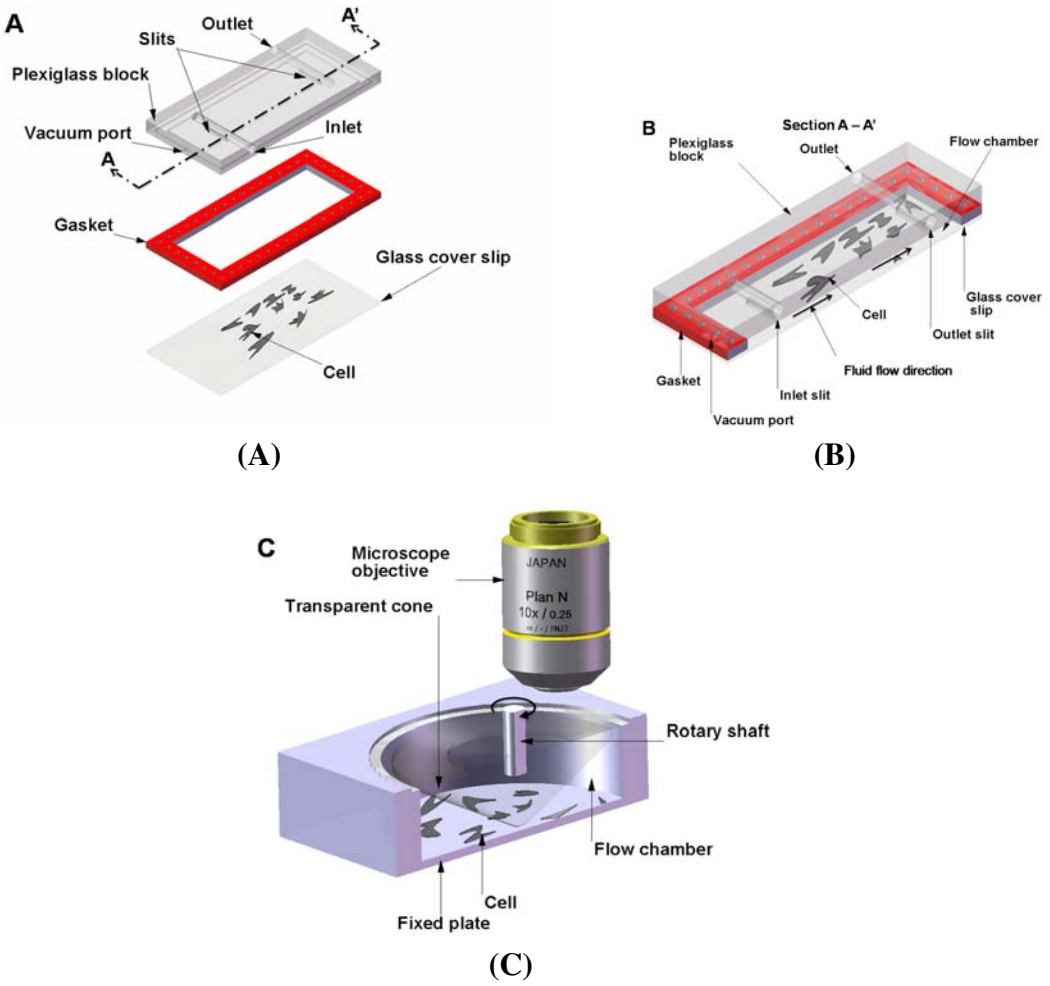

Figure 2.6 Parallel flow and cone-and-plate methods. (A) Schematic showing exploded view of parallel flow system. (B) Schematic showing cut out view of parallel flow system. (C) Schematic showing cut out view of cone-and-plate flow system.Adapted from Furukawa et al[37]

The shear flow chambers can be designed to provide either a constant shear over the entire chamber or a linearly varying shear along the length/width of the chamber. The advantage of the design with linearly varying shear is that it becomes possible to apply different shear stresses between the plates along different sections of the flow chamber without having to change the flow rates or change the dimensions of the chamber. However,

in both cases, the shear stress developed on the bottom of the flow chamber is dependent on many factors, including flow rate, viscosity of the fluid, channel width, and channel height. In the case of the linear varying design, two additional variables come into play. First, channel width is a function of the distance from the input port. Also, the total chamber length determines the pressure drop from the entrance to the exit port, hence affecting the amount of shear stress that can be developed. Hochmuth et al[19] use a parallel plate flow chamber with a constant shear stress at the surface to estimate the elastic shear modulus of erythrocytes adhered to a glass slide. A least squares fit to their data gives a shear elastic modulus of 1.31 ± 0.38 Pa. Their other attempts to use this device involved the investigation of flow effects on cell metabolism and viability, but were not explicitly used to quantify mechanical response or characteristics. Civelik et al[38] examine rat aortic smooth muscle cell contractility in response to fluid shear stress and look at relationships to the Ca^{2+} signaling pathway. They use cell area reduction as a metric of contractility. A minimal shear stress of 11 Pa ($11 dyne/cm^2$) was sufficient to induce contraction. A larger shear stress of 25 Pa caused significant reduction in cell area, due to significant contraction, 3 min after the onset of flow. By 30 min of constant flow, the reduction exceeded 30%. one of their major observations is that this contractile response is Ca^{2+} independent. This observation was borne out by the fact that even at 25 Pa of shear stress, there was no activation of Ca^{2+} signaling pathways, but the cells did mount a normal response when stimulated with Ca^{2+}-dependent agonists like potassium chloride (KCL) and thapsigarin. Ainslie et al[39] employ the parallel plate shear stress chamber to investigate contractile responses of vascular smooth muscle and the role of glycosaminoglycans (GAGs) on contractility and mechanotransduction. They employ a step increase (0 to 25 $dyne/cm^2$) in shear, similar to Civelik et al, as well as a ramp increase. The resultant contractility is similar in both cases. Pretreatment with heparinase III or chondroitinase ABC, which remove the GAGs heparan sulfate and chondroitin sulfate, respectively, results in a marked decrease (~20%) in cell contractility under identical shear stress.

Other labs have used this shear flow device to investigate cell properties and physiological responses, though not to investigate mechanical properties of cells. Frangos et al.[40]

use a recirculation-type flow chamber to examine the effects of pulsatile, steady state, and no flow conditions on the production of prostacyclin in cultured human endothelial cells. A minimum shear stress of 10 Pa is enough to elicit a significant increase of prostacyclin. Pulsatile flow, which produces minimum and maximum shear stress of 8 and 12 Pa at a frequency of 1 Hz, results in a 2.2 fold increase in prostacylin production.

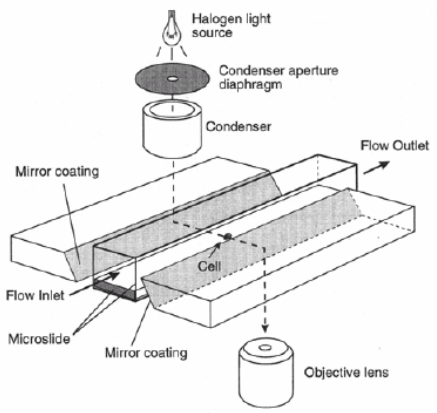

Figure 2.7 Schematic of side-view flow chamber used by Cao et al. for studying cell-surface adhesion under flow conditions. (Reprinted from Cao et al[41], with kind permission from Springer Science and Business Media).

One drawback of all the above experiments involving flow chambers is that none have taken into account the inherent curvature of a cell attached to the bottom of the chamber. This means that the shear stress that is actually experienced by the cell will vary from the top of the cell to its attachment on the bottom and cannot be assumed to be the same as the shear stress on the bottom plate of the flow chamber. The shape of the cell, and hence the forces on it, will depend upon the flow rate and the velocity profile of the fluid around the cell. This is evident in the study by Cao et al.,[41] who use the setup shown in Figure 6d to study cell-surface adhesion under flow conditions. Their apparatus is optimized to obtain a side-view of the cell using mirrored side walls and they can visualize the distortion of the cell with increased flow rate. One could theoretically reduce this error by measuring the cell thickness using confocal microscopy and deducing the average shear stress experience by the cell. However, this process would introduce additional sources of error, since confocal microscopy has a vertical resolution that is substantially less than

transverse resolution.[41–43]

Stretching devices

Using these methods,cells are cultured on elastic membranes made of flexible silicone sheets whose surfaces can be modified with extracellular matrix (ECM) proteins. The stretching devices can be uniaxial, biaxial, or pressure-controlled. In some of these, the stretch can be applied in a cyclic manner at different frequencies. Wang et al[30] subject endothelial cells to 10% cyclic uniaxial stretch on silicone membranes in the presence or absence of 2,3 butanedione monoxime (BDM)a myosin ATPase inhibitor. They show that 40 mM BDM prevents the formation of stress fibers and prevents cells reorienting themselves in response to the cyclic stretch.

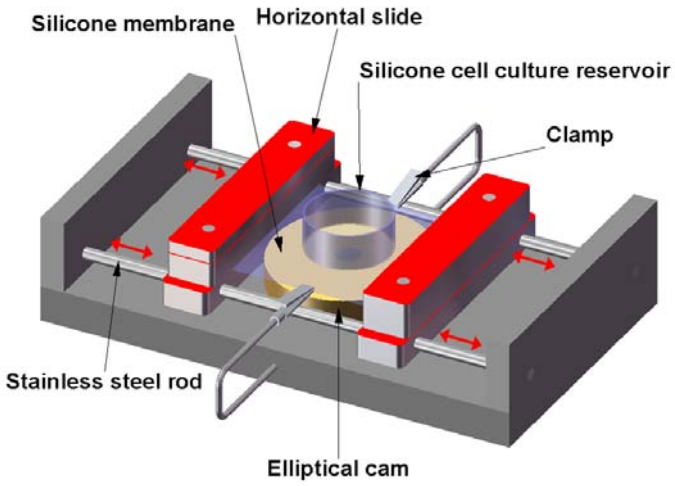

Figure 2.8 Schematic of custom-designed stretching device used by Zhuang et al[44]., which includes a transparent silicone membrane and an elliptical cam whose rotation leads to cyclic stretch of the membrane. The horizontal slide assembly glides horizontally on stainless cylindrical rods (red arrows) and support the transparent silicone membrane. The silicone cell reservoir is a segment of silicone tubing glued to the silicone membrane to form the walls of the culture dish. Two clamps produce slight tension along the central axis of the stretch apparatus and thereby reduce transverse shrinking.

Zhuang et al[44] investigate the role of pulsatile stretch on the electrical and mechanical properties of neonatal rat cardiac myocytes. Figure 2.8 is a schematic of the custom fabri-

cated stretching apparatus they use. Included in the device is a silicone membrane which forms part of the culture dish in which the neonatal rat myocytes were seeded and grown. They use the device to examine the effects of pulsatile stretch on some of the characteristics of transmembrane action potential, as well as its effects on gene expression. They report an increase in N-cadherin expression as the time to which the cells are subjected to pulsatile stretch is increased, but no significant changes in cell area or nuclear size.

The methods discussed above all involve the application of active forces either to single cells or a population of cells in culture. One of the main drawbacks with the use of these stretching devices is wrinkling patterns that develop on the sheets and which tend to distort the actual forces that are applied to the sheets. Zhuang et al. try to minimize this effect by using hooks on either side of the membrane (F). Also, as the sheets are continuous, all deformations and displacements are propagated across the entire surface, making calculation of discrete forces and cellular attachment properties very computationally intensive.

Carbon fiber (CF)-based systems

This method involves the use of carbon fibers, which are normally mounted in glass capillaries and attached to precise position control devices with feedback control mechanisms. The carbon fibers are attached to cells and used as a means to both apply active forces and record forces generated by the cell. The image of the carbon fibers is projected through optics onto a photodiode array which converts this into a usable signal for the feedback control system. The optical system is also connected to an image recording system and can be used to capture and record changes in length of the cell (Figure 2.9(A)). Though this technique could potentially be used for many cell types, it has recently been demonstrated in the literature for use in single cardiac myocytes. Yasuda et al.[45] use this setup to investigate the mechanics of single rat cardiac myocytes under isometric and physiologically loaded conditions. They also investigate the effects of inotropic intervention on myocyte force generation. They report problems with carbon fiber compliance and indicate that it is quite difficult to produce virtually isometric conditions. They plot force-length relationships and extract work-load data. Work output has a maximum value

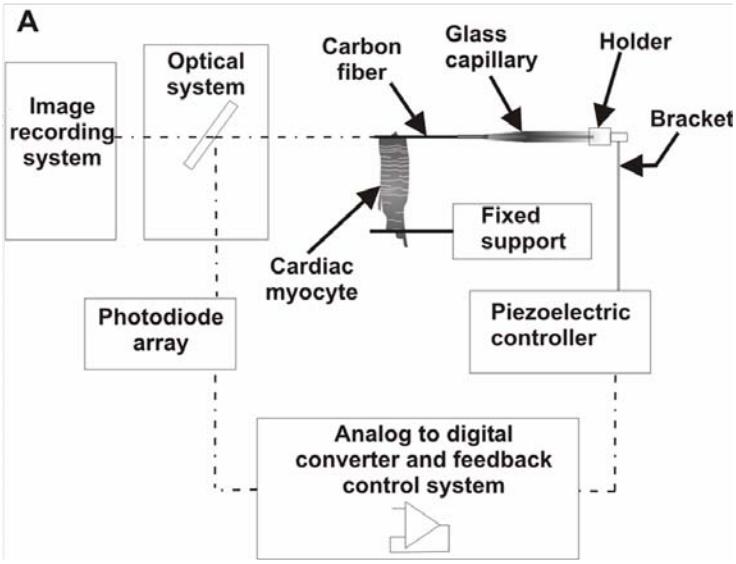

(A)

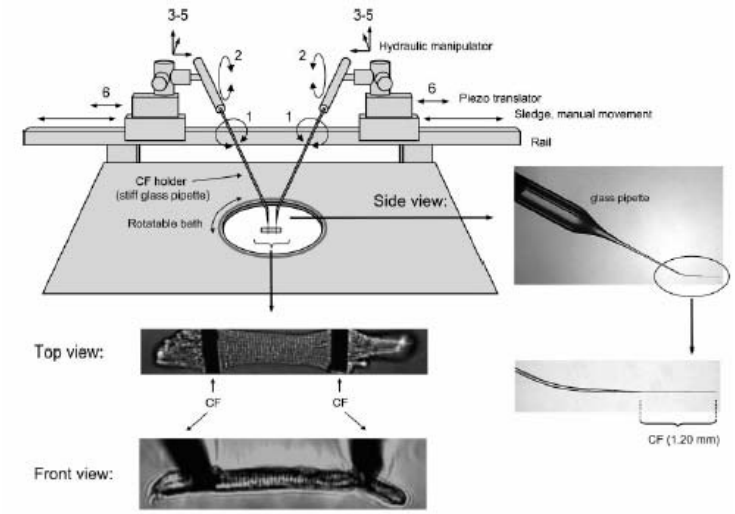

(B)

Figure 2.9 (A) Schematic showing general principle of operation of the carbon fiber system used by Yasuda et al. (Adapted from Yasuda et al.[45]) (B) Experimental setup and images of carbon fibers attached to individual cardiac myocytes (From Iribe et al[46]. Used with permission of the American Journal of Physiology-Heart and Circulatory Physiology.)

at an intermediate auxotonic load, and this falls off above and below this optimal value. Nishimura et al.[47] make modifications and improvements to the feedback control system used by Yasuda et al. and use it to also investigate rat cardiac myocyte mechanics under isometric, unloaded, and physiologically loaded conditions. Some of the limitations they report include damage to the cells during attachment of the fibers, inaccuracy in measuring sarcomere length due to focus issues, and possible bias introduced into the data by avoiding cells that were too irritable to obtain stable recordings. Iribe et al.[46] make further modifications to this setup by introducing the use of bidirectional control instead of the single-sided control used by Yasuda et al. and Nishimura et al., which improved sarcomere blurring(Figure 2.9(B)). They investigate the effects of independently varying preload and afterload, as well as modes of contraction on the force-length relationships of guinea pig ventricular cardiomyocytes. Some of their reported findings include the fact that the end systolic force-length relation is virtually independent of load at sarcomere lengths of 1.85 to 2.05 μm. It is important to recognize that this approach provides true, closed-loop mechanical control of a single cell, in which the compliance of the measurement system can be controlled independently of its displacement, thereby allowing exploration of cellular mechanics over the full range of forces, displacements, and velocities that are required to fully specify the parameters for an active, viscoelastic model of cellular mechanics.

Passive Methods

Detection of the mechanical forces that single cells exert generally involves the use of various flexible substrates which are non-toxic and which are either transparent or reflective to a high degree such that deflections can be measured using light microscopy or a variation of it. The term ”passive methods” is used to describe the techniques outlined below with some caution. Due to the inherent nature of some of the materials used, very soft materials may detect the mechanical forces exerted by the cells isotonically, i.e., without exterting any forces, whereas others being very stiff will detect these forces isometrically with any changes in length of the systems. Some of the techniques are mid way between these two

extremes.

Elastic substratum method

The first successful attempt to measure traction forces of individual cells using artificial flexible substrata was developed by Harris et al[48]. The cells were cultured on substrates made of flexible silicone sheets. These sheets were made by polymerizing silicone fluid using a flame. The stiffness of the sheets could be varied by varying crosslinking time and

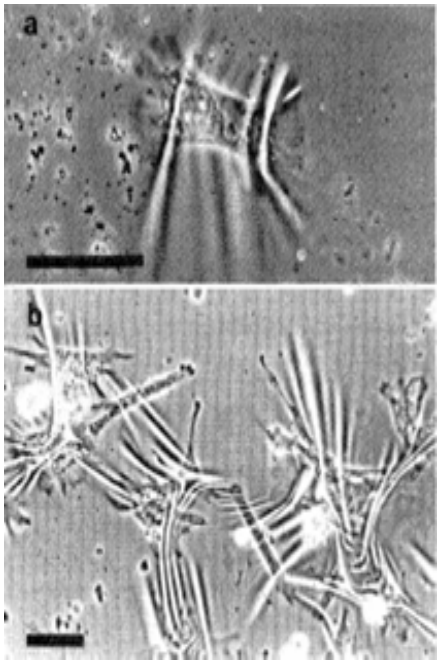

Figure 2.10 Flexible sheets. a),b) Wrinkling patterns produced by chicken heart fibroblasts on silicone rubber sheets. From Harris et al[48]

initial viscosity of the silicone fluid. The sheets were coated with extra-cellular matrix (ECM) proteins to promote cell adhesion and attachment. As the cells exert forces on the sheets, they caused wrinkling patterns which can be visualized under a light microscope. The patterns are compared to those generated by a pulled micropipette which has been calibrated for force. The main drawback with this method is that there is not a simple way of converting the wrinkle patterns formed into a traction force map. Inaccuracy in comparing patterns and hence measures of force introduce significant error.

Flexible sheets with embedded beads

A variant of the above method involves embedding either normal latex beads or fluorescently-tagged beads in the elastic substratum. The positions of the beads are tracked and the displacements over time are recorded. Cellular forces are inferred from the measured displacements. Lee et al[5] use this device to estimate the traction forces exerted by fish keratocytes. They produce vector diagrams by calculating the displaced and undisplaced bead positions with respect to the centroid of a moving cell. They report traction forces ranging from a minimum of 7.5 nN to a maximum of about 20 nN. Pelham and Wang[49] also use raw displacement data as a qualitative map of the local traction, citing the difficulty and computational intensity of de-convolving the displacements to estimate the traction forces. The primary flaw in both of these methods is that neither group was able to account for the inter-dependence of bead displacement data due to the propagation of deformations throughout the entire sheet surface. This flaw has been addressed by other groups.

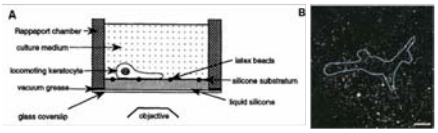

Figure 2.11 Using beads for tracking. a) Setup used by Lee et al[5] for tracking Keratocytes. b)Fluorescent image of a Human airway smooth muscle cell (HASM) cultured on a flexible polyacrylamide gel with embedded fluorescent beads. From Butler et al[50]

Dembo et al[6] address this issue using statistical methods. They estimate traction forces by considering the problem as a superposition of elementary ”delta influences”. They then use likelihood statistical methods to find the most likely amplitude and locations of the traction forces. Using this method they report that a typical locomoting keratocyte generates a maximum traction force of $\sim$ 140 nN. Butler et al use Fourier transform traction cytometry (FTTC) for computing the traction field produced by human airway smooth muscle cells in a bead-embedded flexible substrate. Using this technique, they report a maximum traction magnitude of about 400 Pa. Though such approaches address the critical flaw in this technique, they do however introduce a new disadvantages. Namely, deconvolution

of forces from displacement field maps is both a difficult and computationally intensive process. The other drawback is that it is very difficult, if not impossible, to obtain precise measurements of discrete forces generated by different parts of a cell.

Flexible sheets with micropatterned dots or grids

An improvement to the Lee et al and Butler et al techniques involves imprinting dots on the flexible sheet and observing the deformation of the grid from the ideal. Models of deformation can then be applied to the grid and the cellular forces inferred from the deformations produced. Balaban et al5 use this tool to measure the traction forces exerted by rat cardiac myocytes and endothelial cells. They compute the forces generated at the

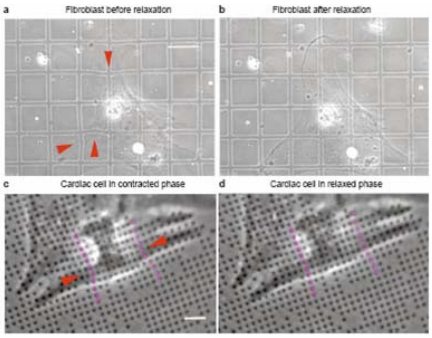

Figure 2.12 Flexible sheets with patterned grids. Rat fibroblast and cardiac myocyte cells cultured on a large grid a),b) and patterned dots c),d) respectively. From Balaban et al[7]

focal adhesions using elastic theory based on the semi-infinite space. Unfortunately, they have to make the same assumption as in the case for the embedded beads. They assume that the forces originate from the measured locations and do not propagate across the substrate. They solve the inverse problem of computing the tractions given the displacements using least square minimization techniques. Using this method they report maximum traction forces of ~20 nN for rat cardiac fibroblast cells and ~70 nN for rat cardiac myocytes.

Micromachined cantilever beam

This technique uses traditional micromachining techniques. A horizontal cantilever beam with an attachment pad at the end and a well beneath is used as a tool for measuring cell traction forces. Chicken fibroblast cells are seeded on the substrates. Cells are observed crawling over the cantilevers which have been calibrated for force using pulled glass micropipettes. A measure of cell traction force is obtained from a product of the cantilever deflection and the stiffness obtained from calibration. Galbraith et al[8] use this micromachined device to estimate the traction forces of chicken embroyo fibroblast cells. They report forces as high as 100 nN for the tail region of the fibroblast. This device does

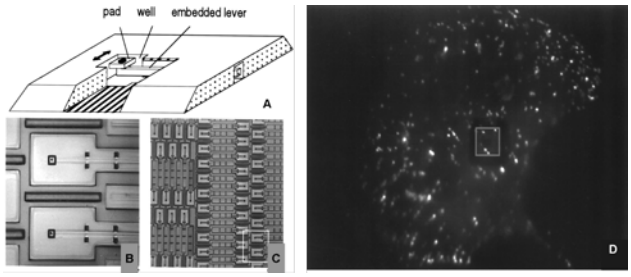

Figure 2.13 Cantilever beam device and fluorescent image of chicken embryo fibroblasts (CEFs) cell plated on the micromachined substrate. From Galbraith et al[8]

not have the problem in which strain propagates across the surface and therefore does not require sophisticated computational algorithms to calculate the cellular forces. There are some disadvantages with this technique though. The cantilever beam can only move in one direction and hence forces generated in directions other than the free axis cannot be measured. Also there is a spatial resolution limitation added to the fact that the fabrication technique is quite challenging.

Array of vertical microcantilevers

This technique overcomes the limitations of the horizontal cantilever system by Galbraith et al. An array of vertical microcantilevers that have two degrees of freedom is used instead of a single horizontal microcantilever. The individual microcantilevers in the

array are usually made of an elastomeric material such as polydimethlysiloxane (PDMS). Tan et al[9] are the first group to report the use of these arrays to investigate cell traction forces. They use soft lithography techniques to make the microcantilevers of PDMS. The arrays in their device have microcantilevers that are 3 μm in diameter and 11 μm tall and a center to center separation 9 μm. They use this device in combination with micropatterning techniques to investigate the traction forces exerted by spread and unspread cells. They show that spread cells exert much greater forces on the microcantilevers than unspread cells. For the spread cells, the record a maximum force of about 90 nN. A variation of

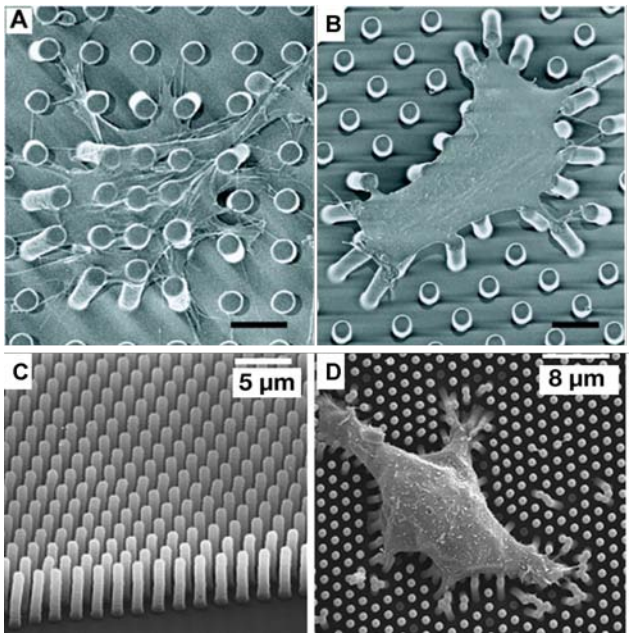

Figure 2.14 Vertical microcantilevers. Differential Interference Contrast and Scanning Electron Micrographs (SEMs) images of bed of Nails. From Tan et al[9]and du Roure et al[11]

this technique has been developed by du Roure et al[11]. They employ photolithographic methods in combination with Deep Reactive Ion Beam Etching (DRIE) to produce the master molds in silicon that have much better spatial resolutions and smaller sizes than that produced by Tan et al. They also use PDMS as the flexible cantilever material. The improvement in scale and resolution is impressive, but this is a considerably more expensive process than that used by Tan et al. Endothelial cells are cultured on the device and allowed to grow to confluence forming monolayers. They report a maximum traction force

of 40 nN exerted by the monolayer at its edge. Individual cells observed on the device generate maximum forces of about 4 nN. Both devices provide a powerful tool which is used to study microforces of expanding monolayers and single cells as well as investigate the relationship between cell shape, focal adhesion area and traction forces generated. Petronis et al[12] have also developed cantilever arrays for investigation of mechanical cell-substrate interactions. They fabricate their force sensitive arrays directly from silicon a major difference from the two previous methods. They also include attachment pads on their arrays. They employ intermediate lithography steps (masking techniques) to

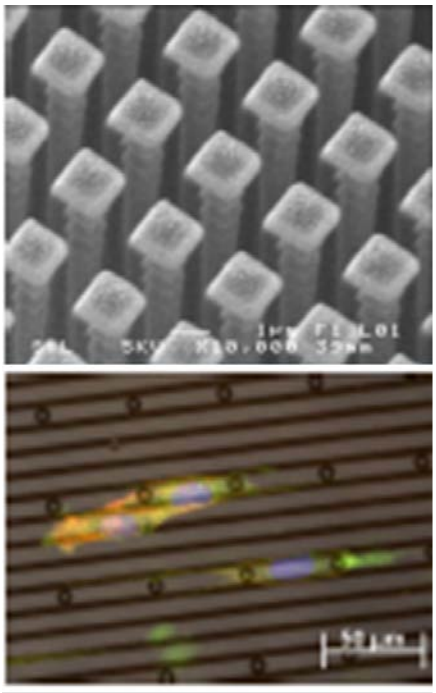

Figure 2.15 Silicon microcantilevers. Array of microcantilevers with attachment pads fabricated in silicon. Ridge and post pattern in silicon showing fibroblast cells attached. From Petronis et al[12]

pattern areas with different cantilever heights thereby generating areas with inherently different mechanical properties. Using a modified design with microcantilevers having a stiffness of 116 $nN/\mu m$ embedded in rigid substrates, they measure the traction forces exerted by primary human saphenous vein endothelial cells (HSVEC). A range of forces between 7 nN and 40 nN are reported. The main drawback with their technique is that rapid reproducibility of the devices is not possible. Since the arrays and ridges are directly

in silicon any damage to it would require reproduction of the entire device again.

Alternative methods for fabrication of vertical cantilever arrays

A number of alternative approaches for making the master molds for microcantilever arrays have been developed, though the arrays have not necessarily been used for studying cellular traction force measurements or mechanobiology. Kim et al[51] use the standard Lithogaphie Galvanik Abformung (LIGA) process using a synchrotron radiation source to make master molds from electroplated nickel. The LIGA technique is well characterized

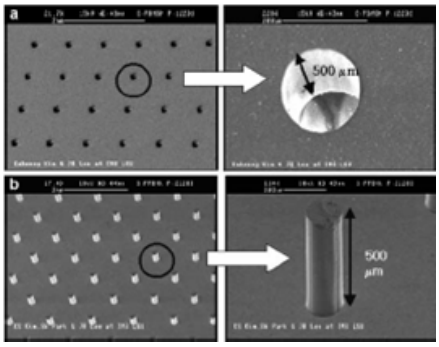

Figure 2.16 LIGA molds. Array of holes and posts made from nickel metal mold using LIGA. From KIm et al[51]

and has been used to produce high aspect ratio microstructures (HARMs) with aspect ratios as high as 100:137. Kim et al then use the metallic master mold to replicate a second mold using PDMS. They report final structures with aspect ratios of 15:1. Figure 3.8 shows SEM micrographs of the master mold with the holes and the final vertical cantilever microcantilevers fabricated using this method. The main drawback with LIGA is the availability and access to a synchrotron radiation source and the relatively high processing costs involved. A cheaper alternative to LIGA, which does not involve any lithographic steps, has been used by Schmitz et al and GroSSe et al[52]. They fabricate the master mold in investment casting wax. They prepare foils of the wax by uniformly pressing the wax at an elevated temperature between a metal or glass plate. Perforations in the wax are made using an excimer laser machining tool coupled to a mask projection

optical system. PDMS pre-polymer is poured onto the perforated wax mold and cured, then peeled off, placed on blotting paper, and heated to allow the wax to melt. The final

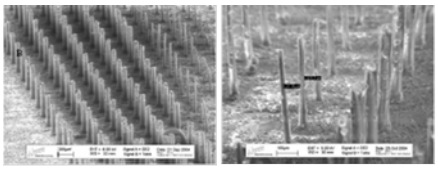

Figure 2.17 Wax Molds. Microcantilever arrays made from laser perforated wax molds. Post defects are due to air bubbles trapped in the holes during fabrication. From Schmitz et al[53] and Große et al[52]

array is then immersed in acetone to remove any remaining wax. Using this method, they are able to make microcantilevers with tip diameters ranging from 12 μm to 60 μm with corresponding base diameters from 37 μm to 90 μm. Average projected height is 450 μm. For the largest of microcantilevers, they report a yield of about 99% and for the medium sized microcantilevers about 75%. For the smallest microcantilevers, only a small percentage of straight microcantilevers are formed. The rest tend to bend into spirals. Even the straight ones only reach 20% of the foil thickness. Figure 2.17 shows SEM micrographs of large and medium microcantilevers made using this technique. Defects on the microcantilevers are attributed to air bubbles trapped in the holes. Though the above method can potentially be used for fabrication of the cantilever arrays, there are some potential problems. Capillary effects during the perforation process can limit the size of the holes that can be drilled in the wax. This can affect the resultant device since much smaller holes, on the order of a few μm, are needed for cell force applications. There may also be technical limitations on the spot size that can be achieved with the lasers. These limitations would depend on the wavelength of light, focal length of the lens and the diameter of the beam entering the lens. The smallest sizes would only be achieved with the smallest wavelength lasers, a wide beam and a very short focal length focusing lens. Short focal length lenses tend to be very expensive and tend to have more optical aberrations associated with them. Increasing the diameter of the beam also introduces problems with the point spread function of the beam and could also limit the minimum size achievable.

Combination of Active and Passive methods

The active methods described above normally give an indication of the cell stiffness or elastic/viscoelastic properties whereas passive methods are used to investigate cell traction forces or tensile stress. The two methods can be combined in order to investigate the relationship between cell stiffness under certain conditions and the corresponding tensile or prestress. Wang et al.[54] attempt to do this using a combination of oscillatory MTC for cell stiffness measurements and flexible polyacrylamide gel substrates with fluorescent beads for measurement of traction forces. Using this method they conclude that there is a strong association between the cell stiffness exhibited by a cell and the level of tensile stress within the cytoskeleton. Snaidecki et al.[55] have used a different approach in pursuit of this goal. They incorporate magnetic Cobalt (Co) nanowires into similar microcantilevers made by by Tan et al. A uniform magnetic field is then applied to the array and any microcantilevers which have nanowires incorporated within are displaced a specified distance. The nonmagnetic microcantilevers together with the magnetic ones are then used to monitor for the changes in forces. They use this system to investigate focal adhesion and traction force response to the active forces applied to the cells via the magnetic microcantilevers. Included in some of their findings is a significant difference in average focal adhesion area at actuated magnetic microcantilevers versus nonactuated with the former being larger. They find that multiple stimulations also produce larger focal adhesion areas than single actuations.

Theoretical Models for Analysis and Prediction of Cell Deformation and Mechanics

Most models developed to predict or explain the cell mechanical properties either represent the cell as a continuous medium or consider it to be a discrete collection of cytoskeletal components and other proteins. Mijailovich et al[56], Ohayon et al[57] and Traqui and Ohayon[58] investigate cell deformation, response and transmission of mechanical stress during magnetic bead twisting. They model the cell as a three-dimensional slab with constant local height and width and use representative finite volume elements in their

analysis. Mijailovich et al consider the cellular medium to be homogenous, isotropic and linearly elastic in all analysis performed. One of their analysis, however, considers geometrical nonlinearities due to distortions introduced by bead motion. They estimate apparent cell stiffness based on predicted angular rotation and investigate how the degree of embedding (percentage of bead embedded in cell) affects calculations of apparent cell stiffness. Ohayon et al and Traqui and Ohayon take a slightly different approach in their analysis. They model the cell as a homogenous continuous medium which is hyperelastic with a nonlinear strain-energy function that is used to characterize the nonlinear stress-strain relationship observed from experimental results of MTC. They examine the influence of cell material properties represented by constants in the strain energy equation, geometry, and degree of bead embedding on cell deformation, bead rotation and induced stress and strains. They also investigate the effects of nucleus stiffness on bead rotation. Dao et al[20] investigate the mechanics of deformation of the red blood cell when deformed by optical tweezers. Their continuum constitutive law is based on a consideration of the cell as a hyperelastic material with a nonlinear strain energy potential function. Using an estimate of the biconcave shape of the cell and finite element analysis, they examine the deformation response under different uniaxial stretch forces. The paper investigates how the presence or absence of a cytosol affects deformation characteristics. These continuum models developed provide very important guidelines that enable certain experimental observations on the mechanical behavior and characteristics of cells to be readily analyzed and predicted. Their main drawback is the fact that they do not consider the role of the cytoskeleton, which is known to influence cell mechanics and contractility in a very significant manner. Satcher et al[59] consider the deformations of a cell by modeling the F-Actin network using cubical open lattice unit cells, commonly known as open-cell foams, which are interconnected at their midpoints. Each unit cell consists of passive struts which represent the actin filaments. Estimation of cell properties under loading conditions is determined by consideration of the deformation of the network of interconnected unit cells. The model they develop is used to interpret the response of endothelial cells to shear stress in a flow chamber. They also consider the effects of stress fibers which they model as a lumped unit in series or

parallel to the actin network. They show that the predicted shear modulus is fairly close to experimentally reported values. They acknowledge that this approach does not consider interfilament tension, which accounts for cell prestress, and thus it cannot be used to explain the experimentally observed dependence of cell stiffness on cytoskeletal stiffness. Tensegrity can be defined as the interaction of a set of discrete compression elements with a continuous network of tension elements in the aim of forming a stable form in space. A number of publications[60–62] employ the concept of tensegrity to model cell mechanics and deformation characteristics. The actin network comprises the tensional elements, whereas the microtubule network forms the compression elements in tandem with the cell extracellular matrix (ECM)[63]. In the tensegrity models, compression and tension elements are in constant force balance with each other. This model has been used to predict and explain a number of phenomena that have been observed experimentally, both in round, unattached cells as well as in spread, adherent cells. In the tensegrity model, the cell and its cytoskeleton is usually represented by a 30 element (24 elastic and 6 compressive struts) structure. The elastic elements, which are assumed to be Hookean, support the tensional elements while the struts are viewed as rigid bars under compression. In the initial state, the tension (prestress) in the cable elements is balanced by the compression forces in the struts. Forces are applied at specific nodes within the structure and global strains can be deduced from resolution of the general equation system $\{F\} = [K]\{u\}$ which describes the balance of internal and external forces. The stiffness matrix is normally assembled from the stiffness matrices of individual elements within the structure which are constituted from the elastic rigidity as well as the geometric rigidity. Deshpande et al[64] present a mechanical model for cell contractility based on observations of a cell on microfabricated cantilever arrays. They consider an activation signal that triggers the formation of stress fibers within a representative volume element. They assume that the contractility of the stress fibers is dependent on the tension through cross-bridge dynamics. They generalize their model to two and three-dimensional cytoskeletal networks using a homogenization approach. The actual model is implemented by considering a two dimensional 50 μm square cell sitting on four microcantilevers. They investigate the effects of support stiffness

on stress generated within the cell as well as the evolution of stress fiber formation and orientation. This approach is unique in that it represents the first attempt to model not only stress fiber formation but also how this affects stresses generated by a cell on vertical microfabricated cantilever arrays. It also considers for the first time the effect of pillar stiffness on these properties as well. The only obvious critique to their method is the fact that in practice, cells that spread to cover a 50 μm area will be in contact with significantly more than four microcantilevers based on the microcantilever density of current devices fabricated by different groups to date. Mohrdieck et al[65] present a theoretical model to describe the bending dynamics of vertical cantilever arrays to which is attached a network of fibers of arbitrary geometry. This fiber network is used to represent the actin network of at attached cell. They estimate the resultant forces on the microcantilevers by considering contributions due to prestrain in the fibers, elastic and geometric deformation of the fibers, and the bending of the individual microcantilevers. The obvious advantage of this approach is that one can more closely model a cell attached to multiple microcantilevers (more than four). This models primary shortcoming is that it neglects the biochemistry associated with generation of some these mechanical forces. Though it would be greatly improved if such considerations are incorporated, the resulting numerical complexity could make the model unwieldy.

Summary and Dissertation Outline

I began this chapter by looking at the importance of studying cell mechanical properties and force generation. I then summarized the literature regarding methods used to investigate the mechanical properties and microforce generation for cells in vitro. I classified the methods based on two general categories and looked at some of the advantages and disadvantages of the methods used. Table 2.2 is a summary of some of these methods and techniques and their corresponding range of forces that they can detect or apply. The next section considered some alternative techniques that have been used for fabrication of cantilever arrays and the merits of each of these methods. Finally I closed by presenting a brief overview of theoretical models that have been developed to study cell mechanics and cell force generation.

Table 2.2 Summary of Methods and Techniques in Cellular Biomechanics.

Method	Principle	Range of forces that can be applied or detected	References
Atomic Force Microscopy (AFM)	Relative deformation of cantilever tip and substrate(cell) is used to estimate forces	~ 10 pN $\leqslant F_x \leqslant$?	16
Micropipette Aspiration	Gentle suction applied to micropipette attached to cell	10 - 20 pN $\leqslant F_x \leqslant$?	66
Stretching devices	Flexible membrane attached structures that enable membrane to be stretched.	Qualitative-At least 25% from unstretched state	30
Carbon Fiber (CF)-based systems	Carbon fibers that are attached directly to cell and controlled using feedback systems.	? $\leqslant F_x \leqslant 5$ μN	45–47
Magnetic tweezers/Magnetic twisting cytometry	Magnetized ferromagnetic/superparamagnetic beads are moved by weaker directional magnetic fields.	2 pN $\leqslant F_x \leqslant 50$ nN	28,67

Continued on next page

Table 2.2 (continued)

Method	Principle	Range of forces that can be applied or detected	References
Optical tweezers	Dielectric beads of high refractive index are moved using laser beams.	2 pN $\leqslant F_x \leqslant$ 600 pN	[20,21]
MEMs in silicon	Movable parts are fabricated in silicon and various methods such as piezo actuation are used to move them.	0.5 nN $\leqslant F_x \leqslant$ 1.5 μN	[35,36]
Flow chambers	Enclosed chambers with inlet and outlets for fluid flow are used to subject cells to fluid shear stress.	30 Pa $\leqslant P_x \leqslant$?	[19,38,39,41]
Elastic substratum method	Wrinkling patterns developed in artificial flexible sheets are used to infer cell traction forces.	Qualitative	[48,68]
Flexible sheets with embedded beads	Displacements of beads within flexible sheets are used to infer cell traction forces.	140 nN $\leqslant F_x \leqslant$?	[5,6,49,50]

Continued on next page

Table 2.2 (continued)

Method	Principle	Range of forces that can be applied or detected	References
Flexible sheets with micropatterned dots/grids	Deformation of grid or dot patterns from ideal used to infer cell traction forces.	70 nN $\leqslant F_x \leqslant$?	[7]
Array of vertical microcantilevers	Horizontal deflection of individual vertical microcantilevers is used to infer traction forces.	50 pN $\leqslant F_x \leqslant$ 100 nN	[9–11]
Micromachined horizontal cantilever	Horizontal deflection of cantilever with attachment pad is used to infer traction force.	2 pN $\leqslant F_x \leqslant$ 100 nN	[8]

The main purpose for undertaking this research was to develop a BioMEMS platform that could successfully be used to investigate cellular biomechanics and mechanotransduction in an *in vitro* setting. An outline of the dissertation is provided below.

Chapter 3 looks at microfabrication of the microcantilever arrays using soft lithography techniques. It discusses some lithography improvements to previously published methods. Details of a quantum dot labeling technique to facilitate easier tracking of microcantilever deflections is introduced. Preliminary results using this system to investigate traction forces generated by human airway smooth muscle cells are presented.

PVA was used as a lift-off agent to attach structures to the microcantilevers. Details of this technique are outlined in chapter 4. A summary of results from experiments involving mechanical agitation of the attached structures is also presented.

An investigation of cardiac myocyte adaptation to the microcantilever array is discussed in chapter 5. Analysis of myofibril structure and sarcomere formation is presented. The use of the array as a potential tool to examine myofibrillogenesis is discussed. Analysis of contracting myocytes on the microcantilevers using a user defined divergence and curl metric is also presented.

Chapter 6 examines the use of cryogenic etching of silicon to microfabricate the master molds. It addresses optimization of etch parameters to obtain the desired sidewall profile.

In chapter 7, the response of mesenchymal stem cells to the microcantilever arrays produced using the technique described in chapter 6 is presented.

Chapter 8 is a summary of chapter 3 through 7 and the objectives of the research. It also looks at future work that can be done in this research area. Research considerations and possible societal implications are also discussed.

References

[1] Liao, Z., Feng, S., Popel, A., Brownell, W., Spector, A. Outer hair cell active force generation in the cochlear environment. *Journal of the Acoustical Society of America* **122**, 2215–2225, 2007.

[2] Ali, M., Schumacker, P. Endothelial responses to mechanical stress: Where is the mechanosensor? *Critical Care Medicine* **30**, S198–S206, 2002.

[3] Lehoux, S., Tedgui, A. Cellular mechanics and gene expression in blood vessels. *Journal of Biomechanics* **36**, 631–643, 2003.

[4] Grodzinsky, A., Levenston, M., Jin, M., Frank, E. Cartilage tissue remodeling in response to mechanical forces. *Annual Review of Biomedical Engineering* **2**, 691–+, 2000.

[5] Lee, J., Leonard, M., Oliver, T., Ishihara, A., Jacobson, K. Traction forces generated by locomoting keratocytes. *The Journal of Cell Biology* **127**, 1957–1964, 1994.

[6] Dembo, M., Wang, Y. L. Stresses at the Cell-to-Substrate Interface during Locomotion of Fibroblasts. *Biophys.J.* **76**, 2307–2316, 1999.

[7] Balaban, N., *et al.* Force and focal adhesion assembly: a close relationship studied using elastic micropatterned substrates. *Nature Cell Biology* **3**, 466–472, 2001.

[8] Galbraith, C. G., Sheetz, M. P. A micromachined device provides a new bend on fibroblast tractionforces. *PNAS* **94**, 9114–9118, 1997.

[9] Tan, J., Tien, J., Pirone, D., Gray, D., Bhadriraju, K., Chen, C. Cells lying on a bed of microneedles: An approach to isolate mechanical force. *PNAS* **100**, 1484–1489, 2003.

[10] Roure, O. d., *et al.* Microfabricated arrays of elastomeric posts to study cellular mechanics. *Proc.SPIE* **5345**, 26–34, 2004.

[11] du Roure, O., *et al.* Force mapping in epithelial cell migration. *PNAS* **102**, 2390–2395, 2005.

[12] Petronis, S., Gold, J., Kasemo, B. Microfabricated force-sensitive elastic substrates for investigation of mechanical cell–substrate interactions. *Journal of Micromechanics and Microengineering* **13**, 900–913, 2003.

[13] Chien, S., Sung, K., Skalak, R., Usami, S., Tozeren, A. Theoretical and experimental studies on viscoelastic properties of erythrocyte membrane. *Biophys.J.* **24**, 463–487, 1978.

[14] Mathur, A. B., Collinsworth, A. M., Reichert, W. M., Kraus, W. E., Truskey, G. A. Endothelial, cardiac muscle and skeletal muscle exhibit different viscous and elastic properties as determined by atomic force microscopy. *Journal of Biomechanics* **34**, 1545–1553, 2001.

[15] Schmid-Schonbein, G., Sung, K., Tozeren, H., Skalak, R., Chien, S. Passive mechanical properties of human leukocytes. *Biophys.J.* **36**, 243–256, 1981.

[16] Weisenhorn, A., Khorsandi, M., Kasas, S., Gotzos, V., Butt, H.-J. Deformation and height anomaly of soft surfaces studied with an AFM. *Nanotechnology* **4**, 106–113, 1993.

[17] Jones, W. R., Ping Ting-Beall, H., Lee, G. M., Kelley, S. S., Hochmuth, R. M., Guilak, F. Alterations in the Young’s modulus and volumetric properties of chondrocytes isolated from normal and osteoarthritic human cartilage. *Journal of Biomechanics* **32**, 119–127, 1999.

[18] Alexopoulos, L. G., Haider, M. A., Vail, T. P., Guilak, F. Alterations in the Mechanical Properties of the Human Chondrocyte Pericellular Matrix With Osteoarthritis. *Journal of Biomechanical Engineering* **125**, 323–333, 2003.

[19] Hochmuth, R. M., Mohandas, N., Blackshear, P. L. Measurement of the elastic Modulus for red cell membrane using a fluid mechanical technique. *Biophys.J.* **13**, 747–762, 1973.

[20] Dao, M., Lim, C., Suresh, S. Mechanics of the human red blood cell deformed by optical tweezers [Journal of the Mechanics and Physics of Solids, 51 (2003) 2259-2280]. *Journal of the Mechanics and Physics of Solids* **53**, 493–494, 2005.

[21] Henon, S., Lenormand, G., Richert, A., Gallet, F. A New Determination of the Shear Modulus of the Human Erythrocyte Membrane Using Optical Tweezers. *Biophys.J.* **76**, 1145–1151, 1999.

[22] Radmacher, M., Tillamnn, R., Fritz, M., Gaub, H. From molecules to cells: imaging soft samples with the atomic force microscope. *Science* **257**, 1900–1905, 1992.

[23] Radmacher, M., Tillmann, R., Gaub, H. Imaging viscoelasticity by force modulation with the atomic force microscope. *Biophys.J.* **64**, 735–742, 1993.

[24] Radmacher, M., Fritz, M., Kacher, C., Cleveland, J., Hansma, P. Measuring the viscoelastic properties of human platelets with the atomic force microscope. *Biophys.J.* **70**, 556–567, 1996.

[25] Hoh, J., Schoenenberger, C. Surface morphology and mechanical properties of MDCK monolayers by atomic force microscopy. *J Cell Sci* **107**, 1105–1114, 1994.

[26] Lele, T. P., *et al.* Tools to Study Cell Mechanics and Mechanotransduction. In *Methods in Cell Biology Cell Mechanics*, vol. Volume 83, 441, 443–441, 472. Academic Press, 2007.

[27] Chen, J., Fabry, B., Schiffrin, E. L., Wang, N. Twisting integrin receptors increases endothelin-1 gene expression in endothelial cells. *Am J Physiol Cell Physiol* **280**, C1475–C1484, 2001.

[28] Ziemann, F., Radler, J., Sackmann, E. Local measurements of viscoelastic moduli of entangled actin networks using an oscillating magnetic bead micro-rheometer. *Biophys.J.* **66**, 2210–2216, 1994.

[29] Bausch, A. R., Moller, W., Sackmann, E. Measurement of Local Viscoelasticity and Forces in Living Cells by Magnetic Tweezers. *Biophys.J.* **76**, 573–579, 1999.

[30] Wang, J. H.-C., Goldschmidt-Clermont, P., Yin, F. C.-P. Contractility Affects Stress Fiber Remodeling and Reorientation of Endothelial Cells Subjected to Cyclic Mechanical Stretching. *Annals of Biomedical Engineering* **28**, 1165–1171, 2000.

[31] Chu, Y. S., *et al.* Force measurements in E-cadherin-mediated cell doublets reveal rapid adhesion strengthened by actin cytoskeleton remodeling through Rac and Cdc42. *The Journal of Cell Biology* **167**, 1183–1194, 2004.

[32] Grayson, A., *et al.* A BioMEMS review: MEMS technology for physiologically integrated devices. *Proceedings of the IEEE* **92**, 6–21, 2004.

[33] Xia, Y., Whitesides, G. M. Soft Lithography. *Annual Review of Materials Science* **28**, 153–184, 1998.

[34] McDonald, J., *et al.* Fabrication of microfluidic systems in poly(dimethylsiloxane). *Electrophoresis* **21**, 27–40, 2000.

[35] Yang, S., Saif, T. Micromachined force sensors for the study of cell mechanics. *Review of Scientific Instruments* **76**, 044301–044308, 2005.

[36] Serrell, D., Oreskovic, T., Slifka, A., Mahajan, R., Finch, D. A uniaxial bioMEMS device for quantitative force-displacement measurements. *Biomedical Microdevices* **9**, 267–275, 2007.

[37] Furukawa, K. S., *et al.* Quantitative analysis of cell detachment by shear stress. *Materials Science and Engineering: C* **17**, 55–58, 2001.

[38] Civelek, M., Ainslie, K., Garanich, J. S., Tarbell, J. M. Smooth muscle cells contract in response to fluid flow via a Ca2+-independent signaling mechanism. *J Appl Physiol* **93**, 1907–1917, 2002.

[39] Ainslie, K. M., Garanich, J. S., Dull, R. O., Tarbell, J. M. Vascular smooth muscle cell glycocalyx influences shear stress-mediated contractile response. *J Appl Physiol* **98**, 242–249, 2005.

[40] Frangos, J., Eskin, S., McIntire, L., Ives, C. Flow effects on prostacyclin production by cultured human endothelial cells. *Science* **227**, 1477–1479, 1985.

[41] Cao, J., Usami, S., Dong, C. Development of a side-view chamber for studying cell-surface adhesion under flow conditions. *Annals of Biomedical Engineering* **25**, 573–580, 1997.

[42] Dong, C., Cao, J., Struble, E. J., Lipowsky, H. H. Mechanics of Leukocyte Deformation and Adhesion to Endothelium in Shear Flow. *Annals of Biomedical Engineering* **27**, 298–312, 1999.

[43] Leyton-Mange, J., Yang, S., Hoskins, M. H., Kunz, R. F., Zahn, J. D., Dong, C. Design of a side-view particle imaging velocimetry flow system for cell-substrate adhesion studies. *Journal Of Biomechanical Engineering-Transactions Of The Asme* **128**, 271–278, 2006.

[44] Zhuang, J., Yamada, K. A., Saffitz, J. E., Kleber, A. G. Pulsatile Stretch Remodels Cell-to-Cell Communication in Cultured Myocytes. *Circ Res* **87**, 316–322, 2000.

[45] Yasuda, S.-I., *et al.* A novel method to study contraction characteristics of a single cardiac myocyte using carbon fibers. *Am J Physiol Heart Circ Physiol* **281**, H1442–1446, 2001.

[46] Iribe, G., Helmes, M., Kohl, P. Force-length relations in isolated intact cardiomyocytes subjected to dynamic changes in mechanical load. *Am J Physiol Heart Circ Physiol* **292**, H1487–1497, 2007.

[47] Nishimura, S., *et al.* Single cell mechanics of rat cardiomyocytes under isometric, unloaded, and physiologically loaded conditions. *Am J Physiol Heart Circ Physiol* **287**, H196–202, 2004.

[48] Harris, A., Stopak, D., Wild, P. Fibroblast Traction As A Mechanism for Collagen Morphogenesis. *Nature* **290**, 249–251, 1981.

[49] Pelham, J., Robert J., Wang, Y. L. Cell locomotion and focal adhesions are regulated by substrateflexibility. *PNAS* **94**, 13661–13665, 1997.

[50] Butler, J. P., Tolic-Norrelykke, I. M., Fabry, B., Fredberg, J. J. Traction fields, moments, and strain energy that cells exert on their surroundings. *Am J Physiol Cell Physiol* **282**, C595–C605, 2002.

[51] Kim, K., *et al.* Rapid replication of polymeric and metallic high aspect ratio microstructures using PDMS and LIGA technology. *Microsystem Technologies* **V9**, 5–10, 2002.

[52] Große, S., Schröder, W., Brücker, C. Nano-newton drag sensor based on flexible micro-pillars. *Measurement Science and Technology* **17**, 2689–2697, 2006.

[53] Schmitz, G., cker, C., Jacobs, P. Manufacture of high-aspect-ratio micro-hair sensor arrays. *Journal of Micromechanics and Microengineering* **15**, 1904–1910, 2005.

[54] Wang, N., *et al.* Cell prestress. I. Stiffness and prestress are closely associated in adherent contractile cells. *Am J Physiol Cell Physiol* **282**, C606–C616, 2002.

[55] Sniadecki, N. J., *et al.* From the Cover: Magnetic microposts as an approach to apply forces to living cells. *Proc Natl Acad Sci* **104**, 14553–14558, 2007.

[56] Mijailovich, S., Kojic, M., Zivkovic, M., Fabry, B., Fredberg, J. A finite element model of cell deformation during magnetic bead twisting. *J Appl Physiol* **93**, 1429–1436, 2002.

[57] Ohayon, J., *et al.* Analysis of nonlinear responses of adherent epithelial cells probed by magnetic bead twisting: A finite element model based on a homogenization approach. *Journal of Biomechanical Engineering-Transactions of the Asme* **126**, 685–698, 2004.

[58] Tracqui, P., Ohayon, J. *Acta Biotheoretica* **52**, 323–341, 2004.

[59] Satcher, R., Dewey, C. Theoretical estimates of mechanical properties of the endothelial cell cytoskeleton. *Biophys.J.* **71**, 109–118, 1996.

[60] Coughlin, M., Stamenovic, D. A tensegrity model of the cytoskeleton in spread and round cells. *Journal of Biomechanical Engineering-Transactions of the Asme* **120**, 770–777, 1998.

[61] Stamenovic, D., Ingber, D. Models of cytoskeletal mechanics of adherent cells. *Biomechanics and Modeling in Mechanobiology* **V1**, 95–108, 2002.

[62] Ingber, D. Integrin signaling, cellular tensegrity, and control of angiogenesis. *Faseb Journal* **11**, A1288–A1288, 1997.

[63] Wang, N., *et al.* Mechanical behavior in living cells consistent with the tensegrity model. *PNAS* **98**, 7765–7770, 2001.

[64] Deshpande, V. S., McMeeking, R. M., Evans, A. G. A bio-chemo-mechanical model for cell contractility. *PNAS* **103**, 14015–14020, 2006.

[65] Mohrdieck, C., *et al.* A theoretical description of elastic pillar substrates in biophysical experiments. *Chemphyschem* **6**, 1492–1498, 2005.

[66] Hochmuth, R. M. Micropipette aspiration of living cells. *Journal of Biomechanics* **33**, 15–22, 2000.

[67] Wang, N., Butler, J., Ingber, D. Mechanotransduction Across the Cell-Surface and Through the Cytoskeleton. *Science* **260**, 1124–1127, 1993.

[68] Harris, A. Tissue-Culture Cells on Deformable Substrata - Biomechanical Implications. *Journal of Biomechanical Engineering-Transactions of the Asme* **106**, 19–24, 1984.

CHAPTER III

A FLEXIBLE, QUANTUM DOT-LABELED CANTILEVER POST ARRAY FOR STUDYING CELLULAR MICROFORCES

Kweku A. Addae-Mensah,[1,2] Nicholas J. Kassebaum,[2] Michael J. Bowers II,[3] Ronald S. Reiserer,[2] Sandra J. Rosenthal,[3,4] Paul E. Moore,[5] John P. Wikswo,[1,2,4,6]

[1]Department of Biomedical Engineering,

[2]Vanderbilt Institute for Integrative Biosystems Research and Education

[3]Department of Chemistry

[4]Department of Physics and Astronomy

[5]Department of Pediatrics

[6]Department of Molecular Physiology and Biophysics

Vanderbilt University, Nashville, TN

Portions of this manuscript have been published in:

Kweku A. Addae-Mensah, Nicholas J Kassebaum, Michael J. Bowers II, Ronald S. Reiserer, Sandra J. Rosenthal, Paul E. Moore, John P. Wikswo. *Sensors & Actuators A* Vol 136 (2007)385 – 397

Abstract

We describe improvements to a passive array of cantilevers, termed the bed of nails(BoN), for detecting cellular microforces and studying in vitro cell mechanics. The BoN consists of vertically-arranged PDMS posts that behave as simple cantilever beams when stressed horizontally by cells cultured on them. We modified the standard SU8 protocols to include a contrast enhancement step that removed air-gap effects and enabled fabrication of 2 μm features using contact I-line UV photolithography. We also contact-printed the tops of each post with quantum dot labels that are easily visualized with fluorescence microscopy and that do not interact with cells. To illustrate these improvements, we focus this paper on human airway smooth muscle (HASM) cells, although the system can be generalized to other cell types. We demonstrate how the BoN is a cost-effective, user-friendly system that can be implemented in a relatively short period of time by researchers in asthma and other fields who wish to conduct short-term and long-term studies to examine cellular microforces in vitro.

Introduction

Mechanical forces developed by individual cells are of paramount importance in phenomena such as the motility of cells in embryogenesis, growth, wound healing, immune responses, and cancer; the mechanical integrity of solid tissues formed by collections of cells; and the contraction of smooth, cardiac, or skeletal muscle cells and tissue. As a clinically important problem involving smooth muscle cells, asthma is a disorder characterized by excessive airway tightening that can provoke wheezing, coughing, chest tightness and difficulty breathing. It is closely correlated with allergic reactions. Excessive airway inflammation is a hallmark for the disease and many individuals are known to have specific triggers that lead to asthma exacerbations. Innate hyperresponsiveness of airway smooth muscle is also believed to play a role in the development of asthma, as well as in determining its severity. Significant time and energy have been spent developing animal models and complementary in vivo and in vitro assays for the study of asthma. In vitro

studies strive to understand the mechanical properties of human airway smooth muscle (HASM) cells in culture. The dynamics of contraction, relaxation, and drug response are measured, as well as the effects of the inflammatory milieu of the asthmatic airway on the HASM cells. Any study of single HASM cells requires a way to quantify mechanical responses and therefore detect cellular microforces in a precise, reproducible manner with high fidelity.

Most methods for studying cellular microforces can be considered to be in one of two general categories: active or passive. Active approaches for detecting cellular microforces aim to probe cell mechanics by applying stresses or strains to the cell surface and measuring resistance to the probing as a proxy for cell tension. Examples include cell poking, atomic force microscopy, laser tweezers, micropipette aspiration and fluid shear stresses[1–4]. Magnetic twisting cytometry (MTC)[5], also in this category, has been successfully employed for the study of large numbers of HASM cells in culture, but has some limitations when it comes to examining the mechanics of individual cells in detail. Inherent degradation in the magnitude of the beads magnetization leads to non-constant baseline measurements, i.e., a 30% change at the beginning of an experiment is not the same as a 30% change at the end of an experiment. Experiments must thus be conducted over short periods of time. MTC can only probe the bulk properties of culture; it does not allow for the study of individual cells[5]. There is also no way to control where on the cell beads are attaching. This is important because if beads preferentially attach at the periphery of the cell, or near the nucleus, results will be skewed, as it is well known that forces are non-uniformly distributed across a cell. Finally, it has been proposed that active deformation of a cell may in and of itself alter the mechanical properties of the cell being studied.

Passive approaches for detecting cellular microforces rely on the ability of a cell to deform the substrate on which it is plated and the researchers ability to quantify the deformation and extrapolate mechanical information. Originally, these experiments were conducted by measuring the perturbation of a continuous fabricated material, such as ”wrinkling” silicon sheets or stretching fluorescently labeled elastic films or gels[6–10]. While

these platforms are reportedly able to resolve forces on the order of 10-30nN, forces are generated and propagated across the material, making it difficult to interpret substrate deformations and computationally intensive to calculate discrete forces generated at distinct cellular attachment points. Other devices attempted to overcome this problem by limiting the surface area of the force-detector substratum with which the cell comes in contact. A horizontally placed pad resting on the end of a lever was developed, with a deformation stiffness of 75.8 ± 11.4 nN/mm[11]. However, as the lever is limited to movement along only one axis, calculated forces must be based upon a biased assumption and corrected accordingly. Tan *et al.*[12]. improved upon this idea by designing a micromolded device with arrays of vertically-arranged posts that behave as simple cantilever beams that can move throughout two axes (Figures 3.1(A)–(B)). Cells are cultured on top of the posts. Focal adhesions are established and as the cells establish their baseline prestress, the posts bend. Bending can be seen optically and then quantified to determine the shear forces that cells are exerting on their substrate. Substrate stiffness can be easily controlled over a wide range of values by changing the geometry of the posts, namely the radius and the height.

Tan *et al.* constructed circular posts with a radius of 3 μm, 11 μm height and 9 μm spacing, corresponding to a stiffness of 32 ± 7 nN/μm per post. Using standard protocols for contact I-line UV soft lithography, it is very difficult to produce features smaller than this due to wavelength limitations, catastrophic adhesion failure and reflow of photoresist. Roure *et al.*[13] were able to make smaller posts in more dense arrays by using a different process involving projection photolithography followed by dry reactive ion etching (DRIE), also called the "Borsch" process. Using this method, they were able to produce posts with 1 μm diameter, 5.2 μm height and 2 μm spacing, for which they report a stiffness of 21.8 nN/μm. This is an impressive improvement in scale. However, there are two significant drawbacks to this approach. First, the equipment and infrastructure required for projection lithography and DRIE are too expensive to be readily available to most researchers and many institutions. Second, posts produced in this manner are not entirely cylindrical and therefore cannot be considered to behave like the simple cantilever beams in Figure 3.1(B). Indeed, another group later showed that such posts appear grossly "scalloped"

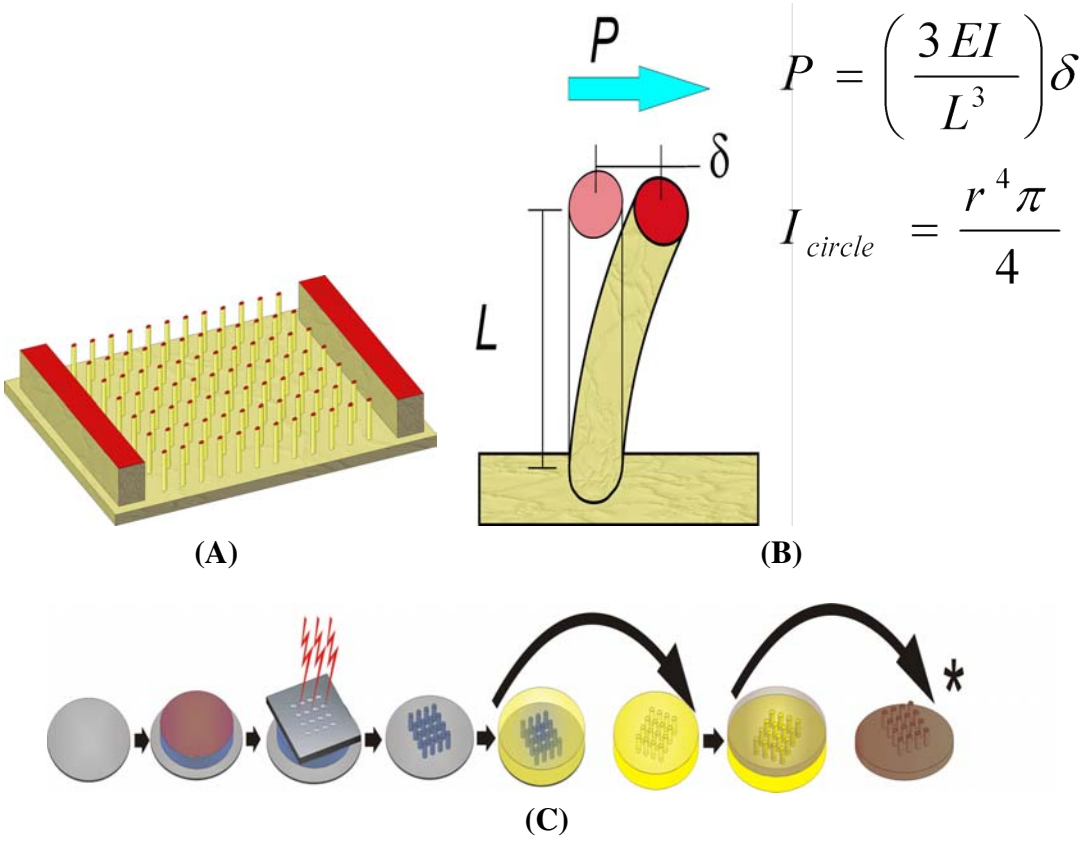

Figure 3.1 Fabrication of Bed of Nails (A)Schematic of the Bed of Nails (B)Posts behave as simple cantilever beams and with a concentrated transverse load P at one end, the deflection observed is dependent on the post spring constant which is a function of post dimensions and material properties. E = Youngs Modulus, L = length (height) of post and I_{circle} is the area moment of inertia of a circle, which is the cross-sectional shape of a post. (C)Schematic of the steps in the BoN microfabrication process using contact I-Line UV soft lithography. An SU-8 master is produced from the negative photoresist using a contrast enhancement agent (red). The SU-8 master is then used as a template to produce a polydimethlysiloxane (PDMS) mold, which in turn is used to cast a workable PDMS BoN, marked by an asterisk.

under scanning electron microscopy and that their bending mechanics are significantly more complex than cantilever beams[14]. This effectively neutralizes the computational advantage of using posts rather than continuous substrates to study cellular forces. The effect also makes mold separation much more difficult. Our experience with the Bosch process suggests that overcoming these difficulties will require either considerable effort or changes in how the technique is applied.

A common difficulty in using a BoN to measure cellular microforces is a lack of clear definition of the location of the top of each post. Because the index of refraction of a cell is close to that of the aqueous media surrounding them, it is difficult to identify the borders

of the cell under bright field microscopy. This can be a significant source of error if not addressed appropriately. Differential interference contrast (DIC) microscopy simplifies identification of the borders of cells, but introduces regions of intermediate intensity that compromise the contrast between cells and posts when the images are spatial bandpass filtered, as required for automatic tracking of post deflection. Confocal microscopy has also been used, though image resolution is lower than DIC. Some investigators have chosen to print the tops of the posts with fluorescently-tagged extracellular matrix (ECM) proteins such as collagen, gelatin, or fibronectin to aid in visualization of the fluorescent posts without DIC[15]. While this is tenable in some circumstances, cells often interact with ECM proteins, degrading and/ or ingesting them. These protein coatings also tend to dissolve in buffers and media used to bathe cells during experimentation, thereby degrading the fluorescent signal in a time-dependent manner. Experiments must therefore be run immediately after labeling and only for a short period of time (usually 60-90 minutes). We know of no published images of live cells on fluorescently labeled posts.

The Bed-of-Nails fabrication process we have developed uses standard contact I-line UV soft lithography with SU-8™negative photoresist and a contrast enhancement step to eliminate the deleterious effects of the air gap between the SU-8 and the photolithographic master, resulting in a process significantly less expensive than projection photolithography and DRIE, to produce fully cylindrical posts with vertical side walls. Though larger than those produced by Roure et. al., the posts in our BoN are sufficiently flexible to respond to shear forces produced by both large and small cells, including HASM cells, and rat aortic smooth muscle cells and dictyostelium (not shown). Additionally, our incorporation of quantum dot-labeling techniques allows precise localization and tracking of BoN posts using standard fluorescence microscopy, minimizing problems associated with discrimination of post-tops and cell edge artifacts generated by DIC microscopy and virtually eliminating time-dependent signal degradation.

Bed-of-Nails design and fabrication

The BoN were designed and fabricated using standard soft lithography methods and SU-8 2000™negative photoresist (Microchem; Newton, MA) in a clean room with some modifications to improve the minimum feature size that could be obtained (Figure 3.1(C)). Vertical support blocks were included on either side of the BoN array to assist in contact printing by preventing crushing of the array. After the softbake step, a barrier coat BC-7.5 (Shin Etsu MicroSi Phoenix Az) was spin coated over the baked photoresist and allowed to dry. Over the barrier coat, we spun a layer of CEM 388SS™(Shin Etsu MicroSi Phoenix Az), a photobleachable contrast enhancement material that is originally opaque to the exposure wavelength and becomes nearly transparent with exposure. . The wafer was then exposed to high energy, collimated UV light through the photolithographic mask using an EXFS Novacure light source. The wafers were rinsed with deionized water on a spinner at high speed and baked to complete SU-8 polymerization. They were then developed, washed and hard baked. The quality of the SU-8 master and subsequent substrates is determined by the resolution of the quartz mask and finding the optimal exposure dose and bake times and temperatures. Liquid prepolymer of the elastomer polydimethylsiloxane (PDMS; Slygard 184, Dow Corning; Midland, MI) was poured over the surface of the SU-8 master, degassed under vacuum, cured overnight at 65°C, then peeled off, leaving a PDMS mold that has a complementary relief pattern (i.e., holes) to that of the SU-8 master. The PDMS mold was oxidized in a plasma cleaner for 30 seconds, then silanized with (Tridecafluoro-1,1,2,2-tetrahyrooctyl)-1-trichlorosilane (United Chemical Technologies; Bristol, PA) under partial vacuum overnight. Liquid PDMS was then poured on the surface of the silanized PDMS mold, degassed, and cured at 65°C for 15 hours. The cured elastomer was peeled from the PDMS mold to yield a Bed-of-Nails. By this process approximately 70% of the BoNs we produced were useable.

Reagents for Quantum Dot Synthesis

Tri-n-octylphosphine oxide (TOPO, 90% tech. grade), hexadecylamine (HDA 90% tech. grade), dibutyl ether (99%+) and octadecene (ODE, 90% tech. grade) were purchased from Aldrich and used as received. Cadmium oxide (CdO, 99.999% Puratrem), tri-n-butylphosphine (TBP, 97%), and selenium powder (200 mesh) were purchased from Strem and used as received. Sulfur powder (ACS Reagent Grade) was purchased from Fisher and used as received. Dodecylphosphonic acid (DPA) was synthesized from commercially available precursors using the Arbuzov reaction.

Synthesis of CdSe/CdS Core/Shell Quantum Dots

Hydrophobic CdSe/CdS quantum dots were synthesized via a one pot method. The cores were synthesized in a similar fashion to that of Peng and Peng[16]. with modifications. Briefly, the one pot technique works based on the principle that the reaction kinetics for high quality CdSe favor being cadmium rich. By using a large excess of cadmium in the initial core synthesis (5:1, Cd:Se), core/shells utilizing the same metal (in this case cadmium) may be synthesized by simply adding a different nonmetal (in this case sulfur) slowly to the reaction mixture once the cores cease to grow. After all reactions were complete, the quantum dots were isolated by precipitation from methanol followed by centrifugation. The resulting pellet was dissolved in a small amount of chloroform and precipitated with the smallest amount of methanol required to cause precipitation, and the quantum dots were again collected by centrifugation. This dissolution in chloroform and precipitation were repeated four more times, yielding CdSe/CdS, core/shell quantum dots which were readily dispersed in non-polar organic solvents (e.g. toluene).

Labeling of BoN array with quantum dots

We selected quantum dots for labeling because they are less prone to photobleaching than organic dyes, making them an ideal choice. We coated the tops of the posts with a very thin layer of PDMS in which was mixed a suspension of quantum dots. Fig-

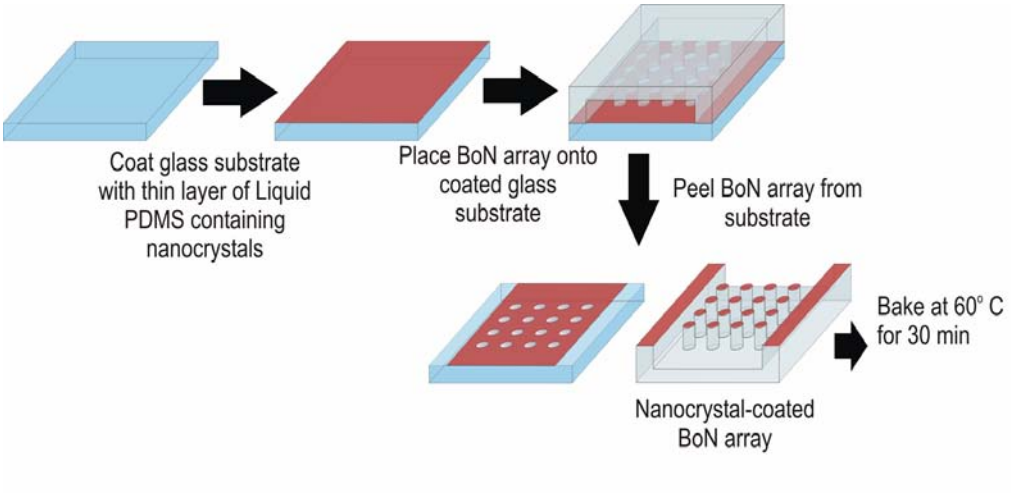

(A)

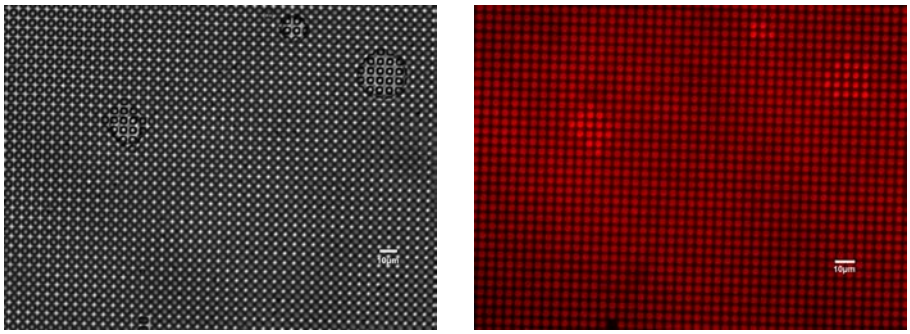

(B) **(C)**

Figure 3.2 Labeling of BoN array (A)Schematic showing labeling of BoN array with fluorescent quantum dots. A glass slide is spin coated with PDMS containing quantum dots, which are then contact printed onto the surface of a plasma-treated BoN (B)–(D) Labeled BoN with cells. (B)Differential Interference Contrast (DIC) image of Human airway smooth muscle cells (HASM)on posts 2 μm in diameter, 5 μm spacing and 7 μm tall. (C) Fluorescent image of same posts labeled with quantum dots.

ure 3.2(A) is a schematic outlining the labeling process. Briefly, a toluene solution of PDMS prepolymer was first prepared by dissolving PDMS prepolymer with toluene in a 1:10 mass ratio[17]. Then 0.20 ml of a suspension of CdSe/CdS core/shell quantum dots capped with TOPO/HDA (trioctylphosphine oxide/ hexadecylamine) in toluene was added to the dissolved prepolymer and mixed well. This was then spin-coated on a glass slide at 2000 revolutions per minute (rpm) for one minute. The BoN was then gently brought into contact with the coating on the slide for 10-15 seconds. The BoN was removed from the slide and inverted in a curing oven at 60 °C for 30 minutes.

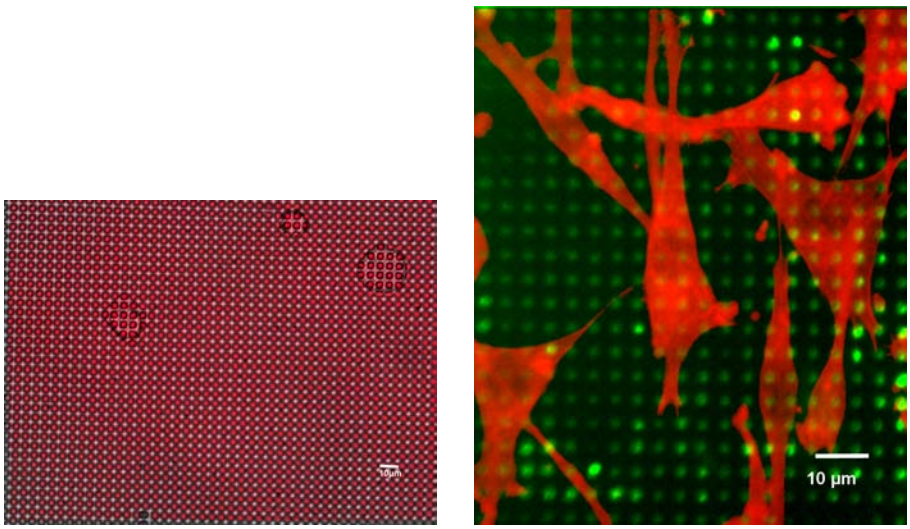

(D) **(E)**

Figure 3.2 —cont. (D) Overlay image of DIC and fluorescent image. (E) Fluorescent image of 3T3 fibroblasts on the beds labeled with CdSe/ZnS (green) quantum dots and fixed and stained with Alexa Fluor®568 Phalloidin (red).

Cell Culture

Human airway smooth muscle (HASM) cells were cultured in plastic flasks in Hams F12 medium with 10% fetal calf serum (FCS) supplemented with penicillin (100 U/ml), streptomycin (0.1 mg/ml), amphotericin B (2.5 μg/ml), NaOH (12 mM), CaCl2 (1.7 mM), and L-glutamine (2 mM). Culture media was changed every 3 - 4 days. Cells were passaged with 0.25% trypsin and 1 mM ethylene diamine tetraacetic acid (EDTA) every 10 14 days. Prior to cell seeding, the BoN array was sterilized by soaking in 90% alcohol for 30 minutes and then allowed to dry. It was then soaked in Collagen I (5μg/ cm^2) for 1 hour at room temperature, rinsed in PBS and dried. Passaged cells were seeded on the BoN array and allowed to settle and attach overnight. The culture medium was then changed and cells were observed over a period of about 2 hours. Cells were also treated with 50 mM potassium chloride (KCL) and observed over the same period of time.

Differential interference contrast and fluorescence microscopy

The cells on top of the posts were observed using both Differential Interference Contrast (DIC) and fluorescence (excitation 400 nm,emission 605 nm) microscopy through 20

and 40 air objectives on a Zeiss Axiovert 200M microscope with a Photometrics CoolSnap HQ camera. The device was positioned with the posts pointing upwards and the images were taken through the PDMS from beneath the array. Cells were also fixed in 100% ethanol at -20°C, washed several times with 1% BSA in PBS, permeabilized and stained for actin with Alexa Fluor®568 Phalloidin (Molecular Probes).

Calibration of BoN array

To account for any variations in post profile or mechanical properties from the ideal cylindrical cantilever, during the fabrication process, we measured the spring constant of posts experimentally. We determined the spring constants of pulled glass micropipettes (World Precision Instruments; Sarasota, FL) by measuring the deflection of the tip produced by single weights in the range of 1 6 mg made from various lengths of gold wire[18,19]. We calibrated the posts for force by moving these micropipette tips against them using a Lang Electronik (Httenberg Germany) motion controller (Ms 21 S) and observing the relative deflections of the tips of the posts and micropipette tips. Using this method, we found that posts 3 μm in diameter and 10 μm tall have spring constants of about 27 nN/μm. Substituting I$_c$*ircle* into the force deflection relationship in Figure 3.1(B), we see that the load P and the displacement δ are related by

$$P = \left(\frac{3}{4}\pi E \frac{r^4}{L^3}\right)\delta$$

where the term in brackets is the spring constant of an individual post. Substituting values of E, r, and L, we calculate the spring constant of a post to be 23.8 nN/μm, which is in good agreement with the calibration experiment. Actual posts used in the experiment were 2 μm in diameter and 7 μm tall, which gives a spring constant of 13.6 nN/μm.

Image analysis and calculation of cell traction forces

We generated a stack of DIC and fluorescent images taken in time-lapse mode using METAMORPH™. We then aligned the stack using image processing software from

ImageJ[20,21]. The local deformation of the posts was tracked and measured using a multi-particle tracking software written in MATLAB™ (Mathworks) and based on image processing algorithms written for colloidal studies[22]. The fluorescence image produced by the quantum dots greatly increases contrast between the post tips and the background and enables the software to identify and track the centroids of fluorescent post tips to sub-pixel accuracy. Prior to running the tracking algorithm, the fluorescent image was smoothed and filtered. To account for error due to long term drift, we obtained a stack of fluorescent images with posts at rest taken over the approximate duration of actual experiments. The posts were tracked and the maximum displacement (1.2 μm) recorded was used as an indicator of the error due to mechanical and thermal drift. The fluorescent image stack from the experiment was also aligned and tracked. Given that the lateral resolution of the optical microscope is limited to about 150 nm and the spring constant of the posts used is 13.7 nN/μm, we were able to resolve forces of 2.05 nN.

Results and Discussion

Minimum feature size in conventional contact photolithography is limited by wavelength, resist thickness and the air gap between the mask and substrate[23]. The theoretical resolution capability for contact lithography is given by[23]

$$2b_{min} = \sqrt[3]{\lambda\left(s + \frac{1}{2}d\right)}$$

where $2b_{min}$ is the grating period or in our case the post spacing, λ the wavelength of light used, s the spacing between the mask and the photoresist surface and d the photoresist thickness. The air gap introduces diffraction and interference patterns which can ruin small features[24], so we used a Contrast Enhancement Material to overcome the air gap problem. The CEM then acts as a secondary mask, but with no gap between it and the photoresist[25]. Thus s can be set to zero. Using this method we have been able to fabricate posts 2 μm in diameter, 5 – 6 μm spacing and 7 – 11 μm tall (Figure 3.3). For the resist thicknesses mentioned above and an exposure wavelength of 365 nm, $2b_m in$ ranges from 3.4 μm to 4.4

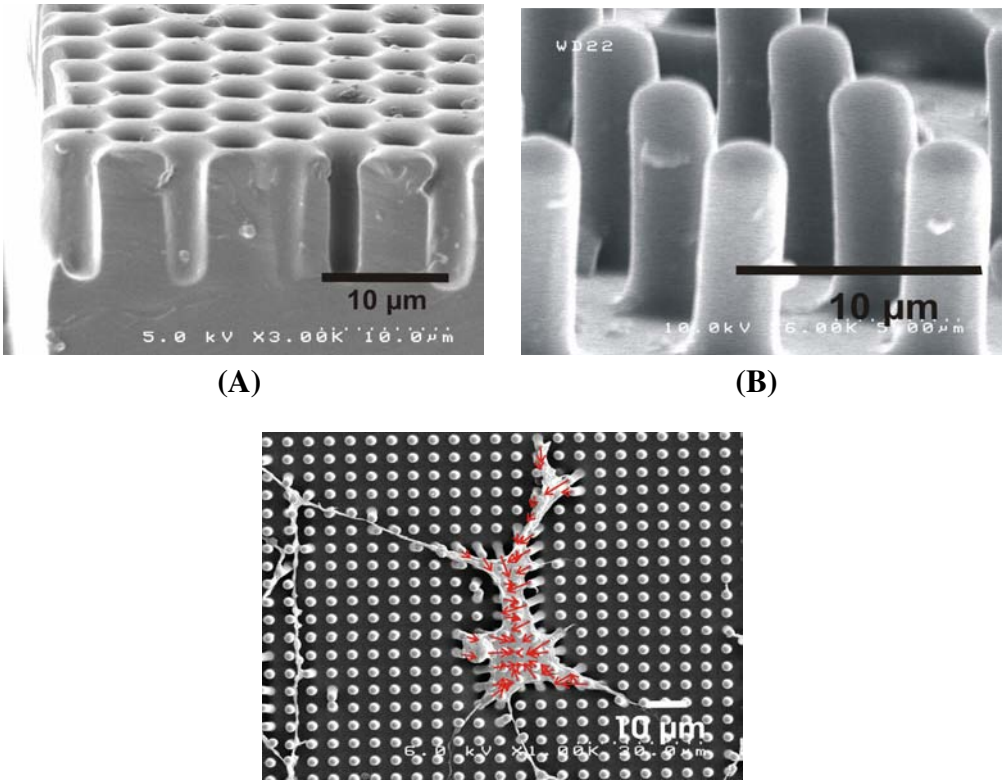

(A) **(B)**

(C)

Figure 3.3 Fabrication of BoN array (A) Scanning Electron micrograph (SEM) of section of PDMS master with 2 μm holes 6 μm spacing and 11 μm deep. (B) SEM of profile of section of BoN 2 μm in diameter 5 μm spacing and 7 μm tall. (C)SEM of a human airway smooth muscle (HASM) cell cultured for 24 hours while spanning about 75 posts.

μm with corresponding minimum feature sizes of 1.70 – 2.12 μm. The 2 μm feature size with the corresponding 5 – 6 μm spacing is therefore close to the theoretical values that can be obtained. Figure 3.3(A) is a SEM micrograph of a sectioned PDMS master mold. The apparent variations in the profiles of the holes are due to the fact that the mold was sectioned manually with a scalpel at an approximate angle of 45°to the horizontal. This ensured that at least some holes would be sectioned perfectly. Prior attempts at sectioning the mold with the blade parallel to the holes were not successful. As can be seen from the figure the second hole from the right is quite cylindrical. Figure 3.3(B) shows a section of the posts in profile showing a uniform cylindrical profile without any variations in profile.

We examined the possibility of whether the quantum dot labeling affected the post profile. Toluene, a non-polar solvent which is used as the suspension medium for the quantum dots as well as a thinning agent is known to swell PDMS[26]. However, we found

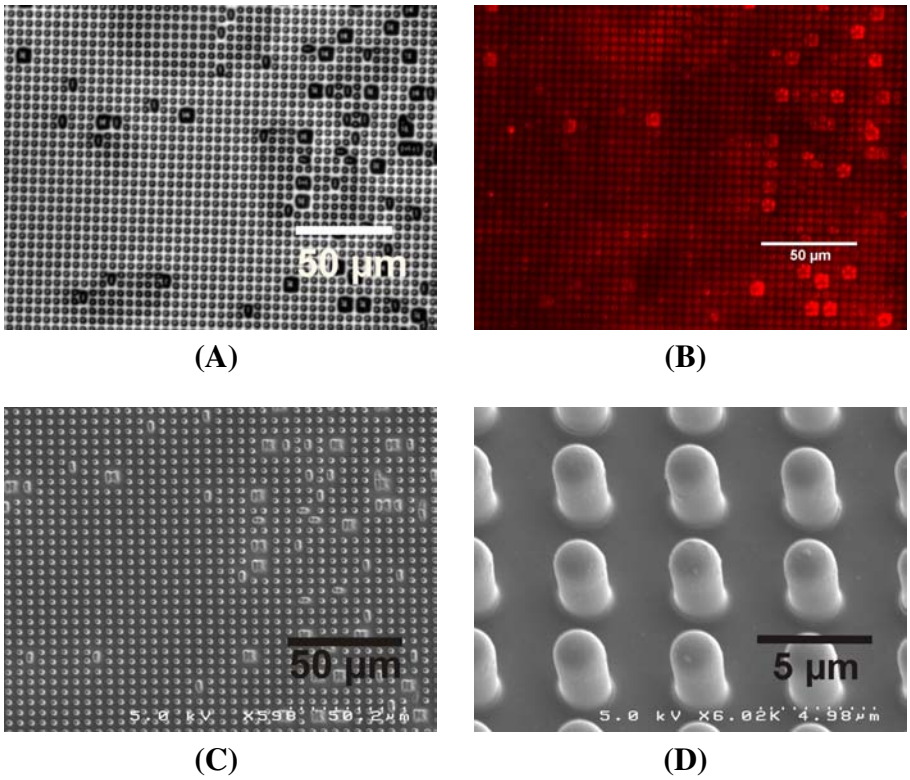

(A) (B)

(C) (D)

Figure 3.4 Results: Quantum dot labeling (A) DIC (B) fluorescent and (C)SEM of approximately the same section of labeled BoN. (D) SEM close up of posts at 45°showing no change in post profile after labeling process.

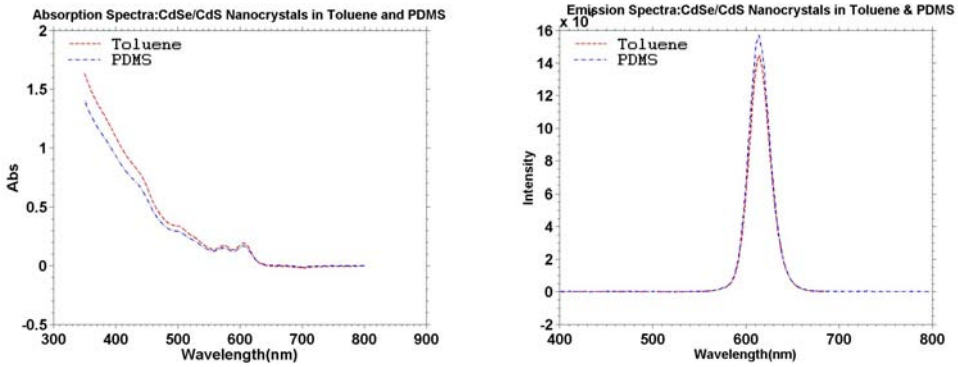

(E) (F)

Figure 3.4 —cont. (E) Absorption and (F) emission spectra of quantum dots in toluene and PDMS solution in toluene showing essentially no difference.

that this had no significant effect (figure 3.4). Also of concern was whether the PDMS used affected the emission and adsorption characteristics of the quantum dots. This was found not to be the case. The absorption spectra were almost identical, and solutions of the quantum dots in toluene and in dissolved PDMS in toluene, excited at 367 nm wavelength, showed the same emission profile and peak wavelength. The difference in peak intensities in figure 3.4(F) was due to slight concentration differences.

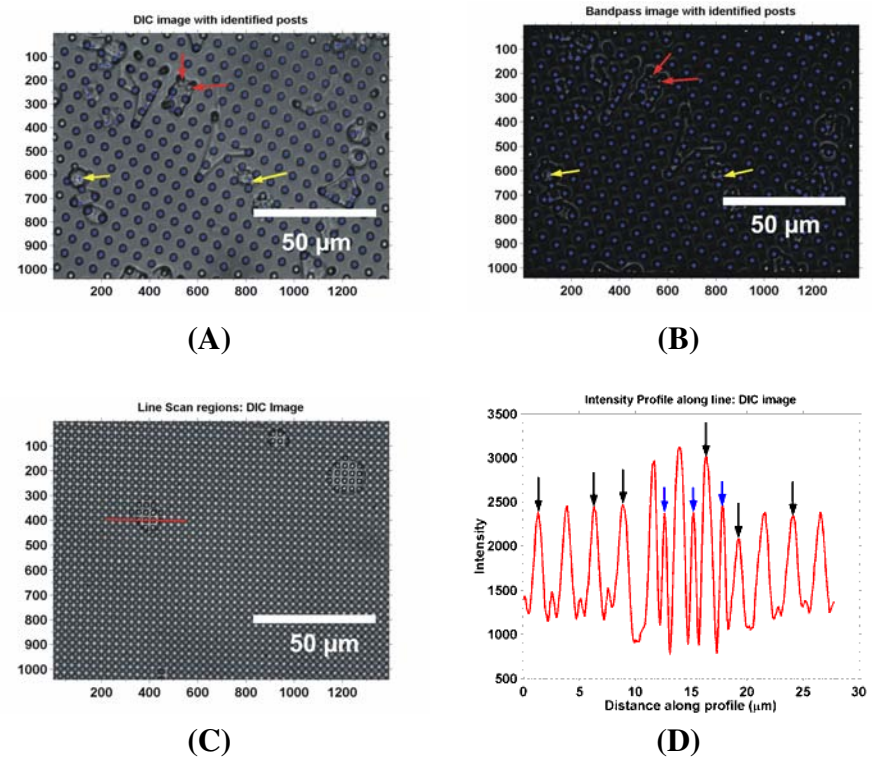

Figure 3.5 Artifacts (A) DIC image of rat aortic smooth muscle (RASM) cells on posts 3 μm in diameter and 11 μm tall with 8 μm spacing and its bandpass filtered version, (B) showing two common artifacts that occurred due to poor contrast. The red arrows show posts tips that could not be identified and the yellow arrows show artifacts that are introduced by the cell body (C) Data from Figure 3.2(C) showing the line (red) along which an intensity profile (D) is generated. The black arrows point to the location of post tips. The blue arrows point to artifacts introduced by the cell that have intensity values close to that of the posts.

Previous attempts to track and measure cell traction forces using differential interference contrast images (DIC) on the BoN proved to be problematic. Image processing steps include using a real–space bandpass filter which smoothes the image and subtracts the

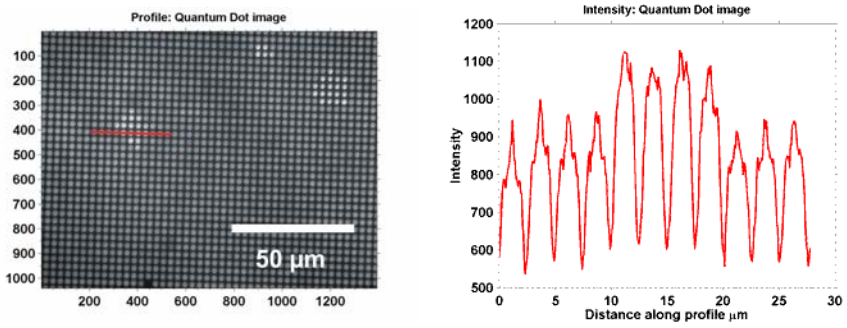

(E) **(F)**

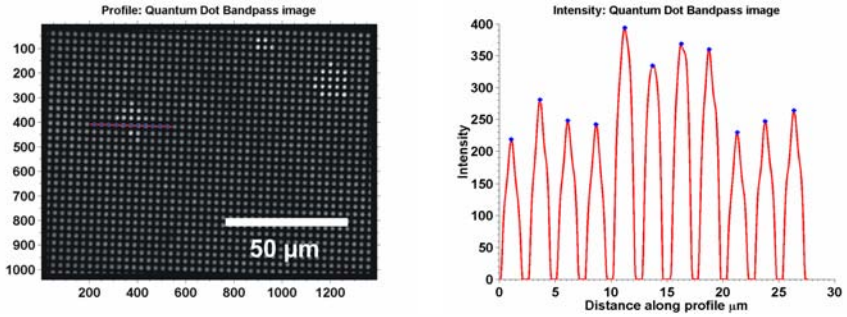

(G) **(H)**

Figure 3.5 —cont. (E) and (F) Data from figure 3.2(D) and its corresponding intensity profile showing the absence of the artifacts. (G) and (H) The bandpass filtered version of figure 3.5(E) and its intensity profile. The blue marks correspond to posts that were identified along the profile

background. However, in areas with significant cell coverage, location and tracking of posts proved difficult if not impossible. Figure 3.5 shows a DIC image and its bandpass filtered version. The particle identification algorithm was run on the bandpass filtered version and the locations of the centroid of the post tips were plotted over both. The red arrows point to post tips that could not be identified. Certain cell areas exhibited features that were incorrectly identified as post tops (yellow arrows).

To test the accuracy and precision of the ImageJ alignment plug-in, we simulated images that had been shifted laterally. The first slice from a stack was used as a reference image and a shifted image was simulated by displacing the whole image either $u(x)$ pixels in the x or $v(y)$ in the y direction, respectively, over a range of values from 0.5 μm to 1.2 μm. The resulting image was then aligned using the plug-in and the maximum displacement corresponded to the registration error. The algorithm used in the plug-in registered the shifted image to within 60 nm.

Neither this study or the others before it[12,13] address the possibility that the differences between the indices of refraction of the cell, the post, and the fluid media will produce refractive artifacts that distort the image and the apparent position of a post relative to cellular structures. With inverted microscopy, the cells are imaged through the PDMS posts, which when bent may act as tilted cylindrical lenses. With upright microscopy, the posts are viewed through the cell, which may have a curved surface that acts as either a convex or concave lens that shifts the apparent position or size of objects beneath it.

To illustrate how our quantum-dot labeled BoN could be used for studying cellular forces we made quantitative measurements of the interfacial forces on cells cultured on the BoN array for 48 hours. Cells were observed under base conditions for 2 hours (Figures 3.6(A) and (B)). Cells were also stimulated with 50 mM KCl and observed for about 2 hours (Figures 3.6(C) and (D)). The range of forces observed for the cell without any stimulation ranged from 0 nN to 7 nN. The cell stimulated with KCl showed a maximum of 2.5 nN. These forces were computed from the displacement field obtained from the tracking program. The histograms of the magnitudes of the forces over the time course of the experiments for both cells are plotted in Figure 3.6(B) and (D). The distributions are skewed with the mean value closer to zero. The distribution of these forces was well fit by a Log-normal distribution, which is in good agreement with a previous study on HASMs cells[27].

A force map was computed from the displacements observed. Figure 3.6(A) and 3.6(C) show overlays of arrows representing the forces computed for both cells. We also computed a force balance using the following metric for individual forces projected in the x and y directions.

$$F_{balance} = \frac{\left|\sum_{i=1}^{N} f_{ix,iy}\right|}{\sum_{i=1}^{N} \left|f_{ix,iy}\right|}$$

where are the resolved forces either in the x or y direction for a particular post. The x forces in figure 3.6(A) balance to within 1.4 % while the y forces balance to within 3.9%. The forces balance to within 0.9% and 5.3% in the x and y directions respectively for the cell in figure 3.6(C). We carried out an evaluation of the change in mean prestress for both cells over the experimental period. The mean prestress (τ) is defined as$\tau = \sigma A_i/A_c$ where

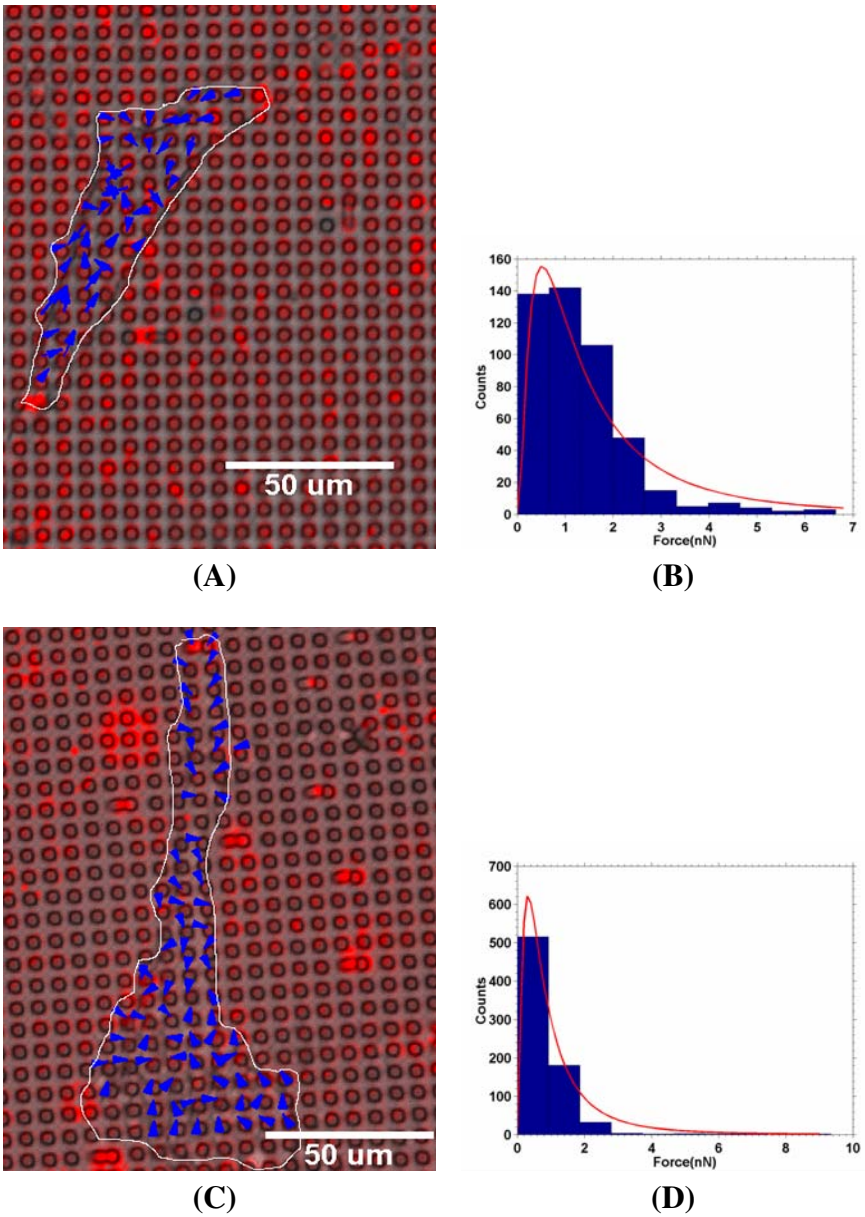

Figure 3.6 Measurement of microforces exerted by HASM cells (A) HASM cell recorded under baseline conditions with a representative force map with arrows 3x the actual size. The longest arrow is equivalent to 7 nN (C) HASM cell recorded after stimulation with 50 mM KCL. The longest arrow is equivalent to 2.5 nN. (B) and (D) Histogram of forces. The fit to a log-normal distribution is shown as the red line over the histogram plot.

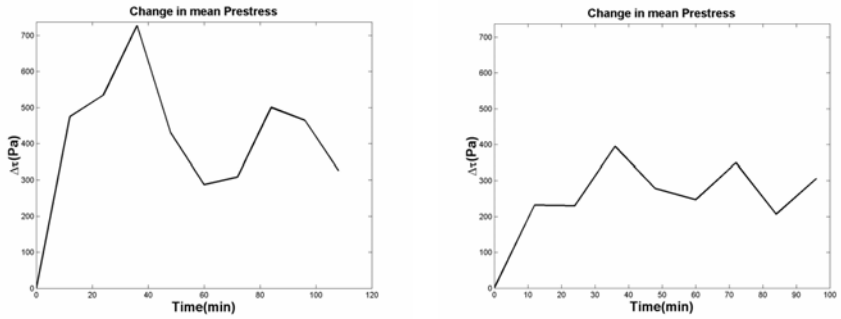

(A) **(B)**

Figure 3.7 Temporal evolution of the change in mean prestress (A) Cell in Figure 3.6(A). (B)Cell in Figure 3.6(C)

σ is the mean traction, A_i is the interfacial area of cell in contact with substrate, and A_c is the cross sectional area of the cell section[28,29]. However, using this metric introduces some error due to the difficulty of estimating the cross-sectional area of the cell section. We estimate the mean prestress using

$$\tau = \frac{\sum_{i=1}^{N} |f_i|}{aN}$$

where f_i is the traction force developed at each post, a is the cross-sectional area of an individual post and N is the total number of posts that are identified and tracked. A possible source of error using this method arises in the case where the cell did not cover an entire post. To reduce this, we selected only the posts that were entirely covered by the cell for analysis. Figure 3.7 shows the temporal evolution of the change in prestress.

We expected the cell stimulated with KCl to show, on average, a greater change in mean prestress over the duration of the experiment; however, this was not the case. A possible explanation is the fact that the initial prestress at the start of experiment was not considered and in future experiments, the initial prestress will be determined by treating the cells with trypsin and then acquiring an image which will be used as the reference image. A previous study on HASM cells has shown that the baseline stiffness affects the change in stiffness when the cells are stimulated by the contractile agonist histamine: stiff cells showed only a 1.8 fold increase whereas less stiff cells showed as much as a 5.2 fold increase from baseline. In the same study, it was also noted that increase in stiffness

relative to base line varied appreciably from cell to cell, with about 10% showing greater than a 10 fold increase, another 10% showing less than 1.25 fold increase, and about 50% showing between 1.25 and 2.5 fold increase[30]. Although the prestress is not equivalent to the cell stiffness, it has been observed previously that there is a close association between cell stiffness and prestress[29] We also analyzed a cell that had been fixed and stained on the BoN. A regular grid representing ideal undeflected positions of the posts was formed over five areas where there was no cell attachment. Figure 3.8(B) is a histogram of the displacements from the ideal for these regions. The mean displacement was 0.24 μm with a standard deviation of 0.17 μm. Figure 3.8(A) shows the cell with the representative computed traction forces.

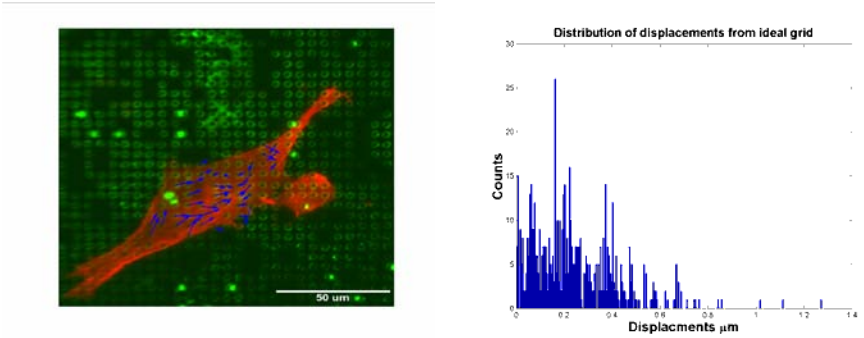

(A) **(B)**

Figure 3.8 Force measurements on fixed cell (A) Overlay of traction forces on a HASM cell fixed and stained on quantum dot labeled posts. The longest arrow is 53 nN. (B)Histogram of displacement of posts from ideal grids.

Conclusion

We have been able to microfabricate BoN arrays using a contrast enhancement photolithography technique. This is a relatively inexpensive microfabrication method that allows feature sizes close to the theoretical limits for contact lithography. To better track forces, we labeled the arrays with fluorescent quantum dots, which provide much better contrast and longer experimental observation times without photobleaching thus improving

the tracking of posts. We show how this can then be used for measuring traction forces exerted by HASM cells. This technique can be extended to other cell types, including dictyostelium, and could be used as a tool for investigating forces generated by cells during chemotaxis.

Acknowledgements

We thank Kevin Seale for assistance with ImageJ plugins, and Pampee Paul Young for providing the fibroblasts and the RASM cells. This work was supported by the Vanderbilt Institute for Integrative Biosystems Research and Education (VIIBRE), The Whitaker Foundation and the U.S. Department of Energy.

References

[1] Mathur, A. B., Collinsworth, A. M., Reichert, W. M., Kraus, W. E., Truskey, G. A. Endothelial, cardiac muscle and skeletal muscle exhibit different viscous and elastic properties as determined by atomic force microscopy. *Journal of Biomechanics* **34**, 1545–1553, 2001.

[2] Evans, E., Yeung, A. Apparent viscosity and cortical tension of blood granulocytes determined by micropipet aspiration. *Biophys.J.* **56**, 151–160, 1989.

[3] Svoboda, K., Block, S. Biological Applications of Optical Forces. *Annual Review of Biophysics and Biomolecular Structure* **23**, 247–285, 1994.

[4] Usami, S., Chen, H. H., Zhao, Y., Chien, S., Skalak, R. Design and construction of a linear shear stress flow chamber. *Annals of Biomedical Engineering* **21**, 77–83, 1993.

[5] Chen, J., Fabry, B., Schiffrin, E. L., Wang, N. Twisting integrin receptors increases endothelin-1 gene expression in endothelial cells. *Am J Physiol Cell Physiol* **280**, C1475–C1484, 2001.

[6] Harris, A., Stopak, D., Wild, P. Fibroblast Traction As A Mechanism for Collagen Morphogenesis. *Nature* **290**, 249–251, 1981.

[7] Beningo, K. A., Wang, Y. L. Flexible substrata for the detection of cellular traction forces. *Trends Cell Biol.* **12**, 79–84, 2002.

[8] Burton, K., Taylor, D. L. Traction forces of cytokinesis measured with optically modified elastic substrata. *Nature* **385**, 450–, Jan 30, 1997.

[9] Burton, K., Park, J. H., Taylor, D. Keratocytes Generate Traction Forces in Two Phases. *Mol.Biol.Cell* **10**, 3745–3769, 1999.

[10] Butler, J. P., Tolic-Norrelykke, I. M., Fabry, B., Fredberg, J. J. Traction fields, moments, and strain energy that cells exert on their surroundings. *Am J Physiol Cell Physiol* **282**, C595–C605, 2002.

[11] Galbraith, C. G., Sheetz, M. P. A micromachined device provides a new bend on fibroblast tractionforces. *PNAS* **94**, 9114–9118, 1997.

[12] Tan, J., Tien, J., Pirone, D., Gray, D., Bhadriraju, K., Chen, C. Cells lying on a bed of microneedles: An approach to isolate mechanical force. *PNAS* **100**, 1484–1489, 2003.

[13] du Roure, O., *et al.* Force mapping in epithelial cell migration. *PNAS* **102**, 2390–2395, 2005.

[14] Zhao, Y., Zhang, X. Cellular mechanics study in cardiac myocytes using PDMS pillars array. *Sensors and Actuators A: Physical* **125**, 398–404, 2006.

[15] Roure, O. d., *et al.* Microfabricated arrays of elastomeric posts to study cellular mechanics. *Proc.SPIE* **5345**, 26–34, 2004.

[16] Peng, Z., Peng, X. Formation of High-Quality CdTe, CdSe, and CdS Nanocrystals Using CdO as Precursor. *J.Am.Chem.Soc.* **123**, 183–184, 2001.

[17] Wu, H., Huang, B., Zare, R. Construction of microfluidic chips using polydimethylsiloxane for adhesive bonding. *Lab on a Chip* **5**, 1393–, 2005.

[18] YONEDA, M. Force Exerted by a Single Cilium of Mytilus Edulis. I. *J Exp Biol* **37**, 461–468, 1960.

[19] Nicklas, R. Measurements of the force produced by the mitotic spindle in anaphase. *The Journal of Cell Biology* **97**, 542–548, 1983.

[20] Thevenaz, P., Ruttimann, U., Unser, M. A pyramid approach to subpixel registration based on intensity. *Image Processing, IEEE Transactions on* **7**, 27–41, 1998.

[21] Abramoff, M., Magelhaes, P., Ram, S. Image Processing with ImageJ. *Biophotonics International* **11**, 36–42, 2004.

[22] Crocker, J. C., Grier, D. G. Methods of Digital Video Microscopy for Colloidal Studies. *Journal of Colloid and Interface Science* **179**, 298–310, 1996.

[23] Thompson, L., Willson, C., J.S.Bowden, M. *Introduction to microlithography : theory, materials, and processing*. American Chemical Society, 1983.

[24] Zhang, J., Chan-Park, M., Conner, S. Effect of exposure dose on the replication fidelity and profile of very high aspect ratio microchannels in SU-8. *Lab on a Chip* **4**, 646–, 2004.

[25] Flack, W., Nguyen, H.-A., Buchanan, J., Capsuto, E., Marks, A. Contrast Enhancement Materials for Thick Photoresist Applications. *Proceedings of SPIE* **5376**, 1190–1205, 2004.

[26] Xia, Y., Whitesides, G. M. Soft Lithography. *Annual Review of Materials Science* **28**, 153–184, 1998.

[27] Tolic-Norrelykke, I. M., Butler, J. P., Chen, J., Wang, N. Spatial and temporal traction response in human airway smooth muscle cells. *Am J Physiol Cell Physiol* **283**, C1254–C1266, 2002.

[28] Wang, N., *et al.* Mechanical behavior in living cells consistent with the tensegrity model. *PNAS* **98**, 7765–7770, 2001.

[29] Wang, N., *et al.* Cell prestress. I. Stiffness and prestress are closely associated in adherent contractile cells. *Am J Physiol Cell Physiol* **282**, C606–C616, 2002.

[30] Fabry, B., *et al.* Signal Transduction in Smooth Muscle: Selected Contribution: Time course and heterogeneity of contractile responses in cultured human airway smooth muscle cells. *J Appl Physiol* **91**, 986–994, 2001.

CHAPTER IV

POLY(VINYL ALCOHOL) AS A STRUCTURE RELEASE LAYER FOR MICROFABRICATION OF POLYMER COMPOSITE STRUCTURES

Kweku A. Addae-Mensah,[1] Ronald S. Reiserer,[2] John P. Wikswo,[1,2,3,4]

[1]Department of Biomedical Engineering,

[2]Vanderbilt Institute for Integrative Biosystems Research and Education

[3]Department of Physics and Astronomy

[4]Department of Molecular Physiology and Biophysics

Vanderbilt University, Nashville, TN

Portions of this manuscript have been published in:

Kweku A. Addae-Mensah, Ronald S. Reiserer, John P. Wikswo.
J. Micromech. Microeng. Vol 17 (2007)N41 – N46

Abstract

While lift-off techniques are common in the fabrication of hard, silicon-based microelectromechanical systems (MEMS), these techniques are not yet in widespread use in soft lithography, where polymer materials are used to fabricate MEMS devices for biological applications (BioMEMS). We present fabrication steps that allow us to make use of Poly(Vinyl Alcohol) (PVA) as a structure release agent in BioMEMS microfabrication. The release method offers a simple, cost effective and reliable way to release microfabricated structures that need to be bonded to other structures or are already bonded to them. We use this technique to release discs made of SU-8 that are attached to a vertical cylindrical microcantilever array that is replica-molded using PDMS. This approach may be used to release structures made from a variety of materials that are not compatible with typical lift-off chemistries, although we address only SU-8 and polydimethylsiloxane (PDMS) in this technical note.

Introduction

The deflection of a cantilever is a well known method for measuring forces[1]. Microcantilevers have a variety of applications in science and engineering[2]. Arrays of vertical microcantilevers fabricated from PDMS have been introduced to measure cellular forces[3,4]. Application of external forces to these cantilevers is problematic because of their small diameter and close spacing. To overcome this limitation, we have developed a technique to enable fabrication of 60, 20 and 10 μm diameter by 2 μm thick SU-8™(MicroChem Corp Newton MA) discs that are attached to the vertical cylindrical microcantilever arrays fabricated from PDMS. These disc structures are designed to enable the application of active forces to individual vertical microcantilevers as well as cells that are cultured on the vertical microcantilever arrays and touching one or more of the attached discs.

The traditional metal lift-off process is an additive pattern-transfer technique that was developed mainly as a means for patterning metals in the microelectronics and semiconductor industry[5–7] and involves deposition and patterning of a sacrificial layer (normally

photoresist) followed by another deposition of the metal before lift-off of the sacrificial layer. It has also been used in the production of thin-film optical devices and electrochemical transducers and sensors[8–11]. A process similar to the lift-off technique has also been widely used in surface micromachining, mainly in the MEMS field. It involves first depositing and sometimes patterning a sacrificial layer. Polysilicon or its variants are then deposited and patterned on the sacrificial layer. The sacrificial layer is then etched from underneath the silicon to release the structure. In most cases the released structure has anchors to a fixed substrate[12–15]. While photoresists are commonly used for MEMS lift-off, the chemistries used are often incompatible with the materials or processing used for soft-lithographic BioMEMs. Many biological materials, gels and some polymers that are currently used for BioMEMS cannot be patterned or released using the common photoresists because the release methods (chemical or thermal degradation) may be too harsh or toxic. Alternative methods that have been developed include the use of patterned elastomeric membranes[16,17], polystyrene[18], parylene-C (poly para-xylylene)[19], poly(Vinyl Alcohol) (PVA)[20–22] and functionally modified poly(acrylic acid)[23].

PVA has traditionally been used in industry as a mold release agent[24–26]. It also has applications in drug delivery and, because of its biocompatibility, it has been used in conjunction with extra-cellular matrix proteins as a tissue scaffold[27,28]. The advantages of using PVA over other materials used to release SU-8 are its low cost and solubility in water, which reduces its environmental impact and makes it more user-friendly[29–31] than most other sacrificial chemistries. An added advantage we found was that water will not attack the PDMS structures and has no noticeable effects on the SU-8 2000™features that were attached to the PDMS vertical microcantilever arrays, which cannot be said for other methods reported in the literature. Toluene, for example, has been used in conjunction with polystyrene to release SU-8 membranes[18]. Though it was shown not to have any effects on SU-8 it is known to swell PDMS[32] and hence would not be an ideal choice. One group[33] has used OmniCoat (MicroChem Corp MA, USA) to release SU-8 structures. We were not successful in creating a thick enough layer of OmniCoat to release without solvent damage to 2 mm $\times$ 2 mm arrays of 60 μm microfabricated SU-8™objects and the

underlying substrate. Table 4.1 is a short summary of various lift-off materials and their corresponding sacrificial or release layers.

Table 4.1 Summary of various lift-off materials and corresponding sacrificial /release layers.

Lift-off Material	Sacrifical/release layer	Etch Chemistry	Application
Pb Alloy	AZ1350 photoresist	Acetone	Metal line pattern[7]
Cr-Ni	AZ1350 photoresist	Acetone	Schottky-barrier FET's[6]
SU-8	Polystyrene	Toluene	SU-8 Membranes[18]
SU-8	OmniCoat™-(Microchem)	Hot NMP(1-methyl-2-pyrrolidinone)	DWP™[33]
SU-8	Polycrystalline silicon	Dry etch. Xenon difluoride (XeF_2)	SU-8 microgripper[34]
SU-8	Poly(acrylic acid)(PAA)	Water	SU-8 discs,metal coated SU-8[23]
SU-8	Copper	Sodium peroxodisulfate ($Na_2S_2O_8$)	Compliant check valves[35]
SU-8	Cr/Au/Cr	Wet Chromium etch	Polymeric cantilever arrays[36]
Organic electronic film	Parylene	Scotch tape (physical peel off)	Organic LEDs[19]
TPD[1],Alq_3[2]	PDMS elastomeic membrane	None (physical peel off)	Electroluminescent materials for optics[17]
Reflective aluminium alloy	Silicon dioxide	Proprietary	TI digital miromirror device (DMD™)[37,38]

Continued on next page

[1]N,N'-diphenyl-N,N'-bis(3-methlyphenyl)-1-1'-4,4'-diamine
[2]Tris(8-hyrdroxyquinoline)aluminium.

Table 4.1 (continued)

Lift-off Material	Sacrifical/release layer	Etch Chemistry	Application
Poly-silicon	Silicon dioxide	Buffered Hydrofluoric acid(BHF)	Cantilever beams[15]
Poly-silicon	Phosphosilicate glass (PSG)	Concentrated (49%) hydrofluoric acid	Plate-on-a-hinge[14],accelerometers[39], micromotors[13]
Au	Poly(vinyl)alcohol (PVA)	Water	Au lines and patterns[22]
AuPd	Polymethyl-methacrylite (PMMA)	Acetone	AuPd electrodes[40]

Materials and Methods

Fabrication and attachment of polymer structures

To microfabricate our array of discs from SU-8 2005™, we made a chrome-on-glass mask so we could use photolithography to create the small features directly on the mask. This negative mask had circular transparent regions with diameters of 60, 20 and 10 μm. The mask was first spin-coated (1500 RPM for 30 s with a ramp from 500 RPM) with a filtered solution of PVA (BC-7.5, ShinEtsuMicroSi, Inc Phoenix AZ) and allowed to dry. The substrate was then spin-coated (3000 RPM for 30 s) with SU-8 2005™that had been thinned out with SU-8 Thinner™in a 3:1 volume ratio to achieve a spin thickness close to 2 μm. Prior to the softbake step, we aligned on the SU-8-coated mask a PDMS vertical microcantilever array that had previously been fabricated using soft lithography methods[32]. The array was gently placed on the glass substrate in contact with the uncrosslinked SU-8 such that the vertical microcantilever arrays were positioned directly over the areas with

the transparent holes. This caused a slight deformation of the uncross-linked SU-8 in the process. The array/SU-8/PVA/mask assembly was then softbaked on a hot plate (ramp of 1 degsign C/min from RT to 95 °C plus an additional 10 mins at 95 degsign C) to remove completely the solvent in the SU-8 layer and also to fix the vertical microcantilever arrays firmly in place. The glass substrate was then exposed to UV light through the back side to initiate cross-linking of the photoresist, and the assembly was baked again (ramp of 1 °C/min from RT to 95 °C plus an additional 15 mins at 95 °C).

In a manner similar to the removal of an edge bead, we used SU-8 developer solution on the spinner at a speed of 3000 RPM to remove photoresist at the edges of the substrate in order to expose the underlying PVA. The assembly was treated in a plasma chamber for 30 seconds to clean the PVA and render it more hydrophilic. We then immersed the assembly in a stirred water bath at 60 °C for about 3 hours. This dissolved all the PVA, thereby releasing the vertical microcantilever array and the attached thin layer of SU-8 from the glass mask. The vertical microcantilever array with SU-8 layer was then immersed in developer solution for 2 minutes to remove all SU-8 that was not cross-linked by the UV exposure, revealing the isolated SU-8 discs. The vertical microcantilever array with discs was then rinsed in isopropyl alcohol (IPA) and gently dried under a stream of nitrogen. The resulting composite PDMS/SU-8 device was hardbaked at 110 °C (ramp of 1 °C/min from RT to 110 °C) for an hour on a hot plate to complete the cross-linking of SU-8. This temperature was chosen to ensure complete cross-linking of SU-8 without affecting the properties of PDMS. PDMS can be cured at 110 °C for 20 hours with negligible effects[3] and is known to be stable and flexible from -50 °C to +200 °C[41]. It must be noted here that this step is not required or may be modified to accommodate materials with lower temperature tolerances.

Figure 4.1 is a schematic summary of our fabrication and lift-off technique. Using this process, we were able to readily create on a prefabricated PDMS vertical microcantilever array thin secular isolated discs, approximately 60, 20 and 10 μm in diameter, mechanically attached to the ends of the vertical microcantilever array by means of their intimate contact with the deformations in the crosslinked SU-8 areas which had been exposed through the

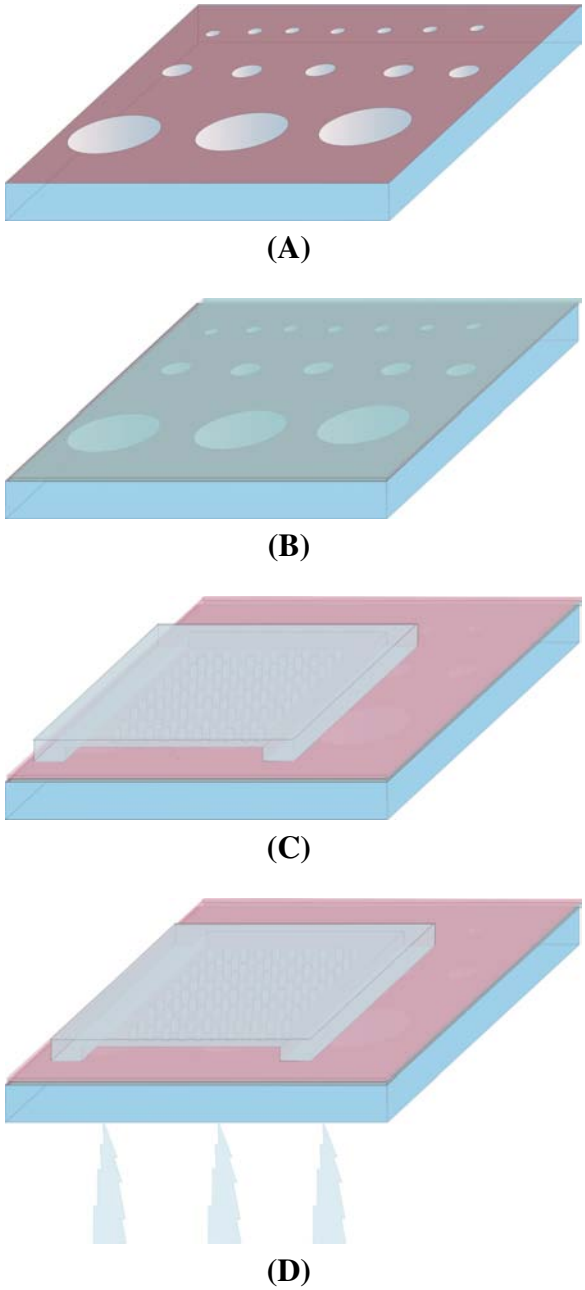

Figure 4.1 Schematic outlining the structure lift-off process (A)Create chrome mask with features (circles) that will be transferred to anchor device (cantilever post array). (B)Spin PVA on substrate and dry for two minutes (C)Spin photoresist (SU-8) on substrate. Align and place cantilever post array on resist layer and softbake (D) Expose the substrate to UV light through the back side of it and do the post exposure bake.

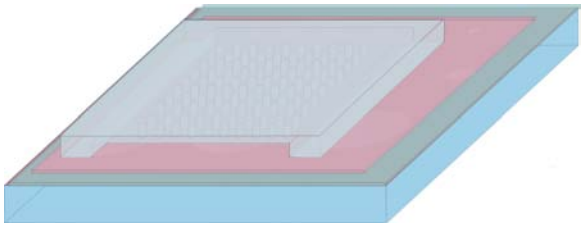

(E)

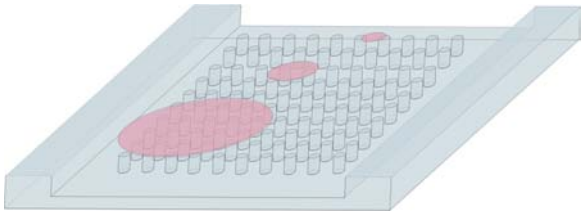

(F)

Figure 4.1 —cont. (E) Remove edge of photoresist to expose PVA layer. Plasma clean device for 30 seconds. (F) Immerse substrate with cantilever post array attached to photoresist layer in bath of DI water at 60 °C with stirring for three hours till PVA completely dissolves and cantilever post array easily detaches. Develop to get final structure with discs attached to tip of cantilever posts.

back side of the glass mask.

Determination of adhesion strength

We determined the adhesion strength both qualitatively, using a basic "Scotch tape"[42,43] test, and quantitatively, using a modified "blister test"[44]. For the Scotch tape test, a piece of 3M™Magic Tape was carefully placed on the device and very gentle pressure was applied to ensure the best possible attachment of the tape to the SU-8 structures. The tape was then pulled back at an angle of about 180°and the sample was examined under an optical microscope to see if there was detachment of the discs from the vertical microcantilevers. This tape test provides a good/poor measure of adhesion. We found that the tape peeled off cleanly, leaving behind the SU-8 structures on the vertical microcantilevers, and this showed that the adhesion was good. We could not provide direct quantitative measurements on the discs that had been attached to the vertical microcantilevers and therefore employed the blister test as a means to determine quantitatively the adhesion strength of SU-8 to PDMS. We cut out a block of cured PDMS about 1 cm2 and punched an access hole using steel tubing. We then placed this block of PDMS onto a layer of SU-8 that

we had spun on a glass slide pretreated with PVA. We subsequently followed a similar protocol to that described above, eventually ending with a membrane of SU-8 adhered to a freestanding block of PDMS. We inserted a steel needle with the appropriate gauge into the hole that had been punched in the PDMS and connected the needle to a source of nitrogen gas (N2). We increased the pressure from atmospheric in steps of about 5 psi (34 KPa) while observing the block of PDMS under an optical microscope to detect the pressure at which the SU-8 peeled off from the PDMS, creating a blister. However, this initial method proved unsuccessful since the SU-8 (about 10 μm thick) was rather brittle and failed (crack formation) at about 30 psi (206 KPa) before a blister could be observed. We modified our protocol by keeping the PDMS/SU-8 attached to the glass slide on which the SU-8 had been spun. We then applied pressure using nitrogen gas again, this time monitored for the pressure at which the PDMS would peel off from the SU-8.

Mechanical agitation of SU-8 structures

The SU-8 discs were mechanically agitated to observe their response. A pulled glass micropipette tip was brought into contact with the discs at a constant speed using an Eppendorf™5171 micromanipulator. The movement of the discs was recorded at 140 fps using a DALSA™CCD camera and a MATLAB™image capture program. A total of five trials each were performed on five different 60 μm discs. 18 trials (11 and 7) were performed on two 20 μm discs and 11 trials were done on the single 10 μm disc that was located. The stack of raw images were again processed in ImageJ™and imported into Metamorph™. The individual microcantilevers under each disc were tracked using an object tracking algorithm. The Euclidean distance of each microcantilever tracked from the contact point of the pipette tip was calculated. The maximum displacement of each microcantilever in the x direction from its initial valid point tracked was extracted. The frame number associated with the maximum displacement was also identified.

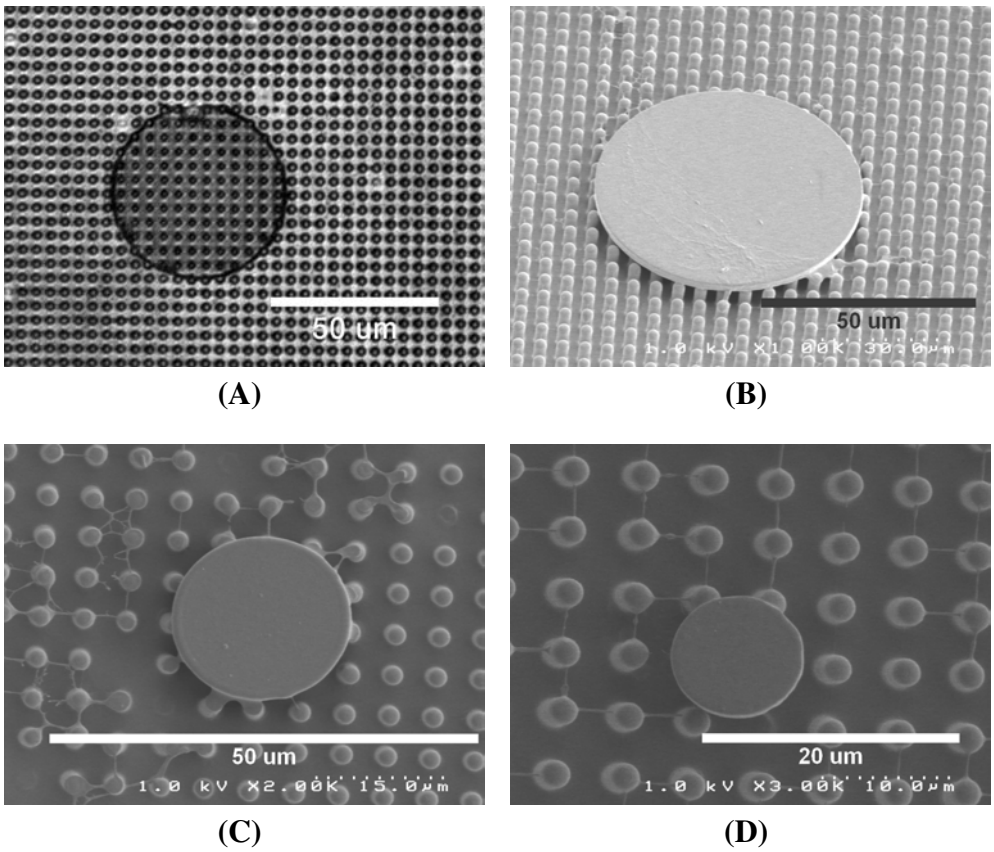

Figure 4.2 DIC and SEM images of attached structures (A)Differential Interference Contrast (DIC) and (B) – (D) Scanning Electron Micrograph (SEM) images of SU-8 discs with diameters of 60 μm, 20 μm and 10 μm.

Results and Discussion

Figure 4.2 shows images of 60, 20 and 10 μm discs that were attached to a vertical microcantilever array using this technique. Due to the 5 μm spacing between the individual vertical microcantilevers, the 10 μm diameter discs could adhere to no more than two vertical microcantilevers, and hence this disc size represented the smallest that could be fabricated and attached to the vertical microcantilever array with a reasonable yield (~30%). The thermal conductivities of crosslinked SU-8 and PDMS are 0.2 W m $^{-1}$ K^{-1} [45] and 0.18 W m^{-1}K^{-1} [46] respectively. These values indicate that the two materials conduct heat energy at almost the same rate. There is, however, a significant difference in their linear coefficient of thermal expansion, with values of 52 $\times$ 10^{-6} K^{-1} [45] and 310 $\times$ 10^{-6} K^{-1} [47] respectively. The fractional change in length, area and volume when the temperature of a solid material changes by ΔT is $\alpha\Delta$T, 2$\alpha\Delta$T and 3$\alpha\Delta$T respectively, where

α is the linear coefficient of thermal expansion[48]. Here α is assumed to be constant within the working temperature range of the material, and the material must be isotropic. The relations for area and volume are approximations which can be made for PDMS and SU-8 since α is very small and the temperature changes considered are on the order of 100 K[48]. We use percentage change in area as a basis of comparison for expansion and contraction experienced by the PDMS and SU-8 materials. During the softbake and post-exposure bakes we are concerned primarily with changes in the PDMS since the SU-8 is not fully crosslinked. The percentage increase in area of the PDMS during these two processes is about 4.7%. However, since the substrate is allowed to cool back to room temperature, the PDMS will shrink back by the same percentage, assuming the expansion and contraction processes are completely reversible. During the hardbake we consider both the PDMS and the SU-8. The percentage increase in area is 5.6% and 0.9% respectively for the PDMS and SU-8. We again make the assumption that for a completely reversible process both materials shrink back to their original dimensions after cooling. However, to reduce the impact of thermal stresses that could be induced due to rapid changes in temperature, we performed the softbake, post-exposure bake and hardbake with a very slow ramp. As can be seen from Figure 4.2(A) there is no noticeable distortion when a row or column of vertical microcantilevers is traced, including areas covered by the discs.

Since cured PDMS is elastomeric it was less likely to fail before debonding occurred. With a 3.8 mm thick PDMS block attached to a layer of SU-8 about 10 μm thick and a with a hole diameter of 0.81 mm, the PDMS block also failed at a pressure of 120 psi (927 KPa) above atmosphere without the formation of a blister. The resulting surface energy can be calculated using the formula[44]

$$\lambda = \frac{0.0883 P_f^2 a^4}{E t_w^3}$$

where P_f is the critical pressure for debonding, a is the radius of hole, E is Youngs modulus of PDMS and t_w is the thickness of PDMS, and should therefore be greater than 0.050 Jm^{-2}. Comparing this to a pressure of 30.7 Torr (4 KPa) above atmosphere (reported by Kastantin et al.[44]) for a 70 μm thick PDMS slab with a hole of 300 μm and with a calculated value of

0.047 ± 0.018 Jm^{-2} surface energy, we can conclude that the adhesion strength is at least as strong as that reported by Kastantin et al. and is probably significantly greater. One conservative upper estimate using the relation above for the case of the 10 μm thick SU-8 membrane on the free standing PDMS block where the SU-8 fails at a pressure of 30 psi, the surface energy was found to be 135 KJm^{-2}. For this estimate, t_w is the thickness of SU-8.

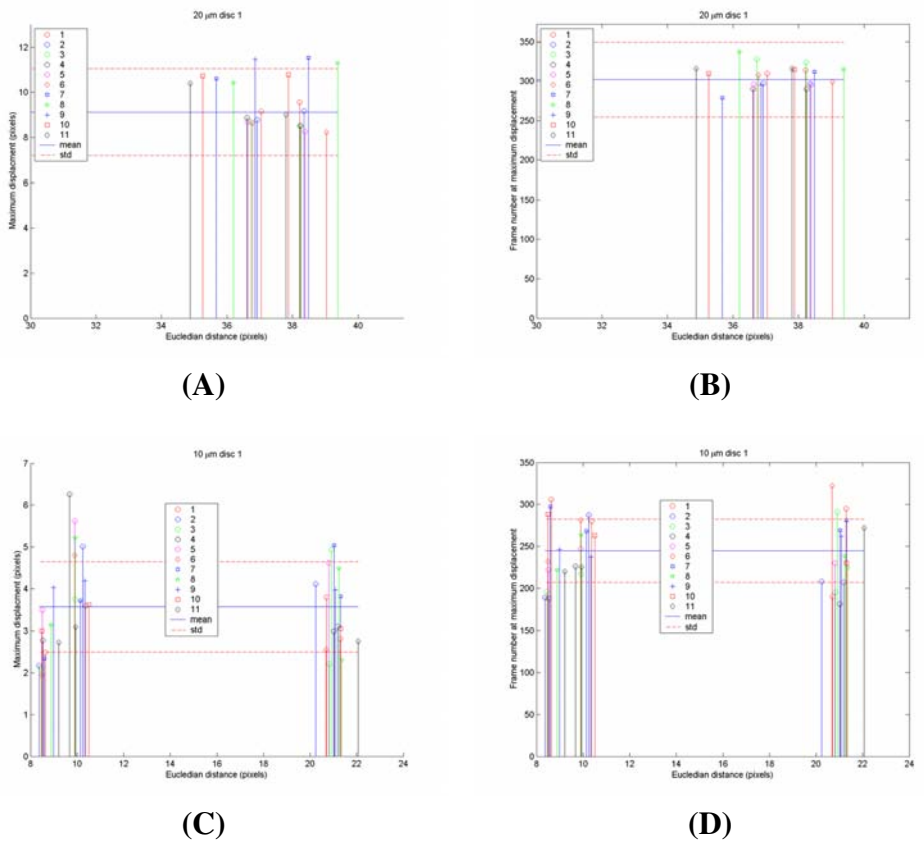

Figure 4.3 Displacements of microcantilevers with 20 and 10 μm discs (A) – (B)Maximum displacement (pixels) and frame number at which the maximum displacement occurs for the 20 μm disc. (C) – (D) Maximum displacement and frame number at maximum displacement for the 10 μm disc.

Figure 4.3(A) – (D) shows data for one of the 20 μmm discs and the 10 μmm disc whiles figure 4.4(A) – (D) shows representative data for two of the five 60 μm discs that were tracked when they were mechanically agitated with the pulled glass micropipettes. The plots are of the maximum displacement versus the Euclidean distance as well as the

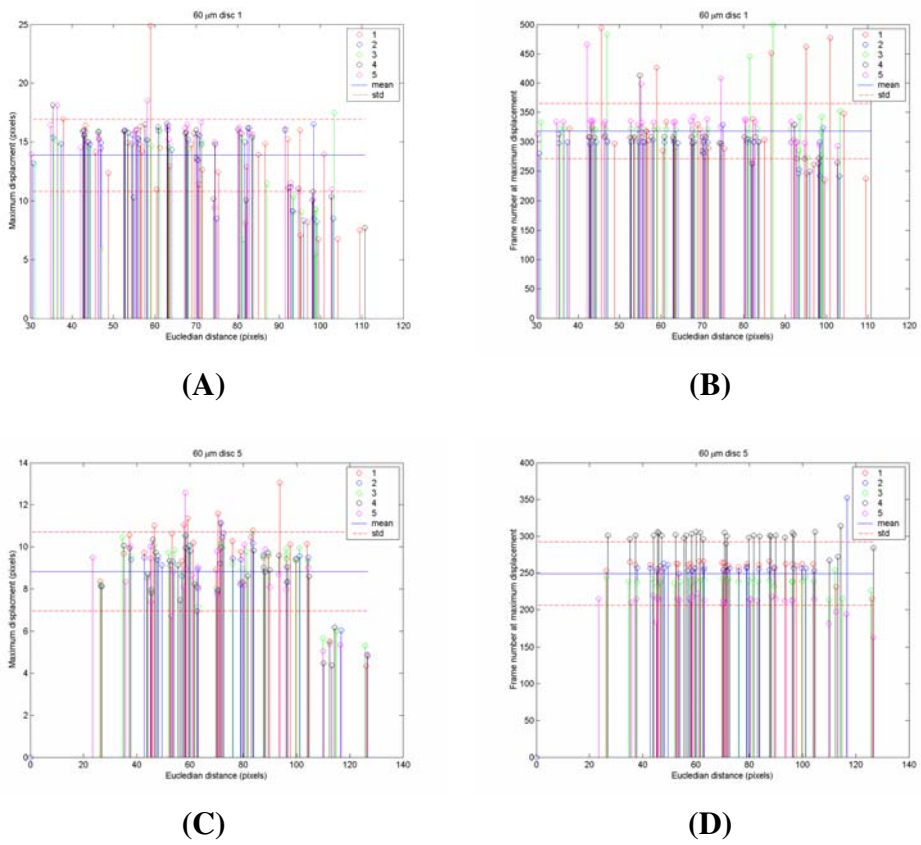

Figure 4.4 Displacements of microcantilevers with 60 μm discs (A) – (B)Maximum displacement (pixels) and frame number at which the maximum displacement occurs for five trials for the first disc. (C) – (D) Maximum displacement and frame number at maximum displacement for the fifth disc.

frame number at the maximum displacement against the Euclidean distance. During the tracking procedure any microcantilevers that were not tracked for greater than 90% of the tracking period were discarded. The means and standard deviations are also plotted on the graphs. In the ideal case it was expected that each microcantilever would show the same maximum displacement independent of the Euclidean distance. This was not the case and for the most part the deviations from the mean maximum displacement can be attributed to inaccuracies and the ability of the tracking program to track all the points at every time point. Moreover for the 60 μm discs, some of the microcantilevers at the edge of image tracked leave the field of view of the camera close to the maximum displacement and this affects the data. Since the discs are ridged in nature it was also expected that all the microcantilevers would move in unison and hence the frame number at which the maximum displacement occurred would be the same. The data shows that for example

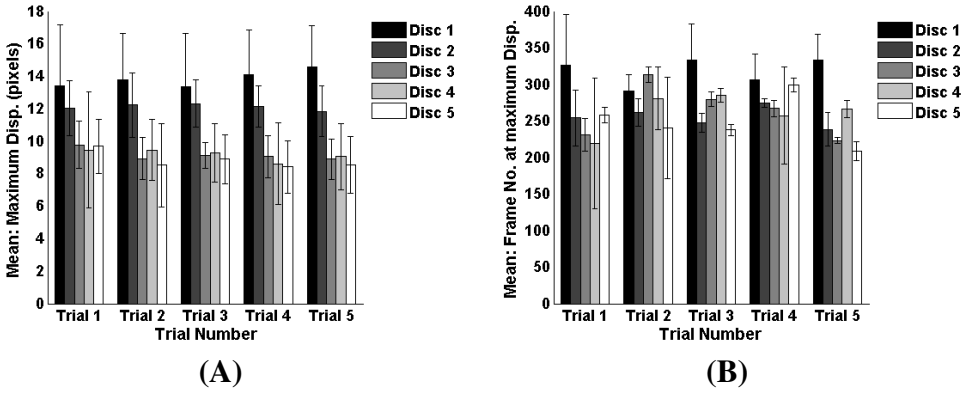

Figure 4.5 Summary of displacements (A) Mean maximum displacement and (B)Mean frame number for maximum displacement for five 60 μm discs tracked.

the standard deviation of the frame number at which the maximum displacement occurred for trial one for the fifth 60 μm disc, or trial five for the third 60 μm disc, are 10.4 and 4.1 frames respectively equivalent to about 74 and 28 ms. Figure 4.5 shows a compilation of the mean maximum displacements as well as the mean frame number for the maximum deviations for the five 60 μm discs. The error bars represent the standard deviations from the mean values for each trial. Looking at these individual trials one can reasonably conclude that the microcantilevers do move together in unison.

Conclusion

These results demonstrate that PVA can be used reliably as a structure release agent for fabrication and assembly of composite BioMEMS devices. Using this technique we have shown that we can attach SU-8 structures to microfabricated vertical cantilever arrays and subsequently move the attached structures with pulled glass micropipettes which also cause the underlying microcantilevers to move. Our approach could potentially be also used for assembling multi-layered structures using successive lithography and release steps.

Acknowledgements

This work was supported by the Vanderbilt Institute for Integrative Biosystems Research and Education (VIIBRE)and The Whitaker Foundation.

References

[1] Galileo, G. Discorsi e dimostrazioni matematiche, intorno due nuoue scienze. *Leida : Appresso gli Elsevirii,* –, 1638.

[2] Cleland, A., Roukes, M. A nanometre-scale mechanical electrometer. *Nature* **392**, 160–162, 1998.

[3] Tan, J., Tien, J., Pirone, D., Gray, D., Bhadriraju, K., Chen, C. Cells lying on a bed of microneedles: An approach to isolate mechanical force. *PNAS* **100**, 1484–1489, 2003.

[4] Addae-Mensah, K. A., *et al.* A flexible, quantum dot-labeled cantilever post array for studying cellular microforces. *Sensors and Actuators A: Physical* **136**, 385–397, 2007.

[5] Geffken, R., Ryan, J., Slusser, G. Contact Metallurgy Development for Vlsi Logic. *Ibm Journal of Research and Development* **31**, 608–616, 1987.

[6] Middlehoek, S. Metallization Processes in Fabrication of Schottky-barrier FET's. *Ibm Journal of Research and Development* **14**, 148–151, 1970.

[7] Feuer, M., Prober, D. Projection photolithography-liftoff techniques for production of 0.2 m metal patterns. *Electron Devices, IEEE Transactions on* **28**, 1375–1378, 1981.

[8] Smith, H. Fabrication techniques for surface-acoustic-wave and thin-film optical devices. *Proceedings of the IEEE* **62**, 1361–1387, 1974.

[9] Madou, M. *Fundamentals of Microfabrication: The Science of Miniaturization*, vol. 2nd. CRC Press, Boca Raton;London;New York; Washington,D.C., 2002.

[10] Fiaccabrino, G., Koudelka-Hep, M. Thin-film microfabrication of electrochemical transducers. *Electroanalysis* **10**, 217–222, 1998.

[11] Trebbe, U., *et al.* A new calcium-sensor based on ion-selective conductometric microsensors - membranes and features. *Fresenius' Journal of Analytical Chemistry* **V371**, 734–739, 2001.

[12] Bustillo, J., Howe, R., Muller, R. Surface micromachining for microelectromechanical systems. *Proceedings of the IEEE* **86**, 1552–1574, 1998.

[13] Tai, Y. C., Muller, R. S. IC-processed electrostatic synchronous micromotors. *Sensors and Actuators* **20**, 49–55, 1989.

[14] Pister, K., Judy, M., Burgett, S., Fearing, R. Microfabricated Hinges. *Sensors and Actuators A-Physical* **33**, 249–256, 1992.

[15] Howe, R., Muller, R. Polycrystalline Silicon Micromechanical Beams. *Journal of the Electrochemical Society* **130**, 1420–1423, 1983.

[16] Jackman, R., Duffy, D., Cherniavskaya, O., Whitesides, G. Using Elastomeric Membranes as Dry Resists and for Dry Lift-Off. *Langmuir* **15**, 2973–2984, 1999.

[17] Duffy, D., Jackman, R., Vaeth, K., Jensen, K., Whitesides, G. Patterning electroluminescent materials with feature sizes as small as 5 m using elastomeric membranes as masks for dry lift-off. *Advanced Materials* **11**, 546–, 1999.

[18] Luo, C., *et al.* Releasing SU-8 structures using polystyrene as a sacrificial material. *Sensors and Actuators A: Physical* **114**, 123–128, 2004.

[19] DeFranco, J., Schmidt, B., Lipson, M., Malliaras, G. Photolithographic patterning of organic electronic materials. *Organic Electronics* **7**, 22–28, 2006.

[20] Lin, S., Tseng, F., Huang, H., Huang, C., Chieng, C. Microsized 2D protein arrays immobilized by micro-stamps and micro-wells for disease diagnosis and drug screening. *Fresenius' Journal of Analytical Chemistry* **V371**, 202–208, 2001.

[21] Kim, T., Kwon, S. Catalyst preparation for fabrication of a MEMS fuel reformer. *Chemical Engineering Journal* **123**, 93–102, 2006.

[22] Nakamastu, K.-i., Tone, K., Matsu, S. Nanoimprint and Lift-Off Process Using Poly(vinyl alcohol). *Japenese Journal of Applied Physics* **44**, 8186–8188, 2005.

[23] Linder, V., Gates, B., Ryan, D., Parviz, B., Whitesides, G. Water-soluble sacrificial layers for surface micromachining. *Small* **1**, 730–736, 2005.

[24] Hua, M., Lau, C., Hui, I., Li, J. Limit analysis on surface roughness and dimensional accuracy of spray metallic crust for rapid tooling production by metal arc spraying process. *International Journal of Advanced Manufacturing Technology* **23**, 720–731, 2004.

[25] Finch C, A. *Polyvinyl alcohol-developments*. Wiley, New York, 1992.

[26] Finch C, A. *Polyvinyl alcohol-properties*. Wiley, New York, 1973.

[27] Li, J. K., Wang, N., Wu, X. S. Poly(vinyl alcohol) nanoparticles prepared by freezing-thawing process for protein/peptide drug delivery. *Journal of Controlled Release* **56**, 117–126, 1998.

[28] Miyashita, H., *et al.* Collagen-immobilized poly(vinyl alcohol) as an artificial cornea scaffold that supports a stratified corneal epithelium. *Journal of Biomedical Materials Research Part B-Applied Biomaterials* **76B**, 56–63, 2006.

[29] Chiellini, E., Corti, A., D'Antone, S., Solaro, R. Biodegradation of poly (vinyl alcohol) based materials. *Progress in Polymer Science* **28**, 963–1014, 2003.

[30] Havard, J., *et al.* Design of Photoresists with Reduced Environmental Impact. 1. Water-Soluble Resists Based on Photo-Cross-Linking of Poly(vinyl alcohol). *Chem.Mater.* **11**, 719–725, 1999.

[31] Schaper, C., Miahnahri, A. Polyvinyl alcohol templates for low cost, high resolution, complex printing. *Journal of Vacuum Science & Technology B* **22**, 3323–3326, 2004.

[32] Xia, Y., Whitesides, G. M. Soft Lithography. *Annual Review of Materials Science* **28**, 153–184, 1998.

[33] Bohl, B., Steger, R., Zengerle, R., Koltay, P. Multi-layer SU-8 lift-off technology for microfluidic devices. *Journal of Micromechanics and Microengineering* **15**, 1125–1130, 2005.

[34] Chronis, N., Lee, L. Electrothermally activated SU-8 microgripper for single cell manipulation in solution. *Journal of Microelectromechanical Systems* **14**, 857–863, 2005.

[35] Seidemann, V., Butefisch, S., Buttgenbach, S. Fabrication and investigation of in-plane compliant SU8 structures for MEMS and their application to micro valves and micro grippers. *Sensors and Actuators A-Physical* **97-8**, 457–461, 2002.

[36] Calleja, M., Tamayo, J., Johansson, A., Rasmussen, P., Lechuga, L., Boisen, A. Polymeric cantilever arrays for biosensing applications. *Sensor Letters* **1**, 20–24, 2003.

[37] Hornbeck, L. The DMD (TM) projection display chip: A MEMS-based technology. *Mrs Bulletin* **26**, 325–327, 2001.

[38] Maluf, N. *An Introduction to Microelectromechanical Systems Engineering*. Artech House Inc., Boston; London, 2000.

[39] Core, T. A., W.K.Tsang, J.Sherman, S. Fabrication technology for an integrated surface-micromachined sensor. *Solid State Technology* **36**, 39–47, 1993.

[40] Marrian, C., Tennant, D. Nanofabrication. *Journal of Vacuum Science & Technology A* **21**, S207–S215, 2003.

[41] Chow, W., Lei, K., Shi, G., Li, W., Huang, Q. Microfluidic channel fabrication by PDMS-interface bonding. *Smart Materials & Structures* **15**, S112–S116, 2006.

[42] Frankel, G., Purushothaman, S., Petersen, T., Farooq, S., Reddy, S., Brusic, V. Corrosion and Adhesion of Multilayer Pad Structures for Packaging Applications. *Ieee Transactions on Components Packaging and Manufacturing Technology Part B-Advanced Packaging* **18**, 709–714, 1995.

[43] Wang, Y., *et al.* The mechanical properties of ultra-low-dielectric-constant films. *Thin Solid Films* **462-463**, 227–230, 2004.

[44] Kastantin, M., *et al.* Integrated fabrication of polymeric devices for biological applications. *Sensors and Materials* **15**, 295–311, 2003.

[45] Ivanova, K., Ivanov, T., Rangelow, I. Micromachined Arch-type cantilever as high sensitivity uncooled infrared detector. *Journal of Vacuum Science & Technology B* **23**, 3153–3157, 2005.

[46] Shin, Y. S., *et al.* PDMS-based micro PCR chip with Parylene coating. *Journal of Micromechanics and Microengineering* **13**, 768–774, 2003.

[47] Kunnavakkam, M., *et al.* Low-cost, low-loss microlens arrays fabricated by soft-lithography replication process. *Applied Physics Letters* **82**, 1152–1154, 2003.

[48] Serway, R. A. *Physics for scientists and engineers, with modern physics*, vol. third. Saunders College Pub., Philadelphia, 1990.

CHAPTER V

MODULATION OF CARDIAC MYOCYTE ADHESION, ADAPTATION AND CONTRACTILE FUNCTION USING MICROCANTILEVER ARRAYS

Kweku A. Addae-Mensah,[1,2] Laura Pentassuglia,[2] Douglas B. Sawyer, [2,3]
John P. Wikswo,[1,2,4,5]

[1]Department of Biomedical Engineering

[2]Vanderbilt Institute for Integrative Biosystems Research and Education

[3]Division of Cardiovascular Medicine

[4]Department of Physics and Astronomy

[5]Department of Molecular Physiology and Biophysics

Vanderbilt University, Nashville, TN

Abstract

We present well-defined vertical microcantilever arrays made of polydimethylsiloxane (PDMS) as a platform for studying the adhesion, growth, remodeling and contractile function of cultured rat adult cardiomyocytes. The microcantilever arrays are made using soft lithographic methods as well as from master molds fabricated from cryogenic etching of silicon. We investigate how microcantilever geometry characterized by diameter and spacing affects myocyte attachment and morphology. We also investigate how different surface treatments of the microcantilever arrays affect myocyte attachment. We found that microcantilever spacing seems to affect the ability of myocytes to develop growth processes and organize sarcomeres in culture. When myocytes attach and adapt to microcantilevers with edge-to-edge spacing of 8 - 10 μm, sarcomeres develop normally, similar to those cultured on laminin-coated culture dishes, and their organization does not appear to be influenced by the array geometry. When the edge-to-edge spacing is reduced (4 - 6 μm), the myocytes develop long lamellipodia-like outgrowths mainly composed of actin stress fibers that appear highly influenced by the array. Moreover, the smaller spacing appears to suppress formation of sarcomeres within these processes. These structures with precise geometry provide a platform for studying the processes that regulate cardiac myocyte adhesion, and the growth and remodeling of sarcomeres. These structures can also be used to investigate how extracellular substrate geometry influences organization of the cardiac myofilaments, a critical parameter necessary to consider for successful tissue engineering. Analysis of myocytes contracting on the microcantilever arrays using a pseudo divergence metric with a 2×2 kernel shows alternating regions of contraction and relaxation which are not as evident when pure displacement data are plotted. A space-time plot of averaged divergence values, however, does not reveal the calcium/contraction waves as was expected probably due to the course sampling time during time lapse capture. The space-time plot still shows alternating regions of contraction and relaxation. Analysis of a curl metric using the same 2×2 kernel was more difficult to interpret. However, we found no correlations between the sign of the divergence and the curl. It was determined that in 22.4% of the cases when there was a positive divergence, the corresponding curl was also positive. The

other values were determined to be 22.8% for negative to negative, 26.8% for positive divergence to negative curl, and 27.9% for negative divergence to positive curl.

Introduction

Myofilament structure and physiology

Myocardial contraction and its control can be understood in terms of the interaction among seven myofibrillar proteins (myosin, actin, tropomyosin, troponin C, troponin I, troponin T, and titin) that, when assembled *in vitro*, exhibit three salient features of cardiac contraction. They hydrolyze adenosine-5'-triphosphate (ATP) and thus are able to liberate chemical energy; when they hydrolyze ATP, they undergo physicochemical changes that are manifestations of tension development and shortening in living muscle; and their interactions are controlled by calcium in a manner that reflects the ability of this ion to couple excitation at the cell surface to the initiation of contraction.

The characteristic light and dark striations in cardiac myocytes differ in brightness when viewed through crossed polarizing lenses. The dark striations are called A-bands and they contain a highly ordered parallel array of thick filaments (Figure 5.1 and Figure 5.2). The light striations are called I-bands and they contain mainly the thin filaments. A dense M-band is found at the center of each A-band, while I-bands are bisected by darkly staining Z-lines, which delimit the fundamental morphological units of striated muscle called sarcomere. The cross striation of the myocardium reflects the organization of the contractile proteins into thick and thin filaments. The thick filaments are mainly composed of myosin and they extend for the entire length of the A-band. Thick filaments also contain supporting proteins, including titin, nebulette, and myosin binding protein C. The I-band is made mainly of thin filaments and extends from the Z-band toward the center of the sarcomere. The thin filaments are composed of actin, which interacts with the myosin cross bridges, and the regulatory proteins tropomyosin and the troponin complex (troponin T, troponin C, and troponin I) (Figure 5.3).

Myosin, the major protein of the thick filament of muscle, is an elongated molecule

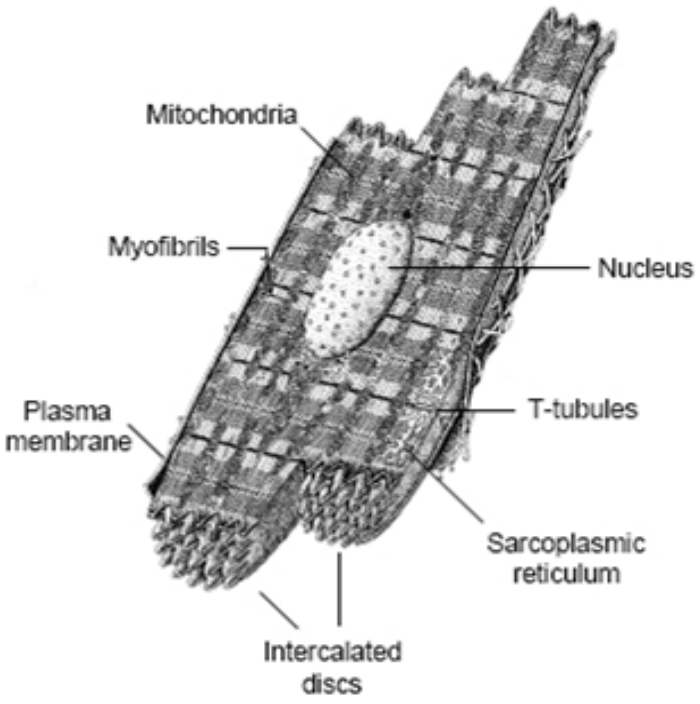

Figure 5.1 Illustration showing the typical structure of the cardiomyocyte. Heart myocytes differ from skeletal myocytes in the absence of syncytia and the presence of intercalated discs. Image from Kristic, R[1]

whose rigid tails are woven and form the backbone of this filament. The globular heads, which project as the cross-bridges, interact with actin in the thin filaments and contain an actin-activated ATPase. Actin is found in all eukaryotic cells. In muscle, actin is abundant in thin filaments and as sarcomeric actin. It provides a scaffold for the rowing movements of the myosin cross-bridges that power contraction. Two actin isoforms, the skeletal actin and the cardiac actin, are found in the heart; these proteins are encoded by distinct genes. The adult human heart contains mainly the cardiac isoform; the fetal heart contains a small amount of skeletal isoform. In the rodent heart, skeletal actin is the predominant isoform during the fetal life and is re-expressed in response to chronic pressure overload. In the failing human heart a similar switch in isoforms occurs. Tropomyosin forms a rigid coiled structure and per se this protein has no mechanical function but plays an important role in muscle regulation. The troponin complex includes three proteins. Troponin I, in concert with tropomyosin, regulates the interaction between actin and myosin; because the most important of these effects is to inhibit the interactions between actin and myosin, this

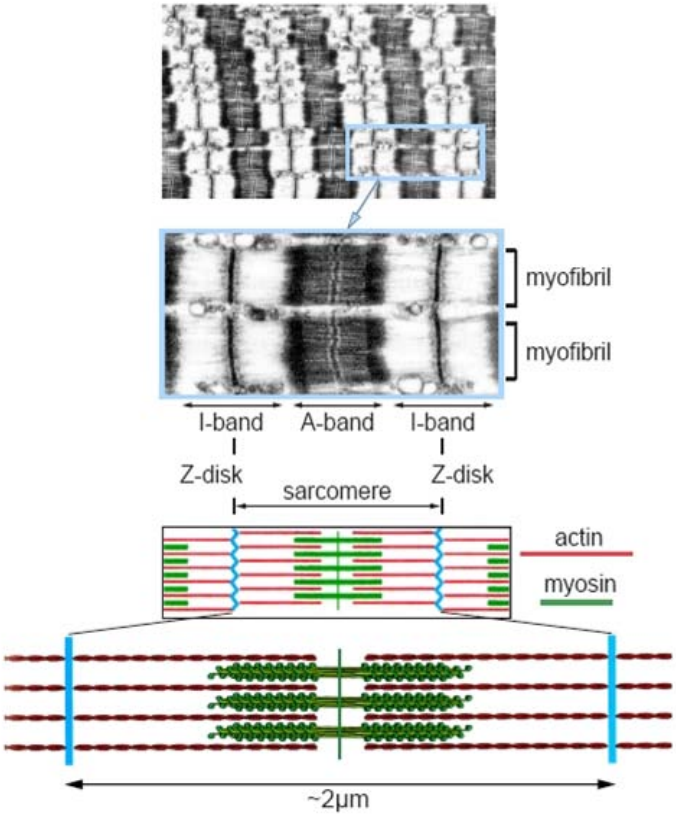

Figure 5.2 Schematic showing basic structure of myofilaments. Myofilaments are a complex structure of thick and thin filaments that slide one over the other during contraction. Image from Alberts *et al.*[2]

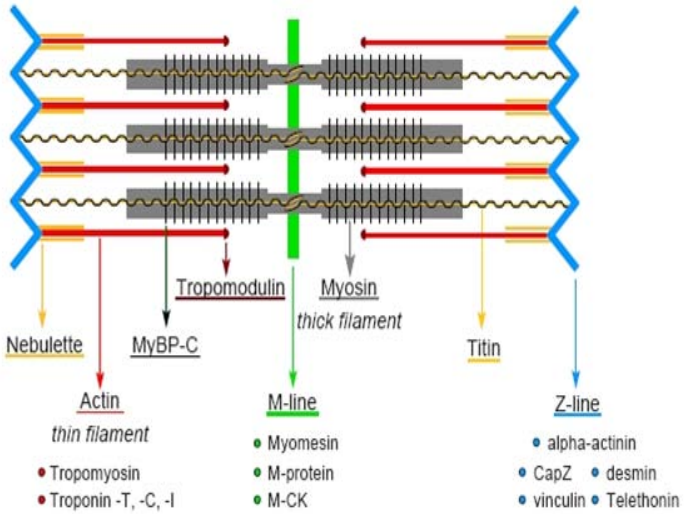

Figure 5.3 Schematic showing proteins and molecules that make up the sarcomere. Image from dissertation by Hefti, M.

protein was named troponin I. Troponin T binds the troponin complex to tropomyosin, and troponin C, which is a member of the EF-hand family of calcium-binding proteins, contains the calcium-binding sites that regulate muscular contraction. Titin is the largest known protein and is an integral part of the myofilament system in vertebrate striated muscle. Full-length titin extends the half-sarcomere from the Z-disk to the M-line, with the I-band region composed of distinct elastic segments that account for the extensibility of titin. Titin has been implicated in the process of sarcomerogenesis, where it is thought to serve as a framework for ordered assembly of myofilament proteins[3].

Excitation contraction coupling

Excitation contraction coupling (EC-coupling) is a term used to describe the association between calcium signaling and sarcomere contraction. In a cardiac myocyte the depolarization of the membrane triggers the influx of calcium from the extracellular environment. This influx is not sufficient in itself to activate the contractile apparatus but triggers calcium release from the saracoplasmatic reticulum. This phenomenon is called calcium-induced calcium release and is essential to initiate sarcomere contraction. Cardiac troponin C has one specific site for calcium and two sites that bind either Ca^{2+} or Mg^{2+}. At rest, the Ca/Mg sites are occupied by either Ca^{2+}or Mg^{2+} and these sites will be almost completely saturated. In this condition troponin I interacts with the actin filaments, inhibiting the formation of cross-bridges. When intracellular calcium rises, as a result of calcium-induced calcium release, the Ca-specific sites are occupied and troponin C affinity for troponin I significantly increases. In these conditions, troponin I can no longer interact with actin and the myosin head will form cross-bridges, initiating contraction. The subsequent steps require ATP to generate mechanical work. For simplicity, we can describe contraction and relaxation in four main steps (Figure 5.4).

1. Hydrolysis of myosin-bound ATP
2. Formation of the active complex with actin
3. Dissociation of ADP

4. Dissociation of actin and myosin

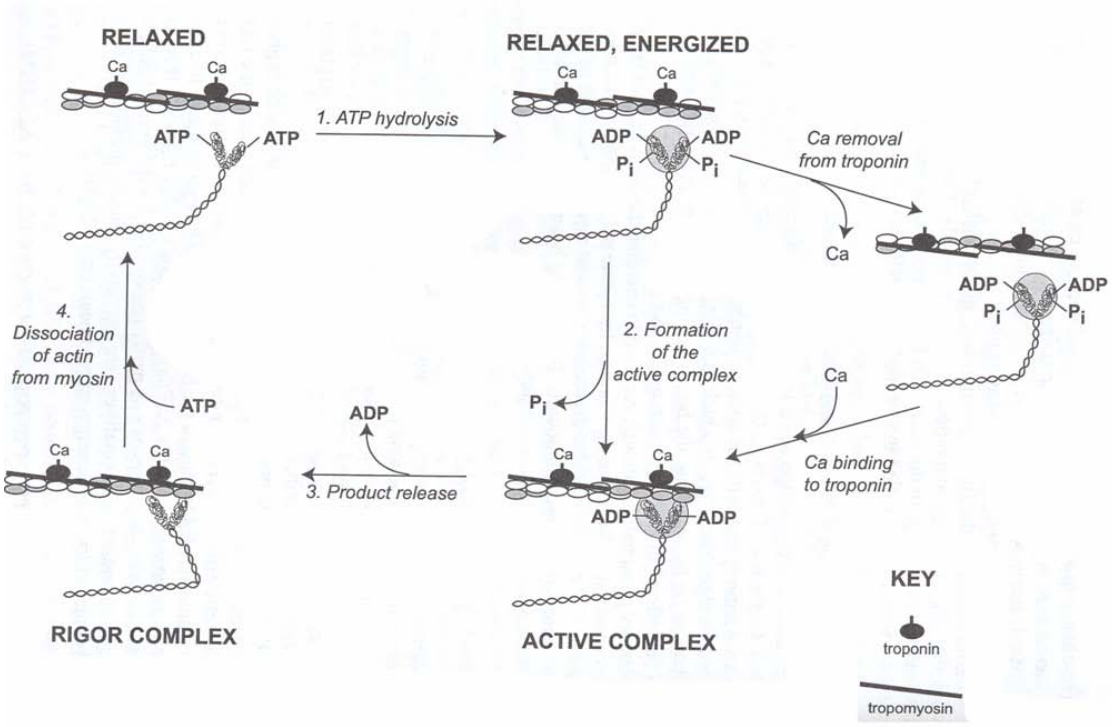

Figure 5.4 Representation of contraction and relaxation of myofilaments. The process can be identified by four key steps. The role of calcium is also highlighted. (Adapted from "Physiology of the Heart" third edition by Katz.

In the relaxed state myosin is bound to ATP and is dissociated from the actin filaments. ATP is rapidly hydrolyzed into adenosine diphosphate (ADP) and a phosphate group, both of which remain attached to the myosin head. The energy release by the hydrolysis of ATP is transferred to the myosin, which becomes energized (step 1). At this point the phosphate group is released and the myosin head interacts with the actin filaments to form cross-bridges (step 2). Once the interaction is established, the chemical energy can be converted into mechanical work. ADP is released at this point, allowing the rowing motion that pulls the thin filaments toward the center of the sarcomere, resulting in the muscle contraction. ADP release is also the limiting step in muscle contraction, being 1000 times slower than the hydrolysis of ATP. As step 2 is the state of highest energy, step 3 is, on the contrary, the state of lowest energy, called rigor complex. The rigor complex causes rigor mortis in dead animals (step 3). To initiate a new cycle of contraction, the cross-bridges

need to dissociate, which is induced by the binding of ATP to the myosin heads (step 4).

Extracellular matrix and cardiac dysfunction

The extracellular matrix is a complex collagen network that supports the cellular and structural integrity of tissue. It plays a critical role in the physiology of the heart, and alterations in the quantity and quality are associated with pathological conditions, such as heart failure and dilated cardiomyopathy. Fibrosis is an event common to several cardiac dysfunctions and consists in the deposition of interstitial tissue in the walls of the heart. It is characterized by an increase in collagen content and type. The type of collagen deposited varies according to the stage and type of cardiac dysfunction. Fibrosis has both maladaptive and adaptive functions. The presence of fibrotic tissue induces myocardial injury, arrhythmias, and impairs filling of the chambers. On the other side, deposition of extracellular matrix proteins allows an increase in wall stiffness, at the same time that it decreases wall stress in the failing heart. In hypertrophy, the presence of fibrosis may explain the differences between pathological (presence of fibrotic tissue) and physiological ("athlete's heart", with little or no fibrotic tissue) condition (Katz,A,M[3]). Alterations in the matrix components and stiffness have been also associated with diabetes. Analysis of diabetic hearts revealed an increased accumulation of collagen, which could lead to hypertrophy of the left ventricle. Several animal models have demonstrated that deposition of collagen is indeed due to diabetes. Moreover, in diabetic hearts left ventricle remodeling and myocytes apoptosis after infarction are higher than in normal hearts[4]. Disruption of the extracellular matrix can lead to cardiac dysfunction too. So far, several factors have been identified to influence the balance between collagen synthesis and degradation, such as inflammation triggered by viral infection. Metalloproteinases are a family of 20 different species of zinc-dependent enzymes that are either membrane-bound or secreted in the extracellular space. These proteins can selectively cleave components of the extracellular matrix and can be activated by interleukins and by tumor necrosis factor (TNF), expressed during myocardial inflammation. These same factors are expressed during inflammation and they can down regulate the expression of TIMP proteins, endogenous inhibitors of

metalloproteinases[5].

Cardiac myocyte mechanotransduction

Mechanical signaling and force transmission within and outside the cardiac myocyte are important players in the mechanotransduction process, and the cytoskeleton is a significant link between the force-generating sarcomere, the cell membrane, and intracellular stress-sensing components. Another mechanical factor involved in the maintenance of cardiac myocytes is attachment. Cardiac myocytes are known to form focal adhesions for attachment at the distal ends. However, they have also been shown to form cytoskeletal-sarcolemmal attachments normally at points where their Z lines form.[6] These sites are termed costameres and have certain attributes that make them similar to focal adhesions. They contain the proteins vinculin, talin and β1-integrin, which are commonly found in focal adhesion sites. They tend to form on the cell closest to the cell-substrate interface, and extracellular matrix (ECM) proteins are deposited on the outer surfaces[7]. It has been suggested that the composition of these costameres makes them likely candidates to mediate the attachment of the lateral aspects of the myofibrillar apparatus to the sarcolemma, and that these sites, like the focal adhesion counterparts, are also responsible for the physical transduction of mechanical forces[8]. Also important in cardiac research with clinical significance are changes in cell shape, size, and contractility as a result of adaptation due to changes in the physiological and patho-physiological environment of cardiac myocytes. For example, heart failure is normally associated with dilated ventricles which are also characterized by increased fibrosis[9]. The increased fibrosis results in a stiffer matrix and a decrease in cardiac contractility.

Myofibrillogenesis

Myofibrils are cylindrical organelles found within muscle cells. They are bundles of filaments that run from one end of the cell to the other and are attached to the cell surface membrane at each end. Contractile proteins responsible for force generation and transmission are supported by these structures. It has been demonstrated that the assembly

of these proteins into their functional units (sarcomeres) is a well coordinated process[10]. Many studies have been performed using primary cardiac myocyte cultures to try to explain this assembly process, also termed myofibrillogenesis. Results from these experiments have led to several models postulated to explain this process.

The importance of studying myofibrillogenesis cannot be overemphasized. Disruptions and mutations in some of the proteins that are involved the process have been linked to certain cardiac diseases, such as familial hypertrophic cardiomyopathy (FHC) and some forms of hereditary dilated cardiac myopathy (DCM)[11].

Stress fiber-like structures as templates

In the model first introduced by Dlugosz *et al.*[12], components of stress fiber-like structures (SFLS) serve as templates for assembly of myofibrils. It proposes that the assembly occurs in two phases. During phase one, small numbers of thick and thin filaments assemble in close proximity to a single SFLS. The second phase involves displacement of the newly forming myofibril from its subcortical domain during which the SFLS to which it had been linked gradually disappears. Other experimental observations which could potentially support this line of arguments were reported by Wang *et al.*[13] and Schultheiss *et al.*[14]

Assembly from several subunits

This model postulates that individual Z band-like materials, which are components of the future I-Z-I bands,[15] are originally in separate areas from which assembly of the myofibrils takes place, and are in scattered arrays[16,17]. Titin, a sarcomeric protein, then promotes assembly of these bodies into mature myofibrils by serving as a joining agent for these scattered I-Z-I bands. Lu *et al.*[18] proposed this model to explain myofibrillogenesis in chick cardiac myocytes isolated from seven day old embryos.

Premyofibrils as myofibril precursors

Rhee *et al.*[19] use immunofluorescence to analyze embryonic cardiac muscle cells in the early stages of spreading in culture. They introduce a premyofibril model of myofibrillogenesis. This model characterizes maturation as a three-step process from premyofibrils which become nascent myofibrils before fully maturing. They identify these three different populations within specific regions of the cardiac cells. The mature myofibrils tend to be centrally positioned and contain muscle-specific proteins. The premyofibrils are located primarily in the periphery of the spreading cells and are dominated by non-muscle myosin II and an absence of muscle-specific myosin. The nascent myofibrils constitute the intermediate phase between the premyofibril state and the mature state and are spatially distributed between the other two.

Assembly without any intermediate structures

Costa *et al.*[20] describe myofibrillogenesis during zebra fish myogenesis *in situ*. Using stains for cytoskeletal proteins actin, myosin, desmin, α-actinin, troponin and titin they propose a very different model for myofribrillogenesis. Experimental observations lead them to conclude that either the accumulation period is very short or there is no need for the formation of the intermediate and transitional SFLS structures. Other sarcomeric proteins such as troponin also appeared striated at the very beginning of myogenesis and seemed to reinforce the notion that myofibrils matured very quickly during myogenesis in the zebra fish. α-actinin, another of the very important proteins shown to be instrumental in myofibrillogeneis[19] in cultured chick cells also appeared striated and no transitional state was detected. Costa's group suggested that the interval between α-actinins expression and striation was too short to detect and could explain this observation. They point out that the intermediate stages where, for example α-actinin, appears as a dotted distribution before becoming striated have been observed mainly in cultured myocytes.

As Sanger *et al.*[16] point out the very nature of culturing myocytes *in vitro* may lead to the formation of intermediate structures which may be the reason for the models that

have been postulated. This idea has also been examined by Ehler *et al.*[10] They argue that cultured cells isolated from hearts already have myofibrils and therefore that situation may not adequately reflect the actual processes that occur *in situ*. They point out that degradation and recycling of myofibrils may occur during adaption to the underlying two-dimensional substrate and that these specific culture conditions may drive formation of intermediate structures such as stress fibers[17,21].

In their study of immunostained whole mount preparations of embryonic chicken hearts, Ehler *et al.*[10] make important comparisons between observations of myofibrillogenesis *in vitro* and *in vivo*. Table 5.1 summarizes these similarities and differences.

Table 5.1 Similarities and differences between myofibrillogenesis *in vitro* and *in situ*

	In vivo	*In situ*
Striations	Striated in the center of the cell with non-striated extensions into the periphery	No transitions between striated and non-striated are seen
Subsarcolemmal adhesion plaques (SAP)	Characterized by concentration of the cell-substrate contact protein vinculin and thought to represent region of new myofibril assembly	No evidence for SAP
Maturation of myofibrils	Nascent myofibrils are intermediates between premyofibrils and mature myofibrils	Observed myofibrillar structures are always either immature or mature with all sarcomeric proteins in correct striation pattern
Premyofibrils	Shown to be present.[19]	No detection of premyofibrils
Importance of non-muscle myosin IIs	Non-muscle myosin IIB must be present as a defining component in premyofibrils that act as a space-holder for muscle myosin isoforms	No evidence for a function of non-muscle myosin IIB

Continued on next page

Table 5.1 (continued)

	In vitro	In situ
Dense body-like structures	Present and composed of α-actinin, N terminus of titin, and actin	Also present

The experiments we conducted did not involve investigation of the other proteins (α-actinin, desmin, titin, vinculin) that have been implicated in myofibrillogenesis in cardiac and other striated muscle cells, therefore we cannot claim that the data presented in this paper necessarily support any of the above mentioned models of myofibrillogenesis. More importantly, as others have attested, myofibril assembly as studied in cultured myocytes may not accurately describe this process.

Investigative tools

Some of the systems that have been designed to investigate these mechanisms *in vitro* have traditionally involved culturing of primary or neonatal myocytes on flat two-dimensional (2D) dishes or membranes[22,23]. Other systems which have tried to mimic more closely the *in vivo* environment involve the use of three-dimensional collagen matrices[24] , microgrooves in polymer substrates[25,26], and biodegradable polymers[27]. Motlaph *et al.*[28] have also used microtextured substrata consisting of pegs or grooves or a combination of and have shown that these substrata alter gene expression, protein localization, and cardiac myocyte shape. Their pegs are on the order of 10 μm in diameter with spacings of 100 μm which is much greater than the individual size of single myocytes.

Recent advances in tissue engineering have required the development of three-dimensional cell culture models *in vitro*[29]. Various techniques have been used in the manufacture of the scaffolding required, including molding from micromachined silicon molds[30] and also from soft lithography methods[31,32]. These methods have been applied to cardiac tissue engineering as well[33].

The microcantilever arrays that have been developed can further be used to address

questions regarding cardiac mechanobiology and remodeling *in vitro* and possibly cardiac tissue engineering. Since the microcantilever arrays that were used have dimensions much smaller than individual cardiac myocytes, it provides a substratum on which remodeling can be investigated. An added advantage is that it can simultaneously be used to measure force generation by the myocytes during contraction. The ability to also modify the dimensions provides an avenue by which the stiffness of the substrate can be altered without changing the surface chemistry.

Materials and Methods

Fabrication of vertical microcantilevers

The vertical microcantilever arrays were designed and fabricated using standard soft lithography methods and SU-8 2000™ negative photoresist (Microchem; Newton, MA) in a clean room with some modifications to improve the minimum feature size that could be obtained as previously described[34]. After the photolithography step, liquid prepolymer of the elastomer polydimethylsiloxane (PDMS; Slygard 184, Dow Corning; Midland, MI) was poured over the surface of the SU-8 master, degassed under vacuum, cured overnight at 65°C, then peeled off. The PDMS mold was oxidized in a plasma cleaner for 30 seconds, then silanized with (Tridecafluoro-1,1,2,2-tetrahydrooctyl)-1-trichlorosilane (United Chemical Technologies; Bristol, PA) under partial vacuum overnight. Liquid PDMS was then poured on the surface of the silanized PDMS mold, degassed, and cured at 65°C for 15 hours. The cured elastomer was peeled from the PDMS mold to yield a the microcantilever arrays. Some of the microcantilevers were also fabricated from silicon master molds that had been etched using cryogenic etching techniques[35]. Similarly, the silicon master molds were also silanized after plasma cleaning and liquid prepolymer was poured on them and degassed under vacuum. However these were cured at 110°C for 20 hours before mold separation.

Cell isolation and culture

Rat cardiac myocytes were isolated using protocols similar to those described in Lim *et al.*[36] Wistar rats weighing 200-250 g were anesthetized (50 mg/kg ip pentobarbital sodium) and heparinized (200 IU iv). The hearts were rapidly excised and immersed in an ice-cold modified cardioplegic Krebs-Bulbring (KB) solution [containing (in mM) 85 KOH, 30 KCl, 30 KH_2PO_4, 3 $MgSO_4$, 0.5 EGTA, 10 HEPES, 50 L-glutamic acid, 20 taurine, 10 2,3-butanedione monoxime (BDM), and 10 glucose]. The hearts were cannulated via the aorta and perfused in a retrograde fashion at a constant perfusion pressure of 90 cmH_2O. The hearts were first perfused for 5 min with nonrecirculating 1.8 mM Ca^{2+} Tyrode solution [containing (in mM) 137 NaCl, 5.4 KCl, 1.8 $CaCl_2$, 0.5 $MgCl_2$, 10 HEPES, and 10 glucose; pH 7.4] followed by Ca^{2+}-free Tyrode solution [containing (in mM) 135 NaCl, 4 KCl, 1 $MgCl_2$, 10 HEPES, 0.33 NaH_2PO_4, and 10 glucose; pH 7.2] for another 5 min. Hearts were then perfused with a digestion solution containing 0.08% collagenase A (Collagenase A, Boehringer-Mannheim; Indianapolis, MN) and 0.02% protease XIV (Sigma; St. Louis, MO). After the hearts were palpably flaccid, the digestion solution was washed out with Ca^{2+}-free Tyrode solution for 30 s. The hearts were then removed from the cannula, and the LV (including septum) was separated, minced, and gently agitated, allowing the myocytes to be dispersed in KB solution. Prior to seeding, the microcantilever arrays were sterilized and then either soaked or stamped with laminin to promote adhesion of the cells to the substrate. The myocytes were cultured for 12 - 14 days and culture medium was changed every 3 - 4 days. The myocytes were monitored for spreading as well as spontaneous contraction. The experiments were performed on microcantilever arrays with differing geometries based on microcantilever size and spacing to see how this affected cardiac myocyte maintenance. As controls to most of the experiments, cells were also cultured on laminin-coated culture dishes and results were compared to those on the microcantilevers. The cells were also fixed and stained for actin and the myofibrilla M-band protein myomesin

Image analysis

Time lapse images when required, were acquired and analyzed for microcantilever displacement using a combination of Metamorph™ and a modified image particle tracking algorithm written in MATLAB™. This represented contractile forces generated by contracting myocytes. In cases where the tracking algorithm could not detect any of the microcantilevers for a particular frame a displacement of zero was assigned. Fluorescent images were acquired using the Zeiss LSM510™ confocal imaging system. This was used to access the degree of sarcomere formation, remodeling, and cell shape and morphology. To be able to access how the spatial arrangement of the microcantilevers could affect the 2D- fast fourier transform (FFT) used to in our analysis, differential interference contrast (DIC) or phase contrast images were taken of plain microcantilevers without an cells attached. These images were converted to binary images using an appropriate automatic threshold algorithm (Otsu thresholding[37,38]) and then 2D-FFTs were computed.

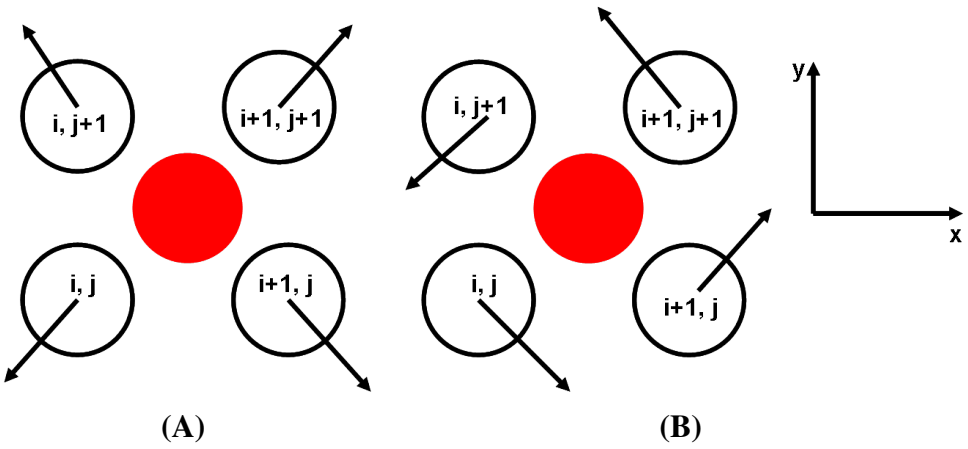

Figure 5.5 Divergence and curl schematics. (A) 2 × 2 kernel for divergence. Arrows represent direction used to represent positive divergence. (B) 2 × 2 kernel curl. Arrows represent directions used to represent positive curl.

Computation of divergence and curl

The force data extracted from the deflection of the microcantilevers (Figure 5.21 - 5.22) does not take into consideration the fact that force is a vector quantity and hence has a directional component to it. To obtain a different perspective on the way the forces are distributed, divergence and curl metrics were computed over the duration of the time lapse movie. Figure 5.5(A) and (B) show schematics of the 2×2 kernel that was used for computation of the metric. The arrows represent the notation that was used to represent positive values. The divergence and curl were calculated using the following equations, respectively:

$$\begin{aligned} \nabla.\mathbf{D}_{i+\frac{1}{2},j+\frac{1}{2}} = \mathbf{D}_{x_{i+1,j+1}} + \mathbf{D}_{y_{i+1,j+1}} - \mathbf{D}_{x_{i,j+1}} + \mathbf{D}_{y_{i,j+1}} \\ - \mathbf{D}_{x_{i,j}} - \mathbf{D}_{y_{i,j}} + \mathbf{D}_{x_{i+1,j}} - \mathbf{D}_{y_{i+1,j}} \end{aligned} \tag{5.1}$$

and

$$\begin{aligned} \nabla \times \mathbf{D}_{i+\frac{1}{2},j+\frac{1}{2}} = \mathbf{D}_{y_{i+1,j+1}} - \mathbf{D}_{x_{i+1,j+1}} - \mathbf{D}_{x_{i,j+1}} - \mathbf{D}_{y_{i,j+1}} \\ + \mathbf{D}_{x_{i,j}} - \mathbf{D}_{y_{i,j}} + \mathbf{D}_{x_{i+1,j}} + \mathbf{D}_{y_{i+1,j}} \end{aligned} \tag{5.2}$$

The computation was skipped in cases where all four microcantilevers could not be identified. Computations on the boundaries were also skipped and not assigned a value (Dirichlet or first type boundary conditions) as is normally the case in finite difference or finite element methods. The computed value was assigned to a complementary grid which is actually the midpoint of the four microcantilevers which are used for computation (red circle in Figure 5.5(A) and (B)).

Results and Discussion

Two dimensional FFTs of plain microcantilevers

Images from the fixing and staining of the myocytes on the microcantilevers sometimes included silhouettes of the microcantilevers and their frequency components appeared in the 2D-FFTs. To determine if these were of any consequence, 2D-FFTs of DIC or phase

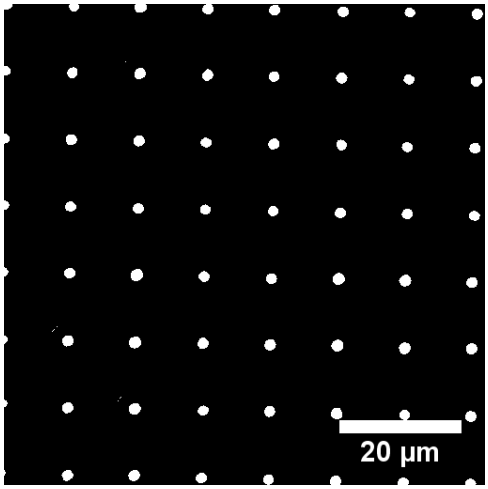

Figure 5.6 Binary image of Figure 5.7(I) used for computing the corresponding 2D-FFT (Figure 5.7(L)).

contrast images of plain microcantilevers with diameters of 1 and 3 μm and edge-to-edge spacings of 1, 2, and 4 μm and 6, 8, and 9 μm respectively were computed. These images were first converted to binary images as shown in Figure 5.6. DIC and phase contrast images and their corresponding 2D-FFT outputs are shown in Figure 5.7(A) - (L). It can clearly be seen that as the edge-to-edge spacing increases for the same diameter of microcantilever, the corresponding spacings in the frequency domain image decrease. This is in agreement with fourier theory where it is known that the fourier transform of a grid is also generally a grid with the reciprocal directions and spacings. The difference between the patterns observed for the 1 μm diameter microcantilevers and the 3 μm diameter microcantilevers is due to the difference in the spatial arrangement of the microcantilevers with the 3 μm diameter ones being in a square arrangement and those with 1 μm diameter being in an hexagonal arrangement.

Comparison of sarcomere formation

In an attempt to quantify the quality/extent of sarcomere formation in the myocytes, the peaks of the intensity values of the fundamental frequency from the two-dimensional FFT were plotted on a logarithmic scale. The values for myocytes fixed and stained after allowing the cells to adhere were compared for cells seeded in the Petri dishes, on the microcantilevers, and those that attached to areas of PDMS where there were no microcan-

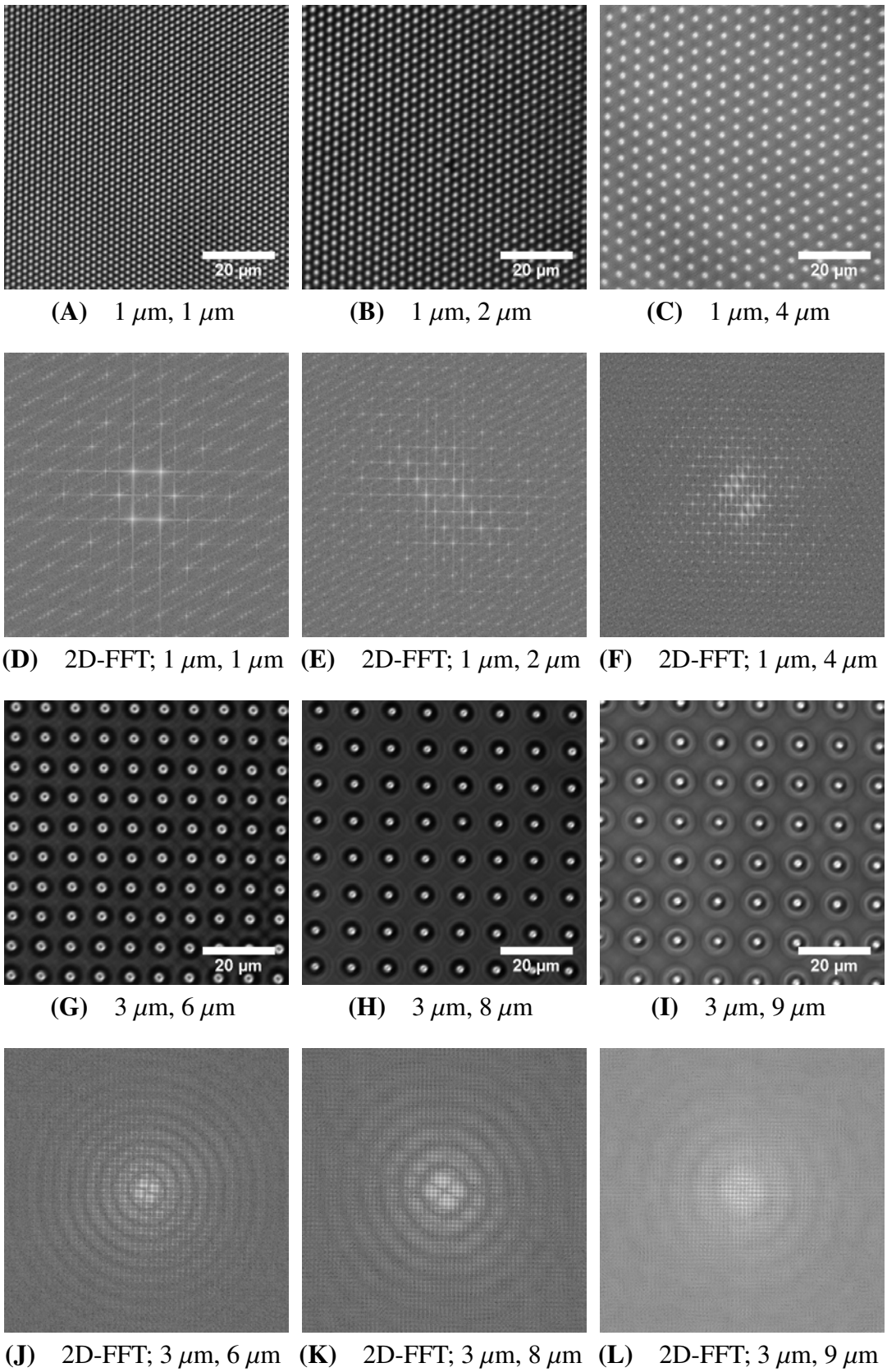

(A) 1 μm, 1 μm **(B)** 1 μm, 2 μm **(C)** 1 μm, 4 μm

(D) 2D-FFT; 1 μm, 1 μm **(E)** 2D-FFT; 1 μm, 2 μm **(F)** 2D-FFT; 1 μm, 4 μm

(G) 3 μm, 6 μm **(H)** 3 μm, 8 μm **(I)** 3 μm, 9 μm

(J) 2D-FFT; 3 μm, 6 μm **(K)** 2D-FFT; 3 μm, 8 μm **(L)** 2D-FFT; 3 μm, 9 μm

Figure 5.7 Plain microcantilevers and their corresponding 2D-FFTs. The first number in the label represents the diameter and the second, the edge-to-edge spacing. Scale bars are 20 μm.

tilevers. The same comparison was made for cells that were fixed and stained after 6 days in culture medium.

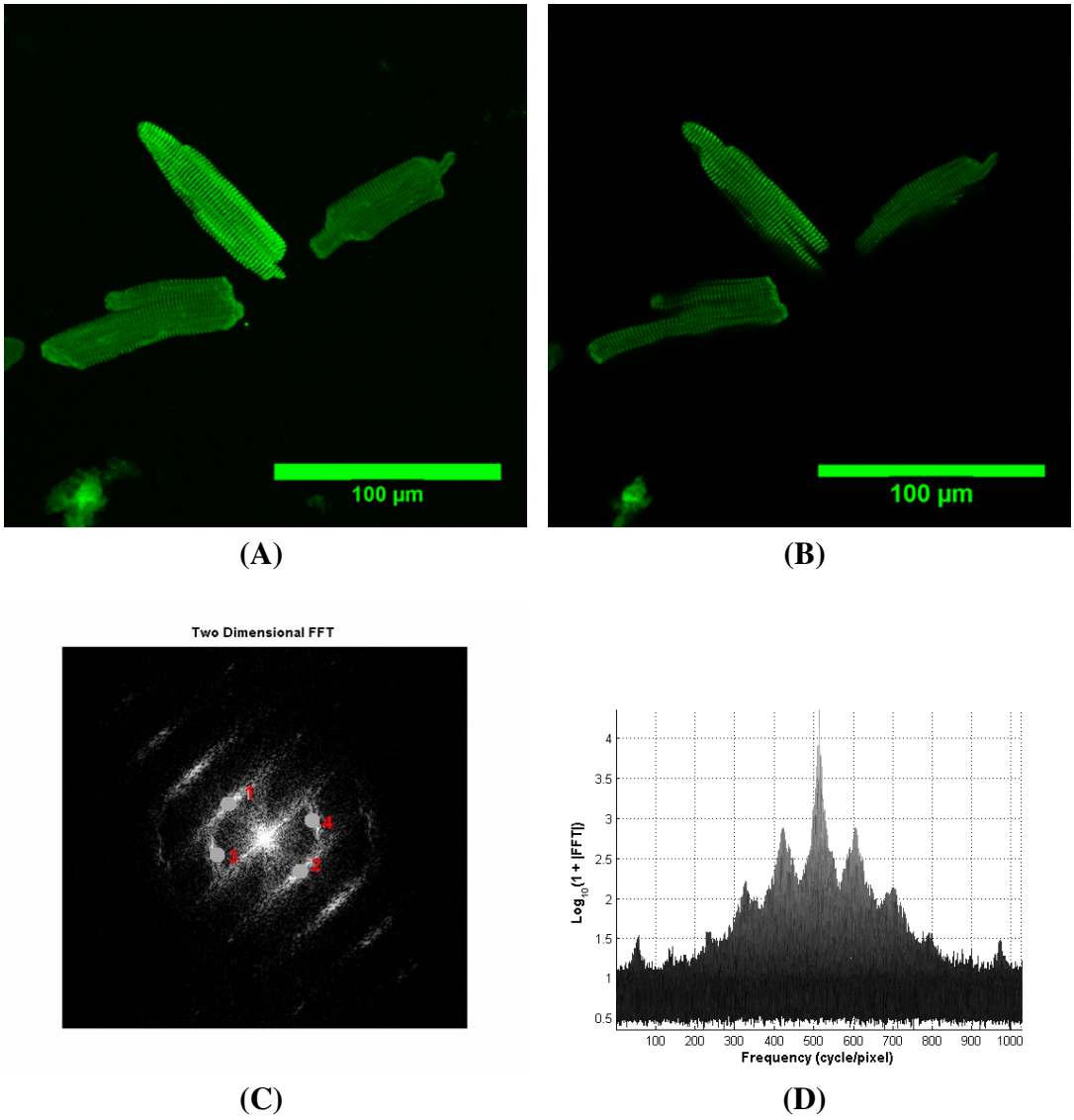

Figure 5.8 Cardiomyocytes fixed and stained at isolation in Petri dishes. (A) Projection of a Z-stack of images taken with the confocal microscope. Sarcomeres are clearly visible and cells are rod shaped, as expected. (B) One slice of the Z-stack of the confocal scan from (A). (C) Two-dimensional fast fourier transform (FFT) of Figure 5.8(A) showing four selected points whose spatial period is determined. (D) Intensity values from Figure 5.8(B) plotted on a logarithmic scale.

Adaptation on culture dishes

Controls for the experiments were done with myocytes that were cultured on Petri dishes. Figure 5.8(A) shows a fluorescent image of myocytes at the time of isolation in Petri dish. The cells were fixed and stained for myomesin. This image is a Z-projection of a confocal stack of images, thus the image shows some blurring though the sarcomere is clearly visible. A two-dimensional FFT of each slice of the stack of images was computed and Figure 5.8(B) shows a projection image of the computed FFT with the quadrants swapped. The spatial frequency in C/μm for the first harmonic/peak was determined. The four values had a mean value of 1.7675 ± 0.0395 which is very close to the reported length of a typical sarcomere (1.842 ± 0.078 μm) for intact rat cardiac myocytes at rest.[39] The magnitude of the intensity values of the two-dimensional FFT on a logarithmic scale was also plotted and the peak values at the fundamental frequency were determined as shown in Figure 5.8(D).

Results after fixing and staining myocytes that had been cultured for six days on the Petri dishes are shown in Figure 5.9(A) – (C). Figure 5.9(A) is a Z-projection of the individual slices of the confocal images and Figure 5.9(B) shows a single slice from the confocal image stack used to generate the Z-projection image. The flattening of the myocytes as they spread out is clearly visible. In this case myofibrils are not in the orderly arrangement of the myocytes fixed at isolation. This makes individual sarcomere more difficult to identify. This outcome manifests in the two-dimensional FFT of the image (Figure 5.9(B))which shows the fundamental frequency peak to be almost circular in shape as a result of the varied orientation of the myofibrils.

The peak intensity value on the logarithmic scale for the fundamental frequency was close to that of the case at isolation, (2.765 ± 0.012728 after 6 days and 2.7695 ± 0.1351 at isolation) showing that sarcomere formation had not really been affected after 6 days in culture. This observation was the same for myocytes that attached to flat areas of PDMS not covered by the vertical microcantilever arrays (2.7790 ± 0.0156 after 6 days and 2.771 at isolation), though they did not seem to have spread out as much as cells did in the flat Petri culture dishes. Figure 5.10(A) and 5.10(B) show Z-projections of confocal images

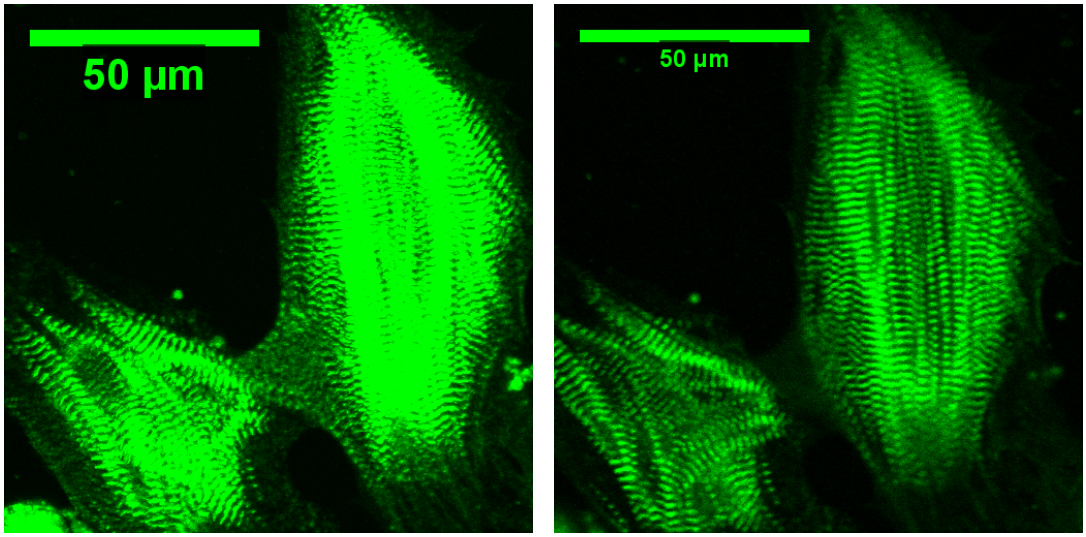

(A) (B)

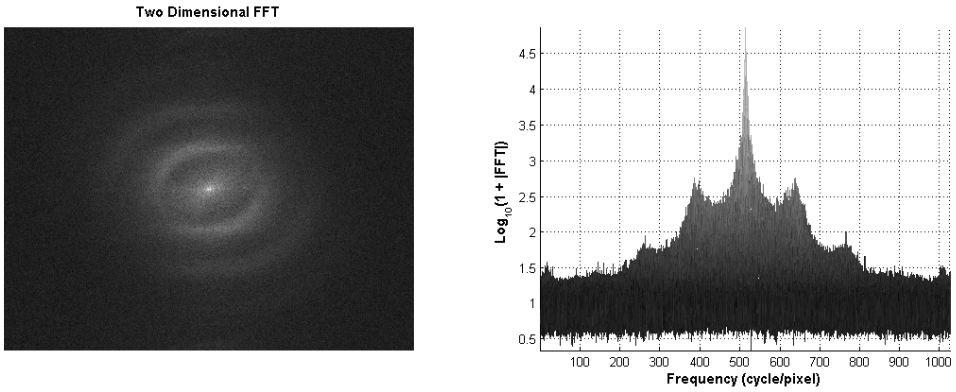

(C) (D)

Figure 5.9 Myocytes fixed and stained at six days of culture on Petri dishes. (A) Projection of a Z-stack of images taken with the confocal microscope. Sarcomeres not as visible in this case as myofibrils are not in an orderly arrangement as is the case at isolation. (B) Single slice of the Z-stack from (A) showing arrangement of myofibrils. (C) two-dimensional FFT of (A) with quandrants swapped (D)Intensity values from (B) plotted on a logarithmic scale

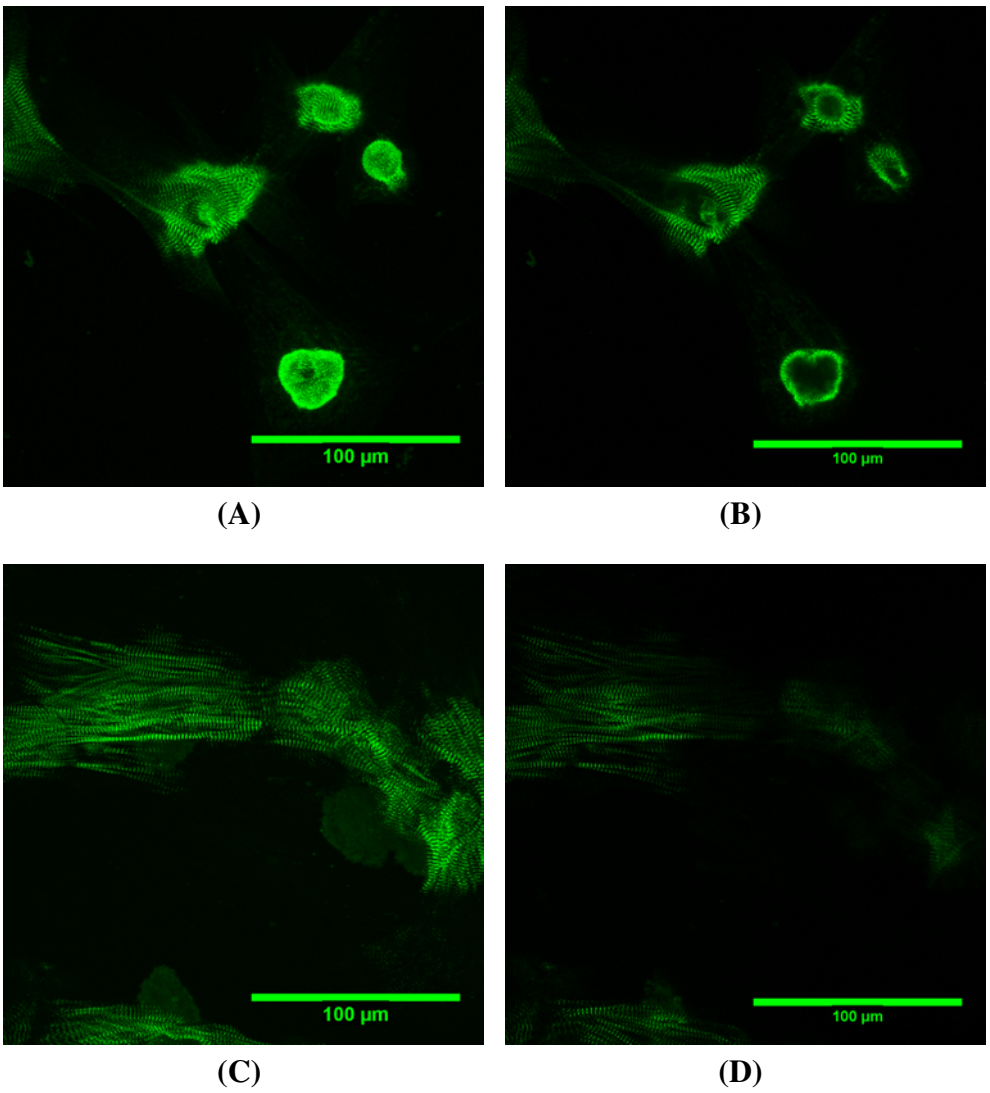

Figure 5.10 Adaptation of cardiomyocytes that were cultured on a flat PDMS surface and fixed and stained after six days ((A) Z-projection, (B) single slice) and after eight ((C) Z-projection, (D) single slice).

for the myocytes after six and eight days of culture on PDMS, respectively.

Adaptation to microcantilever arrays

Myocytes that were fixed and stained a few hours after seeding on the microcantilevers exhibited the same morphological characteristics as those that were fixed and stained a few hours after seeding in the Petri dishes, irrespective of the specific geometry of the microcantilevers. Figure 5.11 and 5.12 show images from two such isolations, showing myocytes that look the same as those isolated on the Petri dishes. These myocytes were

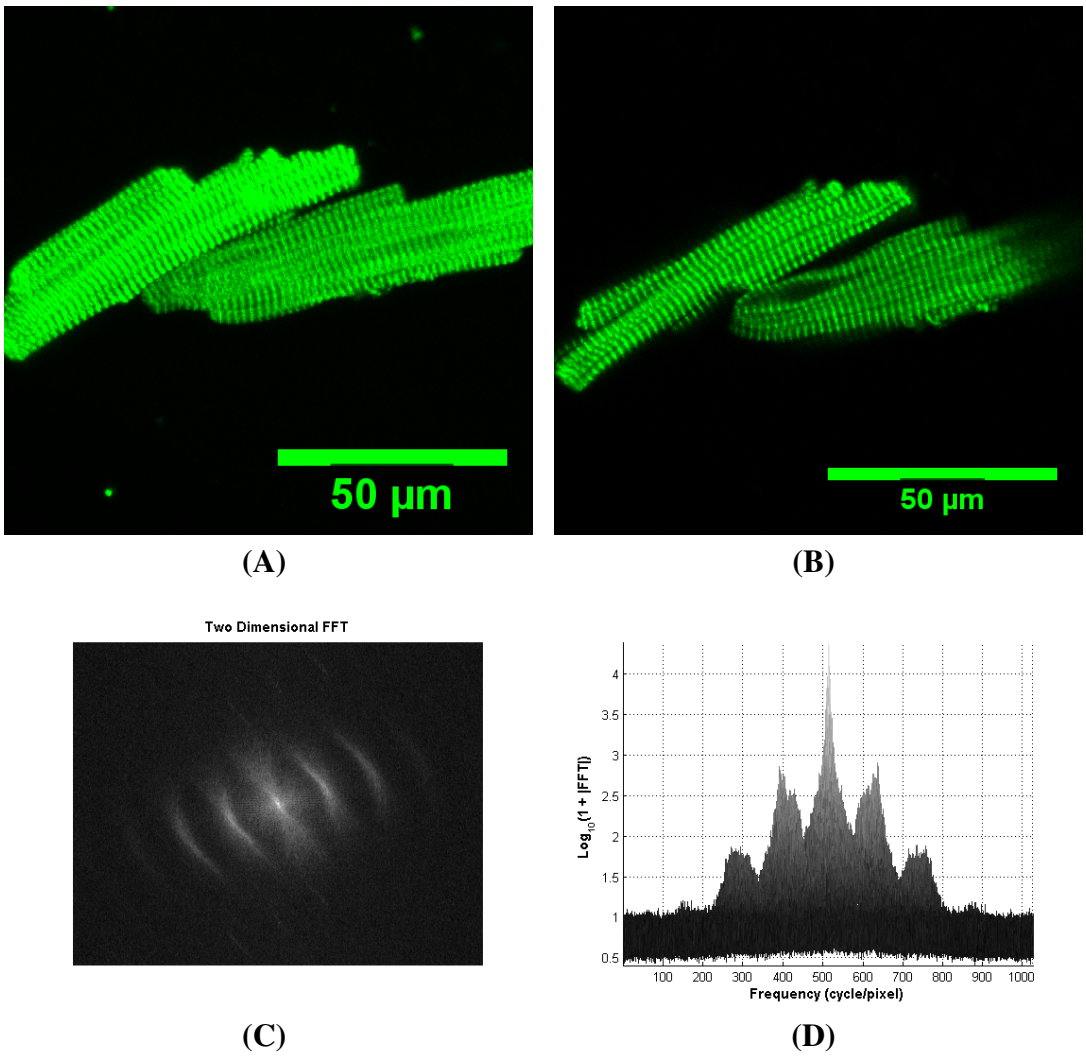

Figure 5.11 Myocytes fixed and stained at the time of isolation on 9 μm separation microcantilevers. (A) Projection of a Z-stack of images taken with the confocal microscope. (C) Two-dimensional FFT of (A) with quadrants swapped (D) Intensity values from (B) plotted on a logarithmic scale.

isolated on microcantilevers that were 3 μm in diameter 11 μm tall with 9 μm edge-to-edge separation (Figure 5.11) and 2 μm in diameter 7 μ tall with edge-to-edge separation of 5 μm (Figure 5.12) respectively.

Cells were removed from culture medium, fixed and stained every two days and confocal images were taken. It was observed during the first two days after isolation that the cells lost their rod shape structure and became more rounded, with a corresponding loss in the orderly arrangement of the sarcomeres. This may be due to protein turnover during the remodeling and adaptation process.[17]

There were noticeable differences between the cells cultured on the Petri dishes and

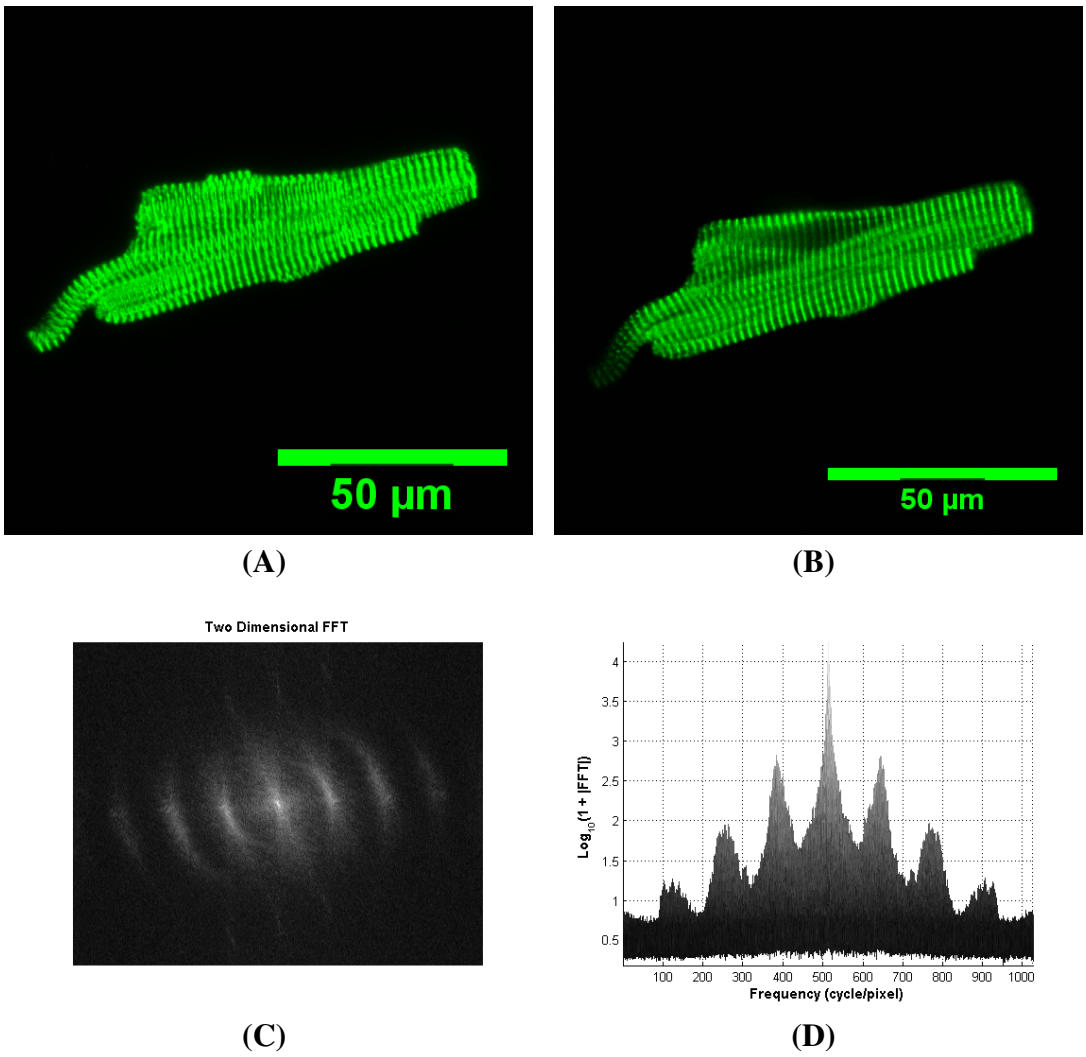

Figure 5.12 Myocytes fixed and stained at the time of isolation on 5 μm separation microcantilevers. (A) Projection of a Z-stack of images taken with the confocal microscope. (B) Single slice of Z-stack of (A) in which sarcomeres are more clearly visible. (C) Two-dimensional FFT of (A). (C) Intensity values from (D) plotted on a logarithmic scale.

those cultured on the microcantilevers. At six days of culture the myocytes on the Petri dishes were mostly spread out with a disorganized arrangement of myofibrils. Cells cultured on the microcantilevers, however seemed to adapt and remodel based on the geometry. Figure 5.13 shows myocytes cultured on microcantilevers with 6 μm edge-to-edge separation and fixed and stained after six days of culture. A Z-projection is shown in Figure 5.13(A). As was observed in the case of myocytes cultured on the Petri dishes, the fundamental frequency band of the two-dimensional FFT was almost circular as well, indicating that the fiber orientation was not orderly as in the case of freshly isolated myocytes.

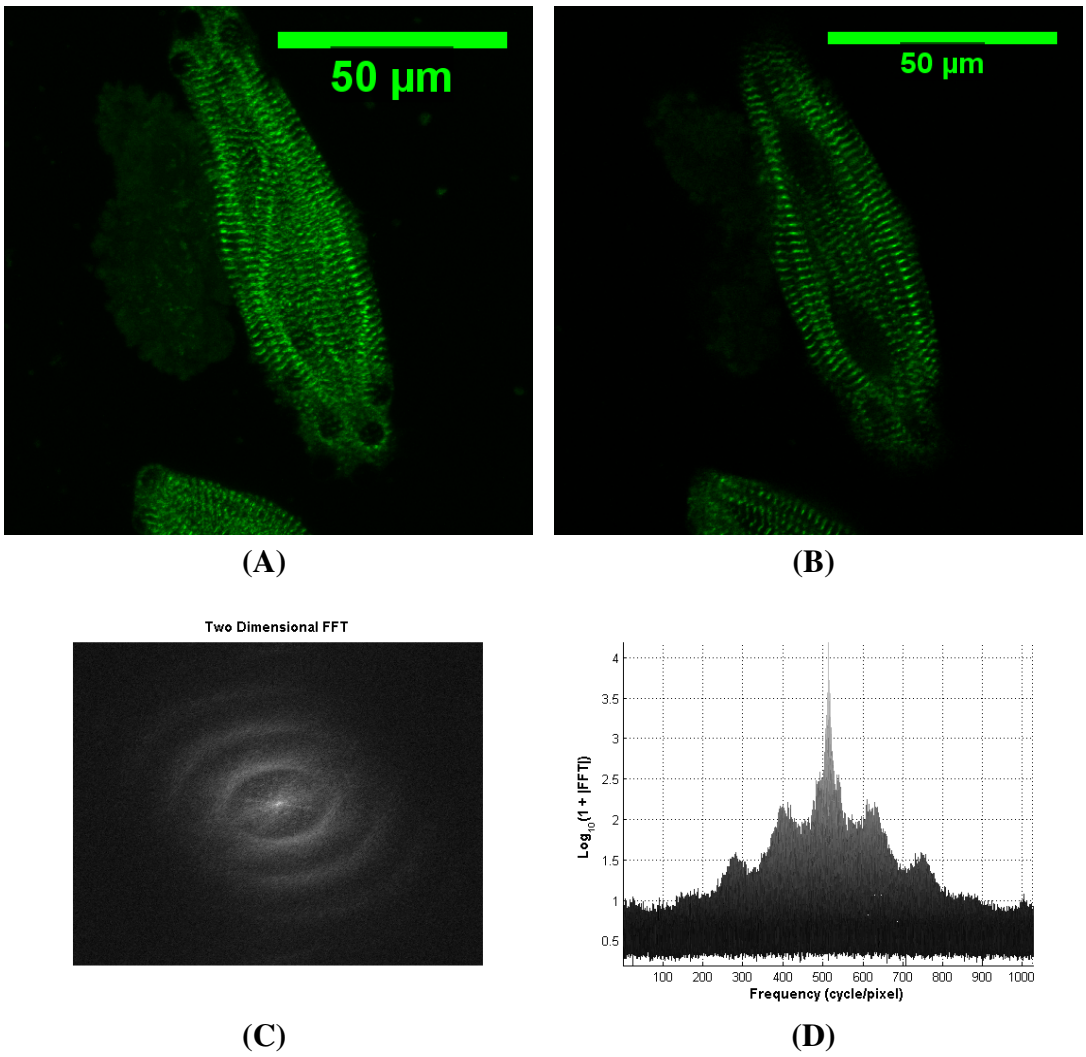

Figure 5.13 Myocytes fixed and stained after six days of culture on 6 μm separation microcantilevers. (A) Projection of a Z-stack of images taken with the confocal microscope. (C) Two-dimensional FFT of (A) showing almost circular arrangement of fundamental frequency which represents the regularly spaced sarcomeres (D) Intensity values from (C) plotted on a logarithmic scale.

It was observed that microcantilevers with 2 μm diameter and 5 μm edge-to-edge separation inhibited the ability of myocytes to form sarcomeres adequately. In this case the myocytes seemed to form long actin-like structures in between the microcantilevers but with very limited formation of sarcomeres. Figure 5.14 shows projections of cells cultured, fixed and stained on day eight of culture and that show this morphology. Figure 5.14(A) shows the myomesin stain and Figure 5.14(B) shows a merged image of the actin and myomesin stains. The two-dimensional FFT of Figure 5.14(A) shows that the fundamental frequency band is barely visible. Other frequencies representing the

microcantilever array are also present and can be seen more vividly in the intensity plot on the logarithmic scale. Myocytes cultured on microcantilevers that were 1 μm in diameter with edge-to-edge spacing of about 1 μm (Figure 5.15) also displayed morphology very similar to those cultured on microcantilevers with 2 μm diameter and 5 μm edge-to-edge separation. However, the actin fibers were not as long as those in Figure 5.14. Sarcomere formation was also inhibited in this case. Figure 5.15(A) and 5.15(B) show a merged image of the actin and myomesin stains and the intensity profile on a log magnitude scale of the two-dimensional FFT, respectively.

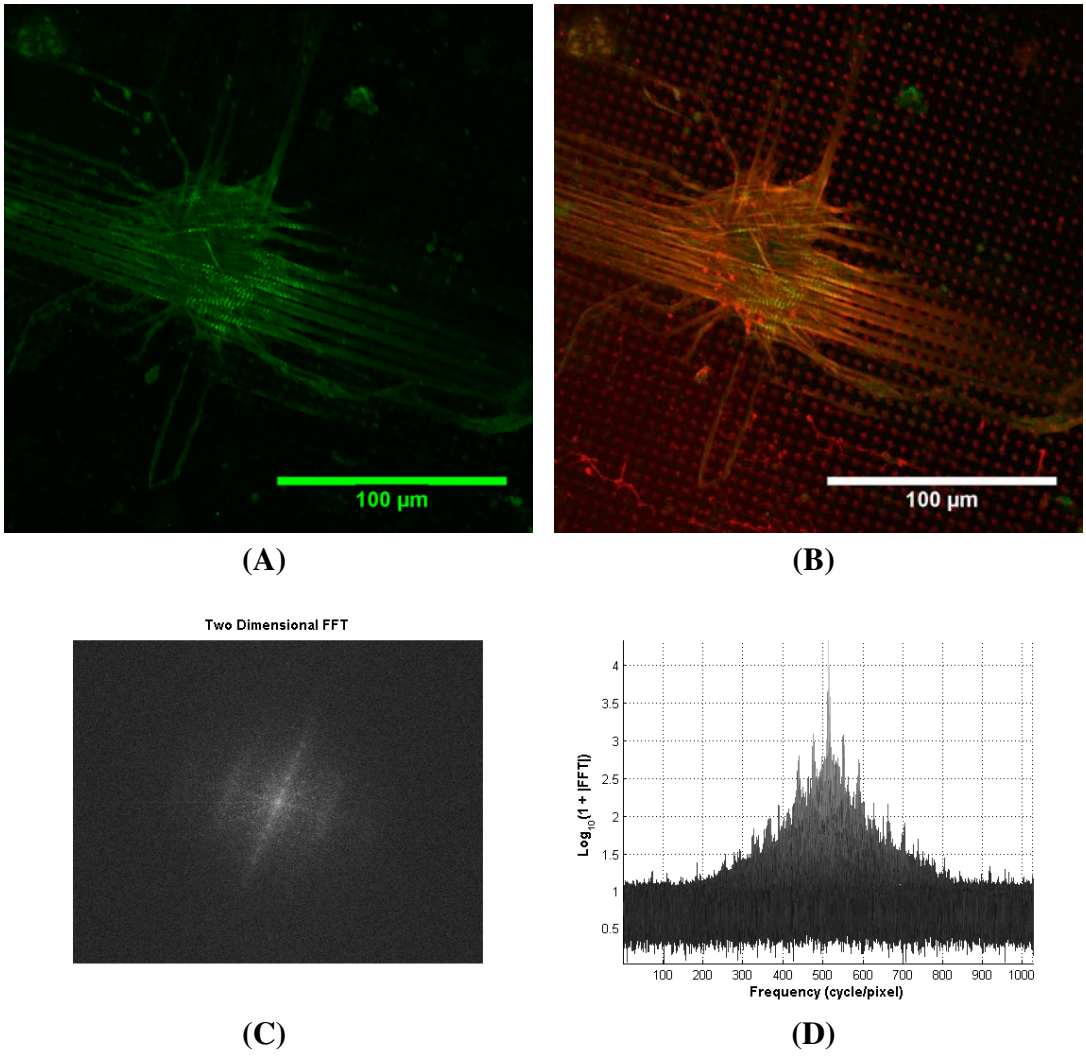

Figure 5.14 Adaptation of myocytes to 5 μm edge-to-edge separation and 2 μm diameter microcantilevers (A) Myomesin stain. (B) Merged image of the actin and myomesin stains. (C) Two-dimensional FFT of (A) (D) Intensity values from Figure 5.14(C) plotted on a logarithmic scale.

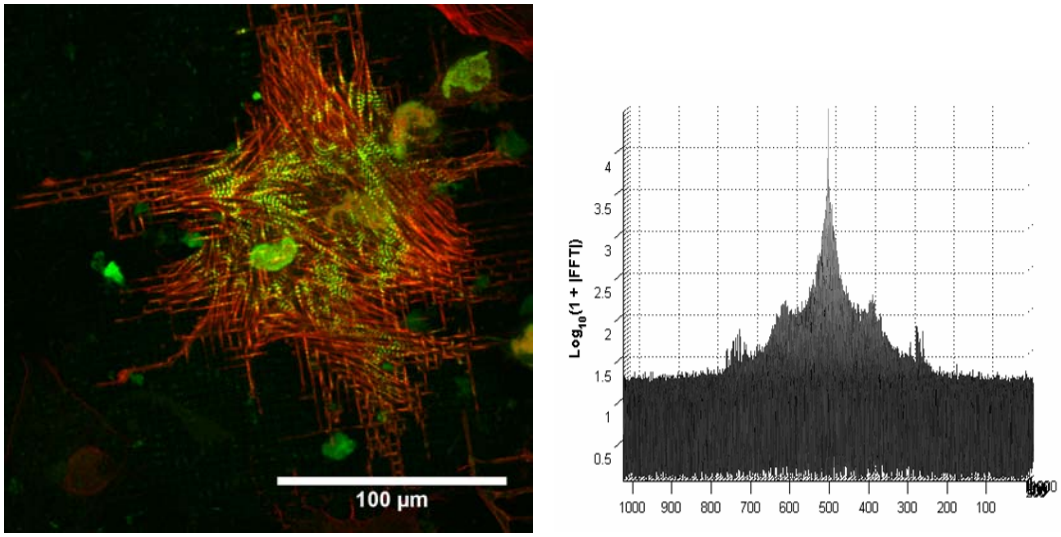

(A) **(B)**

Figure 5.15 Adaptation on 1 μm edge-to-edge separation and 1 μm diameter micro-cantilevers (A) (B) Intensity values from two-dimensional FFT plotted on a logarithmic scale

Depth dependence of sarcomere organization

Another interesting observation was that in some cases the myocytes displayed a more orderly arrangement of fibrils for a few μm when scanning down from the top of the cell. As the cell was progressively scanned from top to bottom there was a noticeable rearrangement of fibrils. Figure 5.16(A) – to (P) is a montage of part of the myocyte in Figure 5.13(A) showing myofibril arrangement at different depths of the confocal scan. The remodeling of the myofibrils is prominent between 19 and 25 μm of the z-scan. At 22 μm the displacement of four microcantilevers is evident and the equivalent forces have been indicated. Figure 5.17(A) – to (F) is another montage of z-scans showing similar effects. To obtain the different perspective on the arrangement of the myofibrils, Figure 5.17 was resliced at an angle of about 50° to the horizontal in steps of 0.5 μm. Figure 5.18(A) and 5.18(B) show results from this reconstruction. Figure 5.18(A) shows four consecutive slices in an area where there are no microcantilevers and Figure 5.18(B) shows four consecutive slices from an adjacent area with microcantilevers.

This was observed for several other myocytes as well. Figure 5.19 shows individual

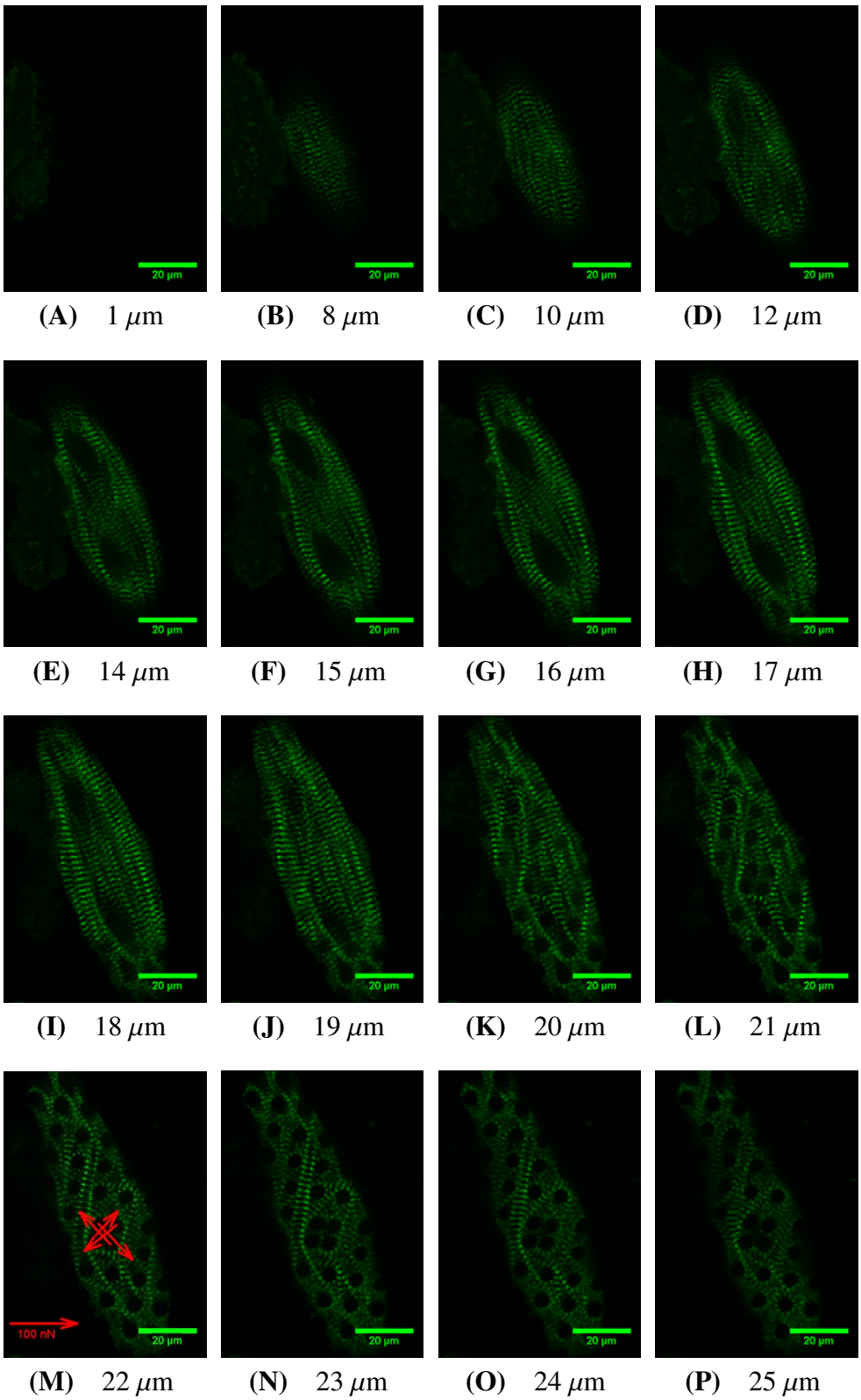

(A) 1 μm **(B)** 8 μm **(C)** 10 μm **(D)** 12 μm

(E) 14 μm **(F)** 15 μm **(G)** 16 μm **(H)** 17 μm

(I) 18 μm **(J)** 19 μm **(K)** 20 μm **(L)** 21 μm

(M) 22 μm **(N)** 23 μm **(O)** 24 μm **(P)** 25 μm

Figure 5.16 Montage of z-scan of Figure 5.13 from 1 μm (A) where the cell is not visible at all to 25 μm (P). Between 7 μm and 10 μm an almost parallel arrangement of fibrils similar to freshly isolated myocytes is evident. After that remodeling seems to affect arrangement of the fibrils with the effect greatest between 19 μm (J) and 25 μm (P) when the scan ends. Arrows shown in (M) represent approximate forces exerted on microcantilevers by surrounding myofibrils.

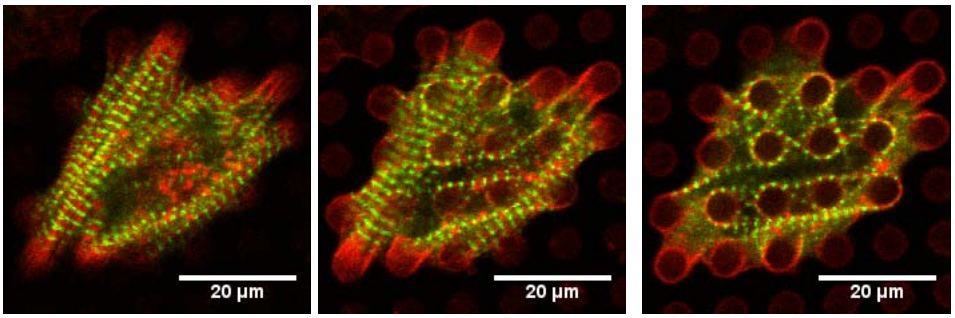

(A) 8 μm **(B)** 10 μm **(C)** 12 μm

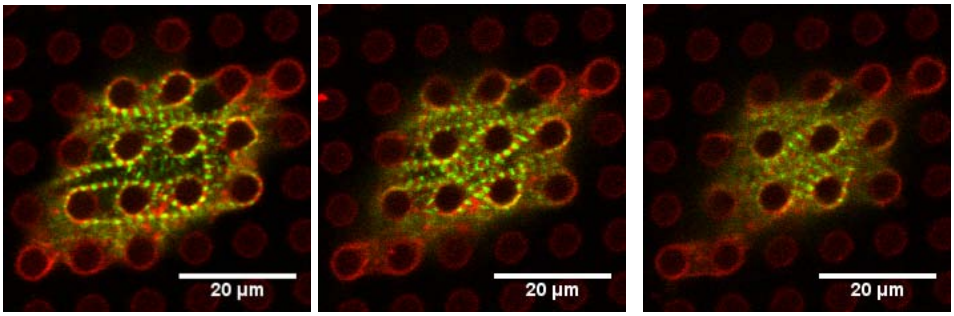

(D) 14 μm **(E)** 16 μm **(F)** 18 μm

Figure 5.17 Montage of z-scan of a myocyte showing adaptation from 8 μm (A) to 18 μm (F). Remodeling seems to affect arrangement of the fibrils, with the effect greatest between 10 μm (B) and 16 μm (E).

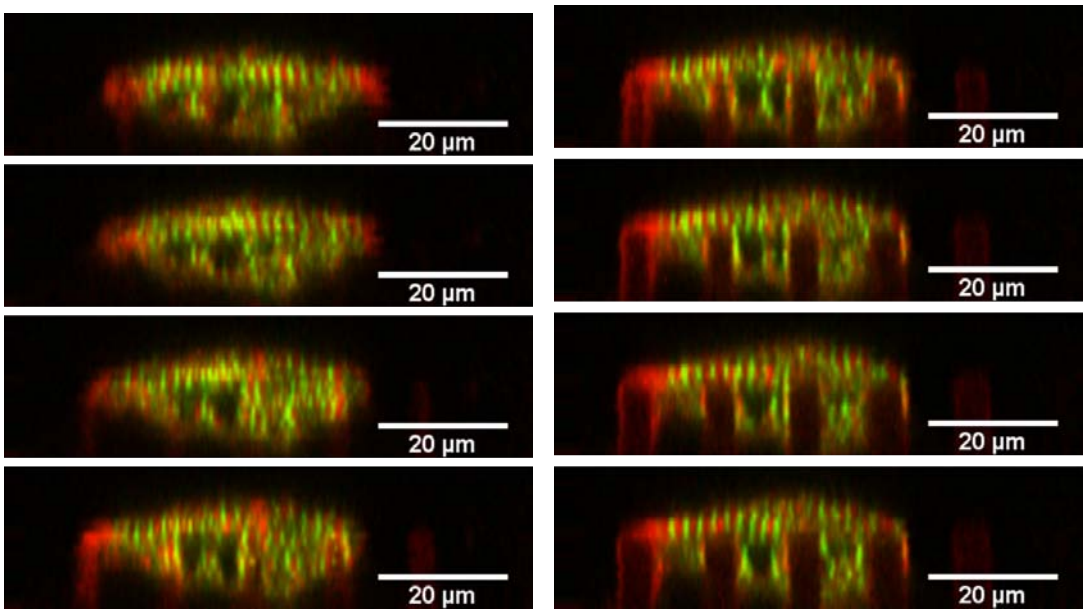

(A) **(B)**

Figure 5.18 Reslice of z-scan of Figure 5.17 at an angle of about 50° to the horizontal showing a different perspective of adaptation to microcantilevers. (A) Four consecutive slices in areas with no microcantilevers (B) Four consecutive adjacent slices that pass through microcantilevers. Slices are at 0.5 μm intervals.

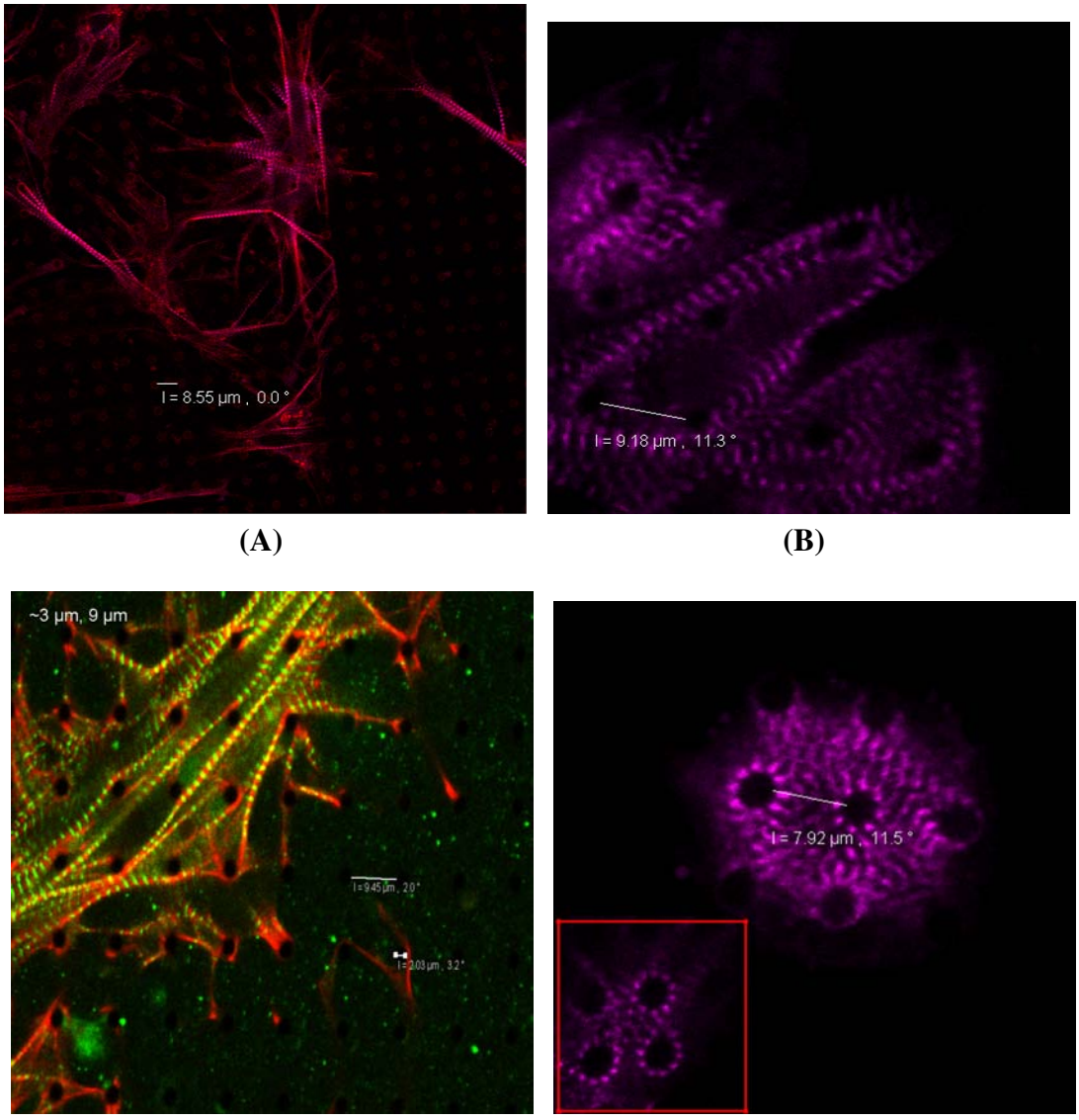

Figure 5.19 Adaptation on microcantilevers. Images showing other observations of myocytes adapting to microcantilevers. (A) - (C) Microcantilevers with 3 μm diameter, 10 μm tall and ~9 μm spacing. (D) Microcantilevers with 3 μm diameter, 10 μm tall and ~8 μm spacing.

slices of z-stacks of some of these other observations. Figure 5.19(C) is an overlay of the stains for actin and myomesin. Figure 5.19(D) shows a circular arrangement around individual microcantilevers and the insert in this figure shows an intriguing "figure 8" arrangement of a fibril.

In summary we observed that at the time of isolation, there was no distinct difference in the peaks for myocytes seeded on microcantilevers with edge-to-edge spacing of 5 μm (2.8205 ± 0.0219), 6 ,8 and 9 μm (2.7680 ± 0.1507), in the Petri dishes (2.7695 ± 0.1351) and those on plain PDMS (2.7710). After 6 days of culture, there were noticeable differences for the myocytes cultured on microcantilevers (edge-to-edge spacing of 2 and 5 μm = 2.1020 ± 0.0594, edge-to-edge spacing of 6,8 and 9 μm = 2.0788 ± 0.1947) as compared to those in the Petri dishes (2.7650 ± 0.0127) and the flat areas of PDMS (2.7790 ± 0.0156). Those on the microcantilever arrays displayed lower values for their peaks while those on the flat areas of PDMS and the Petri dishes had no significant change. Figure 5.20(A) and 5.20(B) show a summary of this data.

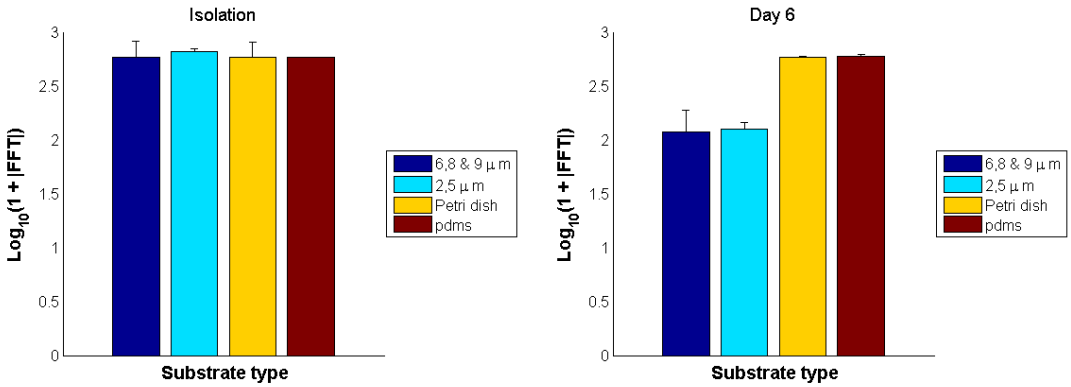

(A) **(B)**

Figure 5.20 Summary of peak data (A) Peak of intensity value on a logarithmic scale for 2D FFT for myocytes fixed and stained at isolation. Data show about the same values irrespective of substrate type. (B) Peak data in the case of myocytes fixed on day 6 after isolation.

Another important consideration in looking at these data is remodeling and growth of the sarcomeres in relation to certain pathological situations in which changes in myocyte phenotype and structure are driven by changes at the sarcomere level[17]. The microcan-

tilevers provide a unique platform that can be used to further elucidate how the nature of three dimensional substrates could affect the remodeling of the sarcomeres. This may not necessarily reflect what happens *in vivo* but could prove important in understanding the various remodeling mechanisms.

It is our opinion that more experiments may have to be done to determine which of the myofibrillogenesis models the data presented here support. However, based on just these observations, it seems the first three models discussed in the subsection myofibrillogenesis (stress fiber-like structures as templates, assembly form several subunits, and premyofibrils as myofibril precursors) are the most likely candidates.

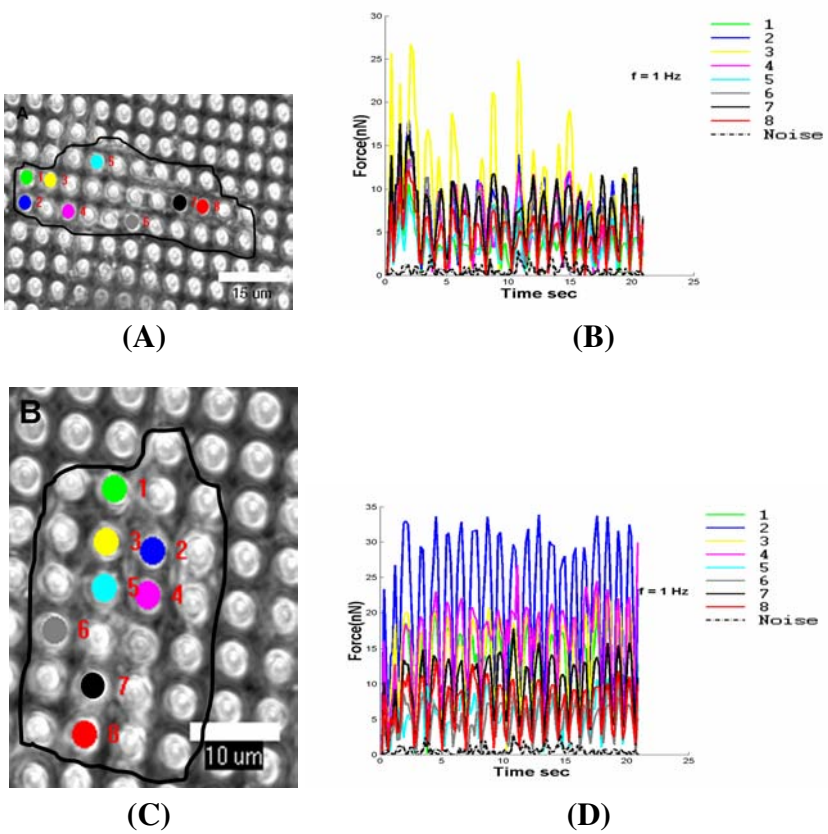

Figure 5.21 Contracting myocytes. (A) Myocyte with overlay showing eight microcantilevers (colored) whose force data have been plotted in (B). (C) Myocyte with overlay showing eight microcantilevers (colored) whose force data have been plotted in (D)

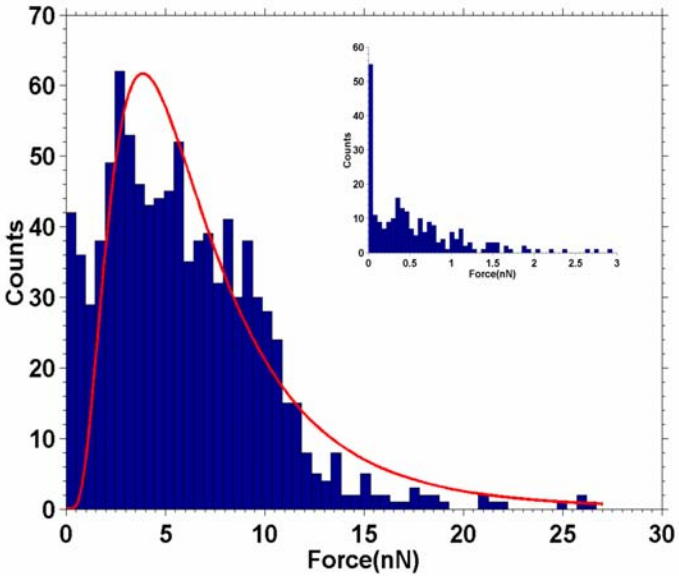

(A)

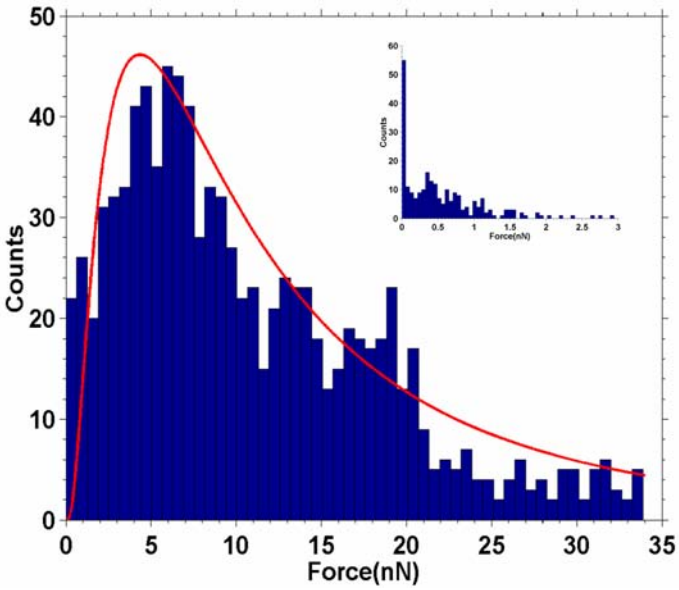

(B)

Figure 5.22 Force distribution in myocytes. (A) Force distribution for the myocyte shown in Figure 5.21(A). The fit to a log normal distribution is shown. The insert is a distribution for the two microcantilevers tracked representing noise. (B) Force distribution for the myocyte shown in Figure 5.21(C).

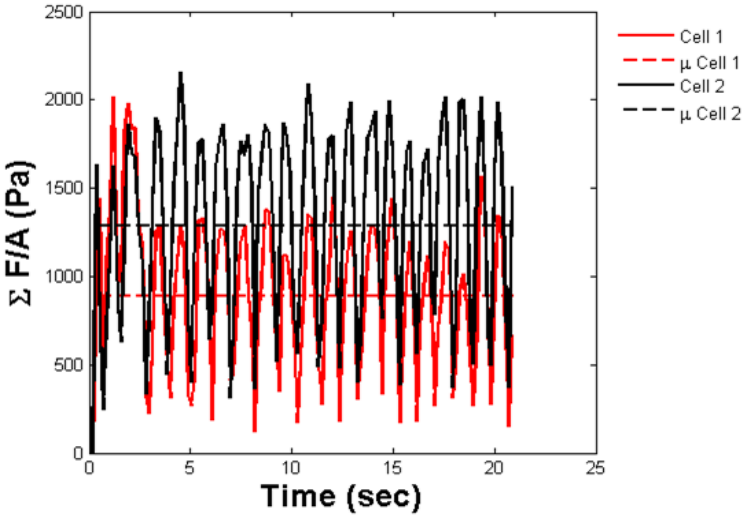

Figure 5.23 Shear forces exerted.

Analysis of contracting myocytes

Spontaneous contraction of myocytes on the microcantilevers was observed in some cases. This provided an opportunity to access the ability of the myocytes to generate force and contraction on the microcantilevers. Figure 5.21(A) and (C) show the outlines of two such cells that were observed. The variation of the magnitude of force with time for these two cells has been shown (in this case only eight of the identified microcantilevers have been plotted).

Two microcantilevers which did not have any myocytes attached were also tracked and plotted. This gives an indication of the noise due to image shifts. Using the number of peaks observed over the time period, the frequency of contraction (beat frequency)was calculated to be 1 Hz. The average shear force generated by these two cells was also computed by summing the total force generated by each cell over the same time period and dividing this by the approximate area that each cell covered. This area was estimated by counting the total number of microcantilevers that each cell covered and then multiplying this by the individual cross sectional area of a single microcantilever. The mean value was determined for both cases and it was observed that the myocyte identified in Figure 5.21(C) had a greater shear stress (1284 Pa) than the myocyte in Figure 5.21(A) (891 Pa). This is plotted in Figure 5.23. The distribution of the forces for both cells was also determined by computing a histogram. In both cases the distribution of forces followed a log normal

distribution, as shown in Figure 5.22(A) and (B). This is in agreement with observed force distributions for smooth muscle cells that have been reported in the literature cite[34,40].

Divergence and curl

To better represent the directional nature of the forces generated, raw displacement data were plotted for positive and negative deflections in the x and y directions for the three regions observed to have contracting myocytes two of which are shown in Figure 5.21. A non-linear color table was used for representing the values due to the non-uniform distribution of computed displacements. The plots for four consecutive frames for the displacements in x and y are plotted in Figure 5.24(A) - 5.24(D) and 5.24(E) - 5.24(H) respectively. Close examination of these show that while there are some observable patterns, they provide very little additional information from what can be learned from the absolute force plots in Figure 5.21. The divergence and curl using a 2×2 computational kernel was

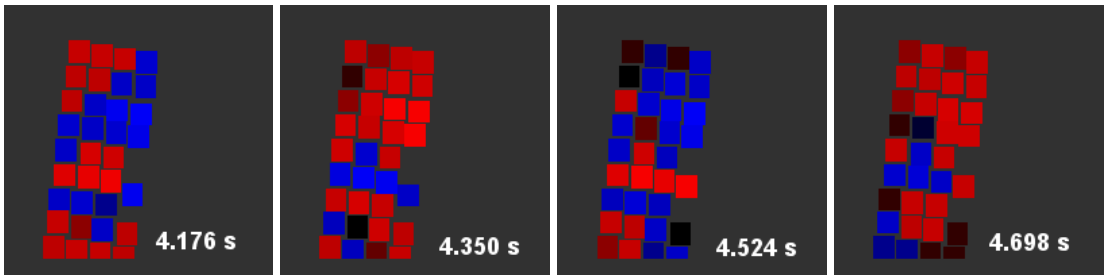

(A) T = 4.176 secs **(B)** T = 4.350 secs **(C)** T = 4.524 secs **(D)** T = 4.698 secs

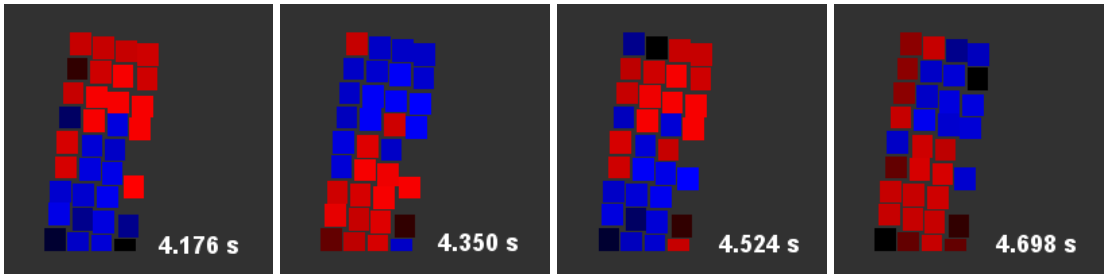

(E) T = 4.176 secs **(F)** T = 4.350 secs **(G)** T = 4.524 secs **(H)** T = 4.698 secs

Figure 5.24 Raw displacements in the x and y directions plotted using the same color table as that for the divergence. (A)- (D) Raw displacements in the x direction. As can be seen they do not exactly match the pattern observed in the divergence in Figure 5.26. (E)-(H) Raw displacements in the y direction. The alternating areas of contraction and relaxation cannot be observed though this is much closer to the divergence case.

evaluated using Equations (5.1) and (5.2), respectively. In both cases the corresponding displacements in the x and y directions for each of the four nearest microcantilevers were utilized. The divergence and curl metrics were computed for four nearest microcantilevers and the resulting value was assigned to a point midway between them.

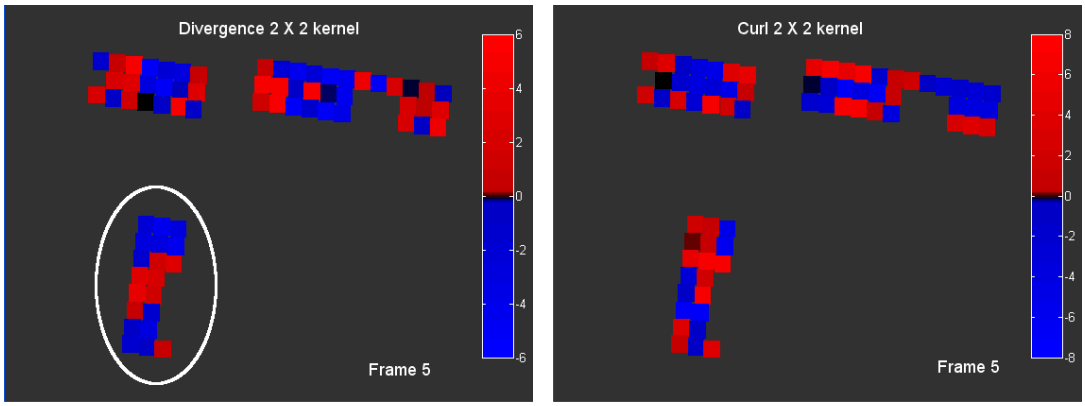

(A) **(B)**

Figure 5.25 Divergence and curl computed with a 2×2 kernel for frame five (time=696 ms) of a movie using non-linear color tables. (A) The computed divergence metric and (B) the computed curl metric.

The two metrics were computed at each time frame for all identified microcantilevers within a certain area of interest using an algorithm written in MATLAB™. The outputs were stored as a sequence of images in *.avi movie format. Figure 5.25(A) and 5.25(B) show the divergence and curl computed for frame five (time=696 ms) in the 120 frame (20.76 seconds) time lapse movie. The distribution of computed values in both cases were not uniform over the full range of possible values. This required the use of non-uniform intervals for representation of the values for the color table with a finer division assigned to the range of values with a higher frequency of occurrence and a coarser division for the range of values with a lower frequency. As can be seen from these images there was a significant difference between the divergence metric and the curl metric.

Computing the divergence and curl metrics provided an opportunity to examine the displacement data in a different light. Not only did it provide a directional element, but the computed metrics gave a representation of the relative movements of the microcan-

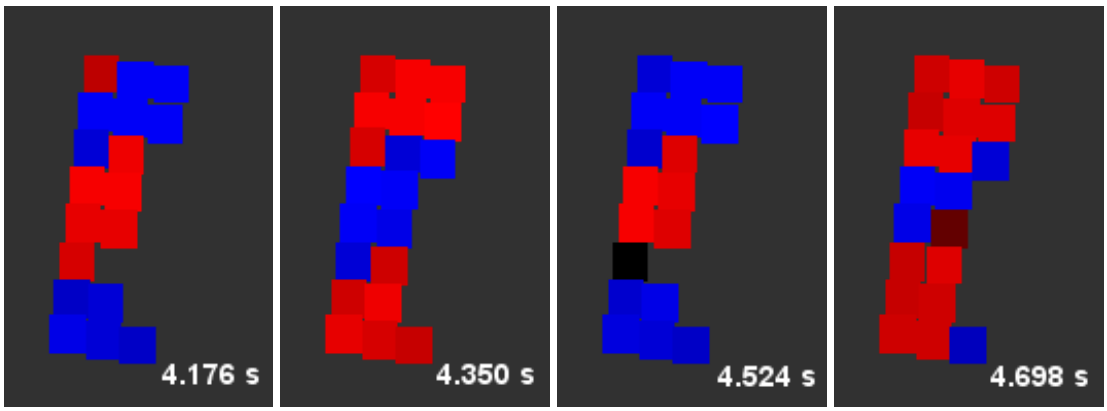

(A) T = 4.176 secs **(B)** T = 4.350 secs **(C)** T = 4.524 secs **(D)** T = 4.698 secs

Figure 5.26 Divergence using a 2 × 2 kernel showing alternating regions of contraction and relaxation (A) – (D) across the cell highlighted in Figure 5.25(A).

tilevers with respect to each other. It was observed that especially in the case of the region representing the cell that has been highlighted with the oval in Figure 5.25(A), there are noticeable differences between areas that were contracting and areas that were relaxing for a particular time frame. In some cases opposite ends of the cell showed in general a positive divergence (relaxation) while the middle of the cell showed the opposite (contraction of the cell). Figure 5.26(A) - 5.26(D) shows this clearly. Computing the divergence and curl metric thus provided a different perspective in analyzing the raw displacement data. These metrics can also be compared to computation of volumetric strain[41,42] and volumetric distortion[43] respectively.

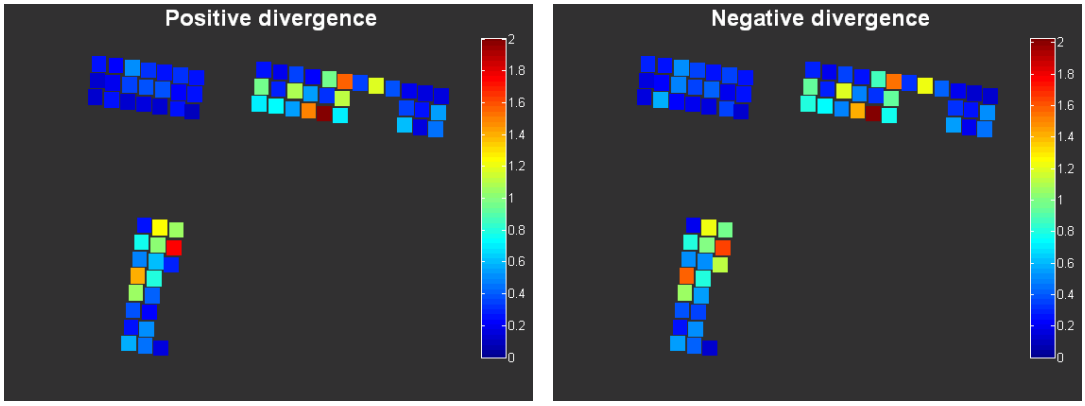

(A) **(B)**

Figure 5.27 Average positive (A) and negative (B) divergence computed using a 2 × 2 kernel and represented using a linear color table.

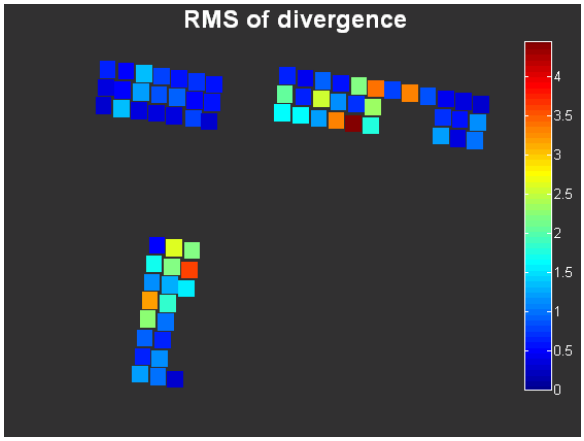

Figure 5.28 Root mean square of divergence using 2×2 kernel showing the distribution represented using a linear color table assignment.

The above observation, was unexpected. However, there have been extensive reports in the literature on calcium and contraction waves in cardiac myocytes[44–46]. Lamont *et al.*[47] also showed that calcium waves originate from either one end or the center of the cell and propagate towards the other end. It is also well known that calcium waves are responsible for contraction waves in cardiac myocytes[48,49].

To provide a hopefully better visualization of these alternating regions of contraction and relaxation, we averaged the divergence values longitudinally or horizontally, depending on the orientation of the areas being analyzed and plotted the average values on a linear grid with time (frame no.) on the vertical axis and space (averaged values along particular dimension) on the horizontal axis to create a space-time plot. Figure 5.29 shows the plots that were obtained for the three different regions shown in Figure 5.25. We did not observe diagonal lines that would represent waves of contraction and relaxation as we were expecting, but rather the same kind of alternating regions of contraction and relaxation that we saw in the divergence data. The reason for this could be due to low sampling frequency during capture of the time-lapse images (5.7 Hz), which could lead to an aliasing effect. This however does not exclude the possibility that the alternating regions we observe are actually due to propagation of slow cardiac calcium waves[45]. Another observation is the fact that in some cases certain areas of the cell remain contracted or relaxed for more than one frame interval.

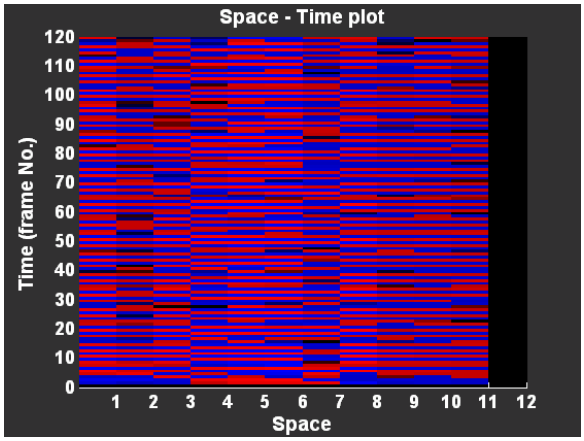

(A)

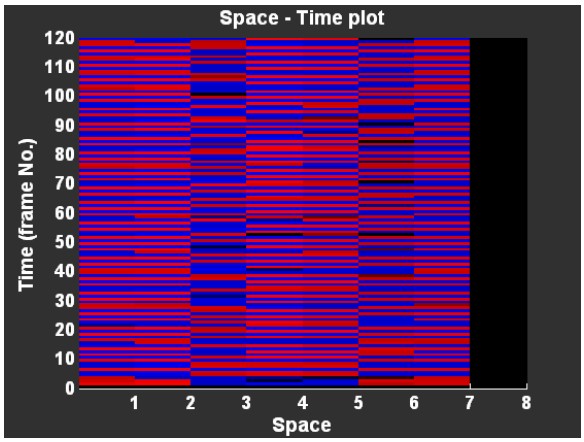

(B)

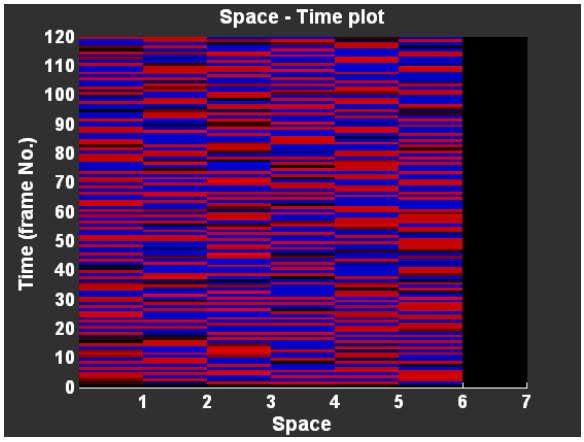

(C)

Figure 5.29 Space-time plots for average divergence for three regions shown in Figure 5.25.

In order to identify possible hot spots of contraction, average values for each metric at each pseudo point were computed for only positive divergence and negative divergence values. Figure 5.27 shows the average values computed. In this case the values were represented using a linear color table. One conclusion we could draw was that there was no significant difference in the average values for positive and negative divergence. This meant that for the most part, the regions analyzed contracted and stretched to about the same degree. One possible explanation could be the alternating contraction and relaxing regions that we have mentioned. The root mean square (RMS) of the divergence was also computed. This provides an insight into the regions that exhibited the most energy dissipation or the areas where the most work was done. This is plotted in Figure 5.28. Generally there was a correlation between the areas that showed the highest values in terms of the average negative or positive divergence and those that showed the most energy dissipated.

The curl metric was computed to investigate the possibility of rotational patterns occurring during the contraction, relaxation, and streching process. The curl operator produces a vector. Because our displacements were restricted to the x-y plane we only needed to compute the z component of the curl. In this case these values represent the rotation or circulation in the plane of the top of the posts per unit area. No significant patterns were observed in the case of the curl metric.

To determine if there were any relations between the signs of divergence and curl, we determined when the positive divergence and curl did and did not coincide. In making this comparison areas with zero values were ignored. It was determined that in 22.4% of the cases when there was a positive divergence the corresponding curl was also positive. The other values were determined to be 22.8% for negative to negative, 26.8% for positive divergence to negative curl, and 27.9% for negative divergence to positive curl. These numbers show that there was no significant relation between the divergence at a point and the corresponding curl. It must be noted that we did not consider the strain-rate dependence of the the elastic modulus of PDMS that has been reported in the literature[50]

We examined the use of a microfabricated microcantilever array as an assay to examine cardiac myocyte adhesion, remodeling, and contractile function. It was observed that generally myocytes adhered better on the plastic-coated dishes than on the microcantilevers. Our observations showed that there was no difference in myocyte sarcomere structure at the time of isolation irrespective of the nature of the substrate the myocyte was adhering to. After culturing the myocytes for about six days we noticed differences in structure between myocytes growing on the flat Petri dishes and on the PDMS microcantilever arrays. The microcantilever arrays seemed to affect the way in which the myocytes adapted, causing a considerable rearrangement of the myofibril structure. Comparing two dimensional (2D) FFT outputs showed significant differences as well. There was no noticeable difference for myocytes cultured on the Petri dishes and those cultured on flat PDMS substrates. In the case of the myocytes on the microcantilevers, array spacing seemed to affect the ability of myocytes to form sarcomeres in culture. Microcantilevers having edge-to-edge spacings of 5 μm were observed to have the greatest inhibitory effect. It must be noted that in computing the two-dimensional FFT the myofibril orientations were not taken into consideration. This could have an effect on the computation and could be responsible for the spreading out of the peak values for the three-dimensional projection on the log scale. A radial profile plot of the two-dimensional FFT instead of the three-dimensional projection could be a possible solution.

We also analyzed spontaneously contracting myocytes on the microcantilever arrays. Absolute force data for some of the tracked microcantilevers fit log-normal distributions. Computing a divergence metric provided a means to observe contraction and relaxation patterns in some of the myocytes. These patterns were not observed when corresponding raw displacement data were plotted. It was also observed that there was no significant relation between the computed divergence at a particular point and its corresponding curl.

These results and observations demonstrate that the microcantilever array can used to investigate myocyte mechanotransduction as well as remodeling *in vitro* especially since it provides an assay to study these phenomena for the case where the cardiomyocyte is

anchored at multiple points unlike other studies where the cardiomyocyte is either free or held at its end. It could also be used as a possible assay for myofibrillogenesis.

Acknowledgements

We acknowledge the support of the Vanderbilt Institute for Integrative Biosystems Research and Education (VIIBRE), the Whitaker Foundation, and the NIH (R01 HLO68144).

References

[1] Kristic, R. Die Gewebe des Menschen und der Sugetiere. *Springer Verlag* 1984.

[2] Alberts, B. *Molecular biology of the cell*. New York : Garland Pub.,, 1994.

[3] Katz, A. *Physiology of the heart*. New York : Raven Press, 2001.

[4] Asbun, J., Villarreal, F. J. The Pathogenesis of Myocardial Fibrosis in the Setting of Diabetic Cardiomyopathy. *Journal of the American College of Cardiology* **47**, 693–700, 2006.

[5] Rutschow, S., Li, J., Schultheiss, H. P., Pauschinger, M. Myocardial proteases and matrix remodeling in inflammatory heart disease. *Cardiovascular Research* **69**, 646–656, 2006.

[6] Pardo, J., Siliciano, J., Craig, S. A Vinculin-Containing Cortical Lattice in Skeletal-Muscle - Transverse Lattice Elements (Costameres) Mark Sites of Attachment Between Myofibrils and Sarcolemma. *Proceedings of the National Academy of Sciences of the United States of America-Biological Sciences* **80**, 1008–1012, 1983.

[7] Sharp, W., Simpson, D., Borg, T., Samarel, A., Terracio, L. Mechanical forces regulate focal adhesion and costamere assembly in cardiac myocytes. *Am J Physiol Heart Circ Physiol* **273**, H546–H556, 1997.

[8] Danowski, B., Imanakayoshida, K., Sanger, J., Sanger, J. Costameres Are Sites of Force Transmission to the Substratum in Adult-Rat Cardiomyocytes. *J.Cell Biol.* **118**, 1411–1420, 1992.

[9] Conrad, C. H., Brooks, W. W., Hayes, J. A., Sen, S., Robinson, K. G., Bing, O. H. Myocardial Fibrosis and Stiffness With Hypertrophy and Heart Failure in the Spontaneously Hypertensive Rat. *Circulation* **91**, 161–170, 1995.

[10] Ehler, E., Rothen, B. M., Hammerle, S. P., Komiyama, M., Perriard, J. C. Myofibrillogenesis in the developing chicken heart: assembly of Z-disk, M-line and the thick filaments. *Journal Of Cell Science* **112**, 1529–1539, 1999.

[11] Ehler, E., Perriard, J.-C. Cardiomyocyte Cytoskeleton and Myofibrillogenesis in Healthy and Diseased Heart. *Heart Failure Reviews* **5**, 259–269, 2000.

[12] Dlugosz, A. A., Antin, P. B., Nachmias, V. T., Holtzer, H. The Relationship Between Stress Fiber-Like Structures And Nascent Myofibrils In Cultured Cardiac Myocytes. *Journal Of Cell Biology* **99**, 2268–2278, 1984.

[13] Wang, S., Greaser, M., Schultz, E., Bulinski, J., Lin, J., Lessard, J. Studies on cardiac myofibrillogenesis with antibodies to titin, actin, tropomyosin, and myosin. *J. Cell Biol.* **107**, 1075–1083, 1988.

[14] Schultheiss, T., *et al.* Differential Distribution Of Subsets Of Myofibrillar Proteins In Cardiac Nonstriated And Striated Myofibrils. *Journal Of Cell Biology* **110**, 1159–1172, 1990.

[15] Legato, M. J. Ultrastructural Characteristics Of Rat Ventricular Cell Grown Inn Tissue-Culture, With Special Reference To Sarcomerogenesis. *Journal Of Molecular And Cellular Cardiology* **4**, 299–&, 1972.

[16] Sanger, J., *et al.* How to build a myofibril. *Journal of Muscle Research and Cell Motility* **26**, 343–354, 2005.

[17] Boateng, S. Y., Goldspink, P. H. Assembly and maintenance of the sarcomere night and day. *Cardiovasc Res* cvm048–, 2007.

[18] Lu, M. H., *et al.* The Vinculin Sarcomeric-Alpha-Actinin Alpha-Actin Nexus In Cultured Cardiac Myocytes. *Journal Of Cell Biology* **117**, 1007–1022, 1992.

[19] Rhee, D., Sanger, J. M., Sanger, J. W. The Premyofibril - Evidence For Its Role In Myofibrillogenesis. *Cell Motility And The Cytoskeleton* **28**, 1–24, 1994.

[20] Costa, M. L., Escaleira, R. C., Rodrigues, V. B., Manasfi, M., Mermelstein, C. S. Some distinctive features of zebrafish myogenesis based on unexpected distributions of the muscle cytoskeletal proteins actin, myosin, desmin, alpha-actinin, troponin and titin. *Mechanisms Of Development* **116**, 95–104, 2002.

[21] Milner, D. J., Weitzer, G., Tran, D., Bradley, A., Capetanaki, Y. Disruption of muscle architecture and myocardial degeneration in mice lacking desmin. *Journal Of Cell Biology* **134**, 1255–1270, 1996.

[22] Zhuang, J., Yamada, K. A., Saffitz, J. E., Kleber, A. G. Pulsatile Stretch Remodels Cell-to-Cell Communication in Cultured Myocytes. *Circ Res* **87**, 316–322, 2000.

[23] Simpson, D., Sharp, W., Borg, T., Price, R., Terracio, L., Samarel, A. Mechanical regulation of cardiac myocyte protein turnover and myofibrillar structure. *Am J Physiol Cell Physiol* **270**, C1075–C1087, 1996.

[24] Zimmermann, W., Fink, C., Kralisch, D., Remmers, U., Weil, J., Eschenhagen, T. Three-dimensional engineered heart tissue from neonatal rat cardiac myocytes. *Biotechnology and Bioengineering* **68**, 106–114, 2000.

[25] Entcheva, E., Bien, H. Acoustic micromachining of three-dimensional surfaces for biological applications. *Lab on a Chip* **5**, 179–183, 2005.

[26] Entcheva, E., Bien, H., Yin, L., Chung, C., Farrell, M., Kostov, Y. Functional cardiac cell constructs on cellulose-based scaffolding. *Biomaterials* **25**, 5753–5762, 2004.

[27] Bursac, N., *et al.* Cardiac muscle tissue engineering: toward an in vitro model for electrophysiological studies. *Am J Physiol Heart Circ Physiol* **277**, H433–H444, 1999.

[28] Motlagh, D., Senyo, S. E., Desai, T. A., Russell, B. Microtextured substrata alter gene expression, protein localization and the shape of cardiac myocytes. *Biomaterials* **24**, 2463–2476, 2003.

[29] Tsang, V. L., Bhatia, S. N. Three-dimensional tissue fabrication. *Advanced Drug Delivery Reviews* **56**, 1635–1647, 2004.

[30] Borenstein, J. T., Terai, H., King, K. R., Weinberg, E. J., Kaazempur-Mofrad, M. R., Vacanti, J. P. Microfabrication technology for vascularized tissue engineering. *Biomedical Microdevices* **4**, 167–175, 2002.

[31] Vozzi, G., Flaim, C., Ahluwalia, A., Bhatia, S. Fabrication of PLGA scaffolds using soft lithography and microsyringe deposition. *Biomaterials* **24**, 2533–2540, 2003.

[32] Borenstein, J. T., Weinberg, E. J., Orrick, B. K., Sundback, C., Kaazempur-Mofrad, M. R., Vacanti, J. P. Microfabrication of three-dimensional engineered scaffolds. *Tissue Engineering* **13**, 1837–1844, 2007.

[33] Park, H., Cannizzaro, C., Vunjak-Novakovic, G., Langer, R., Vacanti, C. A., Farokhzad, O. C. Nanofabrication and microfabrication of functional materials for tissue engineering. *Tissue Engineering* **13**, 1867–1877, 2007.

[34] Addae-Mensah, K. A., *et al.* A flexible, quantum dot-labeled cantilever post array for studying cellular microforces. *Sensors and Actuators A: Physical* **136**, 385–397, 2007.

[35] de Boer, M., *et al.* Guidelines for etching silicon MEMS structures using fluorine high-density plasmas at cryogenic temperatures. *Microelectromechanical Systems, Journal of* **11**, 385–401, 2002.

[36] Lim, C., Helmes, M., Sawyer, D., Jain, M., Liao, R. High-throughput assessment of calcium sensitivity in skinned cardiac myocytes. *American Journal of Physiology-Heart and Circulatory Physiology* **281**, H969–H974, 2001.

[37] Ostu, N. A Threshold Selection Method from Grey-Level Histograms. *IEEE Transactions on Systems, Man, and Cybernetics* **9**, 62 – 66, 1979. Minimize inter class variance.

[38] Jiao, S., Li, X., Lu, X. An Improved Ostu Method for Image Segmentation. In *Signal Processing, 2006 8th International Conference on*, vol. 2, –. 2006.

[39] Weiwad, W. K. K., Linke, W. A., Wussling, M. H. P. Sarcomere Length-tension Relationship of Rat Cardiac Myocytes at Lengths Greater than Optimum. *Journal of Molecular and Cellular Cardiology* **32**, 247–259, 2000.

[40] Tolic-Norrelykke, I. M., Butler, J. P., Chen, J., Wang, N. Spatial and temporal traction response in human airway smooth muscle cells. *Am J Physiol Cell Physiol* **283**, C1254–C1266, 2002.

[41] Knauss, W. G., Zhu, W. Nonlinearly viscoelastic behavior of polycarbonate. II. The role of volumetric strain. *Mechanics Of Time-Dependent Materials* **6**, 301–322, 2002.

[42] Borcherdt, R. D. Volumetric strain in relation to particle displacements for body and surface waves in a general viscoelastic half-space. *Geophysical Journal International* **93**, 215–228, 1988.

[43] Campbell, K. B., Simpson, A. M., Campbell, S. G., Granzier, H. L., Slinker, B. K. Dynamic left ventricular elastance: a model for integrating cardiac muscle contraction into ventricular pressure-volume relationships. *J Appl Physiol* **104**, 958–975, 2008.

[44] Wussling, M., Mair, T. Calcium waves in rat cardiac myocytes underlie the principles of self-organization in excitable media, 1999.

[45] Cheng, H., Lederer, M. R., Lederer, W. J., Cannell, M. B. Calcium sparks and [Ca2+](i) waves in cardiac myocytes. *American Journal Of Physiology-Cell Physiology* **39**, C148–C159, 1996.

[46] Wussling, M. H. P., Krannich, K., Scheufler, K., Schmerling, S. Velocity dispersion of spontaneous calcium waves in rat cardiac myocytes. *Biophysical Journal* **74**, A272–A272, 1998.

[47] Lamont, C., Luther, P. W., Balke, C. W., Wier, W. G. Intercellular Ca2+ waves in rat heart muscle. *J Physiol* **512**, 669–676, 1998.

[48] Pustoc'h, A., Ohayon, J., Usson, Y., Kamgoue, A., Tracqui, P. An integrative model of the self-sustained oscillating contractions of cardiac myocytes. *Acta Biotheoretica* **53**, 277–293, 2005.

[49] Miura, M., Boyden, P. A., Keurs, H. E. D. J. t. Ca2+ Waves During Triggered Propagated Contractions in Intact Trabeculae : Determinants of the Velocity of Propagation. *Circ Res* **84**, 1459–1468, 1999.

[50] Schneider, F., Fellner, T., Wilde, J., Wallrabe, U. Mechanical properties of silicones for MEMS. *Journal Of Micromechanics And Microengineering* **18**, 065008, 2008.

CHAPTER VI

CRYOGENIC ETCHING OF SILICON: AN ALTERNATIVE METHOD FOR FABRICATION OF VERTICAL MICROCANTILEVER MASTER MOLDS

Kweku A. Addae-Mensah,[1,2] Scott Retterer,[5]Darrell Thomas,[5] Nickolay V. Lavrik,[5] John P. Wikswo[1,2,3,4]

[1]Department of Biomedical Engineering

[2]Vanderbilt Institute for Integrative Biosystems Research and Education

[3]Department of Physics and Astronomy

[4]Department of Molecular Physiology and Biophysics

Vanderbilt University, Nashville, TN

[5]Center for Nanophase Materials Science, Oak Ridge National Laboratory, Oak Ridge, TN

Abstract

This paper examines the use of deep reactive ion etching (DRIE) of silicon to produce master molds for vertical microcantilever arrays using fluorine high-density plasmas at cryogenic temperatures. The resultant profiles achieved depend on the rate of deposition and etching of a SiO_xF_y polymer, which serves as a passivation layer on the sidewalls and the bottom of the etched structures in relation to areas that have not been passivated with the polymer. We look at how optimal tuning of two parameters, the O_2 flow rate and the capacitively coupled plasma (CCP) power, determine the etch profile. All other pertinent parameters are kept constant. We examine the etch profiles produced using e-beam resist as the main etch mask, with holes having diameters of 750 nm, 1 μm, and 2 μm.

Introduction

The use of plasma etching techniques for fabrication of devices in silicon has gained widespread use. The semiconductor and microelectronics industry has been the driving force behind this trend. More recently plasma etching has found widespread use in the microelectromechanical (MEMS) and biological micoelectromechanical (BioMEMS) industry. There are some differences between its use in the integrated circuit (IC) industry and the more recent MEMS and BioMEMS applications. Feature sizes are normally in the submicron region and are actually getting smaller for IC fabrication, while those for MEMS and BioMEMS are normally a few microns wide. On the other hand, while the etch depths are only a few microns in ICs, etch depths can reach a few hundred microns in MEMS and BioMEMS fabrication. Some of the requirements in reactive ion etching for MEMS and BioMEMS include generation of high aspect-ratio structures without sacrificing etch rate unduly, maintaining high selectivity of photoresist or etch mask relative to silicon and precise control of sidewall profile. In some applications a smooth surface (average roughness less than 200 nm) is required, as is the case for molds used for polymer hot embossing processes[1,2] or for microneedles used in drug delivery[3].

Anisotropic reactive ion etching involves the delicate balance between passivation of

the side-walls and etching of the bottom of the structures. The etch is mainly produced by bombardment of ions from the plasma discharge. Lærmer and Schilp[4] first developed this etch technique at Borsch. It is also commonly referred to as the "Borsch Process." This technique involves alternating etch and passivation steps in a continuous cycle to achieve the high aspect ratio structures. Both steps are done at room temperature. This technique was later co-developed and marketed by Surface Technology Systems plc(UK) and Alcatel Vacuum Technology (France) on their inductively coupled plasma (ICP) tools[5]. Some of the earliest products using this technology were surface micromachined devices such as the accelerometer for airbag deployment[6]. Another notable application is the fabrication of gyroscopes used in cars for stability control[7]. Typical etch rates are about 2 μm/min, though rates as high as 10 μm/min are achievable today[5,8].

An alternative technique was introduced by Tachi *et al.*[9] This involves etching substrates at cryogenic temperatures, also using fluorine-based high-density plasmas. The main chemical reactions that occur in reactive ion etching are those due to spontaneous etching and those due to ion-assisted reactions[9]. The spontaneous reactions which occur on both the sidewalls and the bottom account for the isotropic etch. To produce anisotropic etches the spontaneous reaction has to be slowed down considerably, and Tachi *et al* accomplished this by controlling the substrate temperature, the rationale for this being that cooler temperatures will reduce the reaction probability or the incident flux of radicals on the sidewalls. It must be noted that the original cryogenic technique described by Tachi *et al.* did not include the use of oxygen (O_2) in the plasma though its use had previously been reported by other labs[10].

Other researchers in this area[11–13] recognized this and combined the Tachi group's original technique with that of Zhang *et al.*[10] and were able to use the addition of O_2 as a very sensitive method for control of the anisotropic etch of silicon (Si). In SF_6/O_2 high-density plasma etching, the decomposition of SF_6 into free fluorine (F) radicals is responsible for the isotropic component of the etch cycle by formation of volatile components which include SiF_4[8,14,15]. Other decomposition by- products include ions like SF_5^+[8,14] which are able to etch SiO_xF_y (ion assisted etching) though this occurs mainly at the bottom of the

structures. Combining the two techniques to produce the desired etch profiles requires tuning of various parameters to achieve the right balance between etching of unpassivated silicon, sidewall passivation, and etch of the bottom of the structures. Even when the desired parameters are obtained they are not necessary applicable to all mask layouts and the process has to be tuned for each specific layout and final desired etch profile.

Vertical microcantilever arrays have been used to study cell mechanobiology and traction forces and provide a platform for investigating cellular biomechanics *in vitro*[16–21]. One advantage they provide over other traditional methods that use for example flexible continuous sheets is that deflections are independent of each other. The original techniques for making these vertical microcantilever arrays have involved using soft lithography on silicon wafers followed by double casting of polydimethylsiloxane (PDMS) to yield the final microcantilever arrays. The double casting results in the use of a secondary master mold for casting the final arrays. The motivation for pursuing the cryogenic etching approach is to overcome the limitations of the original soft lithography techniques that have previously been reported[16,18].

This paper looks at how the cryogenic etching technique is used to create master molds for vertical microcantilever arrays in silicon. We look at how two main parameters, the oxygen flow rate and the radio frequency (RF) excited capacitively coupled plasma power, affect the profile characteristics. The wafer temperature and other pertinent parameters *e.g*, SF_6 flow rate, are kept constant. Other labs[17,22] have reported the use of the Borsch process for making similar master molds in silicon. However, unless process parameters are carefully optimized, it appears that DRIE can produce scalloping on the sidewalls of the silicon master mold, making separation of the polydimethylsiloxane (PDMS) mold very difficult, if not impossible. Second, posts produced in this manner are not entirely cylindrical and therefore cannot be considered to behave like the simple cantilever beams. Indeed, another group has showed that such posts appear grossly "scalloped" under scanning electron microscopy and that their bending mechanics are significantly more complex than simple vertical cantilever beams[23]. Figure 6.1 shows this scalloping effect, which occurs primarily because the cycling of the etch and passivation steps do not occur at the

same time as compared to the cryogenic etch process. Both techniques require extensive fine tuning of etch parameters to obtain the desired sidewall profile. One advantage of the cryogenic etching technique over the Borsch process is that the etch parameters do not have to be as carefully optimized to obtain smooth sidewalls.

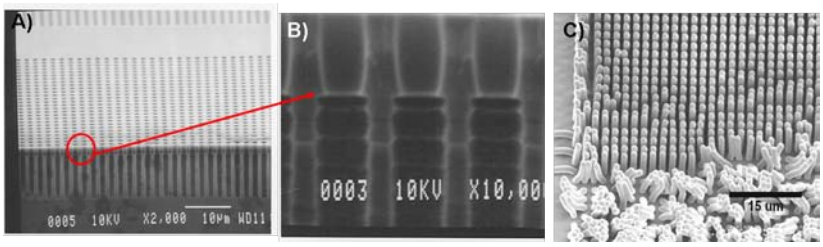

Figure 6.1 (A) Scanning electron micrograph (SEM) of silicon wafer with photoresist layer etched using the Borsch process. (B) Image at higher magnification showing scalloping. (C) PDMS cantilever post array peeled from one silicon master mold showing damage.

Materials and Methods

The circle patterns for the post arrays were originally designed using the free shareware computer-aided design (CAD) tool Layouteditor™. The design files were converted into a format compatible with a JEOL JBX-9300100 kV electron beam lithography system. Silicon wafers were spin coated with ZEP 520A electron beam resist at two spin speeds, 6000 revolutions per minute (rpm) and 2000 rpm, yielding two nominal thicknesses. The wafers were baked on a contact hotplate at 180°C for two minutes. The wafers were then loaded into a JEOL system and exposed. Designed patterns were arrays of circles with diameters of 750 nm, 1 μm, and 2 μm with edge-to-edge spacings of 1, 2 and 4 μm. Each array was designed to be approximately 2 mm^2. A typical four-inch wafer had 12 such individual arrays and the e-beam system took an average of eight hours to write 24 individual arrays. The exposed wafers were developed in xylenes for 40 seconds, rinsed in isopropyl alcohol (IPA) and dried under a stream of nitrogen. The four-inch wafers were either cleaved into four quarters or etched as full wafers. An Oxford 100 DRIE/RIE

system capable of Borsch process etching, cryogenic processing, and standard RIE dry etching of silicon, was used for the etch step. The wafers were maintained at -110°C in all cases. The SF_6 flow rate during the etch was maintained at 80 standard cubic centimeters per minute (sccm). The ICP power was maintained at 1250 W and the CCP and O_2 sccm rates were varied. For initial etch runs the wafers were cleaved and examined using a FEI Nova 600 scanning electron microscope/focused ion beam system to determine etch depth and profile. The photoresist thickness before and after the etch was determined using a Filmetrics F50 profilometer and a Horiba Jobin Yvon MM-16 ellipsometer. The e-beam resist was then stripped using acetone and the wafers were descummed in a plasma cleaner.

The silicon master molds were later oxidized in a plasma cleaner for 30 seconds, then silanized with (Tridecafluoro-1,1,2,2-tetrahyrooctyl)-1-trichlorosilane (United Chemical Technologies; Bristol, PA) under partial vacuum overnight. To test if the master molds could be used successfully to make the microcantilever arrays, liquid PDMS (10:1 ratio of monomer to curing agent mixed using the AR-1000 Thinky™ mixer) was poured on the surface of the silanized silicon master mold, degassed in a desiccator using a vacuum pump (Leybold™ Trivac D2.5E capable of achieving a vacuum pressure of 5×10^{-4} mbar), and cured at two different temperatures (65 and 110°C) for 20 hours. The cured elastomer was peeled from the PDMS mold to yield a vertical microcantilever array.

Results and Discussion

The primary concern regarding the etch process was to obtain smooth sidewalls to facilitate mold separation. Figure 6.2 shows an SEM image of an initial etch sample. The etch parameters were 14 sccm of O_2 with 30 W of CCP power. The etch time was one minute. As can be seen from this image, the scalloping that was evident from the Borsch process does not occur in this case. One factor that affects the etch rate in cryogenic etching is the amount of silicon load (etchable area) to be etched on the target wafer. In both cases where either a quarter of a four-inch or the whole wafer is etched, this load remained approximately the same for three separate 2 mm^2 or 12 separate 2 mm^2 arrays.

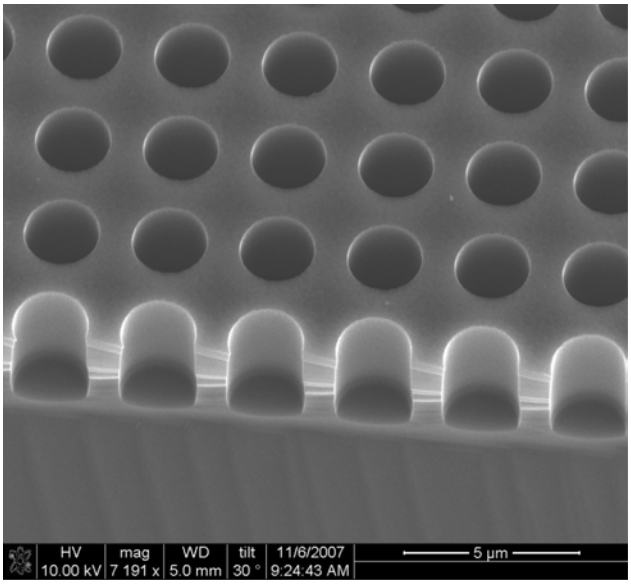

Figure 6.2 SEM image of a cleaved silicon wafer etched using the cryogenic etching technique. Notice the smoothness of the sidewalls. The scalloping which occurs during the Borsch process does not occur in this case.

In both cases the actual load was approximately 5%. Even though the silicon loads are approximately the same, there was still a noticeable variation in the etch rates between the three different diameters, with the smallest feature size showing the slowest etch rate. SEM images of a cleaved wafer showing this effect are shown in Figure 6.3. The parameters for this etch are 15 sccm of O_2 with 4 W CCP power and an etch time of two minutes and thirty seconds. The SEM images are taken with a tilt of 30°, resulting in a 50% foreshortening of the images so that the actual depth is twice that shown in the figure. Figure 6.3(A) and 6.3(B) show the profile for two different hole sizes with original design diameters of 750 nm and 1 μm. As can be seen from the measured depths of 1.68 μ (3.36 μm actual) and 2.03 μm (4.06 μm actual), respectively, the smaller feature size shows a slightly slower etch rate than the larger one.

The etch mask used in all cases was the ZEP 520A electron beam resist. The desired etch depth for the deepest etches was 8 μm, and thus a higher selectivity mask such as chromium was not required. The nominal thickness for the resist at two spin speeds of 6000 rpm and 2000 rpm was ~220 and ~374 nm respectively. Figure 6.4(A) shows a plot of nominal resist left against etch time for seven different etches. The thickness of the resist was measured using the Filmetrics F50 profilometer. In all cases the etch was

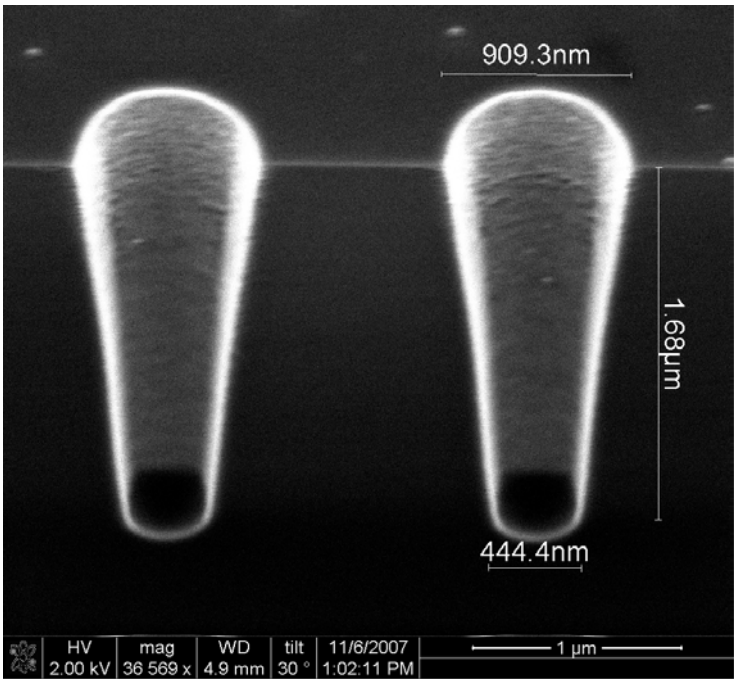

(A)

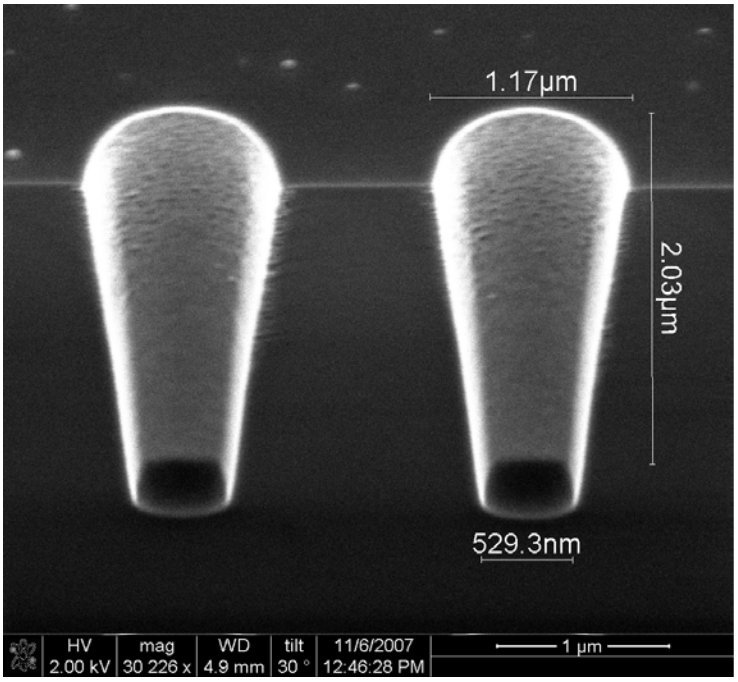

(B)

Figure 6.3 Difference in etch rate. (A) Etch profile showing depth of about 1.68 μm (3.36 μm actual depth corrected for viewing angle) for circular feature with original design diameter of 750 nm (B) Etch profile showing depth of about 2.03 μm (4.06 μm actual) for circular feature with original design diameter of 1 μm.

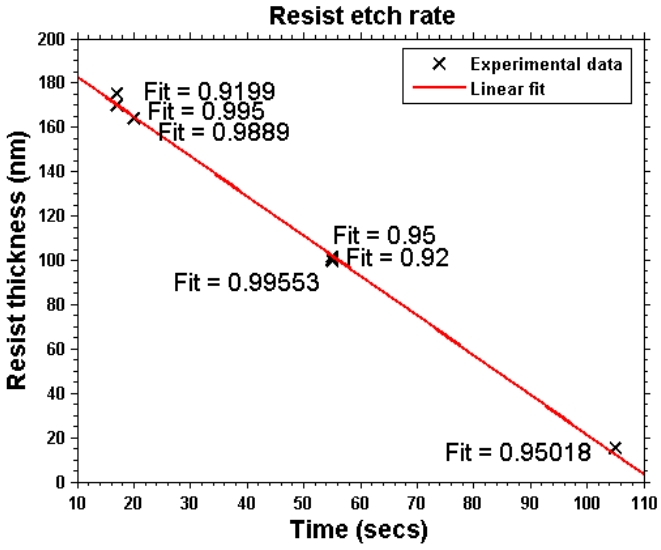

(A)

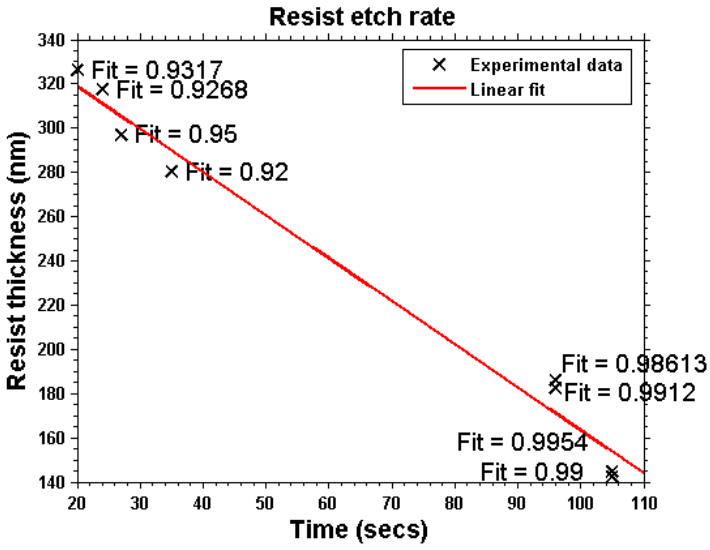

(B)

Figure 6.4 E-beam resist etch rates. (A) Resist etch rate for wafers spun with e-beam resist at speed of 6000 rpm. (B) Resist etch rate for wafers spun with e-beam resist at speed of 2000 rpm.

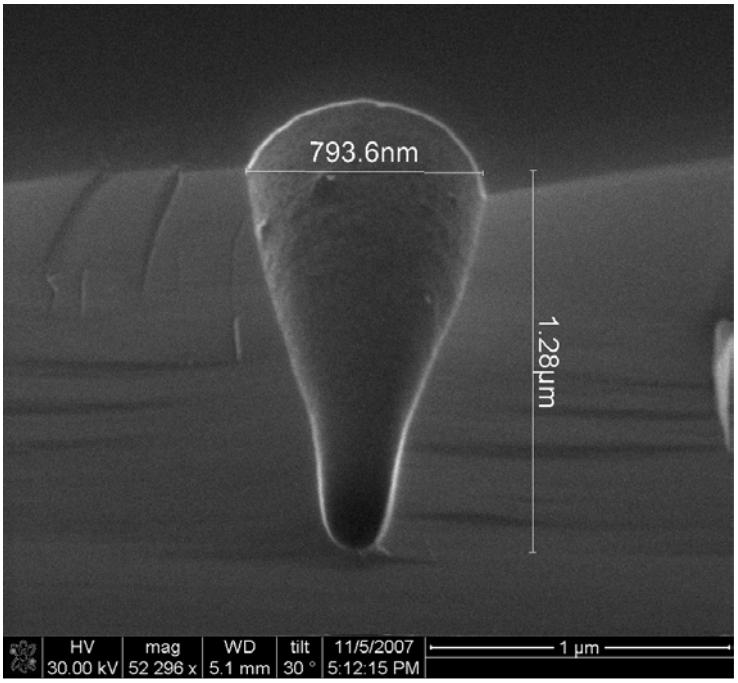

(A)

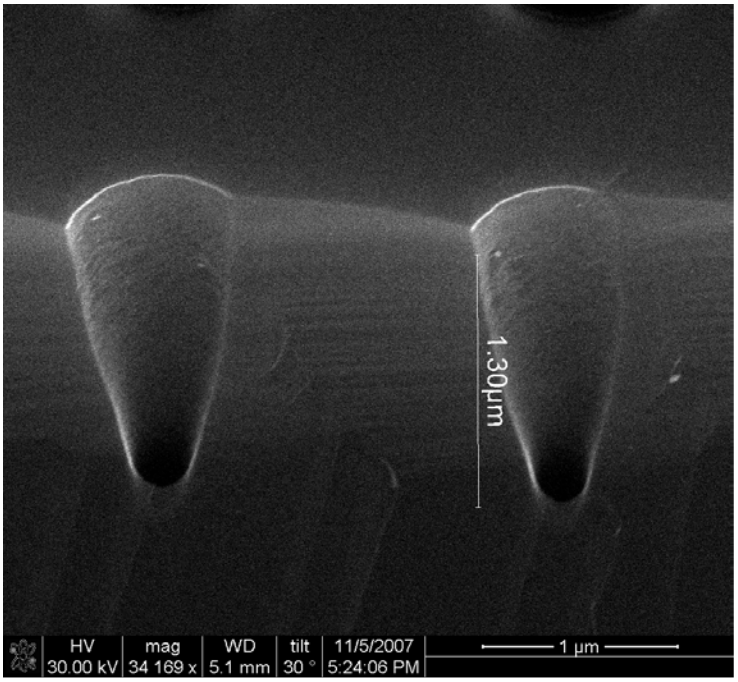

(B)

Figure 6.5 Initial test run. (A) Etch profile showing depth of about 1.28 μm (2.36 μm actual) for circular feature with original design diameter of 750 nm (B) Etch profile showing depth of about 1.30 μm (2.60 μm actual) for circular feature with original design diameter of 1 μm.

done with the following parameters: CCP power of 10 W, and 13 sccm of O_2, for wafers with initial resist thickness of ~220 nm (6000 rpm). Figure 6.4(B) shows a plot for the wafers with initial resist thickness of ~374 nm (2000 rpm). The goodness of fit when each measurement was taken is also included in the plots. A linear fit to the data is also plotted in the two figures. The slope for the case with a spin speed of 6000 is 1.79. This represents an approximate etch rate of 1.79 nm/sec. The slope for the case with a spin speed of 2000 is 1.94, representing an etch rate of 1.94 nm/sec, in close agreement with that for the spin speed of 6000. When we used an etch rate determined for these settings to be about 2.3 μm/min the selectivity of the silicon relative to the resist was about 20:1.

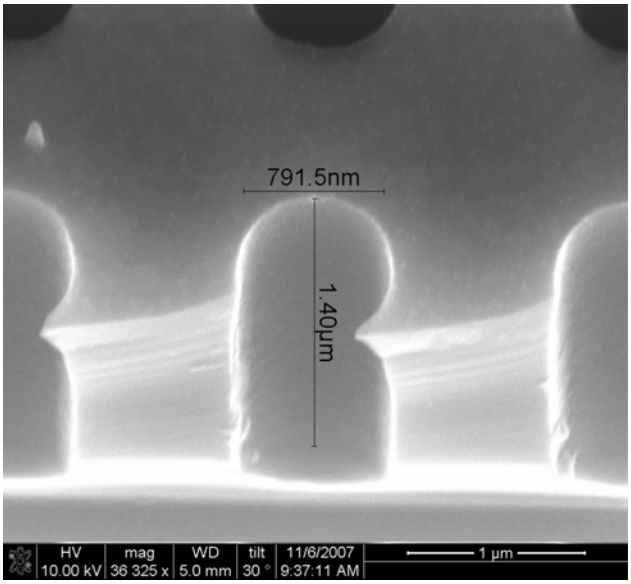

Figure 6.6 The effect of increasing the CCP power from 4 W to 30 W at 14 sccm of O_2. This changes the profile from a positive to almost straight sidewalls. The cusp on the right edges is due to the angle of the cleavage plane for the wafer. The left edges show best the sidewall profile.

The next most critical factor after smoothness of the sidewalls, was the sidewall profile itself. The target was to minimize either positive or negative taper and to produce almost vertical sidewalls. The start position for test runs was a one-minute etch using 14 sccm of O_2 and 4 W of CCP power. Figure 6.5(A) and 6.5(B) show SEM images of the profiles obtained for these parameters. As can be seen, there was a significant positive taper and an acute narrowing at the end of the etch for the 750 nm. The etch rate for these settings was

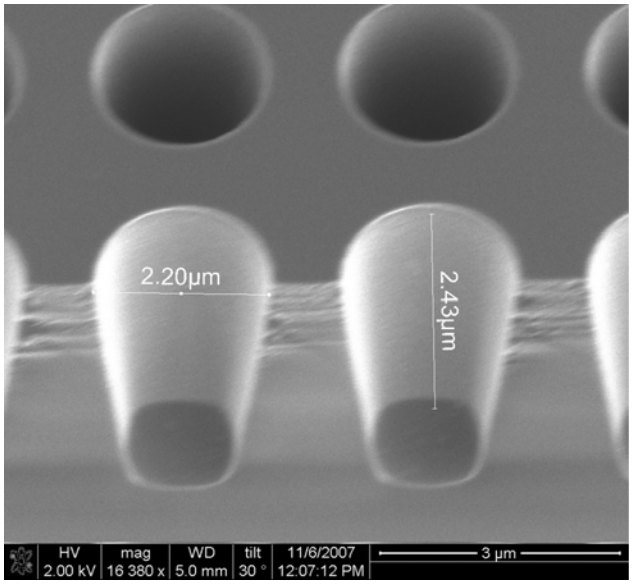

Figure 6.7 At 4 W of CCP power with 15 sccm of O_2 the positive taper is not as pronounced after a two minute etch although the ideal vertical sidewall profile is not achieved.

about 2.6 μm/min.

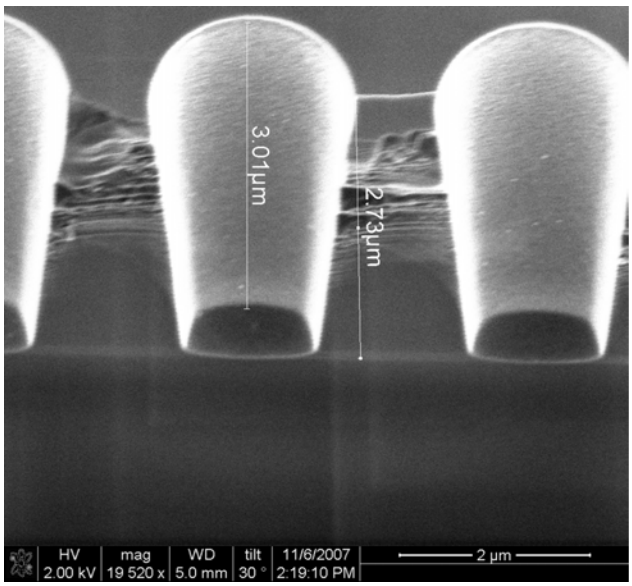

Figure 6.8 At 4 W of CCP power with 14 sccm of O_2 the positive taper improves slightly over that of 4 W at 15 sccm.

Increasing the CCP power to 30 W and keeping all the other etch parameters the same (14 sccm of O_2) produced almost vertical sidewalls; however, the etch rate increased for the resist. Hence the selectivity was reduced considerably, and with these settings it would

not be possible to reach some of the target etch depths. Figure 6.6 shows an SEM image of the result for an etch using these etch parameters.

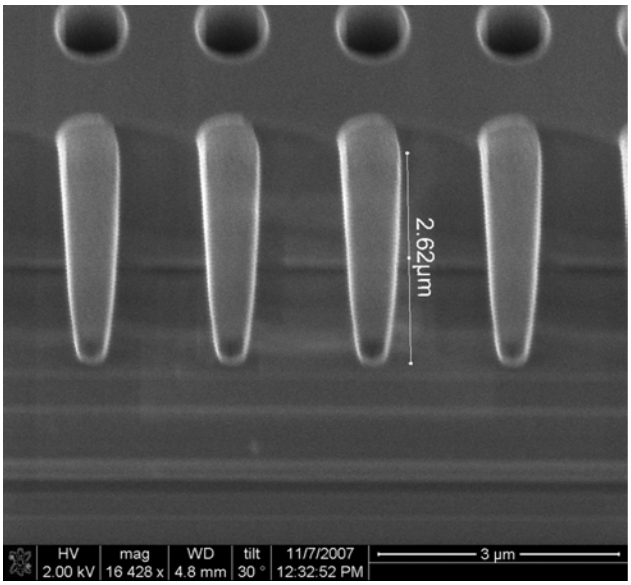

Figure 6.9 At 4 W of CCP power with 13 sccm of O_2 the positive taper is not as pronounced after a three minute etch. There is a noticeable taper at the bottom of the etch.

The 30 W CCP power was obviously suitable if our target maximum etch depth was less than about 5 μm. Etching with 4 W of CCP power with 15 sccm of O_2 produced a much better result. There is still a noticeable positive taper, as can be seen in the SEM image in Figure 6.7. The time for the etch was two minutes. Reducing the O_2 flow rate from 15 sccm to 14 sccm and using 4 W of CCP power did not produce a significant change, as can be seen in Figure 6.8. The etch time was also two minutes in this case. De Boer *et al.*[8] showed in their trend diagrams and tables that increasing the O_2 sccm while keeping the CCP power constant would shift the sidewall profile from negative to positive. We thus reduced the O_2 sccm further down to 13 sccm and kept the power at 4 W. However, we etched for three minutes instead of two. As predicted, the positive taper was reduced however, there was a noticeable taper at the bottom of the etch (Figure 6.9). Another general trend in cryogenic etching of silicon is the change towards a more isotropic profile when the CCP power is increased while the SF_6 and O_2 rates are kept constant.

Our final trial used 13 sccm of O_2 but the CCP power was increased from 4 W to 10

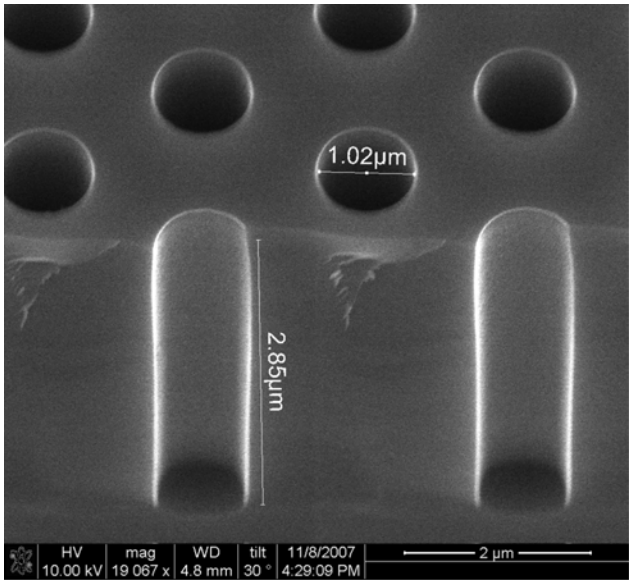

Figure 6.10 At 10 W of CCP power with 13 sccm of O_2 the sidewall profile becomes almost vertical. This is for a two minute thirty second etch.

W. The wafer was etched for two minutes and thirty seconds. Figure 6.10 shows an SEM image of the etch profile that was obtained for this etch. As can be seen, the sidewalls are effectively vertical. The resist (nominal 220 nm for spin speed of 6000 rpm) was totally etched in this case.

Due to the long exposure times required by the e-beam lithographic system, we attempted fabrication using a contact mask aligner with broadband (I-line) wavelength. A vacuum was applied between the mask and the wafer during the exposure. Even in this mode, it was difficult to produce the 750 nm features reliably and there were slight defects in the 1 μm features. The 2 μm features were much better but were not comparable to those produced by e-beam, as can be seen in Figure 6.11(A) and 6.11(B). The resist used in this case was SPR 955CM. Figure 6.12(A) and 6.12(B) show SEM images of etches produced from samples of these molds. The etch parameters were 13 sccm of O_2 with 10 W of CCP power for three minutes. The slight difference in etch rate due to feature size is again evident here.

The PDMS devices that were cast on the silicon master molds were much easier to separate than the ones that had been etched using the Borsch process. We initially assumed that if the molds did not have at least some degree of positive taper, it would not be possible to separate the cured PDMS from the silicon molds even after the salinization process.

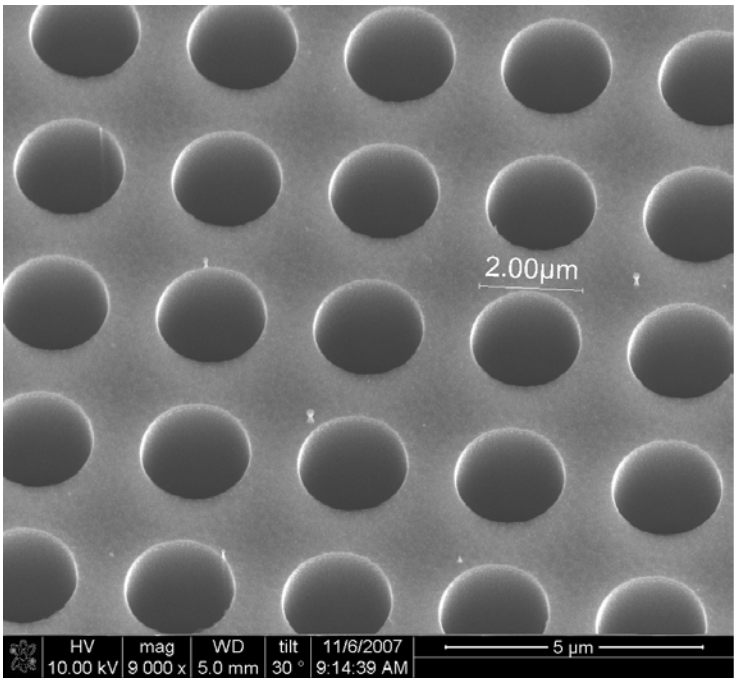

(A)

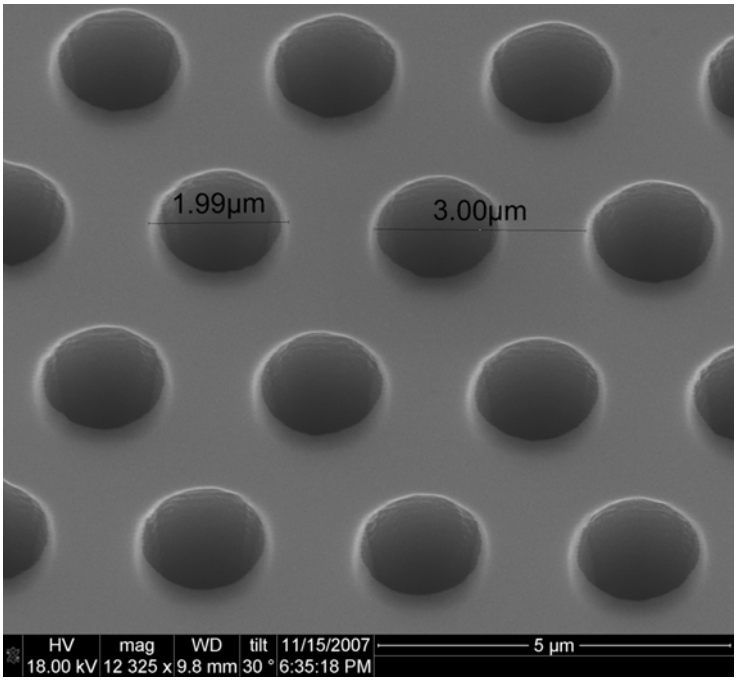

(B)

Figure 6.11 E-beam and contact lithography. (A) SEM showing smooth edges from e-beam lithography (B) SEM showing slightly rough and deformed edges from contact lithography

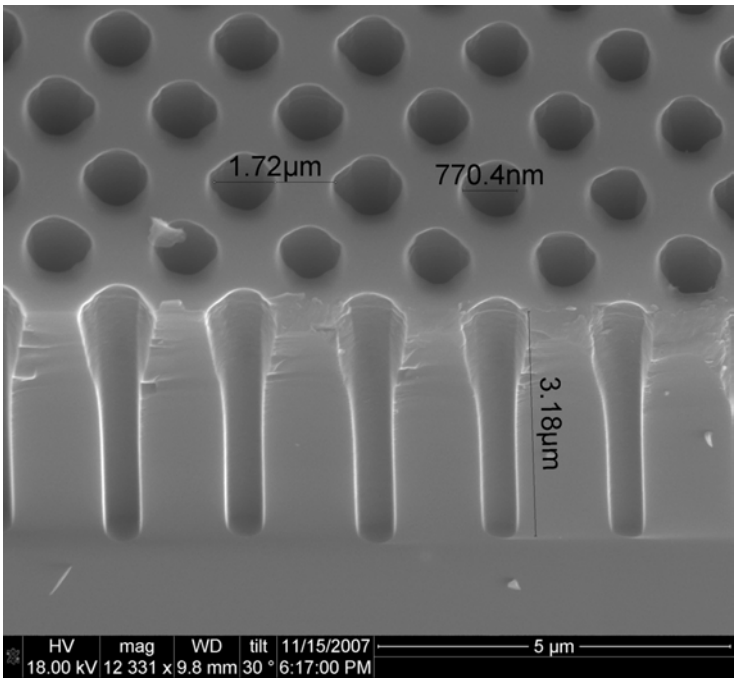

(A)

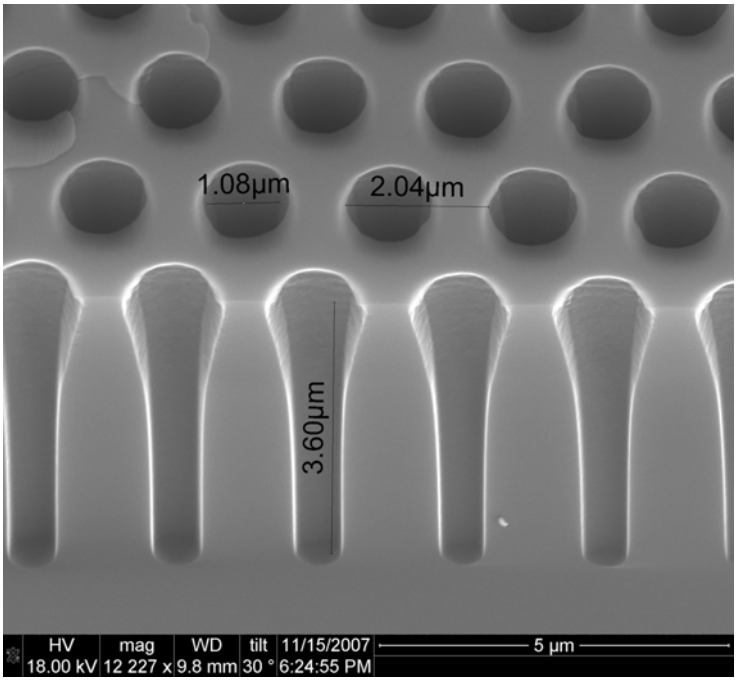

(B)

Figure 6.12 Etch profiles from contact lithography. (A) Etch profile showing depth of about 1.68 μm (3.36 μm actual) for circular feature with original design diameter of 750 nm (B) Etch profile showing depth of about 2.03μm (4.06 μm actual) for circular feature with original design diameter of 1 μm

Initial trials used molds which had taper (etches with parameters of 14 sccm of O_2, 4 W CCP, and etch time of two minutes thirty seconds) and those with the vertical sidewalls (etches with parameters of 13 sccm of O_2, 10 W CCP, and etch time of two minutes, thirty seconds). That assumption proved to be unwarranted. In both cases, the cured PDMS came off relatively easily.

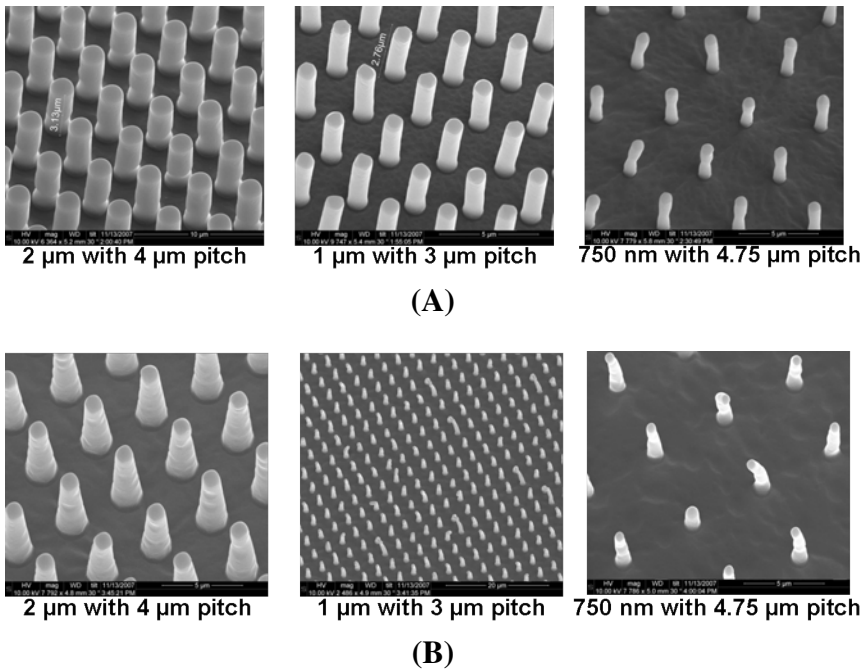

Figure 6.13 PDMS molding results. (A) PDMS microcantilevers from vertical sidewall molds. (B) PDMS microcantilevers from tapered sidewalls. As can be seen the 750 nm tapered ones show more damage than the straight sidewall ones. Devices were cured at 65°C in this case.

Figure 6.13(A) and 6.13(B) show SEM images of PDMS microcantilevers from the silicon master molds. As can be seen, it was possible to obtain microcantilevers with various dimensions for both the positive sidewall silicon molds and the straight sidewall molds. The microcantilevers do show some defects which are especially pronounced in the 750 nm devices. The more pronounced defects in the 750 nm example occur because at this dimension the PDMS polymer is unable replicate the molds precisely. Another plausible explanation is that nanoscopic to microscopic air bubbles could have been trapped in the holes. What was most surprising was the fact that the 750 nm feature size with the positive side taper seemed to show more damage than its straight sidewall counterpart. It

is currently not clear why this happened.

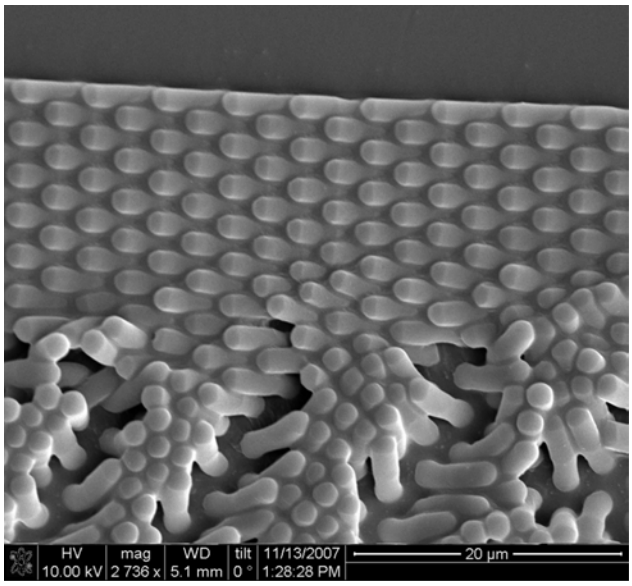

Figure 6.14 Damage and stiction from some molds. Damage observed with the closest spaced microcantilevers when the molds are separated. This effect is not noticeable at higher pitches. Device was cured at 65°C in this case.

The other more interesting fact was that the microcantilevers which had the closest pitches (~2 μm center-to-center or ~1 μm edge-to-edge) seemed to clamp together just as in the case of the microcantilevers from the Borsch process silicon molds. Thus, though the cryogenic etching had solved the problem of the ease of separation of the mold, it did not entirely solve the damage to the separated PDMS microcantilevers, which had also been observed in the Borsch process case as shown in Figure 6.14. This effect may be due to electrostatic charges that build on the surfaces of the PDMS during separation that causes the attractive forces. Another explanation could be the stiction-friction problem that has been reported by others[24,25].

As mentioned in our Materials and Methods section we cured the PDMS at two different temperatures. The cure temperature of 65°C had been successfully used in previous trials for the two steps of the soft lithography process[18]. Tan *et al.*[16] however, used two different temperatures for the two different steps 65°C and 110°C. Our first attempts at molding PDMS from the silicon master were done at 65°C. Subsequent trials using 110°C seemed to solve the problem of the microcantilevers sticking to each other after mold separation. It

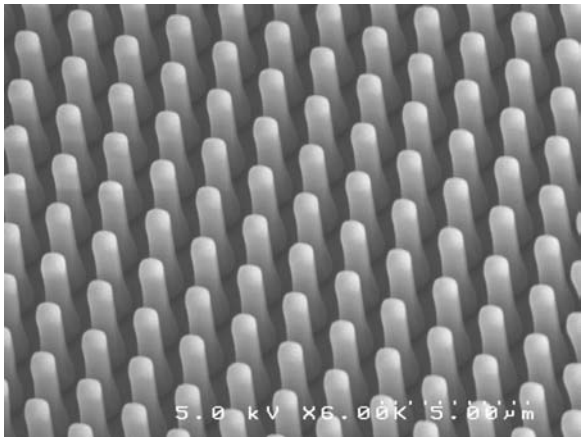

(A)

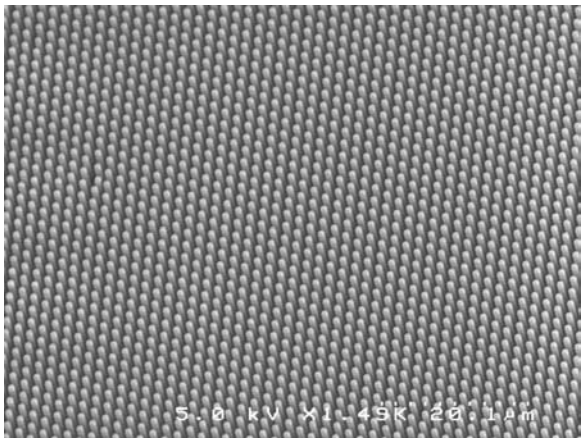

(B)

Figure 6.15 PDMS molding results at. 110°C (A) PDMS microcantilevers from almost vertical sidewall molds with diameters of 1 μm edge-to-edge spacing of 1 μm and about 5 μm tall. (B) The same microcantilevers at a lower magnification

must be mentioned that the PDMS was separated from the silicon mold immediately after removal from the curing ovens without allowing them to cool to room temperature. There was significantly less damage in this case. Figure 6.15(A) and 6.15(B) show SEM images of microcantilevers that are about 1μm in diameter with 1 μm edge-to-edge spacing and about 5 μm tall. It is still not clear why these procedures were effective.

Conclusion

We have been able to show that cryogenic etching of silicon at -110°C can be used as an alternative method to make master molds for making vertical microcantilever arrays. This requires fine tuning of etch parameters to obtain the desired sidewall profile. Curing

the PDMS mold at 110°C seems to alleviate certain defects that could possibly be due to the stiction-friction problem that occurs in soft lithographic microfabrication.

Acknowledgements

This work was supported by the Vanderbilt Institute for Integrative Biosystems Research and Education (VIIBRE), the Whitaker Foundation, the NIH (R01 HLO68144) and the Center for Nanophase Material Science (CNMS) (CNMS2007-230) at Oak Ridge National Laboratory (ORNL).

References

[1] Zhao, Y. J., Cui, T. H. Fabrication of high-aspect-ratio polymer-based electrostatic comb drives using the hot embossing technique. *Journal Of Micromechanics And Microengineering* **13**, 430–435, 2003.

[2] Elders, J., Elders, J., Jansen, H., Elwenspoek, M., Ehrfeld, W. DEEMO: a new technology for the fabrication of microstructures. In Jansen, H. (ed.) *Micro Electro Mechanical Systems, 1995, MEMS '95, Proceedings. IEEE*, 238–. 1995.

[3] Ji, J., Tay, F. E. H., Miao, J. M., Iliescu, C. Microfabricated microneedle with porous tip for drug delivery. *Journal Of Micromechanics And Microengineering* **16**, 958–964, 2006.

[4] Laermer, F., Schilp, A. Method of anisotropically etching silicon. German Pat., DE 4 241 045 granted on 26 May 1994 (US Pat. 5 501 893 granted on 26 March 1996).

[5] Laermer, F., Urban, A. Challenges, developments and applications of silicon deep reactive ion etching. *Microelectronic Engineering* **67-68**, 349–355, 2003.

[6] Offenberg, M., Offenberg, M., Larmer, F., Elsner, B., Munzel, H., Riethmuller, W. Novel Process For A Monolithic Integrated Accelerometer. In Larmer, F. (ed.) *Solid-State Sensors and Actuators, 1995 and Eurosensors IX. Transducers '95. The 8th International Conference on*, vol. 1, 589–592. 1995.

[7] Lutz, M., *et al.* A precision yaw rate sensor in silicon micromachining. In Golderer, W. (ed.) *Solid State Sensors and Actuators, 1997. TRANSDUCERS '97 Chicago., 1997 International Conference on*, vol. 2, 847–850 vol.2. 1997.

[8] de Boer, M., *et al.* Guidelines for etching silicon MEMS structures using fluorine high-density plasmas at cryogenic temperatures. *Microelectromechanical Systems, Journal of* **11**, 385–401, 2002.

[9] Tachi, S., Tsujimoto, K., Okudaira, S. Low-temperature reactive ion etching and microwave plasma etching of silicon. *Appl. Phys. Lett.* **52**, 616–618, 1988.

[10] Zhang, M., Li, J. Z., Adesida, I., Wolf, E. D. Reactive Ion Etching For Sub-Micron Structures Of Refractory-Metal Silicides And Polycides. *Journal Of Vacuum Science & Technology B* **1**, 1037–1042, 1983.

[11] Francou, M., Danel, J. S., Peccoud, L. Deep And Fast Plasma-Etching For Silicon Micromachining. *Sensors And Actuators A-Physical* **46**, 17–21, 1995.

[12] Bartha, J. W., Greschner, J., Puech, M., Maquin, P. Low-Temperature Etching Of Si In High-Density Plasma Using Sf6/O-2. *Microelectronic Engineering* **27**, 453–456, 1995.

[13] Zijlstra, T., van der Drift, E., de Dood, M. J. A., Snoeks, E., Polman, A. Fabrication of two-dimensional photonic crystal waveguides for 1.5 mu m in silicon by deep anisotropic dry etching. *Journal Of Vacuum Science & Technology B* **17**, 2734–2739, 1999.

[14] Dagostino, R., Flamm, D. L. Plasma-Etching Of Si And Sio2 In Sf6-O2 Mixtures. *Journal Of Applied Physics* **52**, 162–167, 1981.

[15] Flamm, D. L. Mechanisms Of Silicon Etching In Fluorine-Containing And Chlorine-Containing Plasmas. *Pure And Applied Chemistry* **62**, 1709–1720, 1990.

[16] Tan, J., Tien, J., Pirone, D., Gray, D., Bhadriraju, K., Chen, C. Cells lying on a bed of microneedles: An approach to isolate mechanical force. *PNAS* **100**, 1484–1489, 2003.

[17] du Roure, O., *et al.* Force mapping in epithelial cell migration. *PNAS* **102**, 2390–2395, 2005.

[18] Addae-Mensah, K. A., *et al.* A flexible, quantum dot-labeled cantilever post array for studying cellular microforces. *Sensors and Actuators A: Physical* **136**, 385–397, 2007.

[19] Addae-Mensah, K. A., Reiserer, R. S., Wikswo, J. P. Poly(vinyl alcohol) as a structure release layer for the microfabrication of polymer composite structures. *Journal of Micromechanics and Microengineering* **17**, N41–N46, 2007.

[20] Sniadecki, N. J., *et al.* From the Cover: Magnetic microposts as an approach to apply forces to living cells. *Proc Natl Acad Sci* **104**, 14553–14558, 2007.

[21] Addae-Mensah, K. A., Wikswo, J. P. Measurement Techniques for Cellular Biomechanics In Vitro. *Experimental Biology and Medicine* **233**, 792–809, 2008.

[22] Roure, O. d., *et al.* Microfabricated arrays of elastomeric posts to study cellular mechanics. *Proc.SPIE* **5345**, 26–34, 2004.

[23] Zhao, Y., Zhang, X. Cellular mechanics study in cardiac myocytes using PDMS pillars array. *Sensors and Actuators A: Physical* **125**, 398–404, 2006.

[24] Wu, D., Fang, N., Sun, C., Zhang, X. Stiction problems in releasing of 3D microstructures and its solution. *Sensors and Actuators A: Physical* **128**, 109–115, 2006.

[25] Srinivasan, U., Srinivasan, U., Houston, M., Howe, R., Maboudian, R. Alkyltrichlorosilane-based self-assembled monolayer films for stiction reduction in silicon micromachines. *Microelectromechanical Systems, Journal of* **7**, 252–260, 1998.

CHAPTER VII

MESENCHYMAL STEM CELL RESPONSES TO MICROCANTILEVER ARRAYS OF DIFFERENT STIFFNESSES

Kweku A. Addae-Mensah,[1,2] Susan R. Opalenik,[2,3] John P. Wikswo[1,2,4,5]

[1]Department of Biomedical Engineering

[2]Vanderbilt Institute for Integrative Biosystems Research and Education

[3]Department of Pathology

[4]Department of Physics and Astronomy

[5]Department of Molecular Physiology and Biophysics

Vanderbilt University, Nashville, TN

Abstract

Cryogenic etching of silicon produced master molds which are used for casting microcantilever arrays with three different spatial densities and two different heights. We then examine whether these six different geometries potentiate the differentiation of mesenchymal stem cells (MSC) of the (C57Bl/6-TgN (ACTbECGF)10sb) cell line. We find that in cases where cells are cultured in osteogenic differentiation media, monolayers of cells were formed that show a marked difference in adhesion based on the spatial densities of the arrays. Microcantilevers with 1 μm edge-to-edge spacing have the most intact monolayers while those with 4 μm have the least. We use image processing techniques to analyze Oil Red O stains of cells cultured in adipogenic medium. Cells cultured on microcantilevers that were 2 μm tall showed areas with fat droplets that were on average much larger than those for microcantilevers cultured in the same adipogenic medium but on microcantilevers 5 μm tall. A tally of the average for total counts of the areas identified as droplets were about the same in both cases. We conclude that this line of MSC's exhibits differences in growth and differentiation that depend upon substrate structure and stiffness.

Introduction

Progenitor cells are found in many different places in the human body. These cells are capable of self renewal. The resulting daughter cells have varying degrees of developmental potential, with some having the ability to differentiate into specific cell types with certain specialized functions. Examples of these progenitor cells, also commonly referred to as stem cells, include the totipotent zygote[1], embryonic stem cells (ESC)[2,3], hematopoietic stem cells (HSC)[4,5], mesenchymal stem cells (MSC)[6–9] and neural stem cells[10]. Based on the degree of developmental potential, these types of stem cells can be classified as either totipotent, pluripotent, multipotent, or monopotent[11].

Evidence for the possible existence of nonhematopoietic stem cells in bone marrow was initially suggested in the 19th century by the German pathologist Cohnheim in experiments he conducted for studying wound healing and repair. His work raised the possibility that

bone marrow may be the source of fibroblasts that deposit collagen fibers as part of the normal process of wound repair[12]. Today, these nonhematopoietic stem-like cells are referred to as mesenchymal stem cells (MSC) because they are able to differentiate into cells and eventually form tissue that can be classified as mesenchymal in nature. They are also sometimes referred to as marrow stromal cells and have been found in a variety of tissues during development. In adults they are prevalent in the bone marrow and contribute to regeneration of mesenchymal tissues such as bone, cartilage, muscle, ligament, tendon adipose, and stroma[7]. Figure 7.1 outlines the mesengenic process.

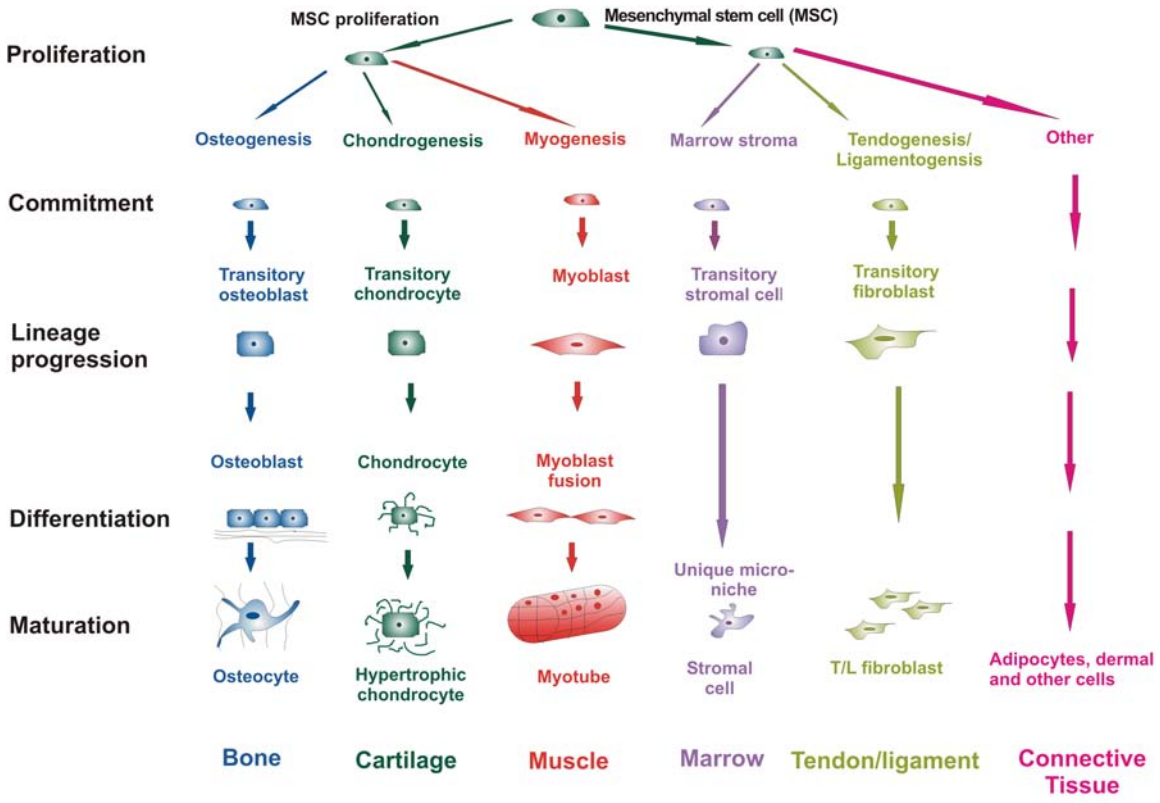

Figure 7.1 The mesengenic process. The cellular transitions from the putative mesenchymal stem cell (MSC) to highly differentiated phenotypes are depicted schematically. This is a simplification, not a complete representation of all of the complex processes, transitions and possible interrelationships of cells moving between pathways, now commonly referred to as plasticity. Image adapted from Caplan *et al.*[9]

It has now been demonstrated that mesenchymal stem cells (MSC) can be expanded *in vitro* over a billion-fold and have been shown to differentiate into cells representing the

three germ layers[6,9,13,14]. *In vitro* studies thus provide a means by which to characterize MSCs and their response to various conditions.

The inductive agents that cause entrance into a particular lineage of mesenchymal stem cells (MSCs) leading to eventual formation of a specific tissue/cell type are normally provided by the niche to which they attach after circulation from their site of origin. These external signals include factors secreted by other cell types, cell-cell interactions, as well as cell-extracellular matrix interactions[8]. The extracellular matrix elasticity has also been shown to have an effect on lineage specification. One *in vitro* study has shown that soft matrices (Shear modulus 0.1 - 1 KPa) that mimic the brain lead to neurogenic cell types; stiffer matrices (10 - 20 KPa) that mimic muscle tend to be myogenic; and the stiffest (< 25 KPa), that mimic collagenous bone, are osteogenic[15]. This study used inert polyacrylamide gels to mimic differing matrix elasticity by modifying concentrations of the individual components used to make the gel, thereby producing various cross-linked densities of the polymer. However, this invariably leads to an alteration of the surface chemistry and could affect cell-surface interaction.

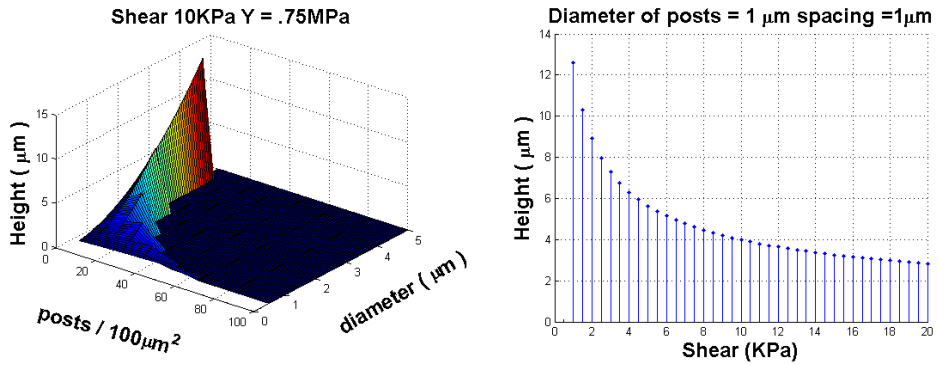

Figure 7.2 Design parameters. (A) Design parameters showing variation of height and diameter with spatial density of arrays for a particular shear stiffness. (B) Variation of height with shear stiffness at a spatial density of 1 μm edge-to-edge spacing

In this study, we examined whether microcantilever arrays designed to have different effective shear stiffness would potentiate differentiation of MSCs into adipogenic and osteogenic pathways in culture medium with reagents designed to elicit these responses

for cells normally cultured on flat plastic culture plates. The arrays consist of individual microcantilevers arranged in three distinct spatial densities and have two different heights thus providing six different surfaces for attachment. We postulate that the arrays with greater effective shear stiffness will potentiate or drive cells farther down the osteogenic pathway while arrays with less shear stiffness will drive cells farther down the adipogenic pathway. An example of the initial design parameters that were used is shown in Figure 7.2. The final designs consisted of arrays of three spatial densities (edge-to-edge spacings of 1, 2 and 4 μm with two distinct heights of 2 μm and 5 μm representing approximate average shear stiffness between 5 and 15 KPa based on our calculations.

Materials and Methods

Design of microcantilever arrays

PDMS is known to have an elastic modulus that is dependent on elastomer base to crosslinker ratio[16–18]. The microcantilever arrays that were used for our experiments were made from PDMS with a 10:1 elastomer to curing agent ratio. However, even for this mix ratio, several values have been reported in the literature for the measured elastic modulus ranging from as low 0.50 MPa to as high as 3.6 MPa[16–19]. For designing the microcantilever arrays, we assumed a value of 0.75 MPa - 1.0 MPa as the elastic modulus. Average shear modulus values from 1 KPa to 20 KPa were used representing, the range of values that had been reported in the literature to have an effect on lineage specification[15]. Spatial densities (Number of microcantilevers per 100 μm^2) were from 1 to 100. Microcantilever diameters ranging from 0.5 - 5 μm were used in our initial design calculations. Depending on the diameter of microcantilevers, certain spatial densities were not possible and these were excluded. Values of 750 nm, 1 and 2 μm for diameters were chosen during the final fabrication process based on results from prior trials. Maximum deflections for individual microcantilevers were assumed to be the edge-to-edge spacing for a particular spatial density. Using these values the corresponding range of heights were calculated using Equation 7.1 where E is the elastic modulus of PDMS, N is the number of microcantilevers

per square area, G is the average shear modulus and δ is the deflection.

$$H = \sqrt[3]{\left(\frac{3}{4}\pi E \frac{N}{100^{-12}} \frac{r^4}{G}\delta\right)} \tag{7.1}$$

Fabrication of microcantilever arrays

The microcantilever arrays were fabricated using a combination of electron beam (e-beam) lithography, cryogenic etching, and molding using polydimethylsiloxane (PDMS). The patterns were originally designed using the free shareware CAD tool Layouteditor™. The design files were converted into a format compatible with a JEOL JBX-9300100 kV electron beam lithography system. Silicon wafers were spin coated with ZEP 520A electron beam resist at two spin speeds 6000 revolutions per minute (rpm) and 2000 rpm yielding two nominal thicknesses. The wafers were baked on a contact hotplate at 180°C for two minutes. The wafers were then loaded into the JEOL system and exposed. Designed patterns were arrays of circles with diameters of 750 nm, 1 μm and 2 μm with edge-to-edge spacings of 1, 2 and 4 μm. Each array was designed to be approximately (2 mm)^2. A typical four inch wafer had 12 of such individual arrays and it took the e-beam system an average of eight hours to write 24 individual arrays. The exposed wafers were developed in xylenes for 40 seconds, rinsed in isopropyl alcohol (IPA) and dried under a stream of nitrogen. The four-inch wafers were either cleaved into four quarters or etched as full wafers. An Oxford 100 DRIE/RIE system capable of Borsch process etching, cryogenic processing, and standard RIE dry etching of silicon was used for the etch step. The wafers were maintained at -110°C in all cases. The SF_6 flow rate during the etch was maintained at 80 standard cubic centimeters per minute (sccm). The inductively coupled power (ICP) power was maintained at 1250 W and the capacitively coupled power (CCP) and O_2 sccm rates were varied. Additional details regarding the optimization of the etch process are provided elsewhere (chapter 6)

The silicon master molds were later oxidized in a plasma cleaner for 30 seconds, then silanized with (Tridecafluoro-1,1,2,2-tetrahydrooctyl)-1-trichlorosilane (United Chemical Technologies; Bristol, PA) under partial vacuum overnight. To test if the master molds

could be used successfully to make the microcantilever arrays, liquid PDMS was poured on the surface of the silanized silicon master mold, degassed, and cured at two different temperatures (65 and 110°C) for 20 hours. The cured elastomer was peeled from the PDMS mold to yield a vertical microcantilever array. Average thickness of the elastomer was 1 mm.

Cell culture and reagents

Culture wells in PDMS were made from punching blocks of PDMS with a 4 mm X 4 mm square punch. Prior to seeding the microcantilevers were pre-treated with normal culture medium overnight. These wells were placed over each individual array and mesenchymal stem cells (C57Bl/6-TgN (ACTbECGF)10sb)[20] at an original concentration of 10^5/mL were seeded into these wells at 40 μL per well giving a final concentration of about 4000 cells/well. Cells were cultured in complete culture medium (CCM) which consisted of 10.0 % fetal calf serum (FCS) and 10 % house serum in α MEM with L-glutamine and penicillin/streptomycin for 7 days. Osteogenic differentiation media (ODM) was prepared by taking 192mL CCM and adding 10 nM dexamethasone (200 μL of 1:100 dilution of 1 mM stock solution in deionized (DI) water), 20 mM β-glycerol phosphate (8 mL of 0.5 M stock in CCM), and 50 μM L-ascorbic acid 2-phosphate (50 mM stock solution in DI water)[21]. Adipogenic differentiation media (ADM) was prepared from 200 mL of CCM with 0.5 μM dexamethasone (100 μL of 1 mM stock in DI water), 0.5 μM isobutylmethylxanthine (20 μL if 5 mM stock in methanol) and 50 μM indomethacin (333 μL of 30 mM stock in methanol)[21]. Control experiments were conducted by incubating cells in CCM on the microcantilevers, on flat pieces of PDMS, and also in normal plastic tissue culture plates. Additionally, cells were also cultured on flat PDMS and in plastic tissue culture dishes in adipogenic and osteogenic differentiation media. Cells were incubated at 37 °C with 5 % CO_2 in the appropriate differentiation or control media which was changed every three to four days. Cells were harvested 7, 10, 15, and 18 days after the initial 7 days of culture and fixed prior to staining to access differentiation. All differentiation reagents were purchased from Sigma (St Louis, MO).

Cell staining

Prior to staining, the incubated cells were rinsed with PBS and then incubated with neutral buffered formalin (NBF) for one hour at room temperature. Cells were then rinsed with either DI water (ODM) or PBS (ADM). Cells were then incubated for 20 minutes at room temperature with Alizarin Red S for detection of osteogenesis or Oil Red O for detection of adipogenesis[21,22]. Cells were rinsed again with DI water or PBS and visualized by light microscopy.

Image processing

Stained images were imaged using a Qcolor 5 (QIMAGING™) CCD color camera. At each time point, at least three different fields were imaged for each spatial density (1 μm, 2 μm and 4 μm) per well. There were three wells each for the two different heights. This gave a total of nine fields per time point for each of the two different heights. To access the stained cells for fat droplet formation after induction of adipogenic differentiation, the images were processed using standard image processing techniques, some of which had been implemented as ImageJ plugins. Color images were converted to gray scale with 256 levels (8 bit). The images were then segmented using the otsu algorithm for auto thresholds[23,24]. This yielded a binary image that could then be processed and analyzed for areas of interest. The minimum size for objects was set at 500 pixels and the maximum was set to infinity. The "analyze particles algorithm" from ImageJ was used and outputs were recorded together with a summary for each image analyzed which recorded the total number of identified particles, the total area, the average area, and the area fraction.

Results and Discussion

Osteogenic differentiation

We expected that the 2 μm tall microcantilevers which had greater average shear stiffness (> 10 KPa based on design parameters) would cause the cells to differentiate farther

down the osteogenic pathway. The 5 μm tall ones with lower average shear stiffness (< 10 KPa) would have less of an effect. Thus, we expected that cells cultured on the 2 μm tall microcantilever arrays would excrete more calcium than the cells on the 5 μm tall arrays.

Alizarin Red S which was used as our stain for detection of osteogenic differentiation does not stain individual cells but rather detects the presence of calcium excreted by the cells. Cells incubated in osteogenic differentiation media became confluent and formed monolayers of cells at a much higher rate than was initially anticipated. Due to the highly confluent monolayer of cells at harvest, there were large sections that showed the red stain though this could not be determined for individual cells. We did not perform any analysis to access the size of areas that had the Alizarin Red stain.

However, a general trend was observed for the arrays that were imaged. In most cases, cells that had been cultured on microcantilevers that had 1 μm edge-to-edge spacing maintained greater contact with the arrays and exhibited less contraction and release from the substrate. It is plausible that contraction and release may be indicative of a more myogenic phenotype. This trend was observed for cells harvested on both day 15 and day 18. The heights of the microcantilevers did not seem to be a factor as the trend was the same for both 2 μm tall and 5 μm tall microcantilevers. In some cases the entire monolayer had contracted and released from the array. This was especially true for the microcantilevers with 4 μm edge-to-edge separation. Figure 7.3 and Figure 7.4 show color images of the observations for cells harvested on day 15 and 18, respectively. One possible explanation for this observation is the differences in area of contact for the three different spatial densities the 1 μm edge-to-edge spacing providing the greatest.

Another possible explanation is the contractile state of the monolayer at the time of fixing and staining. The lower density arrays having lower values of average shear stiffness could cause the monolayers to contract to a greater degree than those on the higher density arrays. We observed during the culturing period and prior to harvesting for fixing and staining that these contracted monolayers wrapped up into folded sheets or balled up in some cases. This balled up or folded sheets would not be ideal for adhering to the arrays and therefore lifted off. The most plausible explanation, however, could be the fact that

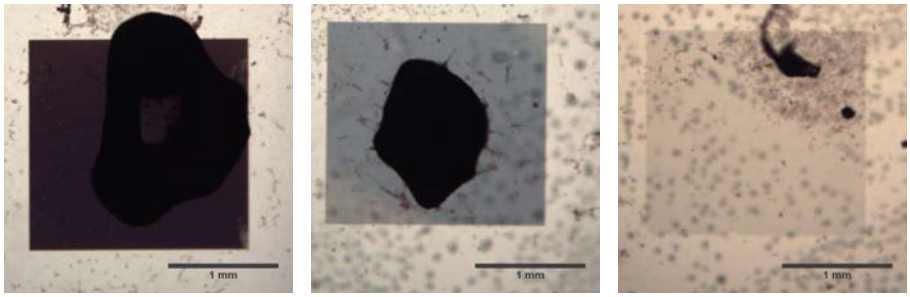

(A) 1 μm spacing **(B)** 2 μm spacing **(C)** 4 μm spacing

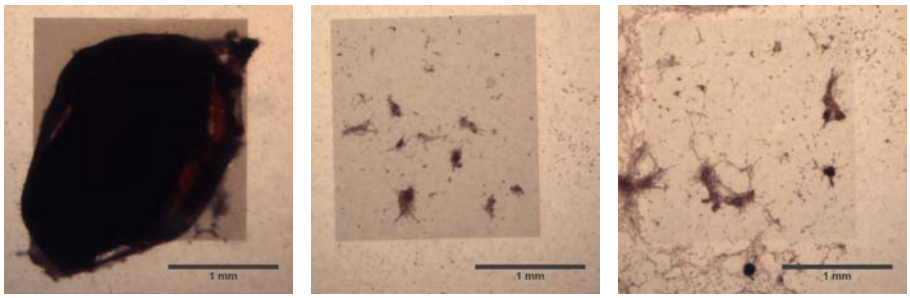

(D) 1 μm spacing **(E)** 2 μm spacing **(F)** 4 μm spacing

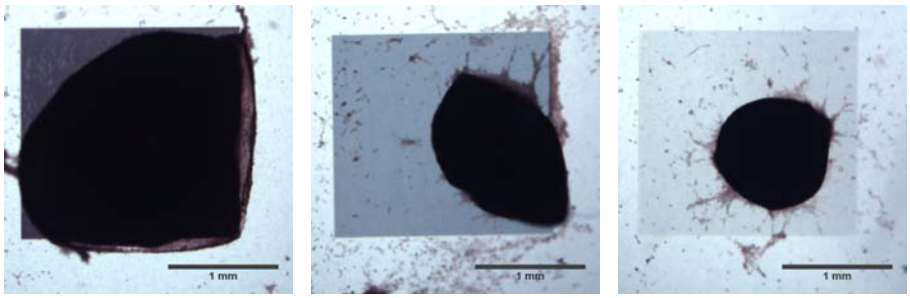

(G) 1 μm spacing **(H)** 2 μm spacing **(I)** 4 μm spacing

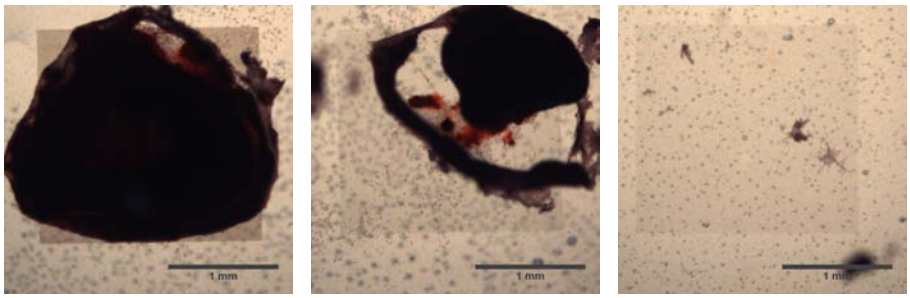

(J) 1 μm spacing **(K)** 2 μm spacing **(L)** 4 μm spacing

Figure 7.3 Osteogenic stains at day 15. Color images of Alizarin Red stains for cells on microcantilevers 5 μm tall (A) - (F) and 2 μm tall (G) - (L) harvested at day 15. In both cases microcantilevers with 1 μm edge-to-edge spacing have cell monolayers that are almost intact. Microcantilevers with 4 μm edge-to-edge spacing have few monolayers remaining. Scale bars are 1 mm.

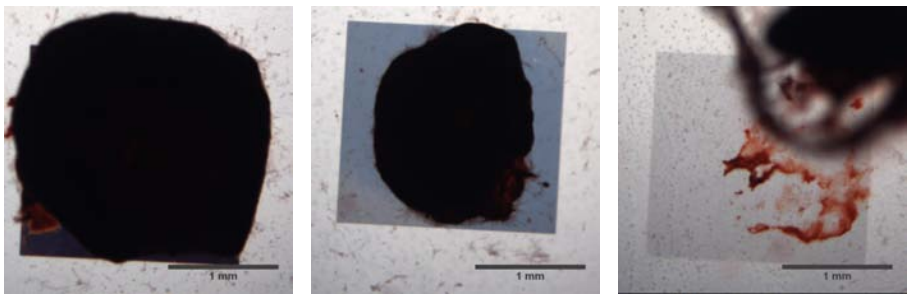

(A) 1 μm spacing **(B)** 2 μm spacing **(C)** 4 μm spacing

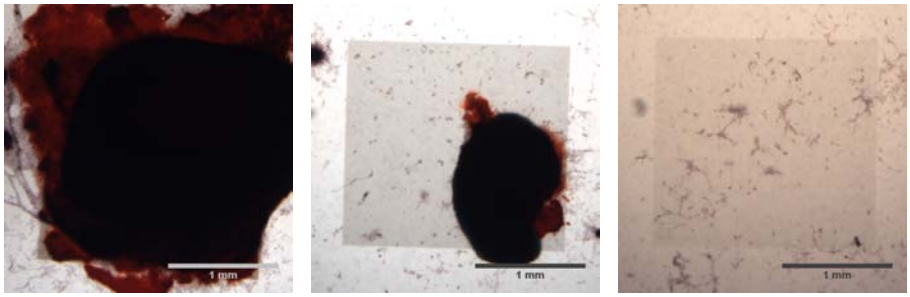

(D) 1 μm spacing **(E)** 2 μm spacing **(F)** 4 μm spacing

Figure 7.4 Osteogenic stains at day 18. Color images of Alizarin Red stains for cells on microcantilevers 5 μm tall (A) - (C) and 2 μm tall (D) - (F) harvested at day 18. Microcantilevers with 1 μm edge-to-edge spacing have cell monolayers that are almost intact. Microcantilevers with 4 μm edge-to-edge spacing have less of an intact monolayer. Scale bars are 1 mm.

the 1 μm edge-to-edge separation provides the best spatial density for anchoring of the monolayer to the PDMS substrate. Further support of this explanation was the general observation that monolayers of cells grown on flat pieces of PDMS as controls generally released from the PDMS during the fixing and staining process, and in osteogenic differentiation medium, only 1 out of 9 (11%) of all those harvested had an intact monolayer of cells. To test the hypothesis that this observation is a result of better anchorage, focal adhesion stains could be done to access the quality of adhesion on the seven different substrate types. It is still possible that two or more of these factors could provide the best explanation.

Adipogenic differentiation

Oil droplets were visible after eight days of culture in the differentiation media, even prior to staining with Oil Red O. This remained the case for the duration of the experiments.

Figure 7.5 shows images taken of cells on flat PDMS as well as on the microcantilevers with heights of 2 μm and 5 μm prior to fixing and staining with Oil Red O on day 15 of culture in the differentiation media.

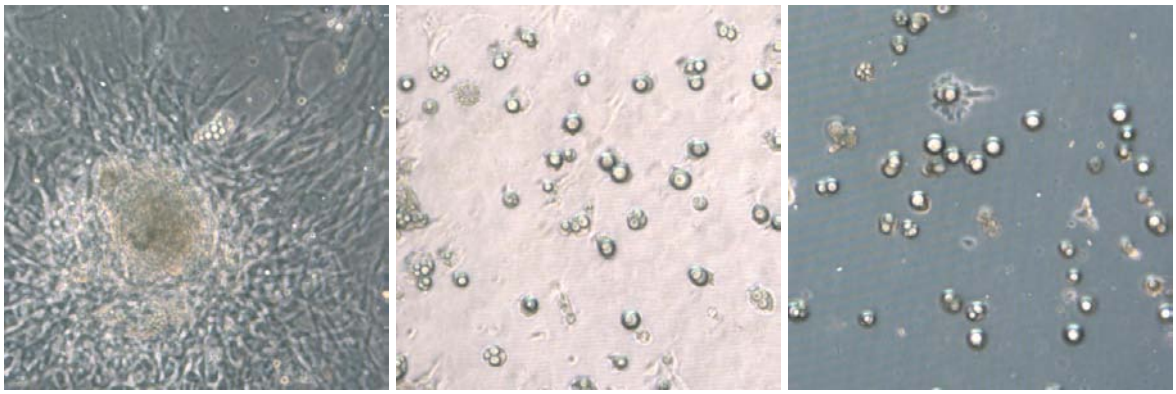

(A) Flat PDMS **(B)** 2 μm tall, 1 μm spacing **(C)** 5 μm tall, 1 μm spacing

Figure 7.5 Oil droplets prior to staining.

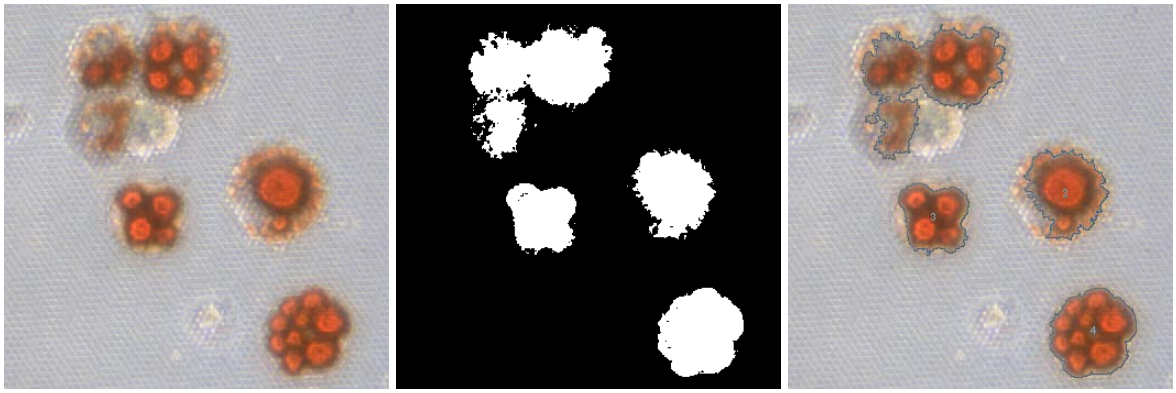

(A) Original Image **(B)** Segmented Image **(C)** Overlay Image

Figure 7.6 Image processing of adipogenic images. (A) Original image showing oil droplets stained with Oil Red O. (B) Segmented output of from otsu threshold. (C) Overlay showing identified regions.

Fixed and stained cells were analyzed using image processing algorithms available as general plugins in ImageJ[25,26]. Output data consisted of counts for identified regions for each image analyzed as well as summary data which included average size of identified regions, total areas, and area fractions. Figure 7.6(A) shows part of one such image. The

segmented image using otsu 8-bit threshold algorithm from ImageJ is shown in Figure 7.6(B) . The overlay showing the identified regions is shown in Figure 7.6(C). Since in some cases there was either significant overlap of the droplets or clustering, watershed separation or other similar techniques could not be applied.

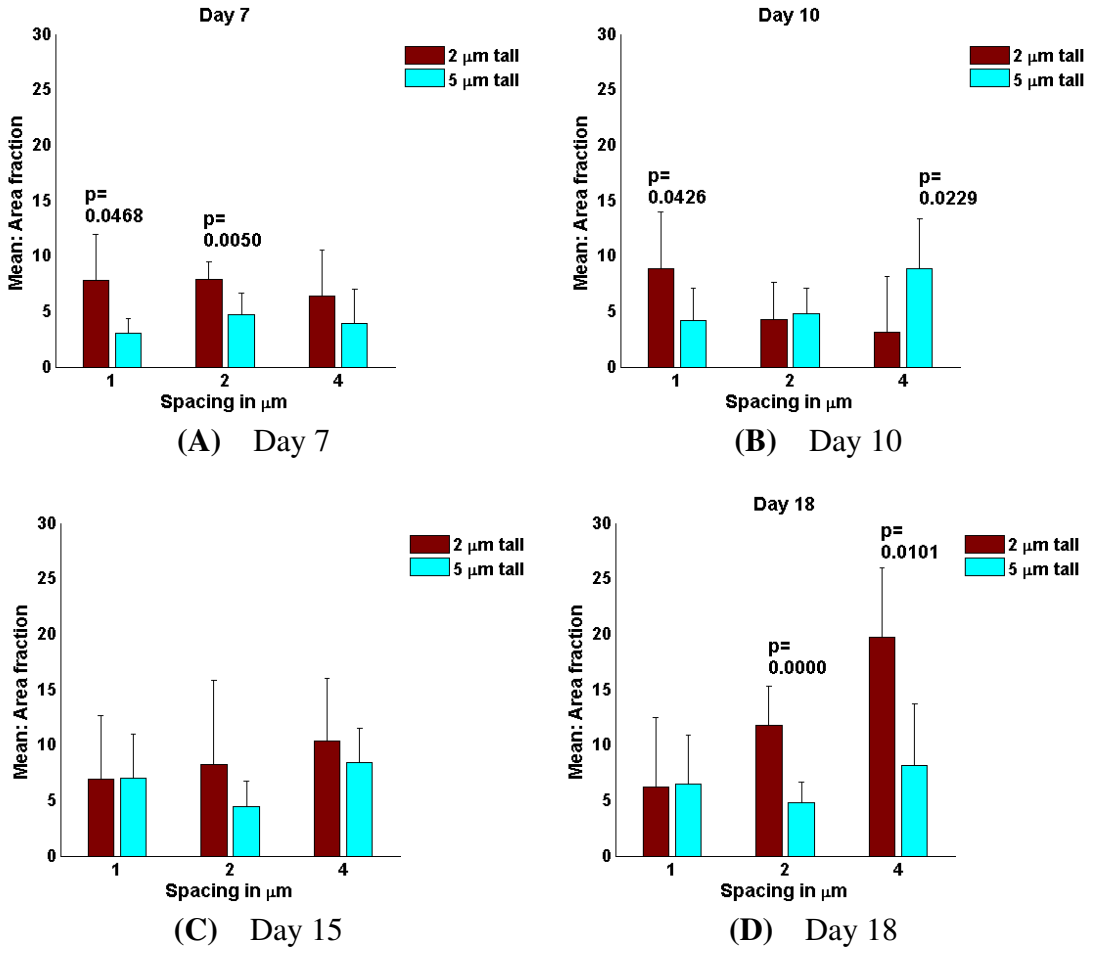

Figure 7.7 Mean values for area fractions of oil droplets for edge-to-edge spacings of 1 μm, 2 μm and 4 μm at harvest day 7 (A), 10 (B), 15 (C) and 18 (D).

Figure 7.7 shows bar charts of means of the area fractions from the summary analysis generated by the analyze particles plugin in ImageJ. This is for spacings of 1 μm, 2 μm, and 4 μ for the 2 μm and 5 μm tall microcantilevers. The error bars were plotted using the one standard deviation from the mean values. Figure 7.8 shows bar fewer oil droplets than the 5 μ cantilevers since they were generally stiffer compared to the 5 μm cantilevers.

The bar charts suggest otherwise. The mean values for area fraction and the average

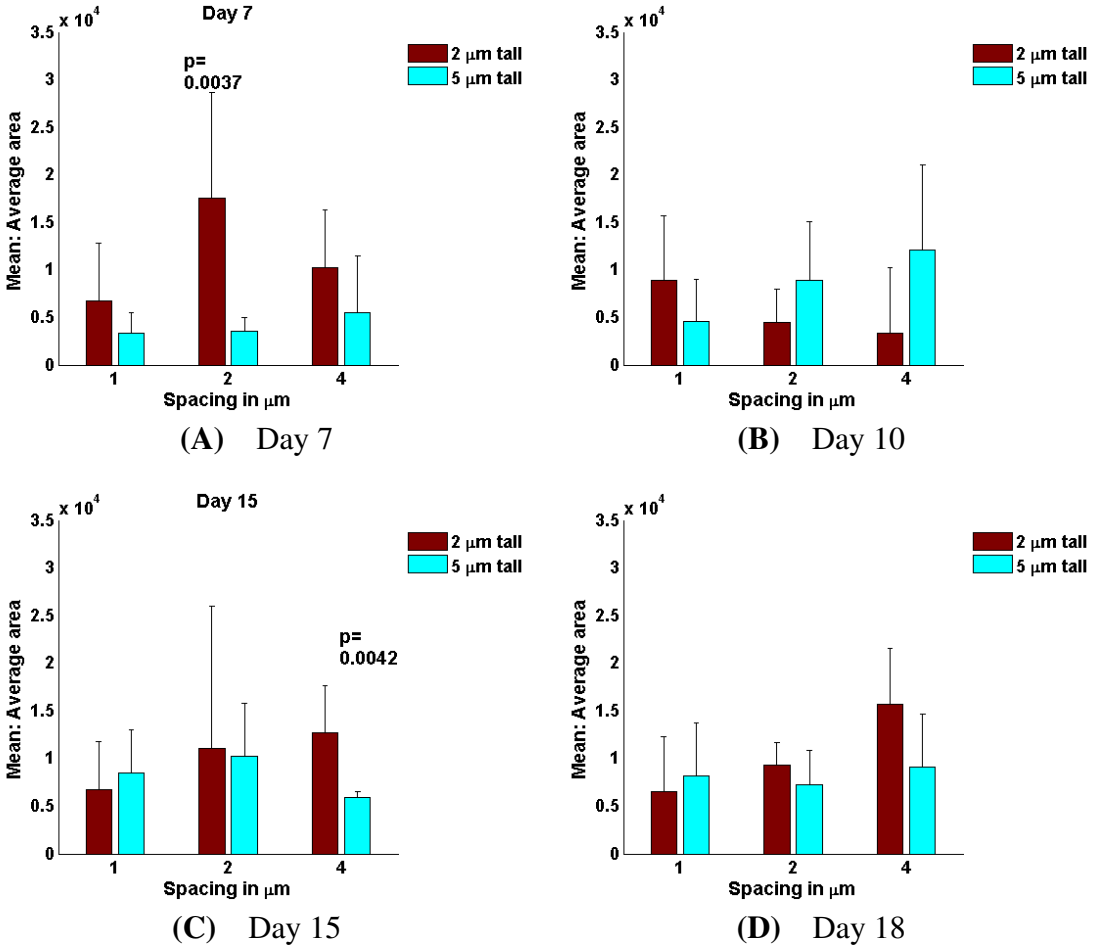

Figure 7.8 Mean values for average area for edge-to-edge spacings of 1 μm, 2 μm and 4 μm at harvest day 7 (A), 10 (B), 15 (C) and 18 (D).

area show that in most cases the values for the 2 μm tall microcantilevers were much higher than in the case for 5 μm. On harvest day 7 statistically significant differences (t-test with 0.95 confidence interval) were obtained for the area fraction and average area for the arrays with 2 μm spacing. On day 18, there was a significant difference between the 2 μm tall microcantilevers and the 5 μm tall microcantilevers for the arrays with 2 μm and 4 μm spacing. There was only one case (Day 10 with 4 μm spacing) in which the area fraction or the average area for 5 μm tall arrays was greater than that for 2 μm tall arrays.

It must be pointed out that in computing the area fraction the total area of the imaged plane is used, which could introduce some bias. A more viable alternative would be to normalize the area with the total cell area. However, this could not be done since for most images taken the cell outlines were not visible and could not be clearly demarcated. Computing this metric in this way would be better since obviously the droplet formation is

dependent on total number of cells present which would be directly related to total cell area. A similar argument can be made in the case for the average area. A large number of cells clustered together would in general produce more oil droplets. Since it was not possible to use any kind of watershed algorithm to delineate individual oil droplets in a cluster, segmentation normally produced one area (particle). This can be seen in Figure 7.6(A) - 7.6(C) where the individual droplets in the area designated as "4' are lumped together. This increased the average size and hence one could not differentiate between many small droplets clustered together versus one big droplet. In comparing the average total counts of areas identified as having fat droplets, day 18 with 2 μm spacing was the only case in which there was a statistically significant difference(Figure 7.9) and in this case too, the 2 μm tall microcantilever arrays had more counts than the 5 μm tall arrays.

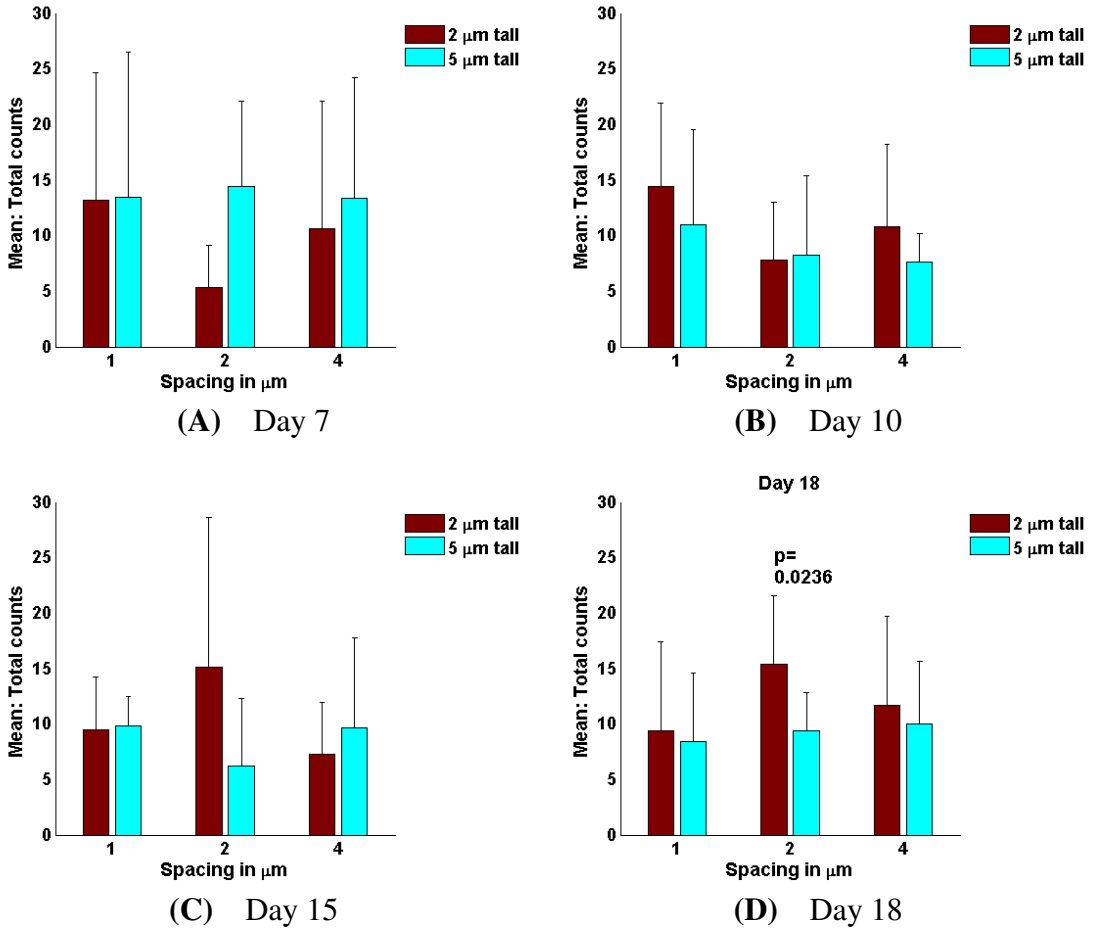

Figure 7.9 Mean values for total counts for edge-to-edge spacings of 1 μm, 2 μm and 4 μm at harvest day 7 (A), 10 (B), 15 (C) and 18 (D).

One explanation of the unexpected results could be due to differences in adhesion. We observed that there was reduction in the total number of cells after the fixing and staining process. If the 2 μm tall microcantilevers provided better anchorage for the cells than the 5 μm tall ones, then there would be many more cells left for analysis in those cases. This could lead to the kind of results reported above.

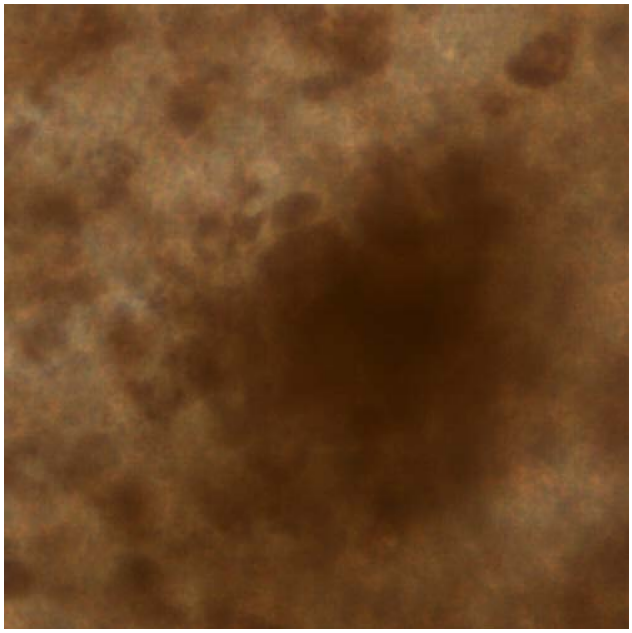

Figure 7.10 Image showing background staining from controls

Controls for the experiments consisted of growing cells in the two differentiation media on normal Petri dishes, as well as on flat pieces of PDMS. Cells were also grown on the different substrates but in normal culture medium. Cells grown on the flat PDMS could not be analyzed. They formed monolayers and then released from the substrate during the fixing and staining process. In some cases there were droplets visible before the staining process as shown in Figure 7.5(A). This could either be due to poor adhesion or a highly contracted state. Similar effects were seen with the cells on the Petri dishes. Cells cultured on the microcantilevers in normal culture medium were also stained with Oil Red O to test for adipogenic differentiation. In most cases any stains detected were regarded as false positives due to background stains that could not be removed even after several washes in PBS. Figure 7.10 shows one example, a background stain from cells that had been

cultured on microcantilevers that were 5 μm tall with 1 μm spacing and that were stained seven days after the cells were switched to differentiation media.

Summary and Conclusions

We used microcantilevers fabricated from silicon molds that had been etched using cryogenic etching techniques to examine how mesenchymal stem cells would respond while being cultured in differentiation media that would elicit adipogenic or osteogenic differentiation. These arrays of microcantilevers had three different spatial densities and two distinct heights. We observed that there were significant differences in cell monolayer adhesion on the microcantilevers for cells cultured in osteogenic differentiation media. Microcantilevers with the highest spatial densities irrespective of the height had the highest percentage of intact monolayers. Using image processing techniques the oil droplets formed during adipogenic differentiation were analyzed. Results showed that contrary to our expectations 2 μm tall microcantilevers which have a higher average shear stiffness than the 5 μm tall microcantilevers had areas of droplets whose average size was higher. There was no difference observed for number of identified areas. It must be acknowledged that the image processing techniques that were employed may not have been optimal for segmenting and identifying the oil droplets. For example Sezgin & Sankur[27] give an extensive review of segmentation algorithms (40 selected thresholding methods) and future work could involve exploring some of these rather than the Otsu method that was used.

Finally, it must be mentioned that only two distinct heights were used in our experiments. It is still possible to examine how the cells would behave on microcantilevers much taller than 5 μm, which would represent arrays with shear stiffness much lower. However, fabricating these may not be possible using current molding techniques where the mold must be separated from the master after casting. Due to limitations on aspect ratios, this becomes untenable for ratios greater than about 10:1. Sacrificial methods such as using wax molds which can be melted, may need to be explored[28].

Acknowledgements

We thank Ronald Reiserer for help in machining teflon molds for curing PDMS at higher temperatures and Phil Samson for machining brass molds for making culture wells. Mesenchymal stem cells were obtained through a materials transfer agreement with Tulane University to Susan R. Opalenik. This work was supported by the Vanderbilt Institute for Integrative Biosystems Research and Education (VIIBRE) and the Center for Nanophase Material Science (CNMS) , Oak Ridge National Laboratory, (ORNL), Oak Ridge,TN.

References

[1] Seydoux, G., Braun, R. E. Pathway to Totipotency: Lessons from Germ Cells. *Cell* **127**, 891–904, 2006.

[2] Pedersen, R. A. Embryonic stem cells for medicine. *Scientific American* **280**, 68–73, 1999.

[3] Vallier, L., Pedersen, R. A. Human embryonic stem cells - An in vitro model to study mechanisms controlling pluripotency in early mammalian development. *Stem Cell Reviews* **1**, 119–130, 2005.

[4] Till, J. E., McCulloch, E. A. Hematopoietic Stem-Cell Differentiation. *Biochimica Et Biophysica Acta* **605**, 431–459, 1980.

[5] Orkin, S. H., Zon, L. I. Hematopoiesis: An evolving paradigm for stem cell biology. *Cell* **132**, 631–644, 2008.

[6] Caplan, A. I. Mesenchymal Stem-Cells. *Journal Of Orthopaedic Research* **9**, 641–650, 1991.

[7] Pittenger, M. F., *et al.* Multilineage potential of adult human mesenchymal stem cells. *Science* **284**, 143–147, 1999.

[8] Watt, F., Hogan, B. Out of Eden: Stem cells and their niches. *Science* **287**, 1427–1430, 2000.

[9] Caplan, A. I., Bruder, S. P. Mesenchymal stem cells: building blocks for molecular medicine in the 21st century. *Trends in Molecular Medicine* **7**, 259–264, 2001.

[10] Gage, F. H. Mammalian neural stem cells. *Science* **287**, 1433–1438, 2000.

[11] Ratajczak, M. Z., *et al.* Hunt for pluripotent stem cell - Regenerative medicine search for almighty cell. *Journal of Autoimmunity* **30**, 151–162, 2008.

[12] Prockop, D. J. Marrow stromal cells as steam cells for nonhematopoietic tissues. *Science* **276**, 71–74, 1997.

[13] Wakitani, S., Saito, T., Caplan, A. I. Myogenic Cells Derived From Rat Bone-Marrow Mesenchymal Stem-Cells Exposed To 5-Azacytidine. *Muscle & Nerve* **18**, 1417–1426, 1995.

[14] Jiang, Y. H., *et al.* Pluripotency of mesenchymal stem cells derived from adult marrow. *Nature* **418**, 41–49, 2002.

[15] Engler, A., Sen, S., Sweeney, H., Discher, D. Matrix elasticity directs stem cell lineage specification. *Cell* **126**, 677–689, 2006.

[16] Brown, X. Q., Ookawa, K., Wong, J. Y. Evaluation of polydimethylsiloxane scaffolds with physiologically-relevant elastic moduli: interplay of substrate mechanics and surface chemistry effects on vascular smooth muscle cell response. *Biomaterials* **26**, 3123–3129, 2005.

[17] Carrillo, F., *et al.* Nanoindentation of polydimethylsiloxane elastomers: Effect of crosslinking, work of adhesion, and fluid environment on elastic modulus. *Journal Of Materials Research* **20**, 2820–2830, 2005.

[18] Schneider, F., Fellner, T., Wilde, J., Wallrabe, U. Mechanical properties of silicones for MEMS. *Journal Of Micromechanics And Microengineering* **18**, 065008, 2008.

[19] Choi, K., Rogers, J. A Photocurable Poly(dimethylsiloxane) Chemistry Designed for Soft Lithographic Molding and Printing in the Nanometer Regime. *J. Am. Chem. Soc.* **125**, 4060–4061, 2003.

[20] Peister, A., Mellad, J. A., Larson, B. L., Hall, B. M., Gibson, L. F., Prockop, D. J. Adult stem cells from bone marrow (MSCs) isolated from different strains of inbred mice vary in surface epitopes, rates of proliferation, and differentiation potential. *Blood* **103**, 1662–1668, 2004.

[21] Reger, R., Tucker, A., Wolfe, M. *Mesenchymal Stem Cells: Methods and Protocols*, vol. 449 of *Methods in Molecular Biology*. Humana Press, 2008.

[22] Chamberlain, G., Fox, J., Ashton, B., Middleton, J. Concise Review: Mesenchymal Stem Cells: Their Phenotype, Differentiation Capacity, Immunological Features, and Potential for Homing. *Stem Cells* **25**, 2739–2749, 2007.

[23] Ostu, N. A Threshold Selection Method from Grey-Level Histograms. *IEEE Transactions on Systems, Man, and Cybernetics* **9**, 62 – 66, 1979. Minimize inter class variance.

[24] Jiao, S., Li, X., Lu, X. An Improved Ostu Method for Image Segmentation. In *Signal Processing, 2006 8th International Conference on*, vol. 2, –. 2006.

[25] Thevenaz, P., Ruttimann, U., Unser, M. A pyramid approach to subpixel registration based on intensity. *Image Processing, IEEE Transactions on* **7**, 27–41, 1998.

[26] Abramoff, M., Magelhaes, P., Ram, S. Image Processing with ImageJ. *Biophotonics International* **11**, 36–42, 2004.

[27] Sezgin, M., Sankur, B. Survey over image thresholding techniques and quantitative performance evaluation. *Journal Of Electronic Imaging* **13**, 146–168, 2004.

[28] Große, S., Schröder, W., Brücker, C. Nano-newton drag sensor based on flexible micro-pillars. *Measurement Science and Technology* **17**, 2689–2697, 2006.

CHAPTER 8

SUMMARY AND FUTURE WORK

Kweku A. Addae-Mensah

Department of Biomedical Engineering

Vanderbilt University, Nashville, TN

The overall goal of this project was to microfabricate vertical microcantilever arrays made from PDMS that could be used as a platform to study cell biomechanics and mechanobiology *in vitro*. These microcantilever arrays were fabricated using two different methods.

a. Soft lithography using SU-8 photoresist to make a master mold followed by double casting to obtain the final device.

b. Cryogenic etching of silicon to obtain the master molds followed by casting of PDMS microcantilevers.

The fabricated microcantilever array was used to examine biomechanics and mechanobiology of different cell types.

The review of measurement techniques for cellular biomechanics *in vitro* in chapter 2 outlined the importance of studying cell biomechanics and mechanobiology. The various tools and techniques that have been developed were discussed and were placed in two general categories, "active" and "passive", as well as methods that involved a combination of the two. Noteworthy were the tools that had been developed using silicon MEMS technology. The advantages and disadvantages of these methods were considered as well as some of the pertinent results that had been obtained. Of particular interest in the passive tools were the vertical microcantilever arrays that had originally been reported by Tan *et al.*[1]

Chapter 3 dealt with microfabrication of the vertical microcantilever arrays using methods similar to Tan *et al.*[1] Some of the limitations of the soft lithography methods were identified. We introduced the use of commercially available contrast enhancement materials that enabled us to reduce feature size and pitch spacing by 33 and 44%, respectively. Other problems identified included the inability to accurately track deflections of microcantilevers when using a stack of DIC images. The problems associated with contact printing of fluorescent proteins in an attempt to overcome this limitation were addressed. A new method which involved labeling the microcantilevers with fluorescent quantum dots

was introduced. The traction forces and change in mean prestress for live human airway smooth muscle cells were examined using the quantum dot labeled microcantilevers. The traction forces for fixed human airway smooth muscle cells were presented. Some of the limitations of this technique were also presented.

One of the limitations of the soft lithography technique that was pointed out in chapter 3 was the inability to fabricate microcantilevers with pitches smaller than 5 μm or diameters less than 2 μm. This is due to the contact photolithography which is used.

In order to be able to apply active forces to cells attached to the microcantilever array, it was deemed necessary to find a way to either move individual microcantilevers or groups of microcantilevers. Moving single cantilevers was achieved using a pulled glass micropipette which was moved using electronically controlled micromanipulators. There were some problems associated with this technique. To be able to move a group of microcantilevers, a new technique was developed which enabled the attachment of SU-8 structures to the microcantilevers. This was outlined in chapter 4. The technique involved the use of PVA as a lift-off agent. It was demonstrated that the adhesion strength of these structures to the PDMS was adequate. Data showed that these structures could be agitated with a pulled glass micropipette and that microcantilevers attached to them exhibited about the same maximum displacements. The time at which these displacements occurred was approximately the same for all the trials.

Chapter 5 dealt with experiments conducted to investigate cardiac myocyte adhesion and adaptation, and contractile dynamics on the microcantilever arrays. The microcantilevers affected the way in which the myocytes built their myofibrils in the process of adapting. Projections of the two-dimensional FFT on a three-dimensional logarithmic scale, showed differences in the peak value equivalent to the first harmonic after six days of culture on the microcantilevers as compared to at isolation when then was no difference. Spontaneously contracting myocytes on the microcantilevers were also analyzed for force. Using a 2×2 kernel, divergence and curl metrics were computed. Alternating regions of contraction and relaxation were observed in some myocytes. This was not evident when raw displacement data was plotted. Space-time plots however, did not reveal contraction

and relaxation waves as was expected probably due to low sampling frequency in the original time lapse acquisition. We did not observe any correlations between the divergence and curl metrics.

Chapter 6 looked at an alternative method to fabricate the master molds for the micro-cantilever arrays. This used cryogenic etching of silicon similar to the DRIE technique that had briefly been mentioned in chapter 3. The critical parameters needed to be tuned to obtain the desired sidewall profile were examined. This technique produced much smoother side walls than those etched using the "Borsch process". Results from PDMS molding on the fabricated master molds were presented. It was much easier to separate the PDMS molds from the silicon master molds than previous silicon master molds that had been etched. However, damage we attribute to stiction which was initially observed for the Borsch process molds was also observed with the newer molds. Curing the molds at 110°C eliminated this problem.

Chapter 7 examined mesenchymal stem cell responses to microcantilevers that were fabricated using the technique outlined in chapter 6 . These microcantilevers were designed to have different stiffness.

Future Work

Two of my original sub aims under specific aim 2 were to

a. Investigate the response of cells when mechanical perturbation is applied to selected microcantilevers

b. To examine the effects of certain drugs and reagents that are known to affect the contractile state and stiffness of human airway smooth muscle cells.

These experiments could not be done. However there is still a rationale for pursuing these experiments further. Living tissues in physiological environments are invariably exposed to different mechanical stresses and strains. These mechanical forces have significant effects on cell and nucleus shape and also play an important role in regulation of cell function. This is because the cytoskeletons of cells reorganize in response to mechanical forces. This

reorganization has indirect effects on the physiological state of the cells as the cytoskeleton is linked to many receptors which are coupled to signaling pathways[2–5]. As outlined in chapter 2, methods used to investigate this relationship have involved the use of fluid shear stress and mechanical stretch[6,7]. Though these methods are widely used they do not allow the simultaneous measurement of changes in traction forces. An alternative method which uses a combination of MTC and beads embedded in a flexible substrate is an improvement. The study looks at the relationship between the stiffness of the cell and its internal tensile stress[8]. The disadvantage with the method is that one cannot probe the substrate directly to elicit the response. It must be noted that Sniadecki *et al.*[9] have developed a method where magnetic nanowires were incorporated in vertical microcantilevers which enabled application of active forces similar to what this technique is intended to achieve. It will therefore be interesting to see the outcome for experiments using this technique. To this end lithography masks for a third generation of structures that could be attached to the microcantilevers have been designed (Figure 8.1(A)). A design configuration for a possible fourth generation device is also shown in Figure 8.1(B). The device could also be used for investigating other phenomena. It could be used as a possible assay for cell-cell adhesion studies and also for traction mediated cytokinesis.

I have been able to demonstrate through preliminary experiments that human airway smooth muscle cells attach to these structures as well as to the microcantilever arrays. Figure 8.2(A) and 8.2(B) show two images taken in DIC mode demonstrating this. The next step would be to get cells to attach on the newer designs and then see if the experiments mentioned can be done.

Contraction and the contractile state in smooth muscle is regulated by the concentration of cytoplasmic Ca^{2+} which comes from both outside the cell, entering due to propagation of an action potential, as well as from the diffuse sarcoplasmic reticulum. The intracellular calcium binds to calmodulin, which initiates the contractile response. There are generally three recognized ways in which the contractile state of smooth muscles can be altered: actions potentials; a change in the local environment due to changes in pH, or CO_2 tension; and the action of hormones binding to receptors which then affect the signaling

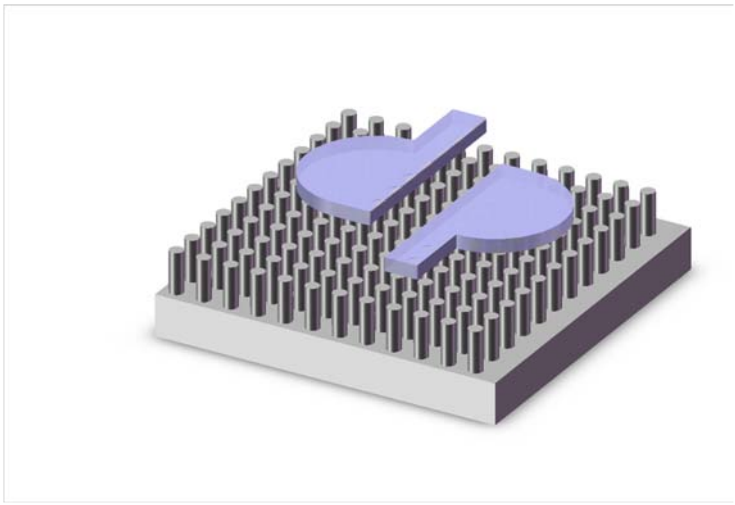

(A)

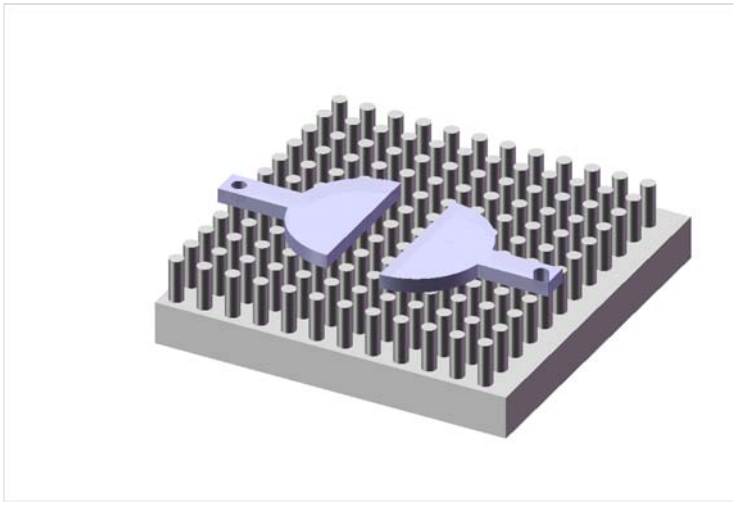

(B)

Figure 8.1 Future designs (A)Schematic showing third generation design of structures that could be attached to microcantilevers and used for active probing. Lithography masks have been designed for these. (B) Schematic showing possible configuration for fourth generation structures

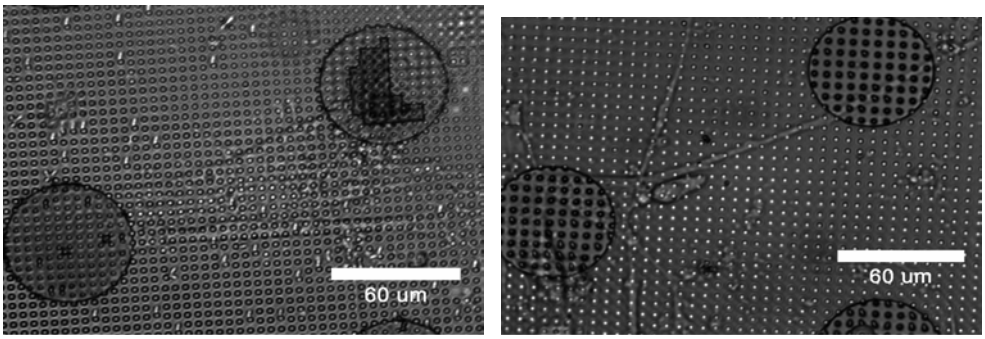

(A) **(B)**

Figure 8.2 Images showing cells spanning and attached to both microcantilever arrays and circular discs.

pathways,though these factors are not mutually exclusive. Molecular mechanisms which mediate smooth muscle relaxation normally involve β-adrenergic stimulation which results in an increase in cAMP and a consequent lowering of intracellular Ca^{2+} concentration[10–12]. The contractile state and mechanical properties of airway smooth muscle (ASM) in the lung have important connections in the development of the physiological conditions related to asthma. It is normally characterized by the reduced capacity of airways to dilate after administration of β2-adrenergic agonists. Previous studies of the contractile behavior of airway smooth muscle cells have used tissue strip preparations. Recently it has been demonstrated that ASM cells passaged in culture can be used as a representative model system. This is because the cells retain the functional responses to agonists that affect some of the signaling pathways that are associated with asthma. Examining the effects of certain drugs and reagents such as potassium chloride (KCl), acetylcholine, isoproterenol (ISO) and dexamethasone on the contraction and relaxation of Human smooth muscle cells will provide further insight into this phenomenon.

Based on the confocal image results of myocytes on the microcantilever arrays, there is no doubt that remodeling of myofibrils occurs during adaptation. One interesting question that arises then is how this will affect excitation-contraction coupling in the myocytes. This obviously provides an area for future investigation. Results from computing the divergence and curl metrics showed the kind of calcium waves that have been reported extensively in the literature. Mathematical models of this phenomenon have also been developed[13,14]. Some work has also been done to relate the *in vitro* observations with these mathematical models though there still remain some significant questions. Work done in relating the waves to force generation or contraction dynamics has involved the measurement of change in average sarcomere distance. This brings up the question of using higher density microcantilevers. We have been able to fabricate these using cryogenic etching techniques as described in chapter 6. The spacing on some of these are on the order of a single sarcomere. Unfortunately, we were unable to successfully culture the myocytes on these arrays. This could be pursued further as it will provide a unique platform to further investigate these phenomena. Computation of divergence and curls from raw displacement data using these

higher density arrays would provide an additional insight into correlations of these waves with force generation and contraction on scales comparable to the single sarcomere. Other areas that could be explored include how anisotropic microcantilever arrays will affect the observed phenomena. As mentioned, myocytes that were analyzed for force were observed contracting spontaneously. It will be interesting to learn,for example, the outcomes from chemical or electrical pacing of the myocytes. Other questions indirectly related include the effect of inhibiting the contractile apparatus.

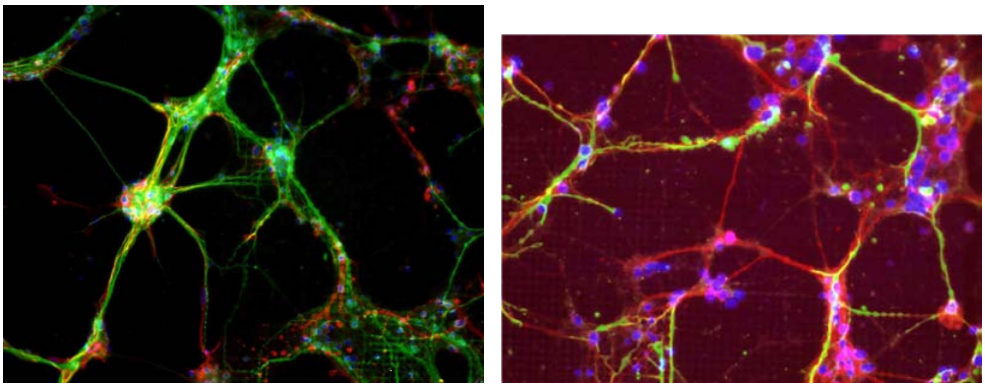

(A) **(B)**

Figure 8.3 Images showing fixed and stained neurons on the microcantilevers

Other possible projects that could be pursued in the future would be to use the arrays as an assay to examine the force generation and contractile forces during the growth of neurons. To this end an initial collaboration was started with Albert Folch's group at the University of Washington, Seattle. They were able to culture cells on our microcantilevers. These had diameters of 3 μm were 10 μm tall, and had three different edge-to-edge spacings of 6, 8 and 9 μm. Initial results are shown in Figure 8.3(A) and 8.3(B). It would be interesting to measure forces generated by these neuronal growth cones and then analyze them using the divergence and curl metrics that was used for examining the cardiac displacement data.

It must be noted that the novelty in this field is remarkable and has provided many opportunities to investigate cell biomechanics. Although there are still some limitations that need to be overcome, the field is rapidly evolving to address some of these issues. A

significant challenge for the future will be to extend some of these techniques and methods to measurement of subcellular phenomena. There are several reasons for this. For example, the cell cytoskeleton has been shown to both support mechanical loads applied to the cell and to generate some of the forces exerted by the cell. It will therefore be necessary to decouple these two to get any measure of quantitative data for cell cytoskeletal mechanics and force generation.

One promising approach has been the use of subcellular laser ablation (SLA) in conjunction with fluorescence recovery after photobleaching (FRAP) to surgically cut portions of the cell cytoskeleton and simultaneously monitor responses.[15] Changes in cell traction forces are determined using the microbeads in the flexible sheets method outlined previously. The combination of active and passive methods may be an alternative route to take in this case. Laser ablation can also be used to determine cell-cell forces in the developing embryo[16,17].

Another challenge deals with the resolution and sensitivities that will be required at this scale. Current techniques are able to detect and produce forces in the piconewton to nanonewton range. If higher resolutions or sensitivities are required, such as in the femtonewton range which may be the case for subcellular recordings, then issues such as thermal effects come into play. Some of the current techniques may not be adequate in this case. The most promising is that of optical tweezers, which have been used to detect and produce forces in the range of a few piconewtons in the study of myosin molecule mechanics[18] and single strand (ssDNA) and double strand (dsDNA) DNA molecules[19,20]. Most of these measurements have been obtained in purified systems where the subcellular components are removed from the cellular environment before measurements are made. Though providing greater insight into cell structure, function, and biomechanics, they do not include temporal and spatial dynamics on the cellular scale, which are equally important and essential for understanding.

One outstanding question is the extent to which all of these techniques and measurement systems inherently affect the behavior and response of the cell; *i.e.*, if the cell behaves in a particular way because of the specific tool and method being used, then is the measured

response a true indication of what was intended to be measured or is it a combination of that and other effects, such as remodeling and reorganization? For example, to what extent does the stiffness of the microcantilever array or the elastomer sheet have on the physiological response of the cells? These devices are not ideally stiff force transducers, but exhibit physical distortions whose amplitudes can approach the dimensions of a cell. It is clear that the stiffness of the substrate can affect cellular phenotype[21,22]. Further studies in the field are needed to find answers to these questions.

Research Considerations

Protection of human subjects

No human subjects were used in this research. The research goal was to develop a platform to investigate cell biomechanics and mechanotransduction. In some cases cells from human donors (human airway smooth muscle cells (HASM)) were used. In such cases all necessary protections were ensured.

In other cases experiments with primary adult rat cardiac myocytes were performed. The laboratory in which these isolations were performed ensured that all protocols used were in accordance with guidelines of the Animal Care and Use Committee of Vanderbilt University and the National Institutes of Health Guide for the Care and Use of Laboratory Animals.

Societal implications

Many diseases have been linked to the contractile state, mechanical properties and the mechanotransduction process, all of which can be traced down to the single cell level. The application of these or similar techniques to biology may allow questions to be answered that have heretofore proved resistant to quantitative analysis. More importantly, the development of new measurement modalities may provide answers to questions that might not have been previously asked, in that there were no means to provide the answers. It is important that those who can bring new force-measurement technologies to biology work

closely with the scientists seeking to understand biological forces, so that the measurement techniques and the questions they answer can evolve in consort.

References

[1] Tan, J., Tien, J., Pirone, D., Gray, D., Bhadriraju, K., Chen, C. Cells lying on a bed of microneedles: An approach to isolate mechanical force. *PNAS* **100**, 1484–1489, 2003.

[2] Komuro, I., *et al.* Mechanical Loading Stimulates Cell Hypertrophy and Specific Gene-Expression in Cultured Rat Cardiac Myocytes - Possible Role of Protein-Kinase-C Activation. *Journal of Biological Chemistry* **266**, 1265–1268, 1991.

[3] Kulik, T., Bialecki, R., Colucci, W., Rothman, A., Glennon, E., Underwood, R. Stretch Increases Inositol Trisphosphate and Inositol Tetrakisphosphate in Cultured Pulmonary Vascular Smooth-Muscle Cells. *Biochemical and Biophysical Research Communications* **180**, 982–987, 1991.

[4] Wang, N., *et al.* Mechanical behavior in living cells consistent with the tensegrity model. *PNAS* **98**, 7765–7770, 2001.

[5] Ingber, D. Tensegrity II. How structural networks influence cellular information processing networks. *J Cell Sci* **116**, 1397–1408, 2003.

[6] Sadoshima, J., Izumo, S. Mechanical Stretch Rapidly Activates Multiple Signal Transduction Pathways in Cardiac Myocytes - Potential Involvement of An Autocrine Paracrine Mechanism. *Embo Journal* **12**, 1681–1692, 1993.

[7] Malek, A., Izumo, S. Mechanism of endothelial cell shape change and cytoskeletal remodeling in response to fluid shear stress. *J Cell Sci* **109**, 713–726, 1996.

[8] Wang, N., *et al.* Cell prestress. I. Stiffness and prestress are closely associated in adherent contractile cells. *Am J Physiol Cell Physiol* **282**, C606–C616, 2002.

[9] Sniadecki, N. J., *et al.* From the Cover: Magnetic microposts as an approach to apply forces to living cells. *Proc Natl Acad Sci* **104**, 14553–14558, 2007.

[10] Shore, S. A., Moore, P. E. Regulation of [beta]-adrenergic responses in airway smooth muscle. *Respiratory Physiology & Neurobiology* **137**, 179–195, 2003.

[11] Hubmayr, R., *et al.* Pharmacological activation changes stiffness of cultured human airway smooth muscle cells. *Am J Physiol Cell Physiol* **271**, C1660–C1668, 1996.

[12] Kotlikoff, M., Kamm, K. Molecular Mechanisms of Beta-Adrenergic Relaxation of Airway Smooth Muscle. *Annual Review of Physiology* **58**, 115–141, 1996.

[13] Bugrim, A. E., Zhabotinsky, A. M., Epstein, I. R. Calcium waves in a model with a random spatially discrete distribution of Ca2+ release sites. *Biophysical Journal* **73**, 2897–2906, 1997.

[14] Subramanian, S., Viatchenko-Karpinski, S., Lukyanenko, V., Gyorke, S., Wiesner, T. F. Underlying Mechanisms of Symmetric Calcium Wave Propagation in Rat Ventricular Myocytes. *Biophys. J.* **80**, 1–11, 2001.

[15] Kumar, S., *et al.* Viscoelastic Retraction of Single Living Stress Fibers and Its Impact on Cell Shape, Cytoskeletal Organization, and Extracellular Matrix Mechanics. *Biophys.J.* **90**, 3762–3773, 2006.

[16] Hutson, M., *et al.* Forces for Morphogenesis Investigated with Laser Microsurgery and Quantitative Modeling. *Science* **300**, 145–149, 2003.

[17] Peralta, X., *et al.* Upregulation of forces and morphogenic asymmetries in dorsal closure during Drosophila development. *Biophys.J.* **92**, 2583–2596, 2007.

[18] Finer, J. T., Simmons, R. M., Spudich, J. A. Single myosin molecule mechanics: piconewton forces and nanometre steps. *Nature* **368**, 113–119, 1994.

[19] Bustamante, C., Bryant, Z., Smith, S. B. Ten years of tension: single-molecule DNA mechanics. *Nature* **421**, 423–427, 2003.

[20] Wuite, G. J., Smith, S. B., Young, M., Keller, D., Bustamante, C. Single-molecule studies of the effect of template tension on T7 DNA polymerase activity. *Nature* **404**, 103–106, 2000.

[21] Paszek, M., *et al.* Tensional homeostasis and the malignant phenotype. *Cancer Cell* **8**, 241–254, 2005.

[22] Engler, A., Sen, S., Sweeney, H., Discher, D. Matrix elasticity directs stem cell lineage specification. *Cell* **126**, 677–689, 2006.